HYDROGEL THERAPY FOR RE-SYNOSTOSIS BASED ON THE DEVELOPMENTAL AND REGENERATIVE CHANGES OF MURINE CRANIAL SUTURES

A Dissertation

Presented to

The Academic Faculty

by

Christopher Douglas Hermann

In Partial Fulfillment

of the Requirements for the Degree

Doctor of Philosophy in Bioengineering in the

School of Biomedical Engineering

Georgia Institute of Technology
August 2012

HYDROGEL THERAPY FOR RE-SYNOSTOSIS BASED ON THE DEVELOPMENTAL AND REGENERATIVE CHANGES OF MURINE CRANIAL SUTURES

Approved by:

Dr. Barbara D. Boyan, Advisor
Department of Biomedical Engineering
Georgia Institute of Technology

Dr. Zvi Schwartz
Department of Biomedical Engineering
Georgia Institute of Technology

Dr. Robert E. Guldberg
Department of Mechanical Engineering
Georgia Institute of Technology

Dr. Niren Murthy
Department of Biomedical Engineering
Georgia Institute of Technology

Dr. Michael J. Yaszemski
Department of Orthopedic Surgery
Mayo Clinic

ACKNOWLEDGEMENTS

I would like to first thank my advisors Dr. Barbara Boyan and Dr. Zvi Schwartz for all their support and encouragement over the years. I first had the opportunity to meet Dr. Boyan over 8 years ago when she informed a room full of future engineers she was going to teach us to “think like a cell.” As a graduate student she has constantly challenged and allowed me to constantly find other applications for my research, even when I ran up a $10,000 micro-CT bill with only a vague idea of what we were going to do with all those images. I have been constantly amazed by her passion and dedication for research which may only be eclipsed by her commitment to the students. No matter how busy the schedule she always had an open door to discuss new ideas, problems with research, or for a “life talk.” Over the years Dr. Schwartz has constantly challenged me to work hard and develop new approaches for seemingly impossible problems, all while reminding me that it is far better to be lucky than good. Even if we didn’t always agree at first, he was always looking out for my best interest.

I am also extremely grateful to the members of my committee. Dr. Niren Murthy for all the support and helpful discussions related to the hydrogel. Dr. Robert Guldberg for his continual advice with all things related to micro-CT and mechanical testing. Dr. Michael Yaszemski for all the advice related to my research, carrier path, and the importance of recognizing “you are not what you do”.

I am perhaps most indebted to the army of undergraduate students who have worked with me for the last 4 years. Megan Richards, who has looked at more micro-CT images of the mouse sutures than anyone on the planet. I am amazed that with processing well over 300,000 images she still managed to remain enthusiastic about the project. Regina Chang for her constant positive

attitude in tackling a never ending list of problems related to PCR and histology. Kelsey Lawrence, for never saying no, her help with the countless mouse surgeries, and the analysis of all the scans. Sidd Gadapelli jumped into the frustrating world of Matlab image processing for the work on the Synchondrosis. More recently to Marcus Walker and Henry Mei, for their efforts to translate some of the snake algorithm work for human applications.

I would also like to thank the many clinicians who have over the years been a mentor and colleague of mine. I am eternally grateful to Dr. Marvin Royster for all he has done for me over the last 10 years. From inviting me into the OR before my surgery in high school, to putting me in the “straight jacket” countless times as an engineering student, and then letting me assist with his cases as a medical student he has been a mentor in more ways than one. I constantly amazed by his endless compassion for patients, students, staff, and most importantly his family. I appreciate the time he has spent with me in over 500 cases that I performed with him which served as a much needed reminder of why I am spending so much time in training. I greatly appreciate Dr. Thomas Moore, whose example is one of the major reasons I decided to pursue a career in academic medicine, despite his persistence in trying to convince me that I didn’t really want to waste my time with a Ph.D. and go right into residency. Dr. Joseph Williams was one of the major drivers and motivators of my project. I am extremely grateful for his advice related to the clinical aspects of my project, countless questions, and letting me assist with craniosynostosis surgeries.

I would also like to thank the numerous collaborators who have worked with me on this and other projects: Dr. Oskar Skrinjar for his assistance and advice with the development of the algorithm; Jonathan Server for the help with optimizing and help when things got stuck with Matlab; for Dr. Xinghi Ning for providing an endless supply of the crossliker; Chris Lee for all the support related to our work with the growth plate; Angela Lin the queen of all things micro-CT; Aqua Asberry for all her support with histology; Dr. Laura O’Farrell, Kim Benjamin, and the PRL staff for all their support with the animal care; Dr. Brani

Vidakovic for his assistance with statistical analysis; Drs. Gang Bao and Won Jon Rhee for all things related to molecular beacons; and Dr. Scott Wilson for all his help with the development of the hydrogel.

I would also like to thank the members of the Boyan lab for their support, advice, and friendship over the years. Most importantly, I would like to thank Dr. Rene Olivares-Navarette who initially began the project involving craniosynostosis and has been an endless supply of answers for all aspects related to my project. To Sharon Hyzy for her constant efforts to somehow keep the lab functioning in spite of all the craziness, complications, and “man-looking”. I would also like to thank Chirs Erdman, Sri Vemula, Chelsea Britt, Megan Merritt, and other members of the lab who assisted with an endless number of mouse surgeries. I am also greatful for the fellows in the lab over the years who have assisted the surgeries; Drs. Jonathan Kaye, Scott Cuda, and Dr. John Kalisvart. I would also like to thank Maribel Baker, Brentis Henderson, and Nicole Beach for all their help trying to organize and track down Dr. Boyan.

I would also like to thank my parents for all their support and encouragement over the years. No matter what was going on they always put my brother and I first, making sure that our every need was fulfilled. To my brother Dan for his service to our country, his determination to never give up, and compassion for others…you are my hero in more ways than one.

Lastly but most importantly, I would like to thank my wonderful fiancée Elizabeth McGee. She has the biggest heart of anyone on the planet and has supported me through some of the toughest parts of grad school. She has endured more than her fair share of “I can’t do dinner because I have to inject mice”, vacations interrupted for work related to research, and “I have to work late…Boyan decided we wanted to write a grant that was due last week and left the country again.”

This research was funded by Children’s Healthcare of Atlanta.

TABLE OF CONTENTS

LIST OF TABLES

Supplemental Tables

LIST OF FIGURES

Supplemental Figures

LIST OF SYMBOLS AND ABBREVIATIONS

µCT	micro-computed tomography
µg	micrograms
µm	micro meters
3D	hree dimensional
Acan	aggrecan
bHLH	basic-helix-loop-helix transcription
BMP	bone morphogenic proteins
C_1	Neo-Hookean coeffivient
Chrd	chordin
Col I	collagen I
Col II	collagen 2
Col X	collagen 10
Col XII	collagen 12
Comp	collagen oligomeric matrix protein
Cor	coronal
CSF	cerebrospinal fluid
CT	computed tomography
DBCO	4-dibenzocyclooctynol
DIFO	difluorinated cycooctyne
Dmp1	dentin matrix protein

DNA	deoxyribonucleic acid
FBS	fetal bovine serum
Fgf	fibroblast growth factor
Fgfr	fibroblast growth factor receptors
GAPDH	lyceraldehyde phosphate dehydrogenase
Grem	Gremlin1
GST	glutathione s-tranferase
H&E	haematoylin and eosin
HA	hydroxyapatite
HCl	hydrocloric acid
Ibsp	bone sialoprotein
ICP	intracranial pressure
IL-1	interlukin 1
IL-6	interlukin 6
Lam	lambdoid
Met	metopic
mgHA	milligrams hydroxyapatite
mL	milliliters
mm	milimeters
mRNA	messenger ribonucleic acid
ng	nanograms
Nog	noggin

Ocn	osteocalcin
PBS	phosphate buffered saline
PEG	poly (ethylene gloycol)
PEG-N3	PEG-based azide
PF	posterior frontal
rmGremlin1	recombinant mouse gremlin
RNA	ribonucleic acid
Runx2	runt-related transcription factor 2
Sag	sagittal
SMAD	SMAD family member
Sos	sphenooccipital synchondrosis
Sost	sclerostin
Sox9	SRY-box containing gene 9
TGF-β	transforming growth factor beta
TNFα	tumor necrosis factor alpha
w:v	weight per volume ratio
σ eng	engineering stress
λ	stretch ratio

SUMMARY

Craniosynostosis is the premature fusion of the cranial sutures early in development that occurs in approximately 1 in 2000 children. If left untreated, craniosynostosis can result in numerous complications related to an increase in the intracranial pressure and/or directly from cranial deformities. This condition can be caused by over 100 known mutations, but most commonly occurs spontaneously. Most cases of craniosynostosis require complex cranial vault reconstruction that is associated with tremendous morbidity. While the complications related to the first surgery are relatively low, the bone rapidly re-grows in up to 40% of children who undergo surgery. This rapid bone growth is called re-synostosis and typically requires additional surgical intervention which is associated with an extremely high incidence of life threatening complications. The overall goal of this research was to develop a therapy to prevent re-synostosis in a pediatric murine model. Our central hypothesis was that the delivery of BMP inhibitors using a click hydrogel would delay rapid post-operative bone growth in our model system.

The development of this surgical model and therapy was based on the analysis of normal and pathologic mouse suture fusion. Mice are a common model of cranial development, but the timing of the normal cranial suture fusion

was poorly understood. To address this we used micro-computed tomography (μCT) to image the posterior frontal and coronal sutures in mice ranging in age from days 6 to 105. The suture fusion was quantified in these images with novel image processing algorithms that were designed to segment complex, discontinuous, and varying structures seen with the cranial sutures. Using these algorithms, we demonstrated that the posterior frontal suture fuses in a bi-phasic process. Between days 12 and 21 the bones of the suture comes together, but there is relatively little increase in the bone volume or mineral. After day 21 the suture undergoes significant mineralization until completing development by day 45.

We developed an algorithm to reconstruct images that are perpendicular to the coronal suture, which undergoes significant curvature about all three axes. Using this algorithm, we compared the normal development of the suture to a mouse engineered to display fusion of the coronal suture. We showed that the bones of the normal coronal suture grew closer together, mineralized, but did not completely fuse. In mice displaying craniosynostosis, the coronal suture developed abnormally and was fused prior to day 6.

Based on the μCT results, we identified genes associated with the key developmental milestones in the normal posterior frontal suture development. We found that there was an increase in cartilage associated genes when the suture began to fuse. The mineralization phase was associated with an increase in BMP2 and markers of osteoblast differentiation. Of particular interest were the

BMP inhibitors that had unique expression patterns associated with the different phases of suture development.

The next aim was to develop and characterize a pediatric murine model of re-synostosis. This has great potential to serve as a model to better understand the mechanisms responsible for re-synostosis and to test potential therapies. Our hypothesis was that creating a defect over the posterior frontal suture in a 21 day old mouse would result in rapid and robust bone growth. This age corresponded to the point when the posterior frontal suture has fused but has not yet mineralized. Mice with the cranial defect were imaged with μCT between 1 to 21 days following surgery and the extent of bone regeneration was quantified using our algorithm developed to examine suture fusion. The results showed that the defect healed in a biphasic process that resulted in a thin bridge of bone on the endocranial surface of the skull beginning on post-op day 3. This was later followed by a substantial increase in the volume of bone on post-op days 14 and 21. To better understand this rapid defect healing, we examined the expression profile of genes that were associated with the fusion of the normal cranial sutures. Immediately after the onset of the defect healing, there was an increase in all of the cartilage associated genes. This was then followed by an increase in the Bmp4, then Bmp2, and finally an increase in late markers of osteoblast differentiation.

To verify that the rapid healing seen with this defect is age and location specific, we created identically sized defects over the posterior frontal suture in an adolescent mouse, lateral to the suture in an infant mouse, and lateral to the

suture in an adolescent mouse. The results from μCT showed that only defects created over the posterior frontal sutures resulted in bridging. Even though the adolescent posterior frontal defect was eventually bridged with bone, this did not occur until much later on post-op day 14. There was an increase in bone volume and mass only in the infant defects, while there was no change in either the bone volume or mineral in the adolescent animals.

Building upon the developmental and regenerative changes in the normal mouse, we examined the regenerative differences in a strain of mice displaying craniosynostosis. The mice were engineered with the same point mutation in the Twist1 gene that is seen in Saethre-Chotzen syndrome. The results from our imaging algorithm and 3D reconstruction showed that the coronal suture in these mice developed fused and also had a greater mineral content than their wild-type littermates. Surprisingly, the posterior frontal suture, remained more open in the Twist mice despite a greater volume of bone. The regenerative capacity of these mice was investigated by creating the posterior frontal defect in 21 day old mice. The Twist mice were also unable to bridge this defect, despite having the same volume of bone as their wild-type littermates. These results demonstrate that mice with the Twist mutation displayed premature fusion of the coronal sutures, but had an inability to fuse the midline sutures and defects.

To address the clinical problem of post-operative re-synostosis, we developed a click hydrogel therapy to deliver BMP inhibitors to delay the bone regeneration in our pediatric mouse model. We demonstrated that we can tailor both the release kinetics and the mechanical properties of the hydrogel by

varying the concentration of our novel cross-linker molecule. We also used unconstrained compression testing to assess the in vitro degradation of the hydrogel and showed that there was a 50% loss in the compressive modulus after 5 days. An in vitro pre-osteoblast MG63 cell culture line was used to verify the biological activity of incorporated proteins following an in situ polymerization. The hydrogel was able to deliver the inhibitor Gremlin to block the BMP2 mediated cellular differentiation in vitro.

The in vivo performance of the hydrogel was first verified by the release of a fluorescently labeled protein in our cranial defect. The proteins incorporated in the hydrogel had a controlled release out to 2 weeks in vivo while proteins delivered with the un-polymerized PEG back bone rapidly diffused out of the defect. We also assessed the effect of the empty hydrogel would have on bone regeneration in our cranial defect model by µCT. The results from our algorithm showed that there was a temporary decrease in the amount of bone early, but by two weeks post-op the bone was able to fully regenerate in the defect in the presence of the hydrogel.

We used our hydrogel to deliver the BMP antagonist Gremlin to delay the bone regeneration in the defect. The combination of Gremlin in the hydrogel resulted in a dose dependent decrease in the defect healing. By 14 days post-op both the empty and hydrogel only defects had nearly complete healing. The low dose of Gremlin had a decrease in the volume of bone and the defect width compared to the other groups. In the mice with the high dose of Gremlin there was no bone growth seen at any of the time points. Furthermore and equivalent

high dose of Gremlin in the un-polymerized backbone of the hydrogel did not delay the bone growth, as there were no differences compared to the empty defect.

In summary, this work has developed new tools, materials, and model systems to better understand and treat craniosynostosis. The imaging algorithms provide an accurate and efficient method to segment heterogeneous bones of the cranial sutures. The pediatric specific re-synostosis model developed has the potential to provide a better understanding of the mechanisms responsible for clinical complications. Most significantly, the click hydrogel therapy developed was able to delay the post-operative re-synostosis following and in situ polymerization with the BMP antagonist Gremlin. This hydrogel therapy has tremendous potential to delay the risks of re-synostosis and reduce the morbidity and complications associated with the treatment of craniosynostosis.

CHAPTER 1 SPECIFIC AIMS

Craniosynostosis is the premature fusion of one or more cranial sutures in the developing skull. If left untreated, craniosynostosis can result in developmental delays, blindness, deafness, and other impairments resulting from an increase in the intracranial pressure. In many cases, the treatment consists of complex calvarial vault reconstruction with the hope of restoring a normal skull appearance and volume. Re-synostosis, the premature re-closure following surgery, occurs in up to 40% children who undergo surgery. If this occurs, a second surgery is needed to remove portions of the fused skull in an attempt to correct the deformities and/or relieve an increase in intracranial pressure. These subsequent surgeries are associated with an incredibly high incidence of life threatening complications. Mice are a common animal model for studying suture fusion because the posterior frontal suture fuses early in the developmental process and a variety of transgenic strains exist that have been engineered to display craniosynostosis. The **overall objective** of this research was to develop a hydrogel based therapy to delay rapid bone regeneration in a murine model of re-synostosis. The **overall hypothesis** was that delivery of key BMP inhibitors involved in regulating normal suture development and regeneration will delay the

rapid bone growth that in seen in a pediatric murine model of re-synostosis. The overall approach is to use micro-computed tomography (μCT) to determine the time course of suture fusion and to identify genes associated with key developmental time points, to develop a pediatric specific mouse model that displays rapid re-synostosis, and lastly to develop a hydrogel based therapy to delay the re-synostosis of a cranial defect.

Specific Aim 1: Characterize normal and pathological suture fusion in mice.

In order to assess the changes that occur during murine suture development it is important to have a thorough understanding of when and how the cranial sutures fuse. The morphological and density changes that occur during the development of the skull make traditional segmentation techniques inaccurate or impractical for characterization of the time course of suture fusion. The **primary objective** was to develop a segmentation algorithm to characterize the temporal changes in the fusion of the posterior frontal and coronal sutures. The secondary objectives were to identify genes associated with key developmental milestones and differences in a mouse model of Saethre-Chotzen syndrome. This was assessed by using the image segmentation algorithms to analyze μCT scans of both normal mice and mice displaying Saethre-Chotzen syndrome. The expression profile of genes associated with the normal murine suture fusion was assessed by real-time PCR. The **hypotheses** were that the snake based algorithm will provide an accurate method for segmentation and

that mice engineered to exhibit craniosynostosis will have prematurely fused coronal sutures.

Specific Aim 2: Develop and characterize a pediatric murine model of re-synostosis.

While rodents have been widely used for calvarial defects, none of these defects recreate the rapid bone growth that is seen clinically with craniosynostosis. The **objective** was to develop and characterize a pediatric specific mouse model that undergoes rapid re-synostosis. This was assessed by creating an identical defect over the posterior frontal suture or just lateral to the suture in both infant and adolescent mice. The extent of bone regeneration following surgery was assessed by μCT and genes associated with this fusion were assessed by real-time PCR. The **hypothesis** was that a defect over the posterior frontal suture in a 21 day old mouse would undergo rapid regeneration that is both age and location specific. Additionally, we expected to see an increase in expression of genes related to chondrocyte and osteoblast differentiation.

Specific Aim 3: To develop and characterize hydrogel based therapy to delay re-synostosis.

Despite the high prevalence of craniosynostosis, there is no clinically available therapy for the treatment of re-synostosis. Delivering growth factors through an injectable hydrogel has the potential to delay bone growth in a cranial

defect to delay re-synostosis. The **objective** of this aim was to develop and characterize an injectable clicked-based hydrogel to delay bone regeneration in a pediatric murine model of re-synostosis. The controlled release of a fluorescently labeled protein from the hydrogel was assessed both in vitro and in the cranial defect model. The effectiveness of the therapy to delay post-operative bone growth was assessed with μCT and histology. The **hypothesis** was that the hydrogel will provide an in situ polymerizable delivery vehicle for controlled release of the BMP inhibitor Gremlin to delay bone growth in a pediatric re-synostosis model.

CHAPTER 2 BACKGROUND AND LITERATURE REVIEW

2.1 Bone Structure and Development

Bone is a dense connective tissue and is the most abundant tissue in the body by mass. It serves many roles related to structural support, endocrine signaling, maintenance of body chemistry, and as a reservoir of many minerals. The two major components of bone are the inorganic calcium phosphate component and an organic collagen, primarily type I collagen [1, 2]. The two components interact to form a composite tissue that is able to withstand a wide range of compressive, torsional, and tensile stresses [3]. While the gross morphology of bones remains relatively consistent, they are very dynamic structures. Bones are constantly being turned over to repair structural damage and accommodate changing mechanical loads. The primary cells responsible for this turn over are osteoblasts and osteoclasts [4]. Osteoclasts are multinucleated cells derived from hematopoietic precursors that function to resorb existing bone. The osteoclasts move along the surface of the bone and dissolve the bone matrix. They are often followed by osteoblasts that are of mesenchymal origin and primarily produce new bone [5]. Osteoblasts secrete a collagen rich immature bone matrix that is called osteoid. This osteoid then becomes mineralized by hydroxyapatite to form fully mineralized bone.

Bones form and heal by two primary mechanisms: endochondral and intramembranous ossification [6]. The main difference between the two types of bone formation is related to the precursor tissues that eventually become

mineralized. In intramembranous ossification, a dense fibrous membranous sheath forms [7]. As the tissue develops, the mesenchymal tissue begins to condense, there is a vascular invasion, and some of the progenitor cells differentiate along the osteoblast lineage. This type of bone formation is seen in the skull and other flat bones in the body. The osteoblasts then secrete osteoid that is eventually mineralized. In endochondral ossification, the developing bones replace a cartilaginous precursor [8]. This method of bone formation is seen in the development and the majority of fracture healing in long bones [6, 9]. In endochondral ossification, chondrocytes undergo proliferation, then hypertrophy, and eventually die. The extracellular matrix then becomes calcified with hydroxyapatite forming mature bone [10, 11]. This progression of chondrocyte proliferation and hypertrophy is similar to what is seen in the development of long bone growth plates [12, 13].

2.2 Normal Cranial Development

The bones of the skull form by intramembranous ossification in paired structures that grow superiorly and medially as the fetus ages [14]. Normal cranial development occurs from the complex proliferation and interaction among tissues of varying embryological origin [15]. Prior to birth, several different cartilages condense to form the cartilaginous base of the developing skull. This structure undergoes endochondral ossification to form the base of the developing cranium in the first two weeks of human development [14]. Shortly after, the calvarial begins to develop from a dense fibrous connective tissue layer that

serves as the foundation for the development of the remainder of the calvaria. These bones, which are also present in the adult skull, are the frontal bone, the parietal bone, the temporal bone, and the occipital bone [16].

As the skull develops, these bones continue to expand and intersect in fibrous joints called cranial sutures [17]. Cranial sutures are composed of the two developing bones and contain dense but disorganized connective tissue between the bones [18]. By birth these cranial sutures intersect to form six fontanels, which in combination with the cranial sutures allow for normal deformation of the skull during birth [16]. The sutures are vital to a child's development because they are the major growth areas of the skull that allow for cranial vault expansion [19]. In the medial most regions of the cranial sutures progenitor cells undergo rapid proliferation [20]. This rapid proliferation allows for continued expansion of the cranial vault to accommodate the expanding brain. Just lateral to this region of rapid proliferation, the cranial progenitor cells begin to differentiate forming the bone of the skull in a region that is called the osteogenic front [21]. The osteoprogenitor cells differentiate into osteoblasts that lay down immature osteoid. The osteoid then becomes mineralized with hydroxyapatite as the skull develops.

Immediately after birth the skull becomes more spherical and the brain continues to grow rapidly. At three 3 months of age the sutures begin to fuse, beginning with the metopic suture, in a highly conserved process [22]. The remaining cranial sutures fuse later in adolescence and early adult hood after the brain has completed development. The timing of the fusion of the cranial suture

is controlled primarily by a complex interaction between the osteogenic front and the dura immediately underlying the suture [23, 24]. The dura is a thick connective tissue layer derived from mesoderm. The dura is the outermost layer of the meninges that surrounds and protects the spinal cord and the brain. The primary role of the dura is to separate the cerebrospinal fluid (CSF) from the circulating blood. In addition to its role as a physical barrier, the dura is believed to drive suture fusion by one or two interrelated mechanisms. Traditionally, the dura is believed to be a source of paracrine signaling which in turn promotes the differentiation of osteoblasts and subsequent fusion of the sutures [25, 26]. There is also limited evidence that suggests the dura may also be a source of the progenitor cells that become incorporated into the fusing cranial sutures [27].

In recent years there has been a growing debate whether the fusion of the cranial sutures occurs through an endochondral or intramembranous mechanism. Historically, researchers have reported that the sutures fuse without the cartilaginous precursor that is seen in endochondral ossification [17]. There is a small but growing body of evidence showing that cartilage may be involved in both normal and pathologic suture fusion [28, 29]. In rodents, the cartilage seen in these studies was present in specific sutures for a short period of time. Additionally, there was a very discontinuous distribution of cartilage along the length of the fusing suture. This has been observed with the increase in cartilage associated genes and the presence of negatively charged tissue on histology. It should be noted that this cartilage does not have the characteristic appearance seen in the development and healing of long bone fractures. As a result, the

majority of papers published on the fusion of the cranial sutures still say that the cranial sutures fuse through intramembranous ossification.

2.3 Craniosynostosis

Approximately 1 in every 1800-2500 children there is a disruption of the normal suture development and the cranial sutures fuse prematurely [30-33]. This results in a condition that is called craniosynostosis. Craniosynostosis can result from a variety causes and has a broad spectrum of severity ranging from mild suture synostosis to pan-synostosis prior to birth [34, 35]. Approximately 60% of the cases of craniosynostosis result from non-syndromic or spontaneous causes [33]. These cases occur from either an unknown genetic mutation or an environmental cause that results in the fusion of the cranial sutures. The remainder of the cases of craniosynostosis are caused by one of over 100 different inherited mutations [19, 36]. In addition to the fusion of the cranial sutures, syndromic cases are associated with other characteristic abnormalities.

If left untreated, craniosynostosis can result in a wide variety of craniofacial and neurological complications. These complications are caused by an increase in intracranial pressure or from the craniofacial deformities themselves [37]. In addition to the obvious cosmetic deformities seen with craniosynostosis, abnormalities in the craniofacial structures can impair normal mastication and airway function [38]. These craniofacial abnormalities can also lead to blindness, deafness, and other sequelae resulting from the compression 9: PAGEREF _Toc325089[35, 39]. Craniosynostosis can also lead to

complications resulting from an increase in intracranial pressure (ICP) [40]. This increase in ICP is caused by the continual growth of the brain inside a fused skull. If left untreated, the increase in ICP can lead to developmental delays, seizures, and in severe cases death [41].

2.4 Genetic Causes of Craniosynostosis

The first genetic mutation identified to cause craniosynostosis was the MSX2 mutation seen in Boston type craniosynostosis [42]. The MSX2 gene is a transcription factor associated with the BMP signaling and osteoblast differentiation. The most common syndromic form of craniosynostosis involves a mutation in the FGFR3 receptor and results in Muenke syndrome [43]. Interestingly this is the only syndromic form of craniosynostosis known to result in uni-coronal synostosis and same mutations in this receptor results in long bone abnormalities and a normal cranial vault. The majority of cases of craniosynostosis are caused by a gain of function mutation in one of the FGF receptors [44, 45]. The FGF receptors are tyrosine kinase like receptors that cross phosphorylate each other in the presence of the target FGF ligand [46]. In the presence of the one of the mutations, the receptors are constitutively active and can phosphorylate in the absence of the target ligand [47, 48]. These mutations give rise to the Crouzon, Pfeiffer, and Aperts syndromes [36]. The majority of mutations in this receptor are located within two exons in the IgIIIa/c domain [45, 49]. Typically these syndromes result in bi-coronal synostosis, mid-face hypoplasia, and limb abnormalities [44, 50]. The syndromes resulting from

mutations in the FGFR2 receptors are among the most severe cases of craniosynostosis due to the bi-coronal suture fusion and the mid-face deformities [50, 51]. These syndromes frequently require complex calvarial reconstruction and frontal-orbital advancement at an early age.

The most common autosomal dominant form of craniosynostosis is Saethre-Chotzen syndrome [52, 53]. Children with this syndrome characteristically display bi-coronal synostosis, microcephaly, facial dysmorphism, short stature, and syndactyly [29, 54, 55]. Saethre-Chotzen syndrome is caused by a heterozygous missense, duplication, or deletion mutation in the Twist1 gene [52, 56]. Twist1 is a basic-helix-loop-helix transcription (bHLH) factor expressed early in suture development and is involved in regulating osteoblast differentiation [57, 58]. Mutations in the Twist1 gene are believed to cause a decrease in the binding capacity to E protein and an increase in homodimer formation [59]. This alteration in normal activity results in an change in expression of genes that in turn promote osteoblast differentiation. Twist1 has been shown to be involved in signaling pathways related to MSX2, RUNX2, FGFR2, and coronal suture development. Mice engineered with a point mutation in the Twist1 gene display fusion of the coronal suture [29, 55].

2.5 Management of Craniosynostosis

The extent and timing of the pathological suture fusion has a significant effect on the management of craniosynostosis. The less severe late onset cases

of single suture fusion can occasionally be treated with helmet molding therapy [60, 61]. As the child's skull grows a series of helmets are custom molded to mechanically reshape the cranial vault. However the majority of cases of craniosynostosis require surgical intervention to correct the fused suture [35]. In the past, surgeons performed strip craniotomies that just removed a strip of bone over the fused suture. This approach has been abandoned for the majority of cases of craniosynostosis because the results were temporary. The bone removed from the defect rapidly re-fused providing little benefit to the child.

The most common procedure currently performed for the correction of craniosynostosis is complex calvarial reconstruction. In this procedure the majority of the calvaria is removed and then reshaped in an attempt to restore normal cranial shape and volume [24, 35]. Surprisingly complex cranial vault reconstruction has a 1% incidence of post-operative complications, which is comparable to other major pediatric surgeries [62]. Despite this low incidence of complications, there is significant morbidity associated with surgical intervention for craniosynostosis [41]. The surgeries are typically 4 to 5 hours in duration and require the implantation of fixation hardware to reconstruct the bones of the skull. Children who have the surgery require multiple blood transfusions and stays in the intensive care unit.

While there are relatively few complications immediately following surgical correction of craniosynostosis, there is a substantial risk for delayed complications. In up to 40% of cases of cranial vault reconstruction, the bones rapidly refuse resulting in a condition referred to as re-synostosis [63, 64]. Re-

synostosis frequently leads to additional craniofacial deformities and complications related to an increase in ICP. To correct these complications additional surgical intervention is required. In many cases, surgeons are forced to perform additional cranial vault reconstructions that are associated with a 13% incidence of life threatening complications [50, 51]. These complications frequently include dural tears, subdural hemorrhages, tearing of the cranial sinuses, stroke, encephalitis, meningitis, and seizures [62, 65]. Some children, especially those who are very young at the time of the first surgical intervention require multiple reconstructions in their first two years of life [63]. After children are about 2-3 years old the rate of brain growth slows dramatically and the risk of needing multiple operations to correct neurological sequelae is drastically reduced. Typically any surgical intervention after age 3 is focused on correcting cosmetic deformities, and not reshaping the cranial vault from complications resulting from re-synostosis.

The incidence and morbidity of complications related to re-synostosis are so severe that it is a major factor in deciding the timing of surgical intervention. Children who are less than 6 months of age at the time of surgery have more than three times the risk of developing re-synostosis, compared to children who are between 6 months to 2 years old [35]. In addition to the age dependent risk, certain syndromic forms of craniosynostosis also have an elevated risk of re-synostosis. It has been reported that children who have Saethre-Chotzen, Apert's, and Crouzon syndrome have up to a 40% incidence of re-synostosis [50, 63]. It is not clear whether this elevated risk is the result of the syndrome itself or

is attributed to the younger age at which these children require surgery. Nearly all syndromic forms of craniosynostosis display bi-coronal suture fusion, which typically necessitates surgical intervention at an earlier age than cases of single suture synostosis. As a result of this age dependent risk of re-synostosis, surgeons would like to delay surgical intervention as long as possible. However the longer intervention is delayed the greater the risk of permanent neurological complications related to the original deformities. There is little empirical evidence to guide the timing of surgical intervention and surgeons typically choose to delay surgeries until neurological signs become evident.

2.6 Animal Models of Craniofacial Development

In the last 30 years, animal models of cranial development have been utilized to examine the molecular mechanisms involved with both normal and pathological suture fusion. The majority of this work has been conducted in rodents due to their ease of use and conservation of the molecular signaling related to bone development. Additionally, there have been a rapidly growing number of commercially available strains of mice engineered with a mutation that is associated with a human syndromic form of craniosynostosis [66, 67]. Despite the conservation of molecular signals, there are significant differences in the craniofacial development between humans and rodents [68]. Unlike humans who stop growing in early adulthood, all rodents continue to grow as they age. This continued growth also occurs in the cranial vault and the brain. The majority of the cranial sutures in rodent remain open to allow for continual expansion of the

calvaria [69]. To accommodate this growth, the open sutures in rodents have a different morphology that typically consists of two overlapping plates [55, 69]. In humans this overlapping structure is not present as all of the cranial sutures in an adult skull are fused.

Despite these differences, researchers have used these model systems to compare the processes that are responsible for normal suture fusion. In rodents, the posterior frontal suture is the only suture in the cranial vault that fuses [69, 70]. This suture is analogous to the human metopic suture which is also the first suture to fuse in the human skull. Traditionally, the patency of fusion of the sutures has been examined using standard decalcified histology. There have been significant discrepancies reported regarding the exact timing of the suture fusion, but all research supports the conclusion that this suture fuses sometime during the first month of life in mice [28, 70, 71].. Researchers frequently compare the fusing posterior frontal to the normally patent sagittal suture [23, 72, 73]. While both sutures are located along the midline of the skull, they are from different embryologic origins and are subjected to different mechanical loading.

This comparison has provided a great deal of information related to the mechanisms responsible for the fusion of the murine cranial sutures. Early work performed by Longaker highlighted the role of the underlying dura in regulating the patency or fusion of the cranial sutures [23]. Using an organ culture model, he removed a portion of bone containing both midline sutures and then changed the position of the suture relative to the underlying dura. Rotation and transposition of the posterior frontal bone over the dura of the sagittal suture

resulted in this normally fusing suture remaining open while the normally open sagittal suture fused over the dura of the posterior frontal dura. Further research examining the role of the dura has found numerous age and location related differences in factors related to osteoblast proliferation and differentiation [25-27, 73-76]. The age and location specific differences in the dura have also been shown to alter the regenerative capacity of overlying cranial defects and the osteoinductive ability of the dura itself [77-79].

The two most widely studied growth factor families in craniofacial development literature are the FGF and TGF-β molecules [21, 68, 72, 80, 81]. The TGF-β members and receptors are involved with osteoblast proliferation and production of extracellular matrix proteins [82, 83]. Several reports have shown that members of the TGF-β family are localized to the osteogenic fronts of the developing sutures in rodents [21, 84, 85]. More specifically, TGFβ2 has been shown to be a major factor responsible for the fusion of the posterior frontal suture [21, 72]. While there are several different molecules in the FGF family studied in relation to craniosynostosis, FGF-2 has been shown to be involved in several aspects of suture fusion including osteoblast proliferation, angiogenesis, and bone formation in rodent calvaria [86-88]. Additionally, the most common forms of syndromic craniosynostosis result from gain of function mutations in FGF receptors. Recently there is a growing body of evidence that supports the interaction between member of the FGF, TGF-β, and downstream transcription factors such as Twist1 [87, 89, 90]. This also seen clinically as nearly all syndromic mutations result in bi-coronal synostosis. Despite the widespread

research in the orthopedic literature, very little work has been performed to examine the role of bone morphogenic proteins (BMPs) in regulating the fusion of the cranial sutures [91]. Additionally, there have been no reports of mutations in the BMP family causing craniosynostosis.

2.7 Animal Models and Therapies for Re-Synostosis

While it would be ideal to have a therapy to prevent the premature fusion of the sutures, this is not feasible with traditional presentations of craniosynostosis [35]. With non-syndromic cases of craniosynostosis, the condition is detected after the sutures have already fused. While it is possible to detect and screen children at risk for a syndromic form of craniosynostosis, the majority of these syndromes present with the suture fusion at birth. As a result there is little opportunity to prevent the suture fusion, but there is an opportunity to reduce the morbidity and complications related to the surgical intervention [62]. To address this there have been a number of recent studies that have developed surgical models of re-synostosis.

The most thoroughly studied model of re-synostosis has been the rabbit [92-95]. Nearly all work focused on re-synostosis of the rabbit has been performed by the Mooney group. This group fortuitously identified a rabbit that spontaneously displayed bi-coronal synostosis [96, 97]. They were able to successfully breed rabbits with this mutation and have developed a colony of rabbits that display craniosynostosis. The underlying mutation that is responsible for causing this synostosis is currently unknown, but it is not a mutation in the

genes known to cause human forms of craniosynostosis. While the mutation is inherited in an autosomal dominant pattern, there is variable penetrance seen among the rabbits [97]. This results in a spectrum of severity where some rabbits display early onset fusion before birth to some born with patent sutures that fuse later in development.

The surgical procedure that is most commonly used with these rabbits is a strip craniotomy made by removing the fused coronal suture [95]. Typically a 3 mm wide defect is created over the coronal suture near the midline of the skull. Depending on the severity of the rabbits' synostosis the surgeries are preformed between 10 days to 3 months of age. Using this model investigators have been able to test the effect of delivering therapies to target the mechanisms believed to be responsible for normal suture fusion. The first of these studies used antibodies against TGFB2 delivered with a collagen gel [95]. This molecule was targeted because it has been shown to be associated with normal suture fusion and mutations in the TGFB receptors are known to cause craniosynostosis. While the researchers were able to achieve statistical significance in their results, there was not a major reduction in the bone regenerating in the defect. Furthermore their control group containing just the collagen with an IgG displayed a decrease in regenerated bone in the defect. This was followed up with an additional study involving the administration of the BMP inhibitor noggin. The researchers were able to find stronger evidence for the effect of Noggin, however they groups with no intervention and the control collagen gel did not display complete fusion of the defect [93]. Interestingly while noggin was able to

delay the re-synostosis in the rabbits, it was not able to prevent the fusion of the coronal sutures in the rabbits with delayed onset coronal synostosis [98].

While there are substantial benefits to performing cranial defect in a larger rabbit model, the strain of rabbits displaying the fused coronal sutures are not commercially available and the mutation resulting in the synostosis is not known. As a result, there are tremendous benefits for having a rodent, especially a mouse, model that undergoes rapid defect healing. This would provide a model system to understand the mechanisms responsible for and to test therapies designed to delay the bone re-closure. Rodents have been widely used to investigate the effect of therapeutic interventions in non-suture associated cranial defects [78, 99]. These defects usually are created in adult animals and located over the parietal bones of the skull. Traditionally, these are critically sized defects are designed to test therapies designed to enhance the production of bone [100]. In the absence of a therapeutic intervention the defects do not undergo complete healing. While they are suitable to test applications designed to enhance osteogensis, they do not recreate the rapid healing seen in cases of re-synostosis.

To address this limitation, a adult murine cranial defect model has previously been developed [93]. In this model, the posterior frontal suture is removed to create a 1.0 mm wide defect along the length of the suture. The investigators delivered cells transfected to overexpress the BMP inhibitor Noggin. Analysis of the defect with μCT showed moderate success of the inhibitor, but the major limitation of this model was that the empty defect did not heal even

after 4 months. The most likely cause for the lack of healing was that the defects were created in 10 week old adult mice. Numerous studies have demonstrated that there are substantial regenerative differences between juvenile and adult animals [74, 75, 78, 93, 101]. Furthermore this difference is seen clinically in the age dependent risk of re-synostosis [63].

2.8 Overview of Long Bone Fracture Healing

While there is benefit in understanding the mechanisms responsible for both the normal and pathological suture fusion, this research does not address the major challenge with craniosynostosis. Clinically the major challenge is controlling the post-operative bone growth seen in a pediatric skull, but there is little research examining the mechanisms responsible for regenerating the cranial bone in pediatric applications. Despite the lack of evidence in the craniofacial literature, there has been a tremendous amount of research in the orthopedic literature examining the mechanisms responsible for the healing of long bone fractures. Long bone fractures heal through two main mechanisms, direct (primary) or indirect (secondary) fracture healing [3, 6, 9]. In direct fracture healing there is the formation of a new haverisan system by the remodeling units composed of osteoclasts and osteoblasts. This type of fracture healing only occurs when there is anatomic reduction of the fracture and very rigid fixation [9].

The majority of long bone fractures heal through indirect fracture healing. This healing involves a combination of intramembranous and endochondral ossification that results in the formation of a fracture callus [102]. The first events

in the healing of a fracture involve the formation of a hematoma and an inflammatory response. This stage is associated with the production of pro-inflammatory cytokines (IL-1, IL-6, and TNFα) and TGF-β [103-105]. The production of these factors results in the recruitment and later proliferation of mesenchyme cells. This is associated with an increase of TGF-β2, TGF-β3, BMP5, and BMP6 [106]. Following proliferation, these cells begin to differentiate into osteo-chondral progenitor cells and angiogenesis begins [107-109]. The early proliferation and differentiation are largely mediated by an increase in the production of BMP-2 [110]. Vascular invasion is needed for mineralization and this vascularization is associated with an increase in angiopoetin-1 [109]. Approximately one week after the fracture occurs, the mesenchymal cells undergo chondrogenesis and form what is referred to as a soft callus [111, 112]. By two weeks this soft callus begins to mineralize forming in response to members of the BMP family. The bone that is produced during this stage of healing is a more disorganized and is called immature woven bone [106]. It is during this phase of fracture healing that the callus becomes visible radiographically. This phase is also associated with a concomitant increase in neo-angiogenesis in response to members of the VEGF family [113, 114]. The final stage of fracture healing is the remodeling of the fracture callus that primarily replaces the woven bone with the stronger lamellar bone. This fracture remodeling may not occur in older adults, but occurs rapidly in children.

2.9 BMPs and BMP Inhibitors

Since their discovery in the mid-1960s by Marshal Urist, bone morphogenic proteins (BMPs) have been shown to be one of the major factors involved in the development and regeneration of mineralized tissues [115]. To date there have been over 20 BMPs identified that are classified into 4 main sub-groups. The two most widely studied sub-groups are group 1 (BMP-2 and BMP-4) and group 2 (BMP-5, BMP-6, and BMP-7) [116]. Nearly all BMPs belong to the TGF-β superfamily. Members of the BMP family form dimeric structures before binding to their respective receptors. There are two major types of BMP receptors (Type I and II) that act as serine/threonine kinase receptors [117]. Traditionally, the BMP dimer binding to the Type I receptor pair then recruits the Type II receptor pair, resulting in the initiation of the signal cascade. The signaling pathway results in the auto-phosphorylation of the receptors that in turn phosphorylates members of the SMAD family (SMAD 1, 5, and 8). This activated SMAD complex then translocate to the nucleus to activate downstream gene transcription.

Nearly all regulation of the BMP pathway occurs extracellularly by the production of numerous BMP inhibitors [118]. Traditionally, when there is an increase in the production of BMPs, inhibitors are also produced as part of a negative feedback loop to control the signal [119]. The majority of BMP inhibitors bind to the BMP complex and prevent binding to the target receptor by steric hindrance. There are a few exceptions to this rule as some inhibitors bind the receptor directly to block signal transduction [116]. Modulation of the BMP

pathway by controlling the action of the inhibitors is an attractive target as all the regulation occurs extracellularly and therapeutic agents do not have to cross the cell membrane.

Of the BMP inhibitors, Noggin has been the most thoroughly studied inhibitor in the craniofacial literature [92, 93, 120]. Noggin binds and blocks the activity of BMP-2, BMP-4, BMP-5, BMP-6, and BMP-7 [121, 122]. It has a major role embryologicaly in the development of bone and the regulation of the associated apoptosis during limb formation. Prior work examining the role of Noggin has demonstrated that this inhibitor is produced in the normally open murine cranial sutures, but is not produced in the fusing posterior frontal suture [120]. Additionally, the delivery of the Noggin over the posterior frontal suture resulted in a widening of the suture. These findings lead to the use of Noggin as a therapy in both rabbit and murine re-synostosis, but this inhibitor only moderately delayed suture fusion [92, 93]. However, the delivery of Noggin did not rescue the fusion of the coronal suture in a rabbit model of delay onset craniosynostosis [98].

Although the BMP inhibitor Gremlin1 (Gremlin) has not been well studied in the craniofacial literature it is a very attractive alternative to Noggin. Gremlin is a member of the Cerebrus and Dan family and acts through the traditional BMP inhibitor mechanism where it binds the BMP dimer extracellularly [123]. Gremlin has been shown to have greater specificity than Noggin as it only blocks the activity of BMP-2, BMP-4, and BMP-7, although it also has some inhibitory activity on the Wnt pathways [124]. Gremlin has been shown to be heavily

involved the regulation of limb and kidney development [125]. A homozygous knock out of Gremlin is lethal in mice and heterozygous knockout results in short stature and osteopenia due to a decrease in trabecular formation in long bones [126]. To our knowledge no one has used Gremlin as a therapy to delay the formation of bone in vivo.

2.10 Imaging and Segmentation of Mineralized Tissues

The presence of the hydroxyapatite mineral in the matrix makes X-ray based imaging modalities an ideal choice for imaging bone. When an X-ray beam encounters the mineralized tissue a substantial amount of the energy is absorbed or attenuated which in turn generates the image. Plain 2D X-rays are widely used for craniofacial and orthopedic applications, but they only provide limited information because the images are a projection of the tissue of interest [35]. The use of computed tomography (CT) uses X-ray radiation to generate numerous projections of the target tissue. These projections are then processed to generate detailed 3D images of the target tissue. CT scans expose the patient to much higher radiation dose, which is a major concern for craniofacial imagining of pediatric patients [127]. In recent years advances in the hardware of micro-focal CT (μCT) have made this modality an attractive choice for imaging mineralized tissue in animal models. The use of μCT allows for the creation of images that are up to 1000 times greater resolution than what is possible with traditional CT imaging.

Traditionally, histology has been used to study developmental and regenerative processes of craniofacial structures. While this modality provides excellent morphologic information, the discontinuity of the cranial structure severely limits the usefulness histology [28]. Cranial sutures fuse a very discontinuous process whereby the structures form discrete bridges of bone [71]. These bridges form randomly along the length of the suture, further complicating analysis. As a result it is problematic to make generalizations regarding the fusion of an entire suture or defect based on a few histological sections. This problem has resulted in widely differing reports with regard to the timing of the fusion of the mouse posterior frontal suture [28, 70]. While it is possible to perform serial sectioning of the sample, this is prohibitively time consuming for high throughput applications. In addition to much faster imaging times, µCT allows for assessment of mineral content in a non-destructive manner.

The use of µCT has been widely used to examine orthopedic small animal models, but there is limited use of this modality in the craniofacial basic science literature. A few small studies have used µCT imaging to examine the development of the cranial sutures. Previous work has verified that µCT can accurately image the morphologic changes related to fusion of the mouse posterior frontal suture [71, 128]. The 3D renderings with µCT have further demonstrated the discontinuity that makes non-serial sectioning inaccurate [71]. The use of µCT has also been used to assess the regeneration of bone in a murine posterior frontal defect [93]. One of the major reasons µCT is not widely

used for imaging craniofacial structures is difficulty in segmenting the bones of the images.

Segmentation is the process of identifying boundaries of structures on medical images. The complexity seen with cranial suture development and regeneration makes segmentation difficult with traditional algorithms [128]. The most widely used segmentation in the craniofacial literature is manual tracing [93, 128]. Not only does this introduce tremendous bias in the assessment, but this is also prohibitively time consuming. For most CT based applications the use of global threshold segmentation provides accurate results as most bone structures display relatively uniform attenuation [129, 130]. With this algorithm, any pixel having a value over the specified threshold is considered bone while all remaining pixels are considered background. The utility of this algorithm is limited when imaging the complex cranial structures. The cranial sutures form and mineralize in a very discontinuous process that produces several gaps in the bone boundaries. Furthermore, the center of the sutures is composed of a dense fibrous connective tissue. While this tissue is not mineralized, it does have a significant attenuation that leads to inaccuracies in the global threshold segmentation boundary. The use of a global threshold is further complicated when examining the development of the cranial sutures because the sutures undergo more than a 10 fold change in density as the animal ages. This requires subjectively selected different threshold based on the age of the animal. As a result of these two differences, even minor variations to the threshold result in widely different segmentation boundaries.

To address many of the issues associated with global threshold segmentation, more advanced imaging algorithms have been developed to provide a more accurate segmentation. One of the most widely used segmentation algorithms is a level set algorithm [129, 131]. Both 2D and 3D level set algorithms grow an initially defined region to optimize a final segmentation boundary. The algorithm modifies the boundary until an optimal solution to the differential equation is obtained that corresponds to the ideal segmentation boundary [132]. This algorithm was initially developed for tracking the geometries of one structure over time and is limited to the segmentation of one object. The multiple bones seen with the cranial suture makes using this image algorithm impractical and inaccurate. The Chen-Vese algorithm was developed to improve upon these limitations by allowing for more advanced performance that allows for branching or fusion of multiple segmentation objects [133]. While this overcomes the challenges with the traditional level set algorithm, the fibrous tissue between the developing sutures results in substantial inaccuracies with this algorithm. More specifically, the algorithm typically incorrectly considers this tissue as bone and “fuses” the suture when in fact the suture was open.

To address these issues associated with parameter selection, required for both the level set and Chen-Vese algorithms, the snake algorithm was developed [134]. This active contour algorithm adjusts the segmentation boundary in order to optimize an energy function. Numerous variations of this energy function have been reported, but the driving force behind the functionality of snake algorithms is optimizing the boundary on a gradient image [133-136]. The gradient image is

a two dimensional derivative of the original image and regions where there is great change, corresponding to an edge, have a high value. The snake algorithm optimizes the boundary to where this gradient is greatest and as a result detects the edges of the structure of interest. This produces a segmentation boundary that is independent of the actual pixel intensity and is dependent only on the rate of change of the structure. This segmentation algorithm is limited for segmenting the cranial applications because the algorithm requires an initial approximation of the object boundary and cannot distinguish between open or closed structures.

2.11 Delivery Systems for Biological Therapeutics

One of the major challenges when using biologically active molecules or proteins is providing controlled delivery to the target tissue. In order to achieve the intended response, it is necessary to have an effective dose for an extended period, while minimizing the negative side effects of the therapeutic agent. Biologically derived delivery vehicles are beneficial in that they generally do not elicit a strong inflammatory response and are easily degraded by the host [137]. The most widely used carrier used in the craniofacial literature is a collagen based sponge or gel [138]. Clinically, this is used to deliver rhBMP2 to enhance bone regeneration [139]. In animal models, this scaffold has been used to deliver BMP inhibitors and antibodies to delay post-operative re-synostosis [92, 93, 98]. While this is an FDA approved carrier, there are significant challenges when trying to provide controlled release of incorporated proteins [140]. As this is a biological tissue, there is little ability to control or delay the release of proteins

from this material. As a result, there have been numerous complications reported in the orthopedic literature that can be attributed to this rapid release profile and associated inflammatory response [141-143].

The use of synthetic materials allow for much greater flexibility in tailoring the material behavior and properties to the intended application [144, 145]. Poly (ethylene glycol) (PEG) hydrogels have been used in a variety of craniofacial and orthopedic applications due to their biocompatibility and the ability to incorporate biologically active molecules [137, 146-148]. Traditionally, synthetic materials are limited by their immune responses and prolonged degradation, although recent advances in material chemistry have made these more attractive [149]. With synthetic materials it is possible to control the release of active agents by altering the material properties, affinity to the therapeutic proteins, and covalently linking the therapeutic molecule to the material [150-152].

There is tremendous benefit for developing an injectable synthetic hydrogel for use in craniofacial applications. The complexity and irregularity seen with cranial vault reconstruction makes pre-formed materials impractical. Numerous polymerization strategies have been reported using PEG to form cross linked gels both in vitro and in vivo. Many of these hydrogels potentially toxic components or UV radiation to form a cross linked hydrogel, which is of great concern as these materials will be introduced directly on to the brain of an infant [153, 154]. While UV light is a safe method for polymerization in other applications, it has the potential to be toxic in neurological applications as UV light is used as a method to induce neuron apoptosis in vitro [155-157].

Furthermore, these materials could not be polymerized in structures that are too deep to be penetrated by UV light.

The introduction of a new spontaneous polymerization strategy has been developed to provide spontaneously polymerizing gels and has been termed “click chemistry”. This method uses a step-growth polymerization strategy whereby macromeres with alkyne and azide functional groups are “clicked” together to form a cross linked hydrogel [158, 159]. These materials offer tremendous potential for creating materials with excellent mechanical properties while still being able to conjugate a variety of biomolecules to the gel. Traditionally, this polymerization occurs via a copper catalyzed cycloaddition reaction [159]. The cytotoxicity associated with this copper catalyst severely limits the utility of encapsulating cells and delivering the gel into living organisms. To overcome this toxicity, researchers have developed a copper free click polymerization strategy, but this polymerization takes over an hour to complete [160-162]. While this has tremendous potential for certain applications, the slow polymerization time associated with these hydrogels limits their utility as injectable materials.

CHAPTER 3 ALGORITHM TO ASSESS CRANIAL SUTURE FUSION WITH VARYING AND DISCONTINUOUS MINERAL DENSITY

3.1 Introduction

The cranial sutures are joints between the bones of the developing skull and are regulated by a complex interaction among the bones, the mesenchymal tissue between the bones, and the underlying dura. [23, 27] Early in normal development the cranial sutures have very active osteogenic fronts and they play a major role in cranial expansion. [18, 163] Craniosynostosis is the premature fusion of one or more of the cranial sutures early in development, occurring in approximately one out of 2,000 births. [19, 30, 164] Craniosynostosis is a very heterogeneous condition that most often results from spontaneous mutations, but can be caused by over 100 known syndromic mutations. [36] The variability associated with different types of craniosynostosis has made diagnosis and prediction of outcomes particularly challenging. The diagnosis of suspected cases of craniosynostosis is currently made based on the appearance of the cranial vault on x-rays and/or computed tomography (CT) scans. [35] These imaging studies are then used to provide a qualitative description of whether each of the cranial sutures is open or fused. Even with three dimensional (3D)

CT reconstructions, the complexity and irregularity of the cranial sutures in cases of craniosynostosis make diagnosis challenging. [165] To our knowledge there is no reliable way to correlate complications, outcomes, or risk of post-operative re-synostosis based on the current imaging techniques. To address this unmet clinical need we developed and validated an image processing algorithm to accurately quantify normal suture fusion.

A murine model of cranial development was selected to develop and validate the algorithm because of their ease of study, the conservation of molecular signals, and the increasing number of genetically engineered strains that display craniosynostosis. [53, 55, 57, 166] In mice the posterior frontal suture, analogous to the human metopic suture, fuses early in development (Figure3-1a). [28, 70] In contrast, the coronal, sagittal, and lambdoid sutures remain largely open to allow for continued expansion of the developing rodent calvaria. [66, 70, 167] Additionally, many mouse strains engineered with the mutations seen in the syndromic forms of craniosynostosis display pathologic fusion of the normally open coronal suture. [55, 166, 168, 169]

Histology has been the gold standard method to analyze suture fusion and morphology in numerous animal models; however, there are significant limitations with using histology to quantify suture fusion. [17, 28, 70, 87] The discontinuity during suture fusion and the irregular mineralization patterns seen with the developing sutures limit the validity of making generalizations from a few histology sections to the entire suture. [28] In contrast to the relatively straight

posterior frontal and sagittal sutures, the normally open coronal and lambdoid sutures undergo significant curvature along their length (Figure 3-1a). [70, 80]

Traditional techniques used for examining cranial sutures do not take this curvature into account when examining the suture morphology. Instead, the coronal suture has been examined in straight coronal sections or images moving along the length of the coronal suture. [70, 168] This results in relatively perpendicular sections for the medial regions of the skull, but very oblique sections relative to the suture in the lateral regions of the skull. By not correcting for these rotations, it is very likely that the variations in morphology previously reported along the length of the coronal suture are largely caused by performing sections at different angles relative to the direction of the suture.

There have been several studies that have used computerized tomography (CT) based imaging to examine cranial sutures, changes in cranial phenotype, and calvarial defect healing in both humans and rodent models. [71, 128, 168] Despite the growing use of CT, there are substantial limitations with traditional image processing algorithms when examining cranial development. The majority of the CT based analyses of cranial sutures in animal models has been performed using a global threshold or manual tracing for segmentation, which is the process of identifying a tissue of interest in an image. [71, 93, 128, 130, 169] Not only is manual tracing time consuming, but it also introduces the potential for user bias in the analysis. [93] Global threshold segmentation is limited when analyzing images that are heterogeneous or have varying intensity. Furthermore, connective tissue between the bones of the suture can lead to

dramatic changes in the suture boundaries from relatively minor changes in the threshold (Figures 3-1b-d). [129, 170] This can lead to gaps in the segmentation boundary of the sutures when using a global threshold, because this method does not take into account any neighboring pixels when performing segmentation. [171]

To address the limitations of both histology and traditional CT image processing algorithms, we have developed a semi-automated algorithm to accurately segment the complex and discontinuous bones of cranial sutures. The algorithm approximates and then optimizes the segmentation boundary using an implementation of the snake algorithm. The snake algorithm is an adaptive contour segmentation algorithm that is used to detect object boundaries in an image. [134, 171] To correct for the rotation of the coronal suture, we have developed an algorithm to digitally reconstruct images that are perpendicular to the cranial suture about all three axes. Clinically, the algorithm has the potential to make diagnosis of craniosynostosis easier and more accurate, but more importantly will hopefully improve the management of craniosynostosis by providing physicians with a better understanding of the suture fusion.

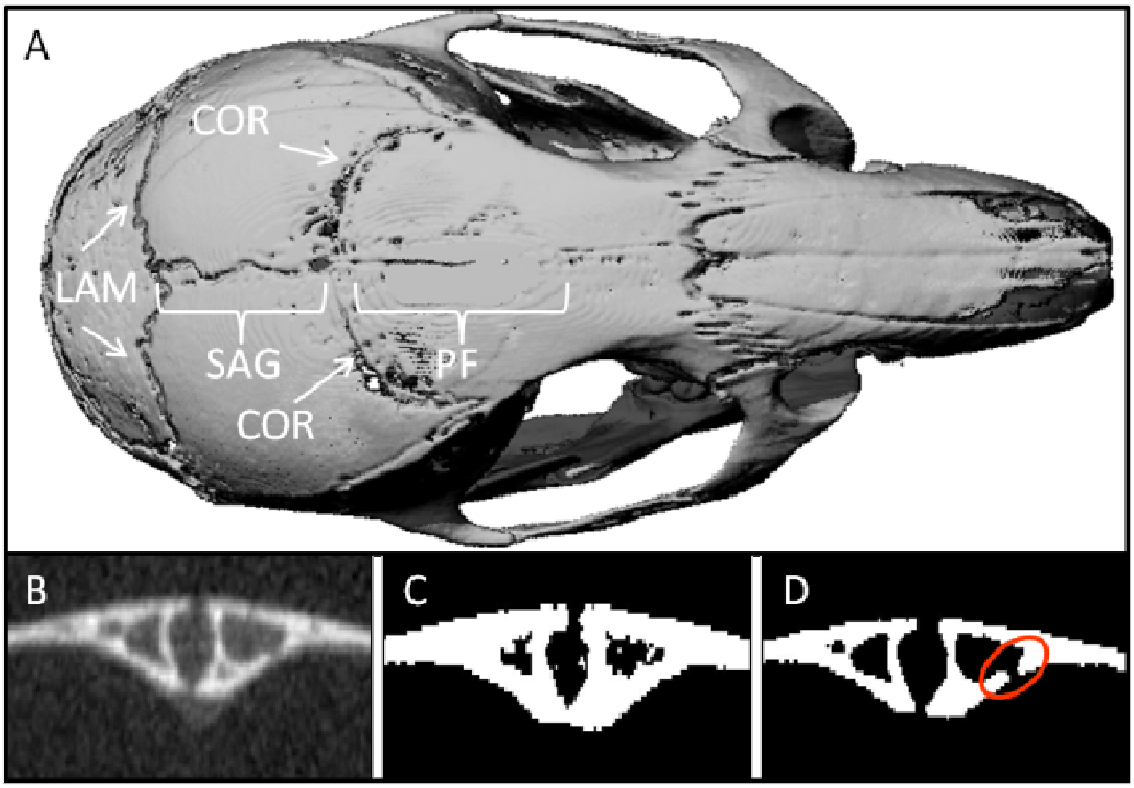

Figure 3-1: Sample images of normal mouse sutures. (a) The 3D rendering of a 25 day old mouse shows the posterior frontal (PF), coronal (COR), sagittal (SAG), and lambdoid (LAM) sutures. (b) A 2D representative image of a 20 day old mouse posterior frontal suture showing fibrous connective tissue located between the developing sutures. (c) Decreasing the global threshold applied to the same image less than 5% changes an image that would be considered fused (d) to one that was open and also introduces gaps in the bone boundary (red oval).

3.2 Methods

3.2.1 Animal Care and Imaging

Under approval of the Georgia Tech Institutional Animal Care and Use Committee, C57Bl/6J male mice (Jackson Labs, Bar Harbor, ME) were housed in a light and temperature controlled environment. Pups were kept with natural birth mothers until weaning at 21 days post-natal or euthanasia. All mice were provided food and water ad libitum. Mice 20 days old or older were euthanized by CO_2 asphyxiation and pups under 20 days were euthanized by intraperitoneal injection of pentobarbital. Six male mice were euthanized at each of the following time points: post-natal days 6, 12, 20, and 25. The calvaria were removed from soft tissues and fixed in 10% neutral buffered formalin (Sigma, St. Louis, MO). The approximate region of the posterior frontal and coronal sutures was identified from the most posterior molars in the maxilla and moved posteriorly 6.6 mm. The samples were imaged with micro-CT (μCT) with isotropic voxels 10.5 μm in size, an energy of 55 kVp, and contained within a 21 mm sample holder (Viva CT 40, Scanco Medical, Bruttisellen, Switzerland). The exact location of the sutures was identified on 3D reconstructions made using a global threshold and was used to create 1.5 mm tall by 2.5 mm wide DICOM images. The posterior frontal suture was defined as the midline suture running between the posterior most aspect of the inter-frontal ridge to the bregma. The coronal suture region was defined as

the anterior most aspect of the coronal suture moving posteriorly until the bregma.

3.2.2 Imaging Algorithm

The algorithm developed consists of three main stages: an initialization phase, a snake algorithm phase, and a suture morphometry phase. The initialization phase of the snake algorithm rotated all of the images using bi-cubic interpolation so the suture was horizontal and applied a global threshold to create a binary image. The global threshold was selected by two independent reviewers examining representative μCT images from all the ages of mice imaged and this same threshold was used for all images analyzed. The outer boundary of the bones was identified for the one or two medial most bones (Figure A-1a-b). If the suture was open, the medial boundaries of both bones were identified and the horizontal distance between the bones was measured at all the locations where the bones overlapped (Figure A-1c). This region was identified from the superior most overlap of the two bones and moved inferiorly until the distance measurements exceeded the mean of the distances plus two standard deviations. The distances between the bones of the osteogenic front were then used to perform a least squares fit of a cubic polynomial which was used to separate the bones into left and right images (Figure A-1c).

This separation was necessary to prevent the snake algorithm from "jumping" to the other bone when the bones were in close proximity and/or the medial boundary was poorly defined (Figure A-2a). The separation was

performed by replicating the pixel value of the border pixel horizontally for the reminder of the image (Figure A-2b). Without this replication, a large artifact is created on the gradient image that is used by the snake algorithm phase resulting in errors of the segmentation boundary (Figure A-2c-f). After processing the images through the initialization phase, the images were inspected for any errors by a blinded reviewer. If an error was found, it was corrected by manually separating the bones, adjusting the global threshold, and/or applying a Gaussian filter to the image. These infrequent corrections are the only steps in the algorithm that require user interaction, while the remaining steps of the algorithm are fully automated.

An implementation of the snake algorithm phase then used the approximate boundary from the initialization phase to optimize a final segmentation boundary. A Fourier descriptors model was fit through these points with the following form:

$$x(t) = a_0 + \sum_{k=1}^{K} (a_k \cos kt + b_k \sin kt), \qquad (1)$$

$$y(t) = c_0 + \sum_{k=1}^{K} (c_k \cos kt + d_k \sin kt); \qquad (2)$$

where a_0 and c_0 are constants corresponding to the centroid of the curve, K is the number of harmonics, and a_k, b_k, c_k, and d_k are coefficients that control the shape of the k^{th} harmonic, and *t* is the parametric variable that ranges from 0 to 2π. The Fourier series description of the boundaries was selected because it allows for an analytic solution of a closed curve that can be modified based on

the complexity of the object to be segmented. The segmentation boundary is composed of a summation of sine and cosine functions of increasing frequency that create a closed continuous boundary. This allows the segmentation boundary to bridge regions in the image that are poorly or heterogeneously mineralized. Additionally, controlling the number of harmonics (K) allows the complexity of the curve to be tailored to the specific application. For the purposes of segmentation of the cranial sutures 25 harmonics were used for all segmentation boundaries due to the complexity and concavity of the sutures.

The curve was optimized by varying the coefficients a_0, c_0, a_k, b_k, c_k, and d_k from Equations 1 and 2 to minimize the following snake energy functional:

$$E = \int_0^{2\pi} \alpha \left| \frac{dV(t)}{dt} \right|^2 dt + \int_0^{2\pi} \beta \left| \frac{d^2V(t)}{dt^2} \right|^2 dt - \int_0^{2\pi} |\nabla I(t)|\, dt, \qquad (3)$$

where *E* is the snake energy, $V(t)$ is the Fourier descriptors equation, α is the coefficient controlling the relative weight of the curvature term, β is the coefficient controlling the relative weight of the stretching term, and $|\nabla I(t)|$ is the magnitude of the gradient image evaluated at each of the points along the curve $V(t)$. This gradient term is calculated by taking the magnitude of the horizontal and vertical central difference derivative over the entire image. The curvature and stretching terms were implemented by taking the first and second derivatives of the Equations 1 and 2. The multiplication of the sine and cosine terms that occur while taking the derivatives reduces all of the terms to a value of either zero or one. As a result the equations simplify to being a summation of the coefficients

a_k, b_k, c_k, and d_k raised to the power of 2 or 4 for the curvature or stretching terms, respectively.

As the curve optimization proceeds to minimize the energy term, the curve will be fit to regions where the magnitude of the gradient is greatest. This allows the algorithm to fit a curve along a path where the edges are sharpest. By controlling the values of α and β it is possible to control how tightly the optimized curve bends and how rapidly the curve changes in length relative to the magnitude of the gradient term, respectively. This algorithm allows for final segmentation that is dependent on the change in intensity rather than the absolute pixel intensity. Additionally, the continuous boundary of the optimized curve allows for bridging of gaps in the images where the edges are poorly defined.

The result from one optimization of the snake algorithm is used as the initialization points for the subsequent iterations of the algorithm. This process is iterated until the snake energy converges resulting in the optimal segmentation boundary. In some instances during the analysis there were two or more substantially equivalent segmentation boundaries that the algorithm would indefinitely alternate between during optimization. These indeterminate solutions were prevented by the introduction of an iteration limit in the algorithm.

The suture morphometric phase of the algorithm used the segmented boundaries of the bone(s) to make morphometric measurements related to suture fusion. For both images where the suture is open and closed, the bone volume and mineralization are found in a 1 mm by 1 mm region within the

segmented bone boundaries (Figure 3-2a). The bone volume was calculated by applying a global threshold to the region inside of the segmented contour then summing the pixels that are above this threshold. Mineralization was used as an indicator of bone mineral content and was calculated by converting the pixel intensities to a known hydroxyapatite standard to give the density of each pixel relative to hydroxyapatite. The hydroxyapatite standard used was composed of 5 different rods 6 mm in diameter that range in concentration between 0-800 mgHA/cm^3. The density values inside the segmented contour were then integrated to give the equivalent mineralization in mg of hydroxyapatite. For images where the suture was open, the region of the segmentation boundary corresponding to the osteogenic front was identified (Figure 3-2b). The segmentation boundary was then followed medially and inferiorly from the superior most boundary pixel until a vertical point of inflection was encountered for an average of four consecutive points. The four-point averaging was used to prevent minor fluctuations in the boundary from causing errors in this boundary. This point was then used as inferior medial border of the osteogenic front. The horizontal distances between the left and right osteogenic fronts on the suture were measured at every vertical pixel for the regions that overlapped. These measurements were then used to find the minimum distance, maximum distance, mean distance, and area between the bones. The percentage of the images that were open along the length of the suture was calculated. This final value is not dependent on the snake algorithm, but is calculated during the global threshold

initialization phase. The functionality of all steps of the algorithm is illustrated using a flow chart (Figure 3-3).

3.2.3 Coronal Suture Reconstruction

To reduce the introduction of distortions when analyzing the curved coronal suture, it was necessary to reconstruct images so that they were perpendicular to the suture about all three axes. This is especially important for the more lateral regions of the coronal suture where straight coronal sections are at the most oblique angle relative to the suture. The first step in the process was to identify the center of the coronal suture once for every 20 unreconstructed coronal images. A third order polynomial was fit through these points and the derivative was taken to find a vector tangential to the suture shown (Figure 3-4a). A global threshold was then applied to the entire image stack and the ectocranial-most points of the skull were found (Figure 3-4b). A bi-cubic polynomial was then fit through these points and used to find a vector normal to the surface of the skull at the specified (Figure 3-4c). The cross product between this normal vector and the tangent vector was taken, resulting in a vector that is orthogonal to the first two. The normal and the cross product vectors were then used to reconstruct a new image that is perpendicular to the image about all three axes using bicubic interpolation (Figure 3-4d). This reconstruction process was repeated at 200 evenly spaced locations along the coronal suture. The reconstructed images were then processed with the snake algorithm described

above. All programming was performed using Matlab 7.9 (MathWorks, Natick, MA) using some components of the image processing toolbox.

3.2.4 Algorithm Comparison

The segmentation boundary from the algorithm described above was compared to both a global threshold and another advanced active contour algorithm based on a level set algorithm. As the many images in developing suture contain more than one bone, the Chen-Vese algorithm was selected as this algorithm allows for automatic segmentation of multiple objects within the image, as described previously. [133] A representative scan from a 20 day old mouse was used as a comparison between the different segmentation algorithms. All segmentation was performed on the same image and the image created using a global threshold with the same value as all images analyzed. The initialization boundary for the snake algorithm image was boundary from this threshold.

3.2.5 Histology Validation

One random sample from each of the 6, 12, 20, and 25 day old mice was decalcified in Calex® (Fisher Scientific, Pittsburgh, PA) for 6 days, changing the solution every 48 hrs. Complete decalcification was verified by plain x-ray (Faxitron X-ray, Lincolnshire, IL) before and after decalcification. The samples were trimmed, dehydrated in a graded series of ethanol washes, and embedded in paraffin. For analysis of the posterior frontal suture, serial sectioning of the entire posterior frontal suture was made with 7 µm thick sections (Microm HM

325, Microm International, Waldorf, Germany). The sections were stained with haematoxylin and eosin and then imaged at 10x magnification with a Leica DMLB microscope (Leica Microsystems, Bannockburn, IL). To provide direct comparisons of the distance measurements between the μCT and histology, the boundaries of the bone(s) were outlined manually for all of the sections. The programming for the manual tracing and morphometric analysis was implemented in Matlab 7.9 (MathWorks).

3.2.6 Human Imaging

To demonstrate the utility of the algorithm on lower resolution clinical CT scans, both the reconstruction and segmentation algorithms described above were applied to a normally open and pathologically fused suture. Under approval of the Georgia Tech and Children's Healthcare of Atlanta institutional review boards, a pre-operative CT scan of a 6 month old boy with non-syndromic metopic craniosynostosis was obtained. The child was imaged with a low dose cranial imaging protocol with isotropic 1 mm^3 voxels. This protocol has an average dosage of 10 mGy, which is roughly a third of the radiation exposure of high resolution CT scans. [127] Human skulls are even more spherical than the murine skull and as a result are subject to even greater distortions from taking images that are oblique to the suture. The 3D reconstruction and segmentation algorithms described above were applied to both the pathologically fused metopic and open coronal sutures. Images were reconstructed perpendicular to

both sutures and analyzed with the algorithm for both the pathologically fused metopic and open coronal sutures.

3.2.7 Statistics

For analysis of the histology validation, the Pearson correlation coefficient was first compared for the number of measurements needed to be statistically significant, with a p value of less than 0.05 being considered significant. A least squares fit linear regression was performed for all measures and an R^2 value was calculated. The normality of the coronal suture data was determined using a Komogorov-Smirnov normality test. This was followed with a one way ANOVA using a Bartlett's test for equal variances. Statistical significance was determined using a Dunnett's Multiple Comparison post-hoc test, with a p value less than 0.05 considered significant. All analysis was performed using Graphpad Prism 5 software (GraphPad Software, La Jolla, CA).

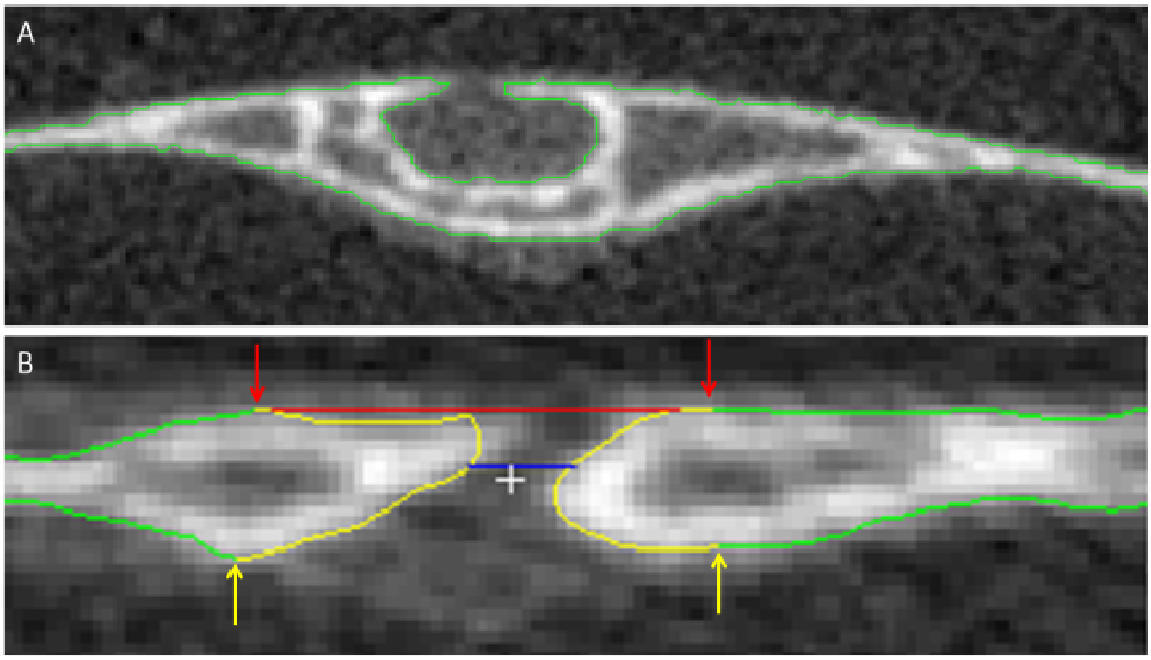

Figure 3-2: Representative segmentation boundary and morphometric measurements. (a) Representative segmentation boundary for an image with one bone. (b) The bone boundaries determined by the algorithm (green line) were used to find the osteogenic front (yellow line). The osteogenic front was defined as the global maximum of the segmented boundaries (red arrows) moving medially until a vertical point of inflection (yellow arrows). This was in turn used to find the minimum distance (blue line), mean distance, maximum distance (red line), and the suture center (white plus).

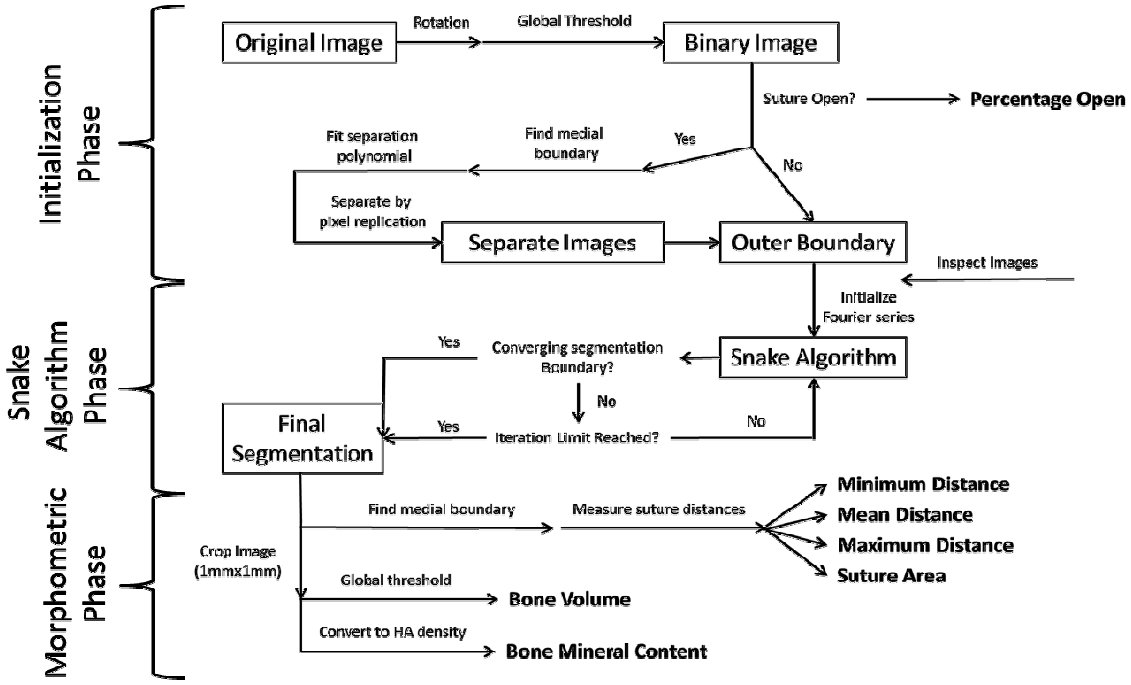

Figure 3-3: Flow chart detailing the functionality of the segmentation algorithm. The algorithm consists of three main phases: initialization phase, snake algorithm phase, and morphometric phase. All steps are fully automated with the exception of one manual interaction point after the end of the initialization phase to inspect the images. The output measurements from the morphometric and initialization phases are bold.

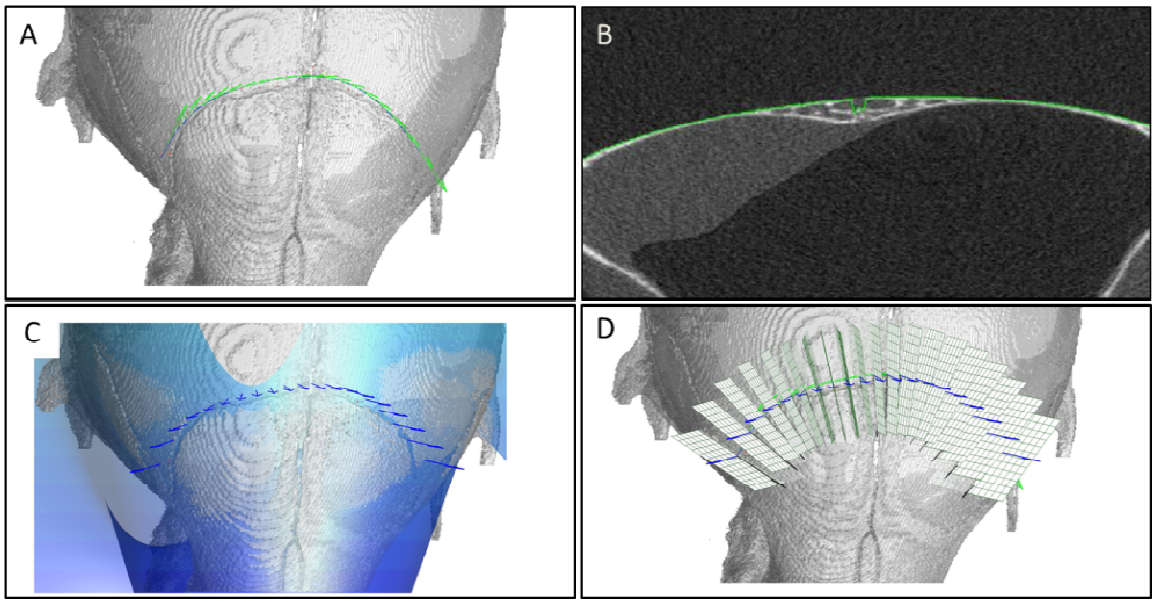

Figure 3-4: Reconstruction of images perpendicular to the coronal suture. (a) A 3rd order polynomial (a, blue line) is fit through the user defined center of the coronal suture (red +); resulting in the vector tangent to the surface (green arrows). (b) A global threshold is applied to find the ectocranial border of the skull (green line). (c) These points are reconstructed to create a bicubic polynomial surface of the skull (blue green mesh) that is used to find the vectors normal to the coronal suture (blue arrows). (d) The cross product of these vectors (black arrows) is then used to define a plane (green grid) that is used to reconstruct the image perpendicular to the suture.

3.3 Results

3.3.1 Posterior Frontal Suture Results

The initialization phase of the algorithm correctly approximated the bone boundaries and separated the images 95-99% of the time along the posterior frontal suture, being more accurate for the older samples. The interactive tool was able to correct all of the initialization errors by manually separating the images and modifying the global threshold.

The percentage of images that were open along the posterior frontal suture showed that at 6 days the entire posterior frontal suture was 84% open and decreased until reaching a plateau by day 20 (Figure 3-5a). The mean horizontal distance did not decrease until day 20 and appeared to reach a plateau (Fig. 5b). The minimum, maximum, and suture area all showed the same trends seen with the mean distance (data not shown). The bone volume of the entire posterior frontal suture remained relatively constant until increasing after day 12. The mineral mass showed identical trends to the bone volume measurements (data not shown). Unlike the two prior measures, the bone volume never reached a plateau for the time points studied (Figure 3-5c). This was identical to what was seen qualitatively with 2D μCT images for mice from day 6, 12, 20, and 25 (Figure 3-6a-d). The final segmentation boundary of the 20 and 25 day old mice shows regions where the segmentation boundary was able to bridge discontinuously mineralized regions (Figure 3-6c-d).

Representative histological images illustrate that the 6 and 12 day old sutures were largely open, but then fused and increased in bone volume for the later time points on days 20 and 25 (Figure 3-7a-d). Comparison between the serial histology and algorithm results showed excellent correlation for the three measures compared between the snake algorithm and the manual tracings of histologic images (Figure 3-7e-g). All three measurements had a statistically significant Pearson correlation coefficient ($p<0.01$) and had a R^2 value of greater than 0.96. The linear regression fit showed that all three measurements were within 1% of the line y=x and the y-intercept was essentially zero (Figure 3-7e-g).

Comparison between the different segmentation algorithms showed varying segmentation boundaries from a representative open 2D μCT image of a 20 day old mouse (Figure 3-8). Using a standard global threshold it is readily apparent that there are two bones in the image, but there gaps in the segmentation boundary from the discontinuous regions along the medial border of the left bone (Figure 3-8b). The segmentation using the Chen-Vese algorithm was able to bridge these discontinuous regions, but the algorithm incorrectly identified the fibrous connective tissue in the suture to be bone (Figure 3-8c). The segmentation boundary from the algorithm described above was able to both bridge the discontinuous regions and correctly separate the left and right bones of the image (Figure 3-8d).

3.3.2 Coronal Suture Results

The algorithm for the 3D reconstructions was able to correct the variations in the coronal suture when moving from medial to lateral. As expected, the algorithm produced a series of images where the bones were horizontal and reduced stretching of the coronal suture in the more lateral regions (Figure 3-9a-b). The initialization phase of the algorithm was able to correctly separate and estimate the bone boundaries 60-80% of the time. The decrease in accuracy of the initialization phase was due to the substantial overlap of the coronal sutures in the mice. Comparing the same image from the lateral coronal suture before and after reconstruction illustrates the effect of the algorithm highlighting a 1.7 fold increase in the distances between the bones when the images are not reconstructed (Figure 3-9a-b).

The coronal suture minimum distance remained relatively constant until day 12 at 0.3 mm, then decreased to a plateau, of 0.1 mm by day 20 (Figure 3-9c). The mean, maximum, and suture area all showed the same trends seen with the minimum distance (data not shown). The coronal suture bone volume remained relatively constant until day 12, then increased at a decreasing rate until day 25 (Figure 3-9d). Mineralization equivalent to hydroxyapatite mass showed identical trends and timing to bone volume (data not shown). In contrast to what was seen with the posterior frontal suture, the percentage of the coronal suture that was open decreased from 80% open on day 6 to approximately 40% by days 20 and 25 (Figure 3-9e).

The decrease in resolution seen with clinical imaging systems can pose a problem to some image processing algorithms when translating the technology to clinical use. The algorithms developed here were able to generate images that were perpendicular to the suture about all three axes for both the pathologically fused metopic and normally open coronal sutures even with the lower resolution clinical scans (Figure 3-10a-c). Furthermore the algorithm was able to correctly initialize 100% of the images for both sutures. The relatively larger size and more homogenous bones of the human skulls allowed for more accurate approximation despite the lower resolution. Representative images with final segmentation boundaries clearly delineate the fused or open sutures (Figure 3-10d-e).

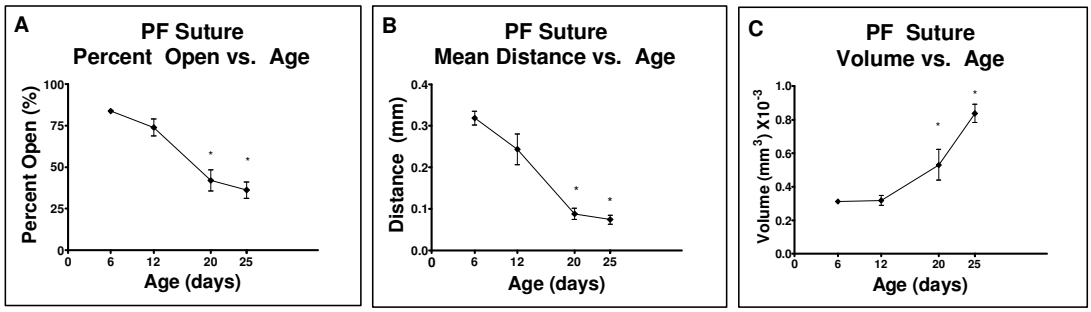

Figure 3-5: Posterior Frontal Fusion Results. (a) The suture was over 80% open on day 6, decreased on day 20, and then reached a plateau by day 25. (b) The mean distance decreased from over 0.3 mm beginning on day 20 and remained relatively constant after that. (c) The volume of bone in the suture began to increase on days 20 and 25. (*= $p < 0.01$ vs. 6 days)

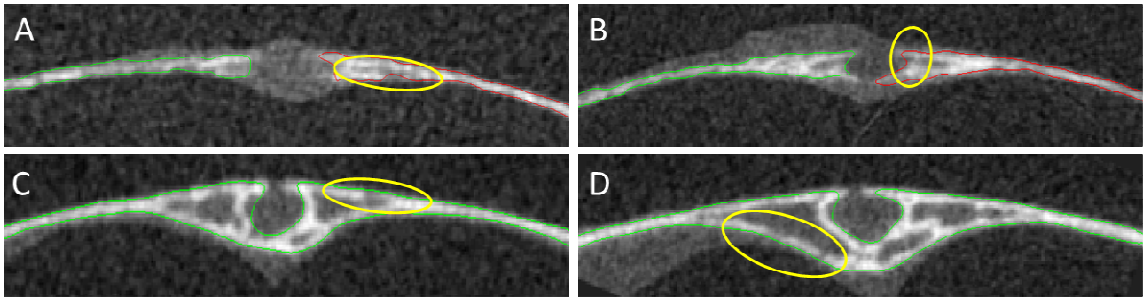

Figure 3-6: Representative µCT images with segmentation boundary. The algorithm was able to accurately segment the bones with low mineralization of the 6 (a) and 12 (b) day old sutures. The same algorithm parameters were able to also segment the images from the 20 (c) and 25 (d) day old sutures. The algorithm was also able to bridge discontinuous regions in images from all ages examined (yellow ovals).

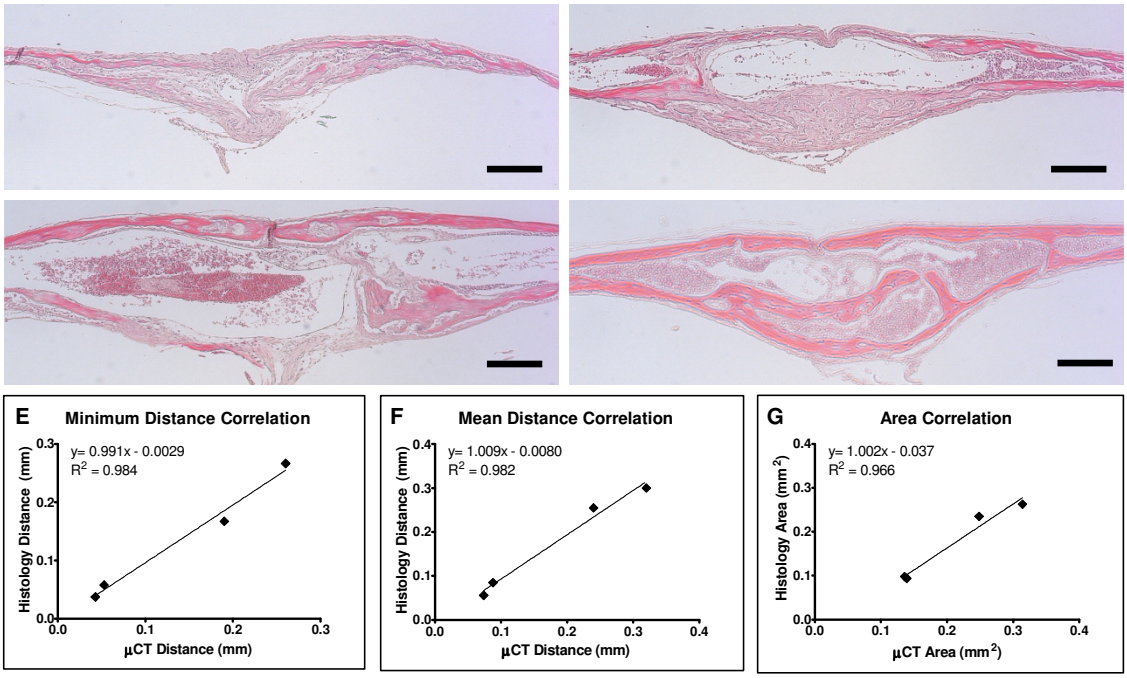

Figure 3-7: Histology validation for posterior frontal suture. (a) At 6 days old the suture is completely open and there is an abundance of fibrous connective tissue in the suture. (b) By day 12 the suture is beginning to close on the endocranial surface and by (c) day 20 the suture appears to be fused along the midline. (d) The most significant change seen between day 20 and day 25 is the increase in the volume of bone in the suture. The algorithm was validated with histology by comparing the (e) minimum distances, (f) mean distances, and (g) area. All three measures had correlation coefficients greater and 0.96 and were within 1% of the values obtained from histology. Scale bar represents 250 µm.

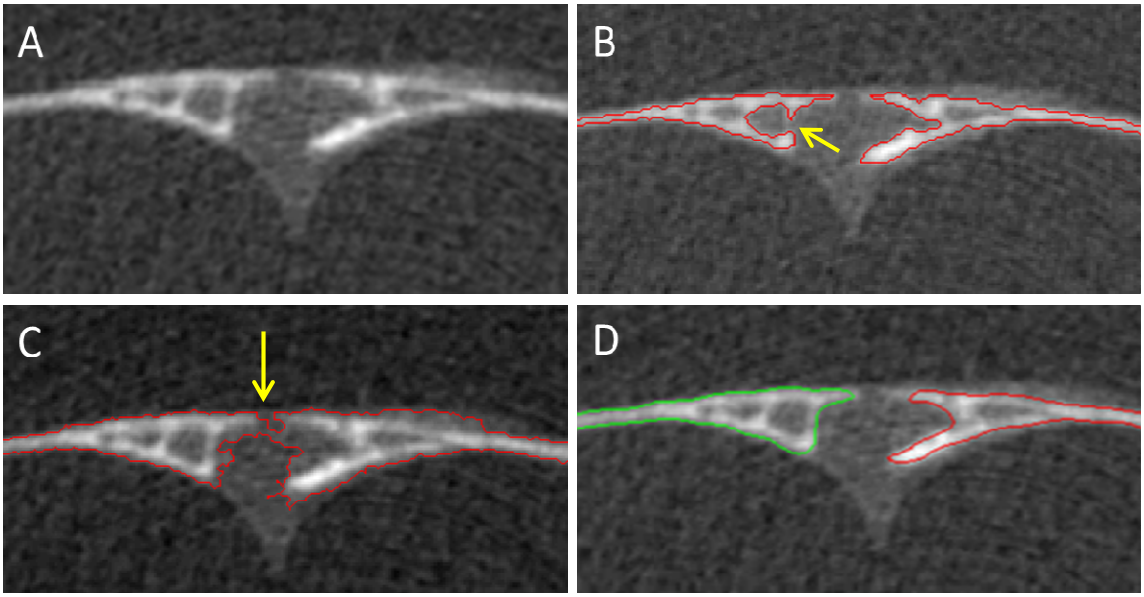

Figure 3-8: Representative µCT images comparing different segmentation algorithms. The original image from a 20 day mouse showing open suture (a). Using a global threshold (b) the algorithm was able to accurately separate the bones, but was not able to bridge discontinuous regions (yellow arrow). The Chen-Vese algorithm (c) was able to bridge discontinuous regions, but did not correctly separate the bones of the suture (yellow arrow). The algorithm presented here was able to correctly separate the bones of the image and also bridge discontinuous regions (d).

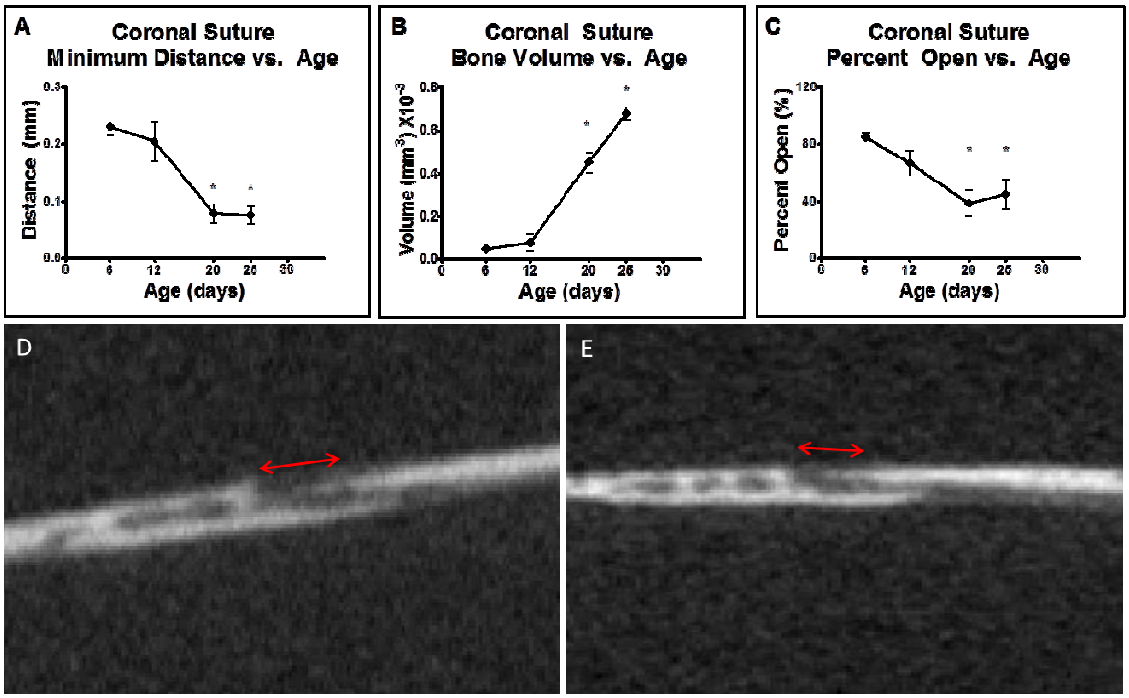

Figure 3-9: Coronal suture reconstruction. (a) The minimum distance of the coronal suture remained constant until day 12 then decreased dramatically until reaching a plateau by day 20. (b) The coronal suture bone volume remained constant then began to increase at a decreasing rate on day 20. (c) The percentage of the suture open decreased from 80% open on day 6 and decreased approximately 20% by days 20 and 25. (*= p< 0.01 vs. 6 days) (d) Before reconstruction the images of the lateral coronal suture, the bones sloped anteriorly to posteriorly and were elongated. (e) After reconstruction, the bones were horizontal and the elongation was not present.

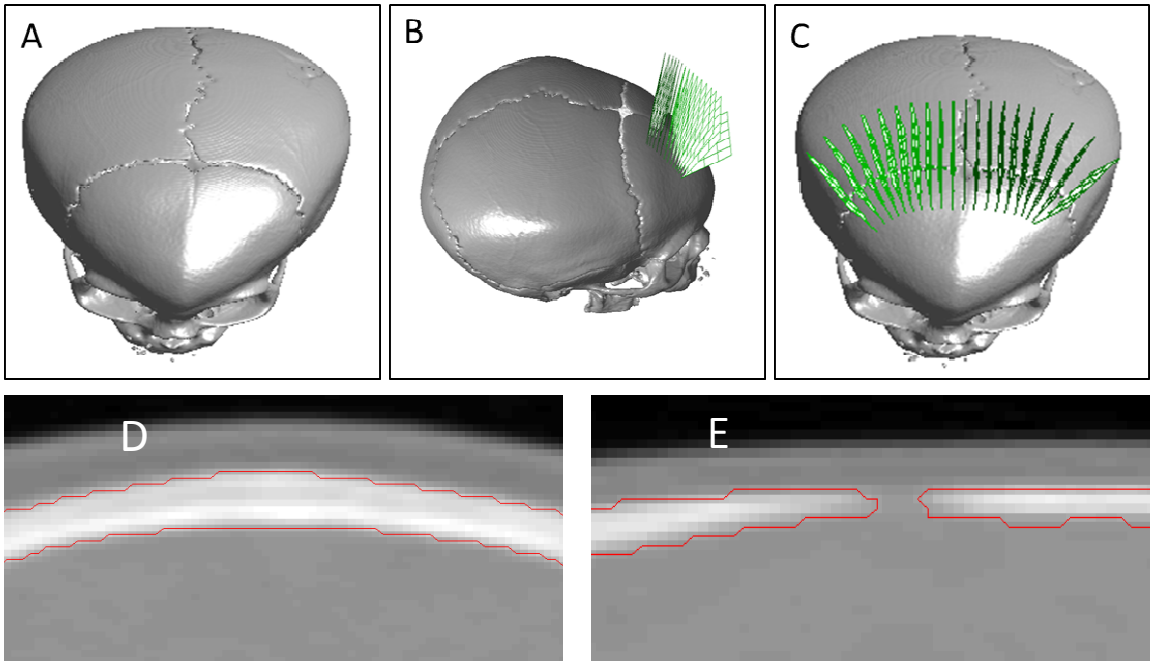

Figure 3-10: 3D Reconstructions of Human Craniosynostosis CT Scans. 3D rendering of 6 month of male with non-syndromic metopic synostosis. The algorithm was used to reconstruct images (green planes) of the pathologically fused metopic sutures (b) and open coronal suture (c). Segmentation boundaries (red line) following reconstruction and segmentation of representative images from fused metopic (d) and open coronal (e) sutures.

3.4 Discussion

The algorithm developed in this manuscript provides an accurate method to segment the bones in the suture. For the mouse posterior frontal suture, the initialization phase of the algorithm correctly initialized the bones of the suture over 95% of the time. The errors that were encountered with this phase in the posterior frontal suture of the mouse were most commonly caused by gaps in the lateral regions of the skull nor related to the suture. Especially in younger mice the suture mineralized discontinuously resulting in small islands of un-mineralized tissue that in many cases was incorrectly identified as the open suture. This was easily corrected manually but this interaction increases the time required to analyze the scans. The algorithms were able to correctly approximate 100% of the images from the human skull, despite the lower resolution. Additional improvements to the initialization phase of the algorithm could be made to make the analysis of the sutures fully automated.

One of the biggest advantages of the algorithm is its ability to segment the bones without relying on the absolute pixel intensities. By optimizing the curve along the border where the gradient was greatest, the algorithm was able to segment bones of very different densities without the need for subjectively altering any parameters. This is of a particular concern when studying processes where the tissues change in density over time, such as bone development or mineralization. Due to the heterogeneity of the posterior frontal suture, small gaps in the segmentation boundary can dramatically alter the measurements

between the bones. These errors are very common with traditional segmentation techniques, such as a global threshold, because they do not take into account any neighboring pixels when defining the tissue of interest. [71, 93, 128] The algorithm developed overcomes these limitations by using a continuous Fourier series representation of the segmented boundary. This allows the algorithm to bridge these gaps in the suture border where there may be regions that are not completely mineralized. The segmentation of cranial sutures is further complicated by the presence of fibrous tissue that is contained within the suture. As a result, minor changes in the global threshold lead to very substantial changes in the segmentation boundary of the sutures. The use of the snake algorithm overcomes this challenge because the final segmentation boundary is not dependent on the pixel intensities; rather it is driven by the relative change between them. This is of additional benefit when examining developmental or regenerative processes where the density of the tissue of interest changes between different groups. The algorithm was able to accurately segment the bones of both the 6 day and 25 day old groups without changing any parameters by using the snake algorithm phase to refine the boundaries.

The results from the algorithm clearly show that the posterior frontal suture, which is analogous to the human metopic suture, fuses early in development. The percentage of the suture open, suture area, and all of the distance measurements began to decrease on day 12 and reach a plateau by day 20. This strongly suggests that the suture has completed fusion before three weeks of age which is similar to what other investigators have shown in a

different strain of mice. [28] While previous studies have examined the process of suture fusion, to our knowledge this is the first method that allows for simultaneous assessment of fusion and mineralization of the entire suture. Bone volume and mineralization remained relatively constant until day 12 and then increased further on days 20 and 25. The increase in both of these parameters can be primarily attributed to an increase in thickness as well as an increase in density of the suture bones. The distance and bone volume measurements indicate that the posterior frontal suture completes fusion by 3 weeks of age and then increases in bone volume. This increase in bone volume never reached a plateau that was seen with the distance measures, which highlights the importance of further work is needed to fully characterize the complete development of the murine cranial sutures.

The serial sections from the histology correlated extremely well with the results from the algorithm. For all of the measures there was excellent linear correlation and as expected the mean distance measure had the highest correlation coefficient. Additionally, there was nearly a prefect one-to-one relationship between the serial histology and snake algorithm measures. The algorithm provides equivalent results to serial histology while being much faster and less expensive. As a comparison most of the serial sectioning took over 20 hours to perform and analyze per sample, while analyzing the same scans with the algorithm developed took on average 10 minutes per sample.

The 3D reconstruction and segmentation algorithms developed here provide a more accurate method to assess coronal suture development and

fusion. This reconstruction corrects for potential distortions along the length of coronal suture. The initialization phase of the algorithm resulted in slightly more errors with the coronal suture as compared to the posterior frontal suture. This is most likely caused by the substantial overlap seen with the bones of the coronal suture. Although these errors were easily identified and corrected by the interactive tool, this did increase in the amount of time the user had to spend processing each scan. The results from the coronal suture data showed that, similar to the posterior frontal suture, the distance between the bones decreased beginning at day 12 and then reached a plateau by day 20. The bone volume of the coronal suture increased at the same time as the posterior frontal suture. The biggest difference between the two sutures was seen with the percentage of suture open. Unlike the 80% decrease seen in the percentage of posterior frontal suture open, the coronal suture only had a 40% decrease. These results suggest that the bones of the coronal suture grow closer together, increase in bone volume, but do not fuse to the same extent compared to those of the posterior frontal suture.

Compared to traditional analysis techniques, the algorithm developed is an extremely rapid and accurate method for the analysis of both the posterior frontal and coronal sutures. Additionally, the 3D reconstruction of the coronal sutures is something that is not possible with the current analysis methods or image processing algorithms.

The biggest advantage of the algorithm is its ability to segment irregular and discontinuous objects of varying density. This is of critical importance when

studying developmental or regenerative changes in tissue that often are very irregular in their composition. Other implementations of the algorithm are currently in use to examine long bone growth plates, long bone segmental defect healing, cranial growth plates, and cranial defect healing in animal models.

There are numerous uses for this algorithm in basic science research, but arguably the clinical applications of the algorithm may be the most valuable. There are direct clinical applications for the algorithm in the field of craniofacial imaging. The preliminary results of the algorithm on clinical CT scans demonstrate the ability of the algorithm to quantify the cranial suture fusion on scans with a low radiation dose. While it is possible to obtain more accurate results from the algorithm with high resolution CT images, this benefit is often outweighed by the risks associated with the increase in radiation exposure to children with craniosynostosis who frequently need multiple CT scans. As a result there is a growing trend in pediatric radiology to use low dose CT protocols for imaging pediatric patients. The lower dose scans result in a decrease in image resolution that in turn has an effect on the precision of the measurements from some traditional imaging algorithms. Even with this lower resolution the algorithm was able to accurately segment both the open and pathologically fused sutures in children with craniosynostosis. The ability to precisely quantify the possibility of pathologic suture fusion has numerous advantages over the largely qualitative diagnoses currently made. This algorithm not only has the potential to dramatically improve the diagnosis of craniosynostosis, but hopefully provide surgeons more insight for the management of craniosynostosis.

The algorithm developed provides a new method to accurately segment bones of varying and heterogeneous mineralized tissues on CT images. The algorithm produces results within 1% of serial histology despite while being able to rapidly analyze the suture fusion and mineralization non-destructively. The results indicate that the posterior frontal suture completes fusion by day 20 and then begins to mineralize. While the bones of the coronal suture come together, increase in bone volume, but do not fuse together. The algorithm can also be used to examine clinical CT scans for the diagnosis of human craniosynostosis and re-synostosis without any additional modification.

CHAPTER 4 COMPLETE TIME COURSE OF THE MURINE POSTERIOR FRONTAL SUTURE FUSION

4.1 INTRODUCTION

Cranial sutures are the fibrous joints that arise from the interaction of the developing skull, fibrous connective tissue, and the underlying dura.[17] During early development, the bones of the skull that contain the suture are composed of active osteogenic fronts. As the skull expands, the cells in these fronts undergo rapid proliferation and differentiation to produce new bone to allow for continued cranial expansion. After the first year of life, the cranial sutures begin to fuse and this process continues in some individuals well into their twenties.[22] The mechanism that regulates the timing and order of the fusion of the cranial sutures remains largely unknown, but is thought to occur from the interplay between these osteogenic fronts and the underlying dura.

Premature fusion of the sutures occurs in 1 in 1,700-2,500 births and results in a condition referred to as craniosynostosis.[34, 164] The majority of craniosynostosis cases are non-syndromic, but approximately 40% of cases result from one of approximately 100 known syndromic mutations.[36, 164] If left untreated, craniosynostosis can cause severe craniofacial deformities and complications resulting from increased cranial pressure.[51, 172] These include blindness, deafness, developmental delays, seizures, upper airway obstructions, and even death.[49]

Mice are a commonly used model to examine normal cranial development due to their ease of study, conservation of molecular signals, and the growing number of transgenic strains of mice that display craniosynostosis. Unlike humans, rodents continue to grow throughout their life. As a result, the majority of the sutures in the rodent skull remain patent to allow for continued cranial expansion.[69] The exception to this is the mouse posterior frontal suture, which is analogous to the human metopic suture and fuses during early development.[70]

Histology has been the gold standard modality to assess suture fusion, but it provides only a limited view of the complex and discontinuous three-dimensional (3D) features of the tissue at each point in time. Recent advances in micro-computed tomography (μCT) hardware have enabled rapid, complete, and non-destructive 3D analysis, making μCT a powerful tool for studying the development of cranial sutures.[71, 128] Despite the potential of this imaging modality for the analysis of the developing murine cranial sutures, traditional image processing algorithms are either not accurate enough, require subjective assessment, or are prohibitively time consuming.[71, 173] These problems are primarily caused by the heterogeneous mineralization and large increase in calvarial density that is seen during suture fusion. To address this challenge, we previously developed a novel image processing algorithm to analyze the fusion of the murine cranial sutures.[174]

Despite the frequent use of mice to study cranial suture development, there have been significant discrepancies reported in the timing of murine posterior frontal suture fusion.[28, 70] These discrepancies have been seen with both traditional histological evaluation as well as μCT, but there is an overall agreement that this suture fuses early in development.[28, 70, 173] The overall goal for this study was to completely characterize the development and fusion of the murine posterior frontal suture. To do

this we used our novel image processing algorithm to quantify the complete time course of both fusion and mineralization of the posterior frontal suture in C57Bl/6J mice.

4.2 METHODS

Under approval of the Georgia Tech Institutional Animal Care and Use Committee, C57Bl/6J male mice (Jackson Labs, Bar Harbor, ME) were housed in a light and temperature controlled environment. Pups were kept with natural birth mothers until weaning or euthanasia. All mice were provided food and water ad libitum. Mice that were 21 days old or older were euthanized by CO_2 asphyxiation and pups under 21 days were euthanized by intraperitoneal injection of pentobarbital. Six mice were euthanized at each of the following time points: post-natal days 6, 8, 10, 12, 14, 16, 18, 19, 20, 21, 22, 23, 24, 25, 26, 27, 28, 29, 30, 35, 40, 45, 50, 56, 70, and 84. After verifying death by absence of a palpable heart beat and blink reflex, the calvaria were removed from soft tissues and fixed in 10% neutral buffered formalin (Sigma, St. Louis, MO).

The approximate region of the posterior frontal suture was identified from the most posterior molars in the maxilla and moved posteriorly 6.6 mm. The samples were contained within a 21 mm sample holder and were imaged with μCT with isotropic voxels 10.5 μm in size and an energy of 55 kVp (Viva CT 40, Scanco Medical, Bruttisellen, Switzerland). The exact location of the sutures was identified on 3D renderings made using a global threshold to create 1.5 mm tall by 2.5 mm wide DICOM images. The region of the posterior frontal suture was defined as the midline suture running between the posterior most aspect of the inter-frontal ridge to the bregma.

The images were analyzed with a novel algorithm that we previously developed and validated with serial histology to examine suture fusion.[174] Briefly, the algorithm uses a combination of a global threshold and snake algorithm to segment the bones of the developing sutures. This allows for accurate identification of the varying and irregular

mineralization of the developing suture. These segmentation boundaries are then used to determine the percentage of suture that is open; the minimum, mean, and maximum distances between the bones; the area between the sutures; the bone volume and equivalent mineralization in µg hydroxyapatite (HA) in a 1 mm by 1 mm region centered over the suture. Additionally, the spatial variation in suture fusion was examined by dividing the suture into four evenly spaced regions moving from the anterior first (1^{st}) quarter to the posterior most fourth (4^{th}) quarter. To ensure that the algorithm would identify fully closed sutures, we also analyzed the parietal bone in a 50 day old mouse using the algorithm and showed that these bones were 100% closed and had a distance measurement of zero.

4.3 RESULTS

At post-natal day 6, the entire posterior frontal suture was 84% open and then decreased until reaching a plateau at approximately day 20 (Figure 4-1A). The suture never completely fused and was approximately 20% open even on day 84. The analysis of the spatial variation showed that the anterior most 1st quarter was nearly 100% open at day 6, 10% open by day 20, and remained approximately 10% open through the remainder of time points examined (Figure 4-1B). The 2nd and 3rd quarters also began nearly 100% open, but the decrease was later and more gradual in the more posterior regions (Figure 4-1C-D). The posterior most 4th quarter, showed no substantial changes over the age range of the animals and was approximately 45% open throughout all ages (Figure 4-1E).

The mean horizontal distance of the posterior frontal suture remained relatively constant at 0.30 mm until day 10, decreased until day 20, and reached a plateau of approximately 0.05 mm (Figure 4-2A). This distance in the 1st quarter was initially 0.40 mm and decreased dramatically until reaching a plateau of less than 0.05 mm by day 20 (Figure 4-2B). The 2nd and 3rd quarters also had a later and more gradual decrease in horizontal distance in comparison to the most anterior region (Figure 4-2C-D). The posterior most 4th quarter showed no changes in horizontal distance over time, with a mean distance of approximately 0.10 mm (Figure 4-2E). The minimum distance, maximum distance, and suture area all showed identical trends and timing to what was seen with the mean distance (Figures A2-4).

Total bone mineral of the entire posterior frontal suture remained relatively constant at 0.04 mg HA until day 20, then increased until reaching a plateau beginning

on day 40 to 0.15 mg HA (Figure 4-3A). Spatial analysis of the anterior three quarters showed that the total mineral increased later and more gradually from anterior to posterior (Figure 4-3B-D). The posterior most 4th quarter showed no change in mineral with time (Figure 4-3E). Bone volume measurements showed identical trends and timing for the overall suture and for each of the 4 quarters (Figure A-5).

Three-dimensional reconstructions of the posterior frontal suture support the snake algorithm results. At 6 days of age, the posterior frontal suture was mostly open and by 12 days of age, the anterior region had begun to close in discontinuous segments (Figure 4A-B). By day 20, the anterior most three quarters were mostly fused, but there were small segments that still remained open (Figure 4-4C). Between days 20 and 55, the most significant change was an increase in the thickness of the bone surrounding the sutures, corresponding to the increase in mass and volume seen with the snake algorithm (Figure 4-4D). It is important to note that even on day 50 there were regions of the posterior frontal suture that remained open. These were largely found in the posterior region of this suture, but regions of open suture were also found in multiple mice in the anterior most quarter even on day 50. This was seen with both μCT and histology (Figure 4-5).

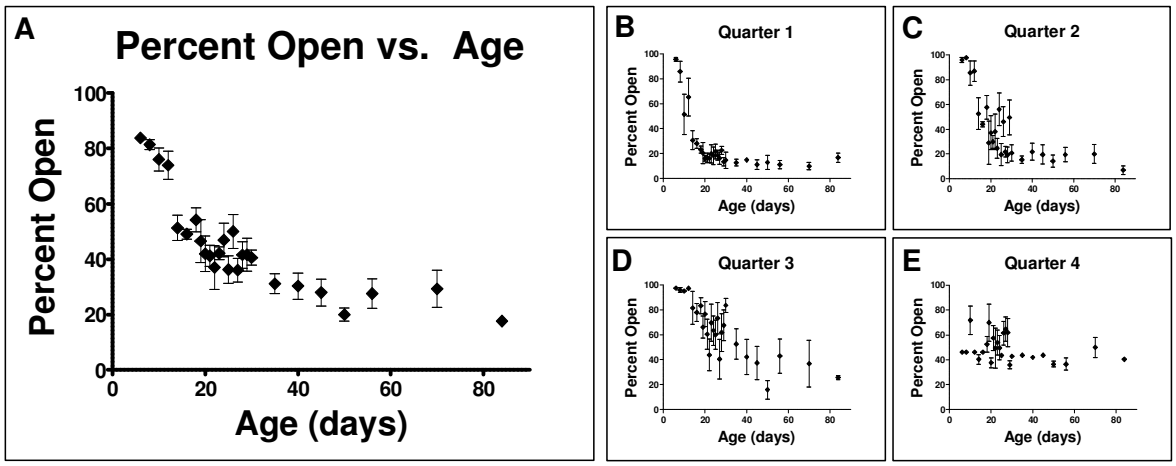

Figure 4-1: Percentage of the suture open. The entire suture (A) was approximately 85% open on day 6, began decreasing on day 12, and then reached a plateau of approximately 20% open beginning on day 20. The anterior most quarter (B) of the suture showed first and fastest decrease in percentage of suture that was open, followed by the second (C) and third quarter (D). There were no changes seen the posterior most fourth quarter (E).

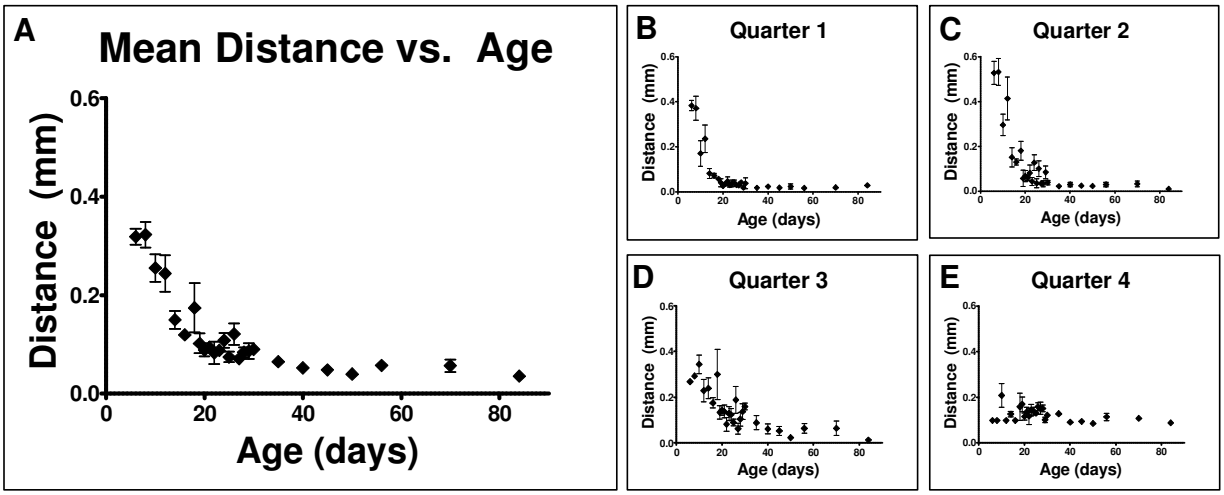

Figure 4-2: Mean distance between the bones of the posterior frontal suture. The entire suture (A) had a mean distance of 0.35 mm on day 6, began fusing on day 12, and then reached a plateau of 0.05 mm beginning on day 20. The anterior most quarter (B) of the suture had the first and fastest decrease in distance, followed by the second (C) and third quarter (D). There were no changes seen in the distances for the posterior most fourth quarter (E).

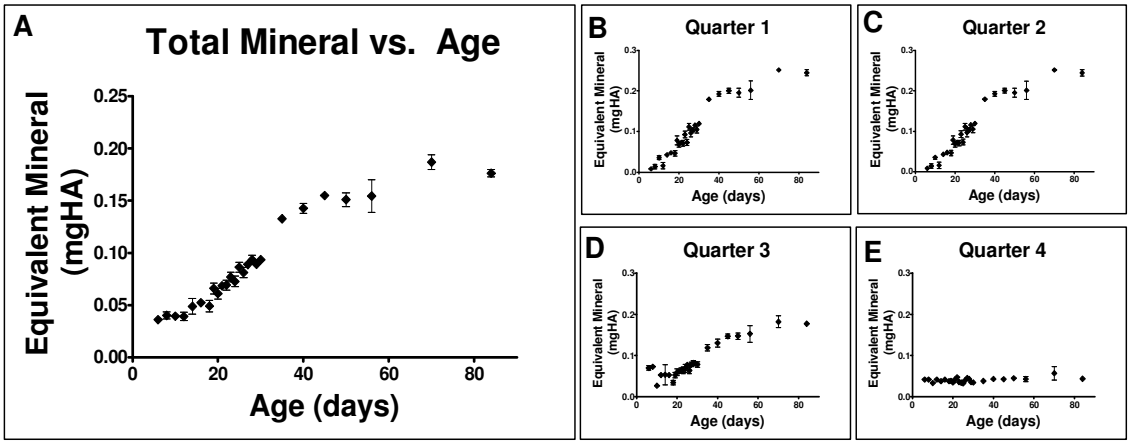

Figure 4-3: Total mineral in a 1 mm by 1 mm region of the posterior frontal suture. The mass of bone in the entire suture (A) remained relatively constant at 0.04 mg HA until day 20 and then reached a plateau beginning on day 40 at 0.15 mg HA. The anterior most quarter (B) of the suture had the first and fastest increase in mass, followed by the second (C) and third quarter (D). There were no changes seen in the bone mass for the posterior most fourth quarter (E).

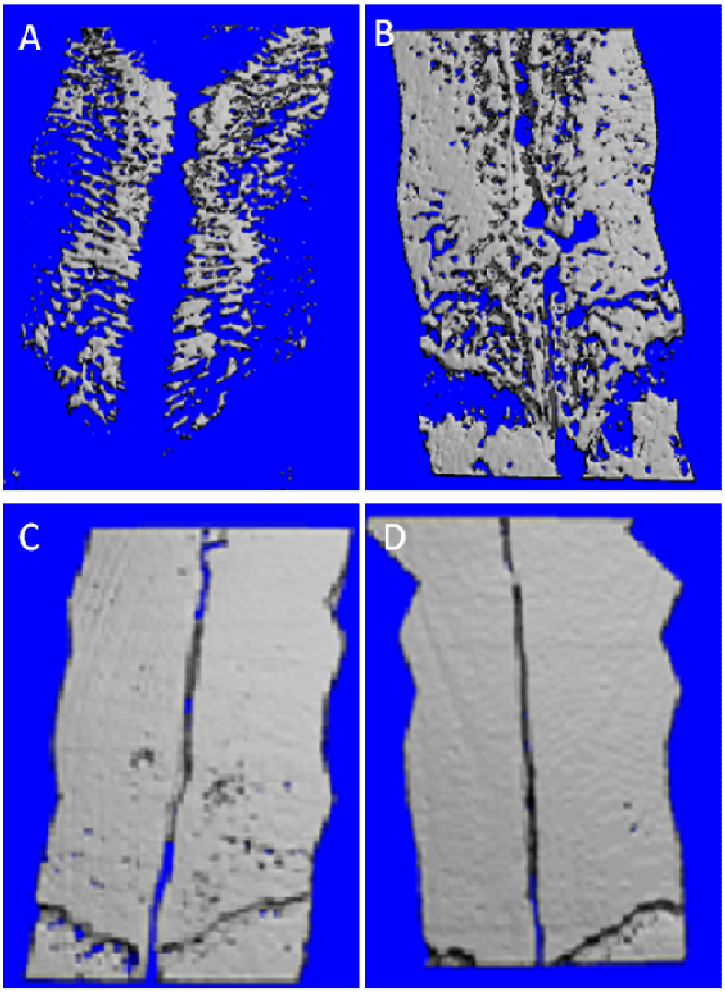

Figure 4-4: 3D reconstruction of the key developmental time points in posterior frontal suture fusion. The reconstructions are made using a global threshold and the same threshold was applied to all the ages examined. The image of the 6-days old PF suture shows the suture completely open (A) and by 12 days the suture has begun to fuse (B). The suture fusion is greatest anteriorly, but the suture fusion is very discontinuous. By day 20 the suture nears complete fusion (C) and day 50 there is a thickening of the bones in the suture (D). Even at day 50 there are still some regions of the suture posteriorly that are not fused (D).

Figure 4-5: Histology of the anterior most quarter of the posterior frontal suture in a 50 day old mouse. The image shows that endocranial region of the suture is completely open. The ectocranial boundaries of the bone appear in close proximity, but there is no bone bridging the suture. Stained with haematoxylin and eosin.

4.4 DISCUSSION

The results from the algorithm clearly show that the posterior frontal suture fuses early in development. The percentage of the suture open, suture area, and all of the distance measurements remained constant until day 10, began to decrease after day 12, and reached a plateau by day 20. After this point there was essentially no change in any of these measurements. This demonstrates that the posterior frontal suture fuses between days 10 and 20, but the fused sutures were not completely mineralized.

Others have shown that the posterior frontal suture fuses early in development, but there is not agreement on when the tissues actually fuse. The most commonly cited study suggests that the suture fuses between days 25 to 45, in an anterior to posterior direction.[70] In contrast, our results show that the suture was already fused by day 25 and that this time frame corresponds to the increase in bone volume and mineral. One explanation for the difference is that the algorithm allows for complete analysis of the entire suture, whereas non-serial histology only examines a very limited region of the suture. The discontinuous nature of suture seen both by us and other investigators makes generalization from a few histology sections unreliable.[71]

Our results are similar to those reported by Sahar et al. using serial histology to examine suture fusion in CD1 mice.[28] Both data sets suggest that the posterior frontal suture has fused before the first 3 weeks of life, but there are some differences noted between the two studies, most likely due to inherent differences in the strain of mice that were used. We examined C57Bl/6J mice, which are known to have different craniofacial bone density than other mouse strains.[175]

The spatial analysis of suture fusion from the snake algorithm showed that the anterior regions of the posterior frontal suture fused first and more rapidly than the

posterior regions of the suture. Others have also reported similar findings using histological assessment.[70] Taken together, the posterior frontal suture fuses from anterior to posterior. Even in the anterior regions of the oldest mice, there was never 100% suture closure nor did the distance measurements ever reach zero. This indicates that the suture never completely fuses and that there are always at least small regions where the suture is open. These gaps were seen with histology, the grayscale μCT images, and the 3D rendering of the skulls. Analysis of the parietal bone in a 50 day old mouse using the algorithm showed that these bones were 100% closed and had a distance measurement of zero, indicating that these gaps are not an artifact from μCT or errors from the algorithm. Additionally, the spatial variation of the posterior most quarter showed that this region did not fuse or increase in bone mass like the remainder of the suture. This is most likely caused by the close proximity of this region to the bregma.

Our results demonstrate that suture fusion is a biphasic process. The bone mineral and volume remained relatively constant during the first 20 days and did not increase until after the suture fusion was essentially completed. Beginning on day 21, the bone volume and mineral content increased and reached a plateau by day 45. The increase in mineral and volume can be attributed to an increase in thickness as well as an increase in density of the suture bones. These observations indicate there are significant developmental changes after the suture fusion has occurred.

The algorithm used for this study is the first method that allows for simultaneous non-destructive quantification of both fusion and mineralization of the entire suture. While it is possible to obtain a complete understanding of suture fusion with serial histology, it is prohibitively time consuming and expensive for large numbers of samples. Using the combination of μCT and the algorithm we were able to analyze each sample in less than one thirtieth the time and one tenth the cost of serial histology. Additionally the

algorithm not only provides a qualitative “open” vs. “closed” assessment, but it also provides a more precise quantification of the distances and area between the bones of the suture. These measurements more accurately reflect the process of suture fusion and show that the percentage of the suture open had the largest variation of all the measures examined. The results from this study clearly demonstrate that the murine posterior frontal suture fuses discontinuously from anterior to posterior. This fusion occurs through a biphasic mechanism consisting of an early fusion phase between day 10 to 20 and a later mineralization phase between days 20 to 45.

CHAPTER 5 GENES ASSOCIATED WITH EARLY CARTILAGE INDUCTION OF SUTURE FUSION

5.1 INTRODUCTION

Fusion of the cranial sutures results from a complex process requiring tightly controlled interactions among the bones of the skull, the fibrous connective tissue between these bones, and the underlying dura.[17, 73, 87] During early development the cranial sutures have very active osteogenic fronts where cells undergo rapid proliferation and differentiation to produce new bone to allow for continued cranial expansion. Craniosynostosis is the premature fusion of the cranial sutures and occurs in approximately 1 in 1700-2500 births.[34, 164] Most cases of craniosynostosis require calvarial remodeling to treat the complications that can result either directly from the craniofacial deformities or increased cranial pressure.[35] Despite the frequency and severity of complications associated with the treatment of craniosynostosis there still are no clinically available therapies to biologically target this premature fusion or complications relating for re-synostosis of the skull.

Mice are commonly used to study the mechanisms responsible for cranial suture development due to their relative conservation of molecular signals and rapid development.[55, 87] The major difference between murine and human cranial

development is that only the posterior frontal (PF) suture, analogous to the human metopic suture, fuses in the mouse.[70] The remaining sutures remain patent to allow for continued expansion of the brain and skull.

The dura underlying the sutures has been implicated as a major regulator of suture fusion or patency.[23, 176] Studies using organ cultures have shown that the underlying dura can alter the fate of these normally open or fused sutures.[23] Moreover there are regional and age differences in the dura with differences in osteogenic gene expression and a varying ability to re-heal calvarial defects.[25, 75] Despite the growing body of evidence examining the differences between the open and fused sutures, there has been relatively little work focused on the developmental changes that occur over time in both the bone and dura that are responsible for normal suture fusion. [28, 70]

Using a novel image processing algorithm to analyze micro-computed tomography (micro-CT) images, we previously determined that the murine posterior frontal suture fuses through a biphasic process.[177] Between post-natal days 10-20, the PF suture fused through a discontinuous process moving from anterior to posterior. This was followed by a mineralization phase during which bone volume and mineral content increased, occurring between days 20-45.

Our overall goal for the present study was to identify genes that are associated with the developmental changes seen during normal cranial suture fusion. Based on the changes observed with using micro-CT, we chose the following time points to examine the changes in gene expression associated with the bi-phasic suture fusion process: post-natal day 6, which is prior to fusion; day 9, which immediately precedes the onset of suture fusion; day 12, which is immediately after onset of suture fusion; day 16, which is the midpoint of suture fusion; day 20, which is the end of fusion and the beginning of mineralization; day 25, which is the midpoint of mineralization phase; and day 55, at

which time the suture is fully developed. Analysis was performed using both PCR arrays to screen and real-time PCR to confirm changes in gene expression in both the bone and dura that are associated with both phases of suture development.

5.2 METHODS

Under approval of the Georgia Tech Institutional Animal Care and Use Committee, C57Bl/6J male mice (Jackson Labs, Bar Harbor, ME) were housed in a light and temperature controlled environment. Pups were kept with natural birth mothers until weaning or euthanasia. All mice were provided food and water ad libitum. Mice 21 days old or older were euthanized by CO_2 asphyxiation and pups under 21 days were euthanized by intraperitoneal injection of pentobarbital. Nine mice were euthanized at each of the following post-natal time points: days 6, 9, 12, 16, 20, 25, and 55. The skulls were isolated from surrounding soft tissues and the jaw, skull, base, and brain were removed. Skulls were washed with chilled phosphate buffered saline and the sutures were visualized under 4x magnification. The anterior most 75% of the PF suture region was isolated to form an approximately 1.5 mm wide by 2.0 mm long tissue sample. The posterior most 25% of the PF suture was not used for this study because this region of the calvaria does not undergo fusion.[177] The dura was meticulously dissected from the bone using a 30 gauge needle taking care not to include any of the fibrous mesenchymal tissue in the suture or the periosteum. The periosteum was also dissected away from the bone and discarded. Tissue samples were snap frozen in liquid nitrogen and stored at -80°C until RNA extraction was performed.

The bones and the dura from three mice were pooled for each sample to ensure that there was at least 1 µg of RNA available for analysis. Bone samples were placed in liquid nitrogen and ground using a molar and pestle. Dura samples were ground in glass homogenizer tubes at room temperature. Samples were allowed to thaw to room temperature and then incubated in 4.5 mL of Trizol supplemented with 10 µl/mL of

Proteinase K warmed to 55 ℃ for 5 minutes (Qiagen, Valencia, CA). After incubation, 0.9 mL of chloroform was added to each tube, vigorously shaken for 15 seconds, and then centrifuged at 10,000 RPM for 30 minutes. The supernatant was combined with an equal volume of 70% ethanol then passed through an RNeasy (Qiagen) column for purification and elimination of genomic DNA. The RNA was extracted from the column and quantified using the Nanodrop 1000 spectrophotometer (NanoDrop Products, Wilmington, DE).

A Mouse Osteogenesis RT² Profiler™ PCR Array (SA Biosciences, Fredrick, MD) was used to profile 84 genes associated with osteogensis, chondrogenesis, and angiogenesis (Supplemental Table 1). The cDNA library was made using the RT^2 First Strand Kit (SA Biosciences) beginning with a total mass of 1.0 µg of RNA for both the bone and dura. The plates were prepared according to the manufacturer's specifications for mice that were 6, 12, 20, and 55 days old. Gene expression on the arrays was quantified by calculating the delta-delta-CT method and genes that showed statistically significant threefold or greater changes were included for confirmation with real-time PCR. The expression of each of the genes was normalized by an average of 4 housekeeping genes contained on the PCR array.

Primers for real-time PCR confirmation of the microarray results were designed using the Beacon designer version 7 and optimized with RNA from the bone (Premier Biosoft, Palo Alto, CA). Samples from the 6, 9, 12, 16, 20, and 25 day old groups were used. Sequences of all primers are shown in Supplemental Table 2. Although we did not perform an array for the 9 and 16 day time points, we included them in the real-time PCR analysis, as they represented onset and midpoint of suture fusion, respectively. We did not analyze RNA from the 55 day time point, as the array indicated that the gene expression profile was nearly identical to what was seen with the 25 day samples in the

PCR Arrays. The cDNA library was made with the High-Capacity cDNA Reverse Transcription Kit (Applied Biosystems) with 1.0 µg RNA for the bone and 0.3 µg of RNA for the dura. Prior to performing real-time PCR, the cDNA samples were diluted 1:20 for bone and 1:15 dilution for dura in sterile nuclease free water. The starting quantity of the samples was calculated based on a 1:3 serially diluted standard pooled from samples of varying ages. The starting quantity of all genes was normalized by the housekeeping gene glyceraldehyde phosphate dehydrogenase (GAPDH), as this gene showed the least change in expression among the housekeeping genes.

In order to better visualize the temporal expression profile of cartilage associated genes, the data from both real-time PCR and from the fusion of the posterior frontal suture were directly compared. The relative expression from the real-time PCR, the distance between the bones of the developing suture, and the total mineral content of the sutures were normalized so that all values ranges from 0 to 1. All data sets were then plotted on the same set of axes for direct comparison.

To verify the presence of cartilage in the posterior frontal suture with this strain of mice, serial histology was performed on a representative skull from a 12 day old mouse. The skull was fixed in formalin, dehydrated with graded washes of ethanol, and embedded in paraffin. After verifying the start of the posterior frontal suture, 7 µm thick serial sections were made and stained with Safranin-O with fast green counter stain using standard protocols.

Statistical Analysis

The delta-delta-CT values from the PCR arrays were analyzed by performing a 2 sided t-test with Student's modification and determining the relative change of the gene expression relative to the 6 day old group (Matlab R2010a, Mathworks, Natick, MA). The Gaussian distribution of the real-time PCR confirmation results was first verified using

the Kolmogorov-Smirnov normality test. Statistical significance was determined using a 1 way ANOVA and the difference between groups was analyzed using Bonferroni's modification to the t-test where appropriate (GraphPad Prism, GraphPad Software, La Jolla, CA). A $p<0.05$ was considered to be significant. All results are represented as the mean ± the standard error of the mean. All samples contain tissue pooled from 3 mice with a N=3 for all measurements (9 total mice per time point).

5.3 RESULTS

The PCR arrays showed 28 genes for bone and 14 genes for dura that met our inclusion criteria detailed above (Tables 1-2). The genes included many of the collagen proteins, receptors commonly associated with syndromic forms of craniosynostosis, extracellular BMP inhibitors, transcription factors associated with osteoblast and chondrocyte differentiation, members of the TGFβ superfamily, and other growth factors commonly associated with osteoblast differentiation.[164] All of these genes were included for analysis by real-time PCR.

The extracellular matrix protein, dentin matrix protein 1 (Dmp1) was highly expressed prior to the initiation of suture fusion on day 9, and then decreased for the remaining time points (Figure 5-1A). The expression of bone sialoprotein (Ibsp) had a nearly identical expression profile and was highly expressed on days 6 and 9 (Figure A-7). The transforming growth factor beta (Tgfb) family genes showed a biphasic expression profile that closely matched both phases of suture fusion, seen previously with micro-CT.[177] Both Tgfb2 and Tgfb3 peaked in expression immediately prior to the onset of suture fusion on day 9 and again during the mineralization phase on day 25 (Figure 5-1C-D). Tgfb1 (Figure 1B) and the downstream signaling molecules SMAD family member (SMAD) genes (data not shown) showed no significant changes in expression.

All of the genes associated with chondrocyte differentiation and hypertrophy increased expression near the onset of suture fusion on day 12. mRNAs for aggrecan (Acan), a protein typically associated with the cartilage extracellular matrix, increased early during days 6 and 9 before decreasing for the remaining time points (Figure 5-2B).

The transcription factor SRY-box containing gene 9 (Sox 9) that is an early marker of chondrocyte differentiation had peak expression immediately following suture fusion on day 12. Similarly, the cartilage associated extracellular matrix proteins collagen 2 (Col II) and collagen oligomeric matrix protein (Comp) had a peak in expression on day 12 (Figure 5-2D-E). Like the other extracellular matrix proteins, mRNAs for the marker of chondrocyte hypertrophy, collagen X (Col X) had the largest increase in expression on day 12, which was followed by a later peak during the mineralization phase on day 25 (Figure 5-2E). Collagen I (Col I) is a major component of the bone extracellular matrix but showed exhibited no changes in expression (Figure 5-2F).

The expression profiles of genes from the dura under the PF suture differed slightly from what was observed with the bone. Dmp1 had greater expression on day 6, then decreased for the remaining time points (Figure 5-3A). Expression of Dmp1 peaked early in bone and remained high for a longer period. The peak in expression of Sox9 occurred on day 9, which was similar to what was seen in the bone (Figure 5-3B). mRNAs for both of the extracellular matrix proteins Col II and Col X peaked in expression on day 9, whereas peak expression in bone was on day 12 in the bone (Figures 5-3C-D). In contrast to what was seen in the bone, Comp and Col X peaked on day 16 followed by a second and smaller peak on day 25 during the mineralization phase (Figures 5-3E-F).

Normalization of cartilage genes associated with the fusion of the PF suture showed that mRNAs for these proteins correspond closely with the onset of suture fusion (Figure 5-4). The distances between the bones of the suture remained constant until day 12 before decreasing to a plateau on day 20. All cartilage associated genes had low expression early, then peaked in expression on day 12, before decreasing as the bone volume began to increase. The presence of cartilage in the suture was verified

at this time point by the positive staining for glycosaminoglycans in the suture (Figure 5-5). The glycosaminoglycans were localized along the endocranial aspect and between the osteogenic front of the suture.

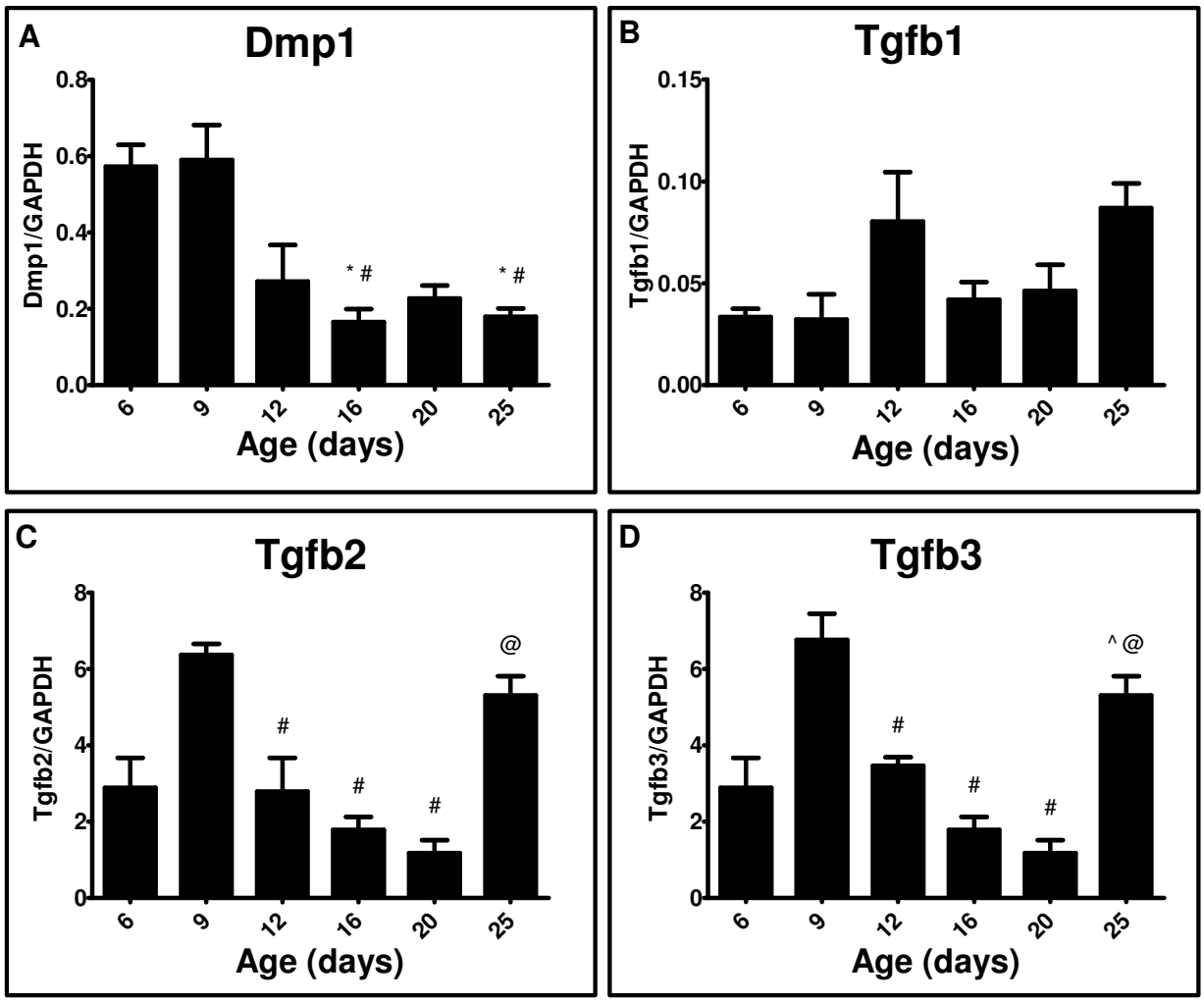

Figure 5-1: Genes showing early expression in bone from the PF suture, measured by real-time PCR: Dmp1 (A), Tgfb1 (B), Tgfb2 (C), Tgfb3 (D). $p<0.05$ vs *=6d, #=9d, %=12d, @=16d, ^=20d.

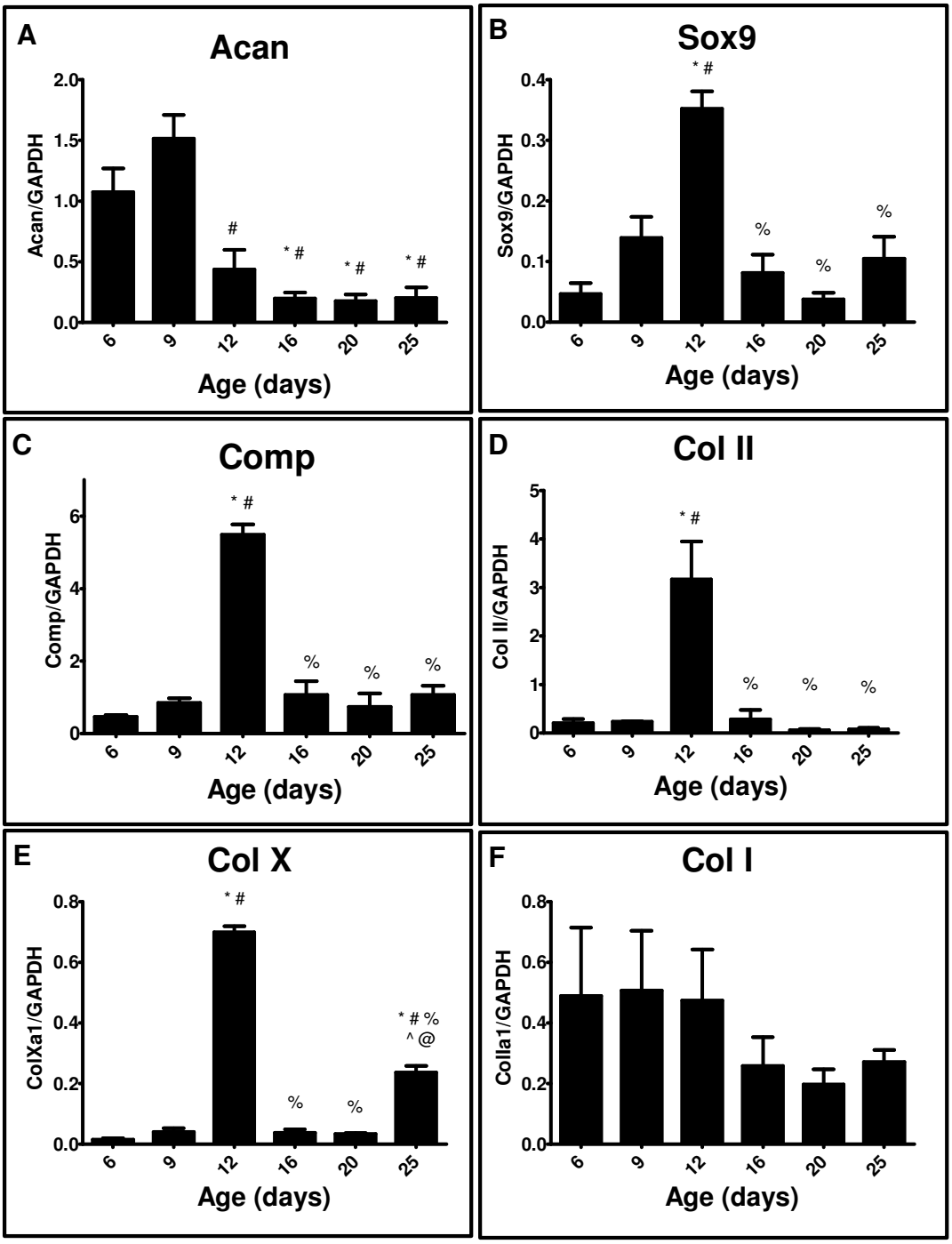

Figure 5-2: Cartilage associated genes expressed in PF bone, measured by real-time PCR: Acan (A), Sox9 (B), Comp (C), Col II (D), Col X (E), and Col I (F). $p<0.05$ vs *=6d, #=9d, %=12d, @=16d, ^=20d.

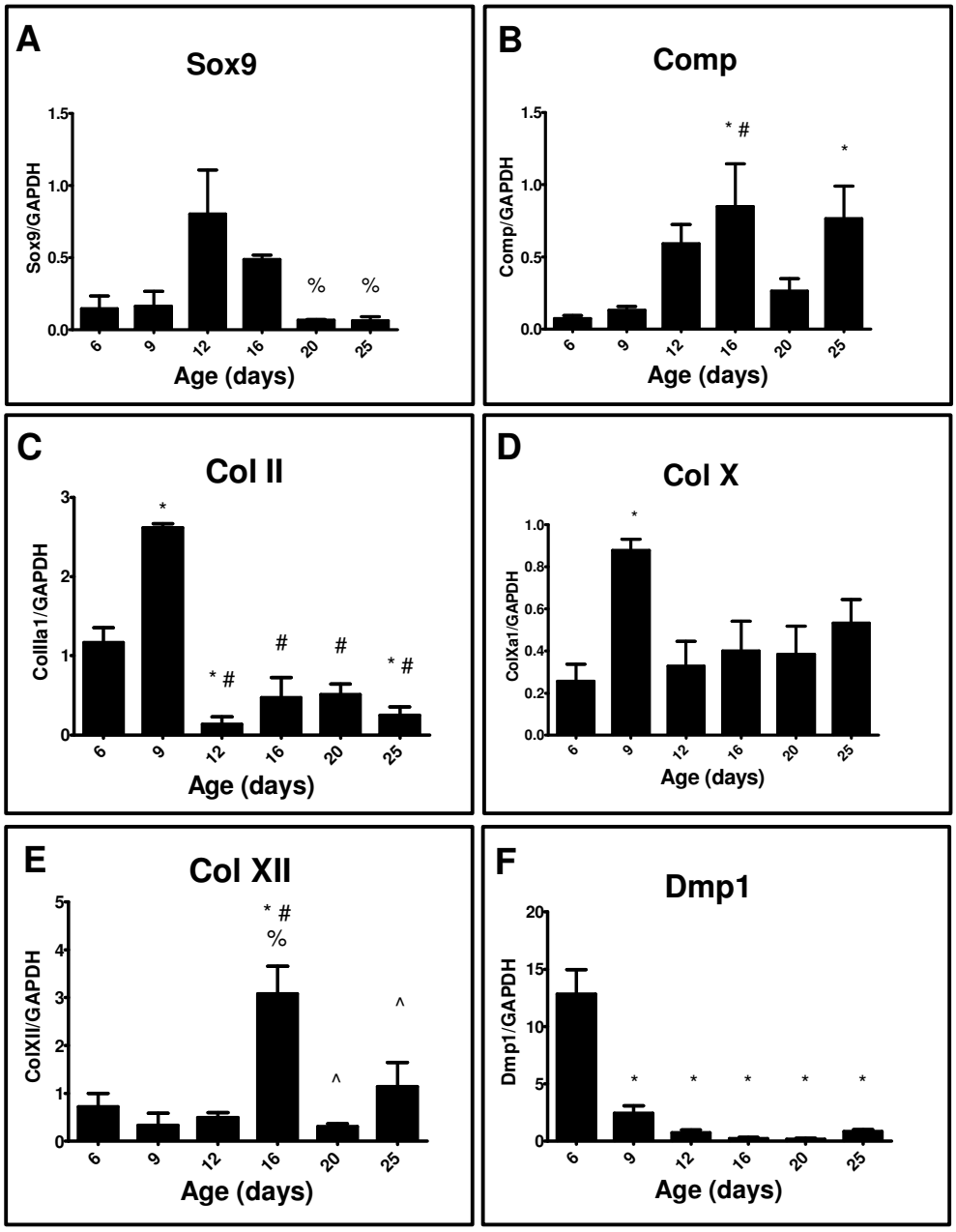

Figure 5-3: Expression profiles for cartilage associated genes in the dura underlying the PF suture. Sox9 (A), Comp (B), Col II (C), Col X (D), Col XII (E), and Dmp1 (F). $p<0.05$ vs *=6d, #=9d, %=12d, @=16d, ^=20d.

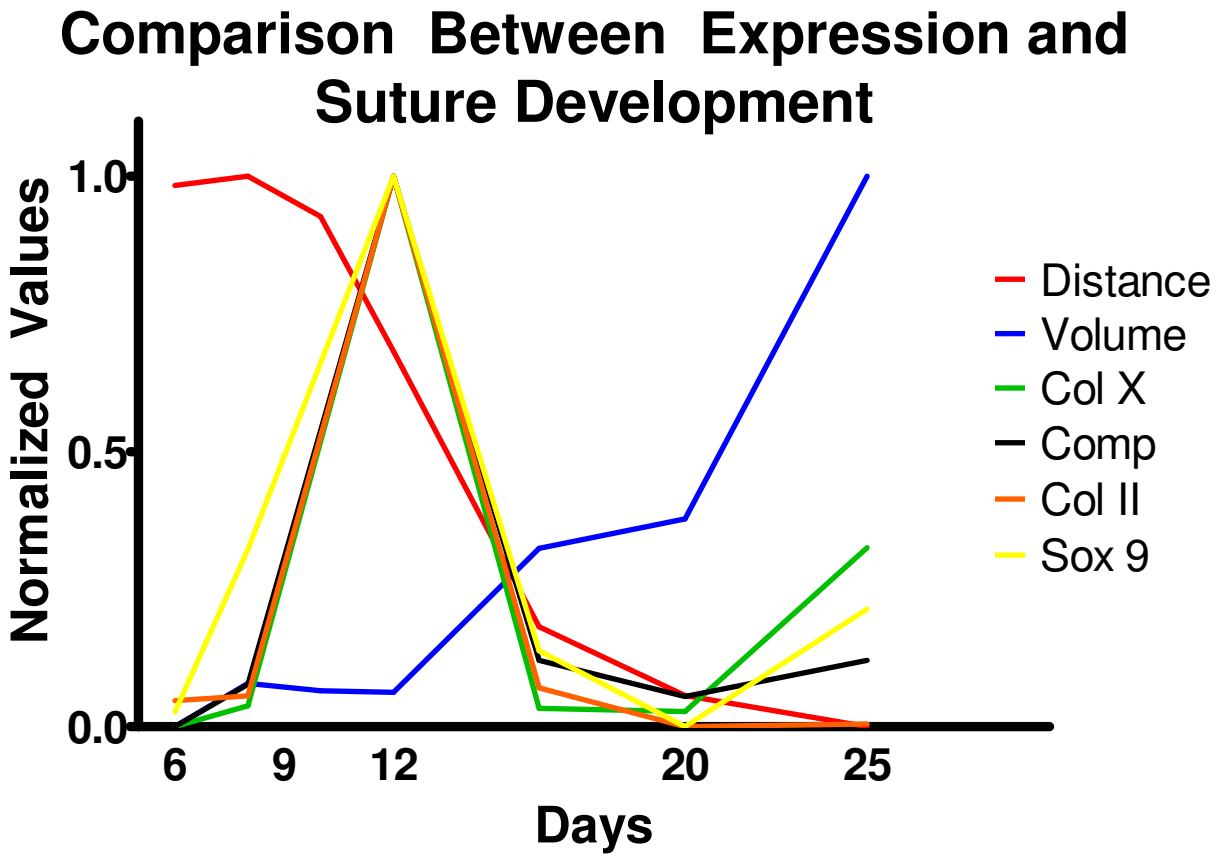

Figure 5-4: Normalized comparison between gene expression, suture distance (red), and suture bone volume (blue) for Col X (green), Comp (black), Col II (orange), Sox 9 (yellow).

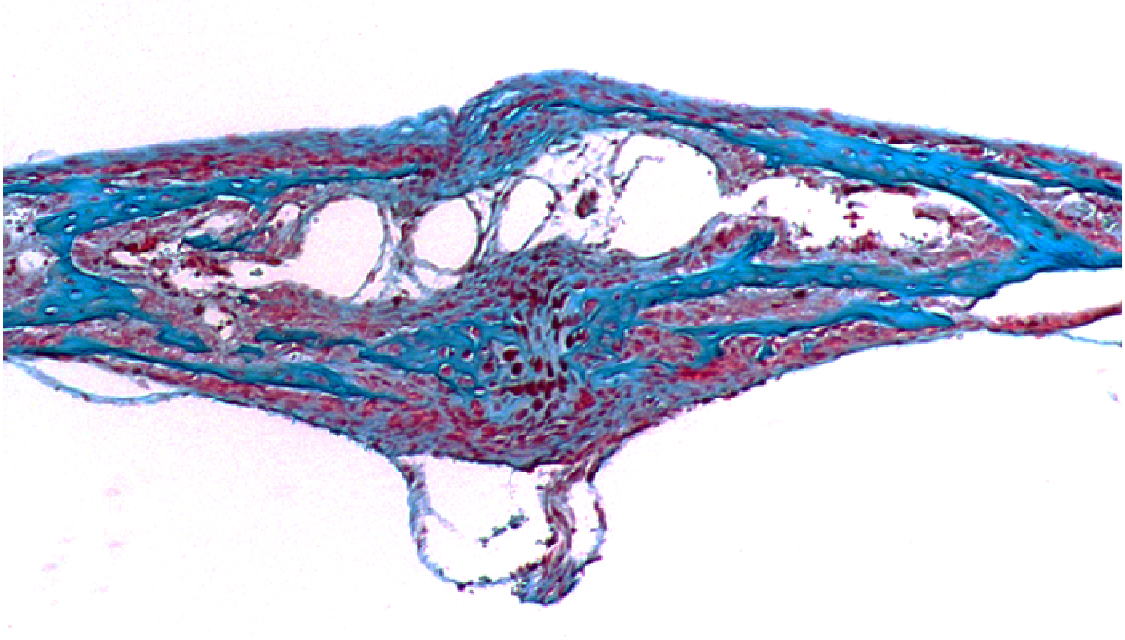

Figure 5-5: Histology confirming cartilage in the posterior frontal suture. Section from 12 day old mouse stained with Safranin-O shows the presence of cartilage in the center of the suture on the endocranial aspect of the suture.

Table 5-1 Genes meeting inclusion criteria from PCR array of posterior frontal bone. Fold change shown is maximal fold change relative to day 6 group and grouped by family. Cartilage associated genes are shown in bold.

Gene	Fold Change	Gene	Fold Change
ECM Proteins		Transcripton Factors	
DMP1	286.1	Runx2	5.7
Collagen II	**90.2**	**Sox9**	**3.8**
Collagen X	**33.2**	TWIST1	3.1
COMP	**7.5**	TGFB Superfamily Members	
Collagen I	5.4	Smad3	23.6
Receptors		BMP2	14.3
IGFR1	13.2	Smad2	9.0
FGFR2	8.3	**TGFB2**	**5.9**
TGFBR2	**8.3**	**TGFB3**	**4.7**
BMPr1a	4.8	SAMD1	3.6
TGFBR1	3.8	BMP4	3.2
VDR	3.8	Growth Factors	
TGFBR3	**3.7**	VEGFa	9.8
Inhibitors		**FGF1**	**8.4**
BMP3	91.4	IGF1	6.8
Sclerostin	3.1	FGF2	3.2

Table 5-2: Genes meeting inclusion criteria from PCR array of posterior frontal dura. Fold change shown is maximal fold change relative to day 6 group and grouped by family. Cartilage associated genes are shown in bold.

Gene	Fold Change
ECM Proteins	
COMP	**63.8**
DMP1	7.8
Collagen X	**4.75**
Collagen XII	4.4
Receptors	
BMPR1b	17.7
nVDR	4.3
TGFBR2	**8.26**
FGFR2	3.38
Cell Adhesion	
Cadherin 11	7.7
VCAM1	7.2
ICAM1	5.77
TGFB Superfamily Members	
TGFB3	**5.4**
Growth Factors	
EGF	5
FGF2	3.2

5.4 DISCUSSION

Of the genes that met the inclusion criteria for this study, the extracellular matrix proteins such as Dmp1 and members of the collagen family exhibited the greatest changes in expression. mRNAs for these genes were greatest prior to and immediately following the onset of suture fusion and then decreased rapidly. Additionally mRNAs for many of the members of the TGFβ super family varied over the time course of the study, suggesting that this family may play an important role in regulating normal suture fusion.

Based on the results of the PCR array we focused on mRNAs for proteins associated with cartilage and extracellular matrix. The results suggest that there is high expression of the members of the non-collagenous SIBLING family, Dmp1 and Ibsp, prior to the onset of suture fusion on day 10. These extracellular matrix proteins are found in all mineralized tissues during development, including the growth plate, and serve as nucleation sites for hydroxyapatite. [178, 179] Additionally, dura also had extremely high expression of Dmp1 during this early time point. These proteins may be major components of the extracellular matrix that later becomes mineralized to form the cranial sutures.

During the time immediately preceding the onset of suture fusion on day 9, there was a strong increase in expression of Tbgfb2 and Tgfb3, but there were no changes in Tgfb1. The expression of Tbgfb2 and Tgfb3 then decreased during the process of suture fusion before increasing again during the latter mineralization phase on day 25. This suggests that these proteins may play a central role in both the initiation and later mineralization of the PF suture. This is supported by prior work done in rats that has shown that TGFβ2 and TGFβ3, but not TGFβ1 are required for the development of normal cranial sutures by controlling the rate of proliferation and apoptosis. [72, 180]

Immediately following the onset of suture fusion on day 12 there was a peak in expression in nearly all genes associated with the development of cartilage. The transcription factor Sox9 has been identified as an early regulator of chondrocyte differentiation in skeletal development and the fusion of the posterior frontal suture showed a slight increase on day 9 followed by a large peak on day 12.[28, 181] The extracellular matrix proteins associated with chondrogenesis Comp, Col II and Col X all had a large increase in expression on day 12. Additionally, Col X, which is associated with chondrocyte hypertrophy, showed a second peak in expression during the mineralization phase on day 25.[182] The presence of cartilage was also verified by Safranin-O staining, which stains negatively changed sulfated glycosaminoglycans. The timing of the expression of chondrocyte associated genes and production of cartilage was slightly different than previously reported[28], but indicates that the fusion of the PF suture is initiated through an endochondral mechanism. The most likely difference in the timing is due to differences in the strains of mice used; the previous work was performed using CD1 mice while the mice examined here were C57Bl/6J mice.

Based on literature examining the development of long bones, the traditional progression of endochondral ossification is an increase in the transcription factor Sox9, followed by an increase in Col II and Comp, and finally an increase in the marker of chondrocyte hypertrophy, Col X.[181, 182] In the posterior frontal suture we saw a nearly simultaneous increase in all genes associated with chondrogenesis. This is most likely the result of the discontinuous process by which the suture fuses. While there may be local regions that are in different stages of endochondral ossification, in the entire suture all stages of endochondral ossification are occurring simultaneously.

CHAPTER 6 BONE MORPHOGENETIC PROTEINS (BMPS) AND THE LATER MINERALIZATION PHASE

6.1 INTRODUCTION

Craniosynostosis is the pathologic premature fusion of one of more sutures early in development.[34] This occurs in approximately 1 in 1700-2500 live births and most commonly results from non-syndromic causes, but there have been over 100 known syndromic forms identified.[34, 164] Craniosynostosis can lead to complications stemming from the craniofacial deformities or from increased cranial pressure. [50, 172] Many cases of craniosynostosis require cranial vault remolding to correct the deformities.[35] Despite the relatively high incidence of craniosynostosis and the morbidities associated with surgical intervention, there are no clinically available therapies available to address the molecular mechanisms responsible for craniosynostosis.[62]

The exact timing and changes in molecular signals responsible for normal suture fusion need to be well understood in order to understand the pathologies responsible for craniosynostosis. Mice are a common model system to examine the mechanisms involved in both normal and pathologic suture fusion due to their ease of use and growing number of strains that have been engineered to display craniosynostosis.[55, 87] Unlike humans, however, rodents continue to grow throughout their entire life. As a result, the majority of rodent cranial sutures remain patent to allow for continued brain

growth.[69] Although it is well established that the mouse posterior frontal (PF) suture, analogous to the human metopic suture, fuses early in development, there is not agreement on the exact timing of the suture fusion.[28, 70]

To address this we previously used a novel image segmentation algorithm to examine the complete time course of the murine posterior frontal suture fusion by microcomputed tomography (μCT).[174, 177] The results indicate that the murine PF suture fuses via a biphasic process. In the first phase, the PF suture remains largely open prior to day 10 and then fuses rapidly before day 20. This is followed by a second phase of mineralization that results in an increase in bone mass and mineral content between days 20-45. Because traditional analysis of the cranial sutures has been performed using de-calcified histology, a second phase characterized by increased mineral content and bone volume was not appreciated. As a result, little work has been devoted to understanding the mechanisms responsible for this later phase of suture development.

We performed a PCR array analysis of genes expressed at key time points during the process of PF suture fusion and observed that the first phase was characterized by mRNAs for proteins associated with endochondral ossification, which was commensurate with the presence of cartilage and new bone formation within the fusing suture.[183] The PCR array also indicated that mRNAs for several bone morphogenic proteins (BMP), their receptors, and their inhibitors were upregulated during the later mineralization phase. This suggests that they might be involved in the onset and progression of bone formation within the suture and raising the possibility that they might be differentially regulated over the time course of PF suture fusion.

Since their discovery in the 1960's, BMPs have been shown to play a critical role in several aspects of bone development and regeneration.[115, 184], [91] It is now

understood that their function is controlled not only by their own availability, but also by the ability of cells to respond to them via receptor/ligand binding and downstream signaling, as well as by the presence of specific inhibitors. Commonly these inhibitors are produced as part of a negative feedback loop to regulate the development of bones. Of the BMP antagonists, noggin has been the most extensively studied inhibitor reported in the craniofacial literature, and it has been shown that the production of noggin differs among the cranial sutures. [92, 120] Early work suggested that other inhibitors such as sclerostin and gremlin did not show a difference among the cranial sutures; however, more recent work has shown that the production of sclerostin is decreased in the adult calvaria. [101, 120]

The overall goal of this study was to determine how BMPs, their receptors, and their inhibitors are associated with fusion of the murine PF suture. To do this we analyzed gene expression in the bone and underlying dura from the posterior frontal suture at key developmental time points previously identified using μCT: post-natal day 6, which is prior to fusion; day 9, which immediately precedes the onset of suture fusion; day 12, which is immediately after onset of suture fusion; day 16, which is the midpoint of suture fusion; day 20, which is the end of fusion and the beginning of mineralization; day 25, which is the midpoint of mineralization phase; and day 55, at which time the suture is fully developed.[177] Analysis was performed using real-time PCR. To better understand how changes in BMPs might relate to bone formation and mineralization, we also examined mRNAs for proteins associated with osteoblast differentiation, extracellular matrix production, and calcification. The temporal expression patterns of each of these key genes were then normalized for comparison to the timing of the posterior frontal suture.

6.2 METHODS

Under approval of the Georgia Tech Institutional Animal Care and Use Committee, C57Bl/6J male mice (Jackson Labs, Bar Harbor, ME) were housed in a light and temperature controlled environment. Pups were kept with natural birth mothers until weaning or euthanasia. All mice were provided food and water ad libitum. Mice 21 days old or older were euthanized by CO_2 asphyxiation and pups under 21 days were euthanized by intraperitoneal injection of pentobarbital. Nine mice were euthanized at each of the following time points: 6, 9, 12, 16, 20, and 25. The skulls were isolated from surrounding soft tissues and the jaw, skull, base, and brain were removed. Skulls were washed with chilled PBS and the sutures were visualized under 4x magnification. The anterior most 75% of the posterior frontal suture was isolated to form an approximately 1.5 mm wide by 2.0 mm long tissue sample. The posterior most 25% of the PF suture was not used because this region of the calvaria does not undergo fusion.[177] The dura was meticulously dissected from the bone using a 30 gauge needle taking care not to include any of the fibrous mesenchymal tissue in the suture or the periosteum. The periosteum was also dissected away from the bone and discarded. Tissue samples were snap frozen in liquid nitrogen and stored at -80°C until RNA extraction was performed.

The bones or the dura from three mice were pooled for each sample. Bone samples were placed in liquid nitrogen and ground using a molar and pestle. Dura samples were ground in glass homogenizer tubes at room temperature. Samples were allowed to thaw to room temperature and then incubated in 4.5 mL of Trizol supplemented with 10 µl/mL of Proteinase K warmed to 55 ℃ for 5 minutes (Qiagen, Valencia, CA). After incubation, 0.9mL of chloroform was added to each tube, vigorously shaken for 15 seconds, and then centrifuged at 10,000 RPM for 30 minutes. The

supernatant was combined with an equal volume of 70% ethanol and ran through an RNeasy (Qiagen) column for purification and elimination of genomic DNA. The RNA was extracted from the column and quantified using the Nanodrop 1000 spectrophotometer (NanoDrop Products, Wilmington, DE).

Our prior PCR array indicated a subset of genes that were increased more than 3 times during suture fusion.[183] For the present study, we focused on mRNAs for proteins associated with osteoblast differentiation (Runt-related transcription factor 2 [Runx2] and extracellular matrix (osteocalcin [Ocn]), in addition to mRNAs for BMP2 [Bmp2], BMP4 [Bmp4], and BMP7 [Bmp7], their type I receptor, BMPR1 [Bmpr1], and their inhibitors (gremlin [Grem1], noggin [Nog], sclerostin [Sost], chordin [Chrd] and BMP3 [Bmp3]). Primers for real-time PCR were designed using the Beacon designer version 7 and optimized with RNA from the bone (Premier Biosoft, Palo Alto, CA) (Supplemental Table 1). The cDNA library was made with the High-Capacity cDNA Reverse Transcription Kit (Applied Biosystems) with 1.0 µg RNA for the bone and 0.3 µg of RNA for the dura. Prior to performing real-time PCR, the cDNA samples were diluted 1:20 for bone and 1:15 dilution for dura. The starting quantity of the samples was calculated based on a 1:3 serially diluted standard pooled from several samples of varying ages. The starting quantity of all genes was normalized by the housekeeping gene GAPDH, which was previously found to remain constant over the different ages examined.

In order to better understand the temporal expression profile of the genes of interest, the data from the real-time PCR were compared to the time course of PF fusion presented in Part 1.[177] The relative expression from the real-time PCR, the distance between the bones of the developing suture, and the total mineral content of the sutures

were normalized so that all values ranged from 0 to 1. All three data sets were then plotted on the same set of axes for direct comparison.

The Gaussian distribution of the real-time PCR results was first verified using the Kolmogorov-Smirnov normality test. Statistical significance was determined using a 1 way ANOVA and when appropriate the difference among groups was analyzed using Bonferroni's modification to the t-test (GraphPad Prism, GraphPad Software, La Jolla, CA). A $p<0.05$ was considered to be significant. All results are represented as the mean ± the standard error of the mean. All samples contain tissue pooled from 3 mice with a N=3 for all measurements (9 total mice per time point).

6.3 RESULTS

Levels of mRNAs for the transcription factor associated with osteoblast differentiation, Runx2 was increased in bone on days 20 and 25 (Figure 6-1A). Ocn mRNAs were initially low, and increased gradually before undergoing a large increase in expression on day 25 (Figure 6-1B). Similarly Bmp2 mRNAs were low until day 25 (Figure 6-1C). Unlike the other genes associated with bone differentiation, Bmp4 mRNAs were high on day 6 (Figure 6-1D). Bmp6 and Bmp7 mRNAs were constant over the time points studied (Figures 6-1E-F). Similarly expression of the Bmp receptor Bmpr1 was high on days 6 and 12, before decreasing over the remaining time points studied (Figure A-8A).

The BMP inhibitors examined in the posterior frontal bone showed very distinct expression profiles that correlated with the expression of other genes examined. Nog mRNAs were high on day 12 and then decreased (Figure 6-2A), most closely resembling the profile of Bmp4. mRNAs for the extracellular inhibitor BMP3 were initially high and peaked on day 9 (Figure 6-2B). Sclerostin mRNAs were highest on day 12 and then returned to baseline (Figure 6-2C). In contrast, Grem1 was initially low, but then increased to a peak on day 25 (Figure 6-2D), similar to Ocn and Runx2. Chrd remained constant throughout the time course (Figure A-8B).

Expression of many of these proteins in the PF suture was different in the dura than in bone. The increase in expression for Bmp2 occurred earlier in the dura, increasing on day 16 and then remaining elevated for the remainder of the time points examined (Figure 6-3A). In contrast to the early high expression in the bone, Bmp4 expression remained constant in the dura (Figure A-9A). Bmpr1 exhibited bimodal

expression, being high on day 6, decreased on day 9, and then high again on days 12 and 16 (Figure A-9B). Noggin mRNAs were increased on day 16 and again to a lesser extent on day 25 (Figure 6-3B). Sclerostin mRNAs were highest on day 9, corresponding to the onset of suture fusion (Figure 6-3C). Grem1, Bmp3, and Chrd did not exhibit any significant changes in expression (Figure A-9C-E).

Normalizing these data with the results from the μCT time course illustrates the biphasic fusion nature of the posterior frontal suture. The distance between the bones decreased and then plateaued, followed by an increase in the bone mineral content after day 20 (Figure 6-4). The expression profile of the genes associated with osteoblast differentiation is nearly identical to the increase in bone mineral content (Figure 6-4A). Similarly the increase in expression of Bmp2 correlated well with the later increase in bone mineral content (Figure 6-4B). The sharp decrease in Bmp4 expression on day 9 was largely completed prior to the decrease in the distance between the bones of the suture (Figure 6-4C).

Each of the BMP inhibitors showed distinct expression patterns that correlated with different developmental milestones in the fusion of the posterior frontal bone. The extracellular BMP inhibitor Bmp3 had a peak in expression on day 9, which corresponded to the period immediately preceding the decrease in the suture distance (Figure 6-4D). The high expression of the Nog early closely matched the timing of the decrease in the distance between the bones of the suture (Figure 6-4E). The peak in expression in Sost occurred during the decrease in the distance between the bones on day 12 (Figure 6-4F). In contrast to the other inhibitors that showed discrete peaks in expression, Grem had a more gradual increase in expression that closely correlated with the increase seen in bone mineral content (Figure 6-4G).

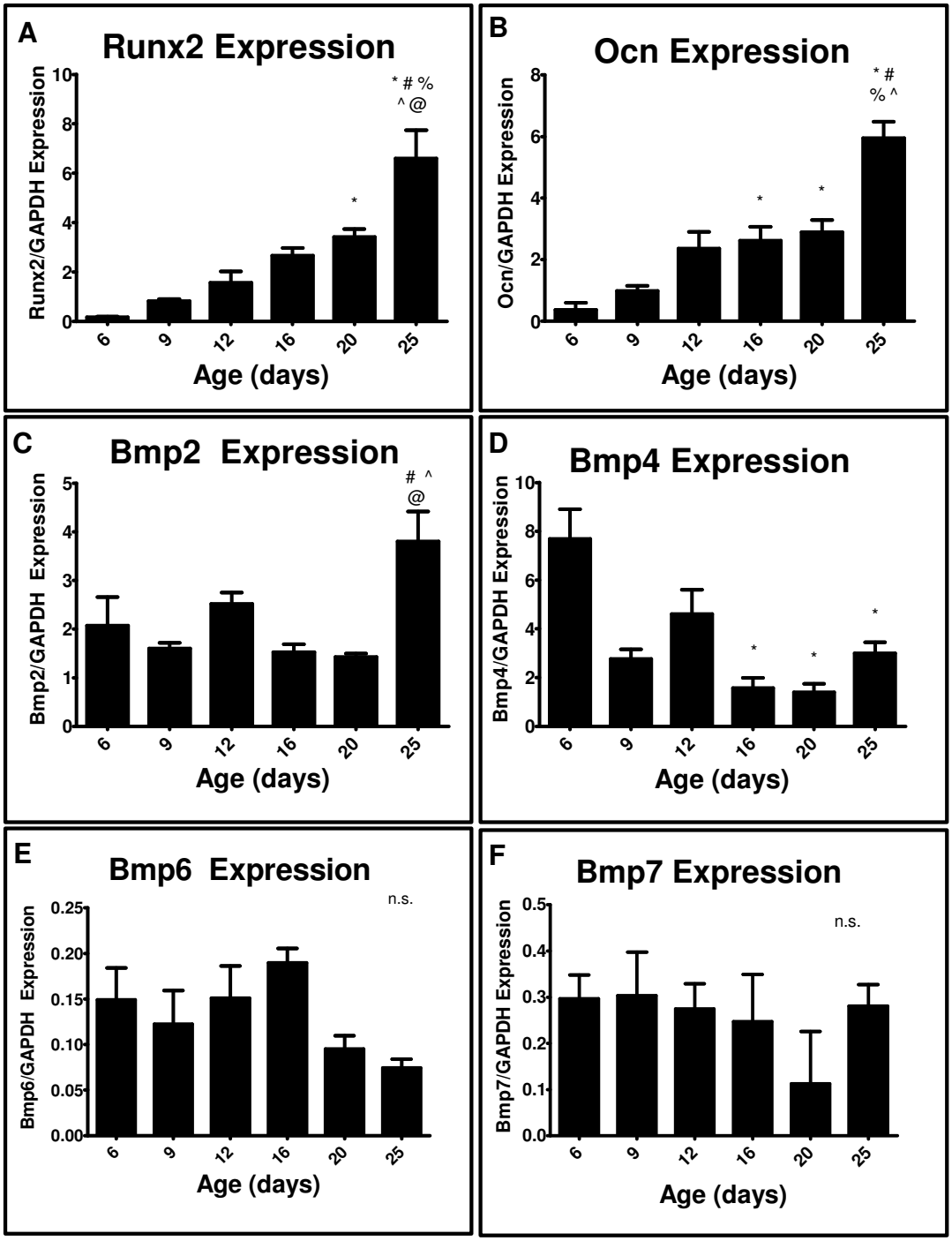

Figure 6-1: Expression of osteoblast differentiation markers and Bmps over time assessed by Real-time PCR. Runx2 (A), Ocn (B), Bmp2 (C), Bmp4 (D), Bmp6 (E), Bmp7 $p<0.05$ vs *=6d, #=9d, %=12d, @=16d, ^=20d. n.s. = no statistical significance.

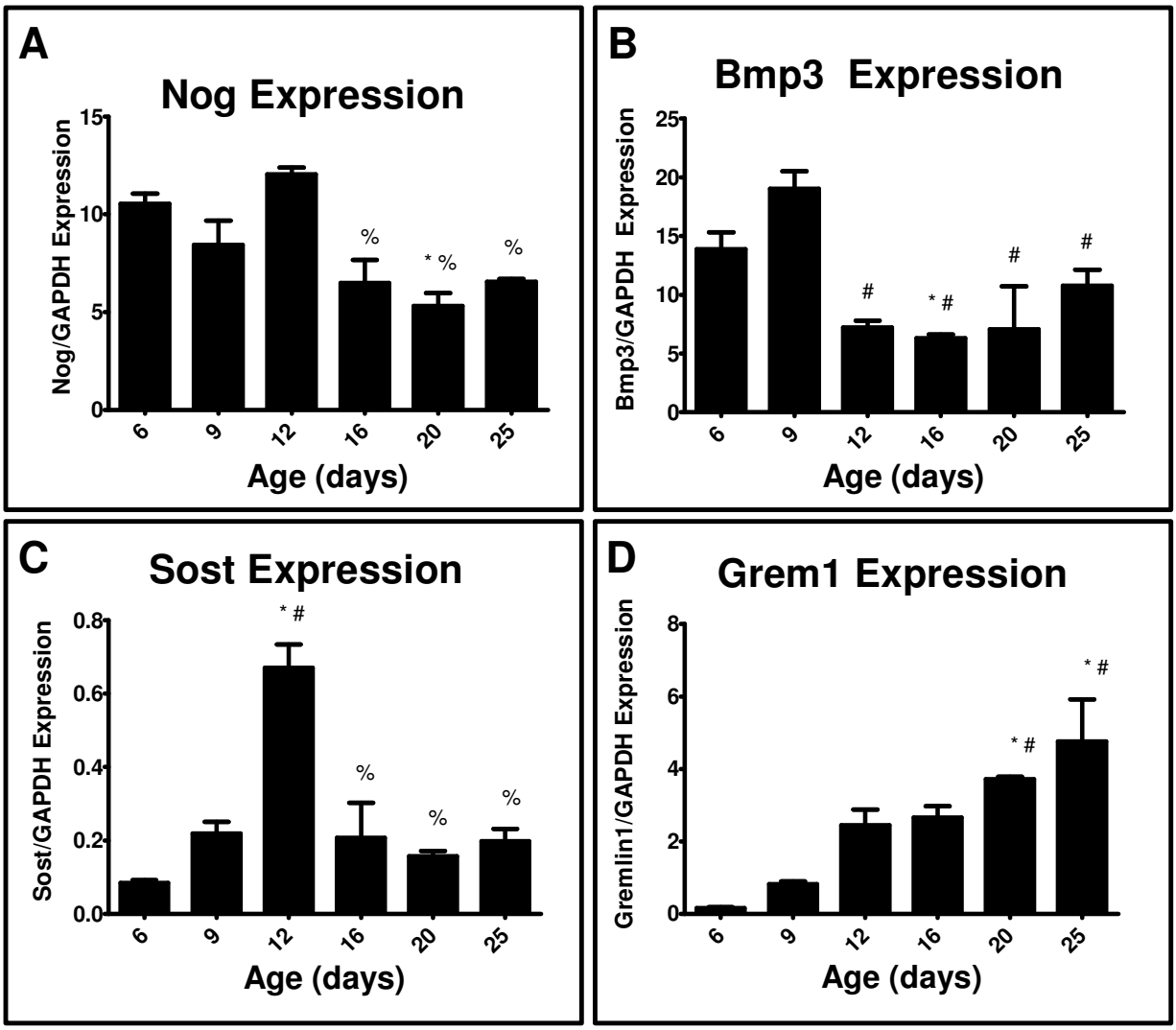

Figure 6-2: Expression of mRNAs for BMP inhibitors in bone of the posterior frontal suture assessed by real-time PCR. Nog (A), Bmp3 (B), Sost (C), Grem1 (D). $p<0.05$ vs *=6d, #=9d, %=12d, @=16d, ^=20d.

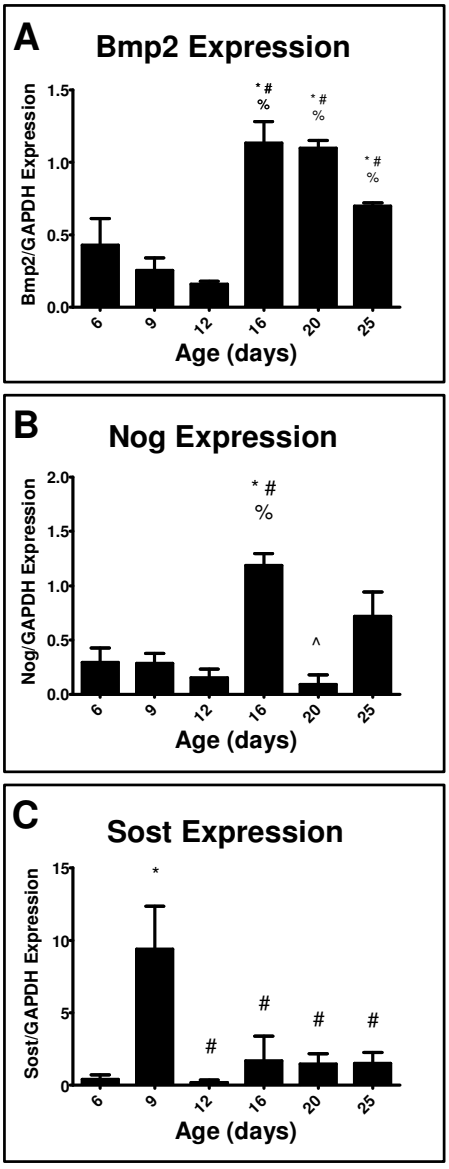

Figure 6-3: Expression of mRNAs for BMP inhibitors in dura of the posterior frontal suture assessed by real-time PCR. (A), Nog (B), Sost (C). $p<0.05$ vs *=6d, #=9d, %=12d, @=16d, ^=20d.

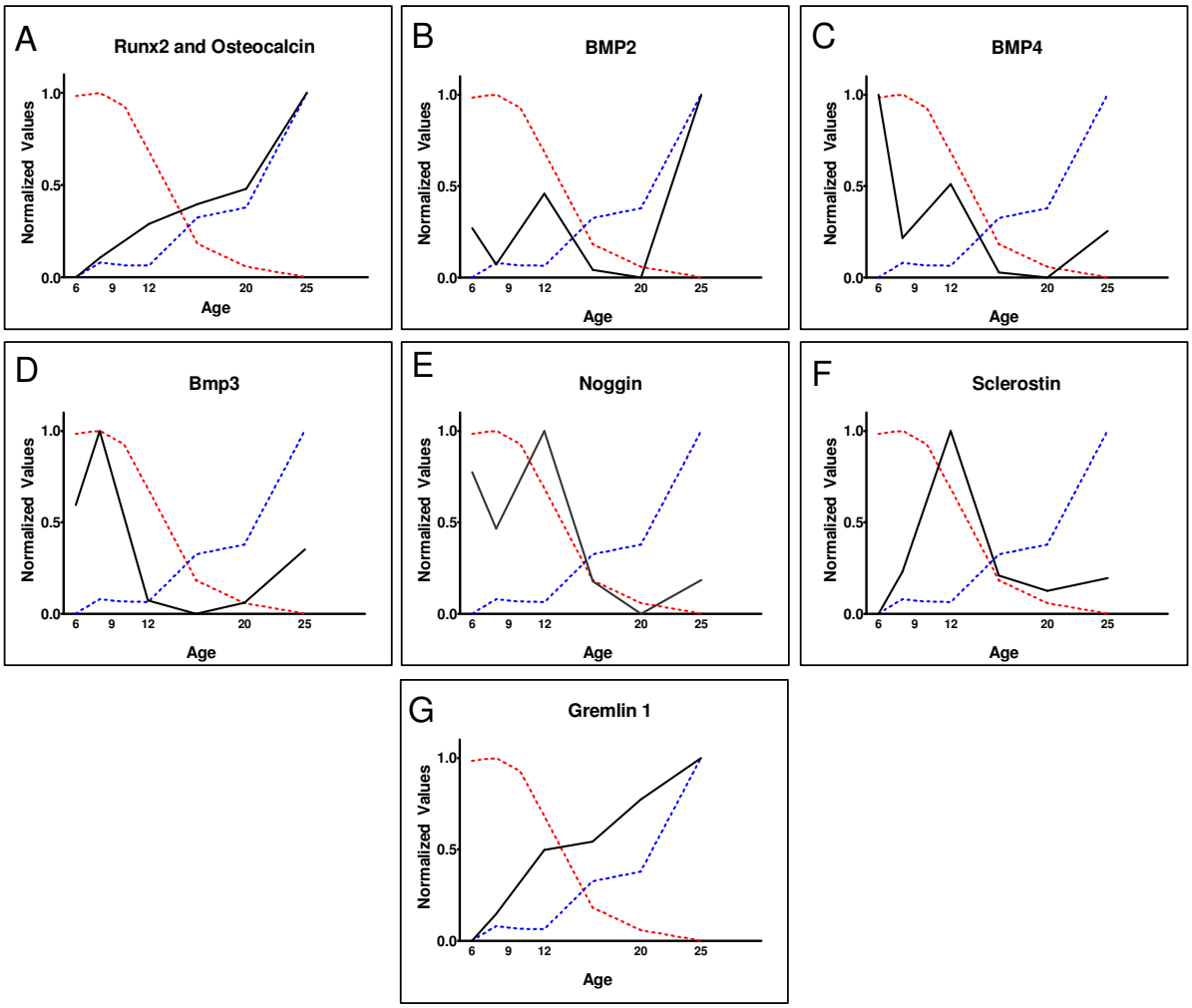

Figure 6-4: Normalized comparison between gene expression (black line), distance between suture bones (red dashed line), and suture bone mineral content (blue dashed line) overtime for: Runx2 and Ocn (A), Bmp2 (B), Bmp4 (C), Bmp3 (D), Nog (E), Sost (F), Grem1 (G).

6.4 DISCUSSION

The BMPs and their inhibitors all had distinct patterns in expression that closely corresponded to the changes seen in the biphasic process of suture fusion. Bmp4 had high expression early, prior to the onset of suture fusion. Bmp4 has been previously shown to be a major factor in the development of both the calvaria and long bones.[184] This indicates that BMP4 plays a more significant role in the early development of the calvaria, but is not associated with the fusion of the posterior frontal suture. In contrast, Bmp2 increased expression only during the latter mineralization phase, after day 20. The dura also had an increase in Bmp2 during the later time points, which further supports the role of BMP2 being responsible for the later mineralization phase, but not the early phase of suture fusion. Also during this later phase, there was an increase in the osteoblast transcription factor Runx2 and the late marker of osteoblast differentiation Ocn. The expression of these genes supports the mineralization of the suture previously reported from our analysis of the development of the posterior frontal suture.[177] During this latter mineralization phase Gremlin 1 had an expression profile that was nearly identical to that of Runx2, Ocn, Bmp2, and the bone mineral, which suggests that this inhibitor of BMP2 may be responsible for regulating this later phase of mineralization. The increase in expression of these genes after the sutures have fused suggests that suture development does not finish when the suture fuses, but continues for nearly four weeks longer.

Each of the BMP inhibitors had distinct patterns of expression that corresponded to the different phases of suture fusion. During the initiation of suture fusion, both Nog and Bmp3 had high expression prior to the onset of the suture fusion on day 12. The

expression profiles of these genes were similar to that of BMP4, a known target of Nog, suggesting that these inhibitors may play a role in regulating the development of the calvaria prior to the onset of suture fusion.[122] The inhibitor Sost showed a strong peak in expression that occurred immediately following the onset of suture fusion on day 12. This pattern of expression was identical to that of the genes associated with chondrogenesis in the cranial suture seen previously.[183] Prior work has shown that sclerostin specifically inhibits BMP6 and BMP7, both of which have been shown to be involved in regulating chondrogenesis. [185-187] Despite the increase in expression of Sost, there were no changes in expression seen with either Bmp6 or Bmp7. This suggests that sclerostin may have actions that are independent of the traditional role of blocking the actions of BMPs.

In conclusion, the results from our study show that expression of different members of the Bmp family is associated with the different phases of suture development. Bmp4 appears to be involved with calvarial development prior to the onset of suture fusion while Bmp2 appears to be involved with the latter mineralization phase of development. Interestingly, none of the Bmps were highly expressed during the early fusion phase, which indicates that this process may be regulated by another pathway.

CHAPTER 7 RAPID RE-SYNOSTOSIS FOLLOWING SUTURECTOMY IN PEDIATRIC MICE IS AGE AND LOCATION DEPENDENT

7.1 INTRODUCTION

Craniosynostosis is the pathologic premature fusion of the cranial sutures early in development, occurring in approximately one in 1500-2500 births [17, 34, 164]. There are over 100 syndromic mutations known to cause craniosynostosis, but most commonly this premature fusion results from a non-syndromic cause [164]. If left untreated, craniosynostosis can result in complications resulting from cranial deformities and/or increased intracranial pressure [35]. These complications include blindness, deafness, developmental delays, seizures, and in extreme cases, death [50, 51].

Both non-syndromic and syndromic forms of craniosynostosis frequently require complex calvarial remodeling to prevent neurologic complications and restore normal cranial vault geometry [35, 65]. Patients undergoing this operation are usually under 12 months of age [65, 188]. The procedure often lasts between

four and five hours, requires blood transfusions, and several days in the hospital, including time in the intensive care unit. Historically, surgical intervention for the treatment of craniosynostosis involved the removal of only the fused suture; however, this approach has been abandoned because the results were temporary. In cases where one adjacent to the suture was also removed, the bone reformed, but synostosis of the region of the pathologically fused suture also occurred.

This rapid re-growth is called re-synostosis and occurs in up to 40% of patients who undergo cranial vault reconstruction [189, 190]. Re-synostosis typically requires additional surgical intervention to reconstruct the skull in an attempt to restore a normal cranial vault and/or relieve the increase in intracranial pressure. While the complications from primary cranial vault surgery are relatively low, subsequent procedures to treat re-synostosis are associated with a high (~13%) incidence of life-threatening complications, which include encephalitis, meningitis, dural tears, intracranial hemorrhages, and cerebrospinal fluid leaks [50, 51, 63, 64]. Patients under six months of age and who have certain syndromic forms of craniosynostosis are at elevated risk for re-synostosis [50, 51].

In order to better understand the mechanisms responsible for re-synostosis, it is necessary to have clinically relevant animal models that exhibit this rapid bone growth. Rabbits displaying craniosynostosis have been used to study suture re-fusion because of their size advantage, but unfortunately they are not commercially available and often display varying severity of craniosynostosis

[66, 94, 168, 169]. Calvarial defect healing has been extensively studied in rodents and other small animals. The majority of this work has focused on critically sized defects in adult rodents, but typically these defects don't heal in the absence of any therapeutic intervention. In contrast, re-synostosis occurs in young children in the absence of any intervention.

Mice are a commonly used model to study cranial development because of the ease of use, conservation of molecular signals, and growing number of genetically engineered strains that display craniosynostosis [55, 87, 93]. While there is extensive literature devoted to the understanding of normal and pathologic suture fusion, there has been relatively little research devoted to understanding the processes responsible for re-synostosis. Previously, adult mice were used as a model for re-synostosis, with a defect placed over the posterior frontal suture, but it was shown that these defects did not completely heal [93]. This suggests that age is an important variable. Unlike the critical sized defects placed in bone lateral to the suture, some healing was evident in defect when the defects were placed over the suture, suggesting that age dependent differences in the dura alter both suture development and re-healing of calvarial defects [23, 26, 27, 75, 76, 94, 180].

The overall goal of this study was to develop a murine model of rapid re-synostosis. Our hypothesis was that a defect over the posterior frontal suture in an infant mouse will undergo rapid re-synostosis, whereas it will fail to do so in older sexually immature mice. Moreover, defects not associated with the cranial suture will fail to heal with bone in infant mice. Two time points were selected

based on our previous work showing that at weaning (21 days post-natal), the posterior frontal suture in C57Bl/6J mice had fused but not mineralized whereas in adolescent mice (50 days post-natal) the posterior frontal suture has completed fusion and mineralization [177]. Defect healing was assessed using image processing algorithms developed and validated previously [174]. Gene expression associated with defect healing was examined using real-time PCR.

7.2 METHODS

This study was conducted under the approval of the Georgia Tech Institutional Animal Care and Use Committee. Male C57Bl/6J mice were used for all surgeries (Jackson Labs, Bar Harbor, ME). All mice were housed in a light and temperature controlled environment with ad libitum access to food and water. At the time of surgery all mice were either 21 days old (infant) or 50 days old (adolescent). Infant mice were shipped with natural birth mothers and were weaned at the time of surgery. The 50 day old mice had not reached sexual maturity at the time of surgery. Mice were anesthetized to a surgical plane with isoflurane for all surgical procedures and preparation. Hair was removed from the top of the skull starting between the eyes and moving posterior 2 cm with depilatory cream (Nair, Churchill & Dwight, Princeton, NJ). The skin was washed with water taking care to ensure no cream or water came in contact with the animals' eyes. The skin was disinfected with three alternating washes of chlorehexidine and isopropanol.

A 1 cm midline incision was made beginning 5 mm posterior to the eyes. The skin and periosteum were elevated from the skull using blunt dissection. Under 28x magnification, the interfrontal ridge, the posterior frontal suture, and the bregma were identified (Figure 7-1A). Using these landmarks as a reference, a custom made template was placed above the posterior frontal suture and

served as a size reference during the creation of the defect. The template contained a central 1.5 by 2.5 mm region, and centering notches that served as a reference for the appropriate defect size throughout surgery. All defects were created using a piezoelectric bone cutting instrument, ensuring that the underlying dura was not damaged (Piezotome, Saltec Acteon, Merignac, France). Piezoelectric instruments cut only through hard tissue by using very high frequency, low amplitude displacement vibrations [191]. This allows for a very controlled cut through bone, while minimizing the damage to the underlying dura. This is of particular concern as damaging the dura can impair the healing of the overlying bone.

For mice in the posterior frontal defect group, the suture was completely removed and the template was referenced to ensure the correct defect size during the procedure (Figures 7-1A-B). The defect was centered over the posterior frontal suture, posterior to the interfrontal ridge, and anterior to the bregma (Figure 7-1B). Care was taken to not damage the highly vascularized interfrontal ridge as damage to this structure leads to exsanguination. Intraoperative and μCT images illustrate the ability to accurately create a defect with the appropriate dimensions and location of the defect, while maintaining the integrity of the underlying dura (Figures 7-1C-D). Any mice with a dural tear were withdrawn from the study and euthanized prior to recovering from anesthesia. The skin was closed with 5-0 silk sutures and the mice were allowed to recover from anesthesia. Post-operative (post-op) analgesia was provided via sub-cutaneous injection of buprenorphine (0.03-0.06 mg/kg) every 8-12 hours for the

first 72 hours post-op. Mice were given access to ground, moistened food for the first 24 hours after surgery to encourage food consumption and weight gain. Any mice displaying age adjusted weight loss greater than 10% or signs of distress were withdrawn from the study and euthanized.

Post-natal day 21 male mice were used to establish the time-course of posterior frontal defect healing in infant animals. Following surgery, five mice per day were randomized for euthanasia on the following post-operative days: 1, 2, 3, 4, 5, 7, 14, and 21 days. Immediately following euthanasia the skull was dissected from soft tissues, imaged using μCT, and snap-frozen in liquid nitrogen for further analysis by real-time PCR or histology. The approximate region of the posterior frontal defect was identified by moving 4.5 mm posterior from the posterior most molars. The samples were imaged within a 21 mm sample holder using μCT (isotropic voxels 21 μm in size, an energy of 55 kVp [Viva CT 40, Scanco Medical, Bruttisellen, Switzerland]). The exact location of the defect was identified with the aid of 3D reconstructions created using a global threshold. These images were then converted to 2.5 mm by 3.5 mm DICOM images for analysis.

The extent of bone regeneration in the defect was quantified using our novel image processing algorithms previously validated with serial histology [174]. Briefly, the algorithm uses a combination of global threshold and the active contour snake algorithm to segment the heterogeneous bone from the μCT images. Slight modifications to the algorithm allowed for segmentation of multiple bones in an image, as compared to the original algorithm that was

limited to two bones. Segmentation boundaries identified by the algorithm were then used to quantify the average defect width, the average thickness of the bones of the defect, the volume of bone in the defect, and the defect mineral content. The defect mineral content was used as an indicator of bone mineralization and was calculated by converting pixel intensities to that of a known hydroxyapatite standard, giving a density value of each pixel relative to hydroxyapatite. The bone volume and mineral content contained within the defect were normalized to the amount of bone found in an intact suture at the time of surgery (21 days post-natal) and a fully mineralized suture (50 days post-natal). All evaluations were performed by a blinded reviewer.

To investigate whether rapid healing of the craniotomy defect was age and location specific, we created identically sized defects over the posterior frontal suture in infant mice, a posterior frontal suture defect in adolescent mice, a defect lateral to the posterior frontal suture in infant mice, and a defect lateral to the posterior frontal suture in adolescent mice. The lateral defects were identical in size to the posterior frontal defects and were placed 1 mm lateral to the posterior frontal suture. They were centered between the interfrontal ridge and the coronal sutures, taking care not to damage either structure. The side of the defect (left or right side) was randomized between mice. All mice were given the same post-operative care as described above and five mice in each group were randomized for euthanasia on post-operative days 2, 5, and 14. The skulls were immediately imaged with μCT and snap frozen. The extent of defect healing was quantified using the same image processing algorithms described above.

Real-time PCR was performed to assess expression of genes associated with rapid defect healing in the posterior frontal defect in infant mice. At each time point, a 1.5 mm by 2.5 mm region of tissue at the defect site was removed under a 4X magnification. The exact location of the defect was verified by comparing the appearance of the skull under magnification to 3D renderings of the μCT scans. The dura was meticulously dissected from the defect bone and the tissues were ground using a mortar and pestle. RNA was extracted from the defect tissue, purified, and quantified from the defect tissue as described previously [183]. A cDNA library was made using a High-Capacity cDNA Reverse Transcription Kit (Applied Biosystems) with 500 ng starting mRNA. The samples were diluted 1:20 in sterile nuclease free water. The starting quantity of the samples was calculated based on a 1:3 serially diluted standard pooled from samples of each time point. The mRNAs for the genes listed in Table 1 were normalized by the housekeeping gene glyceraldehyde phosphate dehydrogenase (GAPDH).

Representative calvaria from the infant posterior frontal suture defect group on post-op days 5 and 14 were fixed in 10% neutral buffered formalin and decalcified using 12% EDTA, changing the solution every 2-3 days. Complete decalcification was verified using plain x-ray (Faxitron X-ray, Lincolnshire, IL) before and after decalcification. The samples were trimmed, dehydrated using ethanol, and then embedded in paraffin. After establishing the location of the defect with histology, 7 μm thick sections were made and stained with haematoxylin and eosin (H&E), or with Safranin-O and a fast green counter stain.

The specimens were imaged at 10X and 60X magnifications with a Leica DMLB microscope (Leica Microsystems, Bannockburn, IL).

Statistical Analysis

The Gaussian distributions of the real-time PCR and μCT results were first verified using the Kolmogorov-Smirnov normality test. Statistical significance was determined using a 1 way ANOVA and the significance among groups was determined by a multiple comparison test with Bonferroni's modification where appropriate (GraphPad Prism, GraphPad Software, La Jolla, CA). Statistical significance for the normalized comparison to the intact suture was using the Mann Whitney U-test test. A $p<0.05$ was considered to be significant. All results are represented as the mean ± the standard error of the mean. The sample size (n=5) for all experiments was determined by a prospective power analysis based on the variance of pilot surgeries.

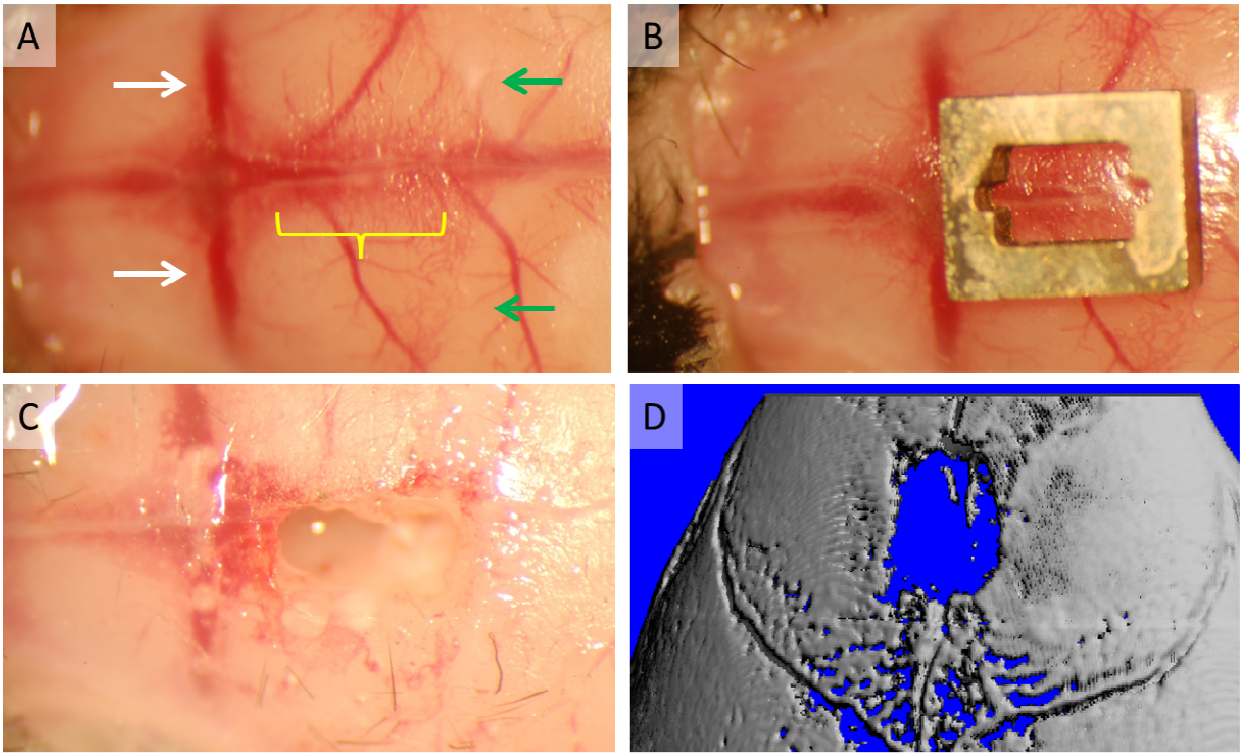

Figure 7-1: Intra-operative images for the infant posterior frontal defect under 30X magnification prior to surgery showing the interfrontal ridge (white arrow), coronal suture (green arrow), and posterior frontal suture (yellow bracket). The template with centering notches was used as a reference throughout the procedure (B). The defect created after removing the posterior frontal suture, showing intact dura in the defect (C). 3D µCT rendering of defect immediately after surgery (D).

7.3 RESULTS

Provided there were no intraoperative complications during the creation of the defect, all mice tolerated the surgical procedure well. A 5% intraoperative mortality rate occurred from complications with anesthesia or from aspiration of the irrigation solution. One mouse, out of the over 100 included in this study, was euthanized due to dural tear, and one was withdrawn because to failure to gain weight.

The analysis of the μCT images using our image processing algorithms showed that the infant posterior frontal defects healed rapidly in a biphasic manner. The width of the defect remained constant for the first two days post-op at approximately 1.2 mm and, then decreased to approximately 0.4 mm for the remainder of the time points (Figure 7-2A). The defect mineral content and bone volume remained constant through post-op day 7 and then increased to levels seen in an intact suture (Figures 7-2B-C). Both parameters more than doubled between days 7 to 14. Similarly, the average thickness of the defect remained constant at approximately 0.1 mm until post-op day 7, where it increased to over 0.3 mm on post-op days 14 and 21.

Normalizing the bone volume in the defect to the starting bone volume in an intact suture of a 21 day old mouse, showed that from days 1 to 5 post-op there was significantly less bone in the defect, no difference on post-op day 7, and significantly more bone in the defect on post-op days 14 and 21 (Figure 7-

3A). Furthermore, the increase on days 14 and 21 was more than double the volume of bone in an intact suture at the time of surgery. Normalizing the mineral content in the defect to the intact post-natal day 21 suture showed identical trends and significance (Figure 7-3B). Comparing the volume of bone in the defect to a fully developed suture (50 days post-natal) showed statistically less bone on days 1 through 7 post-op, but there was no difference on days 14 and 21 post-op (Figure 7-3C). Mineral content in the defect was normalized in the same manner to the day 50 intact suture and showed the same significance that was seen with bone volume (Figure 7-3D).

After establishing the timing of bone healing in the infant posterior frontal suture defect, the effects of age and location on defect healing were assessed on days 2, 5, and 14 post-op. Analysis of the distance between the bones in the defect showed a decrease in the distances between the bones of the suture only for the defects created over the posterior frontal suture. In infant mice, the defect width of the posterior frontal defect was 1.3 mm on day 2 post-op and then decreased sharply to approximately 0.4 mm on days 5 and 14 post-op (Figure 7-4A). Bone volume increased on post-op day 14 to over 0.6 mm^3 (Figure 7-4B). In adolescent mice, the average defect width was approximately 1.3 mm on days 2 and 5 post-op, then decreased to less than 0.3 mm by 14 days post-op (Figure 7-4C). Despite the decrease in width, there were no changes in bone volume. Less than 0.1 mm^3 of bone was present in the defect at all time points examined (Figure 7-4D). The distance between bones in the lateral defects remained over 1.3 mm in the infant mice through day 7. By day 14, this had decreased to 0.7

(Figure 7-4E). Bone increased on day 14 post-op (Figure 7-4F). In the adolescent lateral defects, there were no changes in the defect distance and all distances were approximately 1.3 mm (Figures 7-4G), and there were no changes in bone volume (Figure 7-4H).

Both the 2D and 3D images from the infant posterior frontal defect show that by 14 days post-op the defect was nearly completely bridged with mineralized tissue (Figure 7-5A-B). The bone in the defect displayed a very thick trabecular pattern that was not seen with the normally intact suture (Figure 7-5A). No bone bridging was observed in the lateral defect, but the edges of the bone thickened substantially by 14 days post-op, as seen in the 2D µCT image (Figures 7-5C-D). The adolescent posterior frontal defect showed a discontinuous thin shell of bone bridging the defect on post-op day 14 (Figure 7-5F). Examination of the 2D µCT images revealed that this bridge of bone formed along the endocranial surface of the defect, but lacked the thick trabecular structure that was seen with the infant defect (Figure 7-5E). The adolescent lateral defect did not show any bridging or an increase in bone volume (Figures 7-5G-H).

Analysis using real-time PCR showed distinct expression profiles for genes related to both osteoblastic and chondrogenic differentiation. Expression of Tgfb2 was biphasic with peaks on days 2 and 14 post-op (Figure 7-6A). mRNAs for the extracellular matrix protein Dmp1 were increased on post-op days 3 and 4, corresponding to the time of the early bridging of the infant defect (Figure 7-6B). There was a peak in expression for the early marker of

chondrogenic expression, Sox9 on post-op day 3 (Figure 7-6C). This was followed by an increase in expression of mRNAs for chondrocyte extracellular matrix proteins: Col2, ColX, and Comp. These mRNAs displayed peaks in expression at post-op days 4 and 5 (Figure 7-6D-F).

While mutations in genes encoding proteins related to BMPs have not been associated with craniosynostosis, mRNAs for these proteins were elevated during with the rapid re-synostosis seen in the infant posterior frontal defect. Bmp2 mRNAs remained constant until sharply increasing in expression on post-op day 7 and then gradually decreased for the remaining time points (Figure 7-6G). Bmp4 mRNAs were not expressed until day 3 and peaked on post-op days 5 and 7 (Figure 7-6H). Similar to what was seen with Tgfb2, Bmp6 expression was maximal on post-op day 2 and with a second peak on day 14 (Figure 7-6I). Bmp7 expression was maximal on post-op day 2 with a second peak on day 4 (Figure 7-6J). Ocn mRNAs Ocn, were present as early as day 2, but were at low levels until day 14 (Figure 7-6K). There was a 10 fold increase on post-day 14 that was maintained on day 21. Vdr mRNAs were also present in the tissue at low levels through day 7 (Figure 7-6L). On day 14, expression increased 4 fold and on day 21, mRNAs doubled over the day 14 levels.

mRNAs for BMP inhibitors were differentially expressed. Sost mRNAs were present in the tissue at very levels through day 14, doubling on post-op day 21 (Figure 7-6M). Grem1 was expressed on days 4, 5, and 7 only, with peak levels on day 5 (Figure 7-6N). In contrast, mRNAs for Bmp3 were decreased on

post-op days 5 and 7 (Figure 7-6O). Nog mRNAs were increased 4 fold on days 14 and 21 compared to day 7 (Figure 7-6P).

Staining with haematoxylin and eosin revealed a poorly organized but highly cellular tissue within the defect at 5 days post-op (Figure 7-7A). Cartilage was present in the healing defects based on diffuse Safranin-O positive staining of the extracellular matrix (Figure 7-7B-D). By 14 days post-op, well-organized bone completely bridging the defect was observed (Figure 7-7E). The bone in and adjacent to the defect was thicker and more trabeculated than what is typically seen with an intact suture, supporting the 2D µCT images (Figure 7-5A). No red staining was observed, indicating fully mature bone throughout the section (Figure 7-7F).

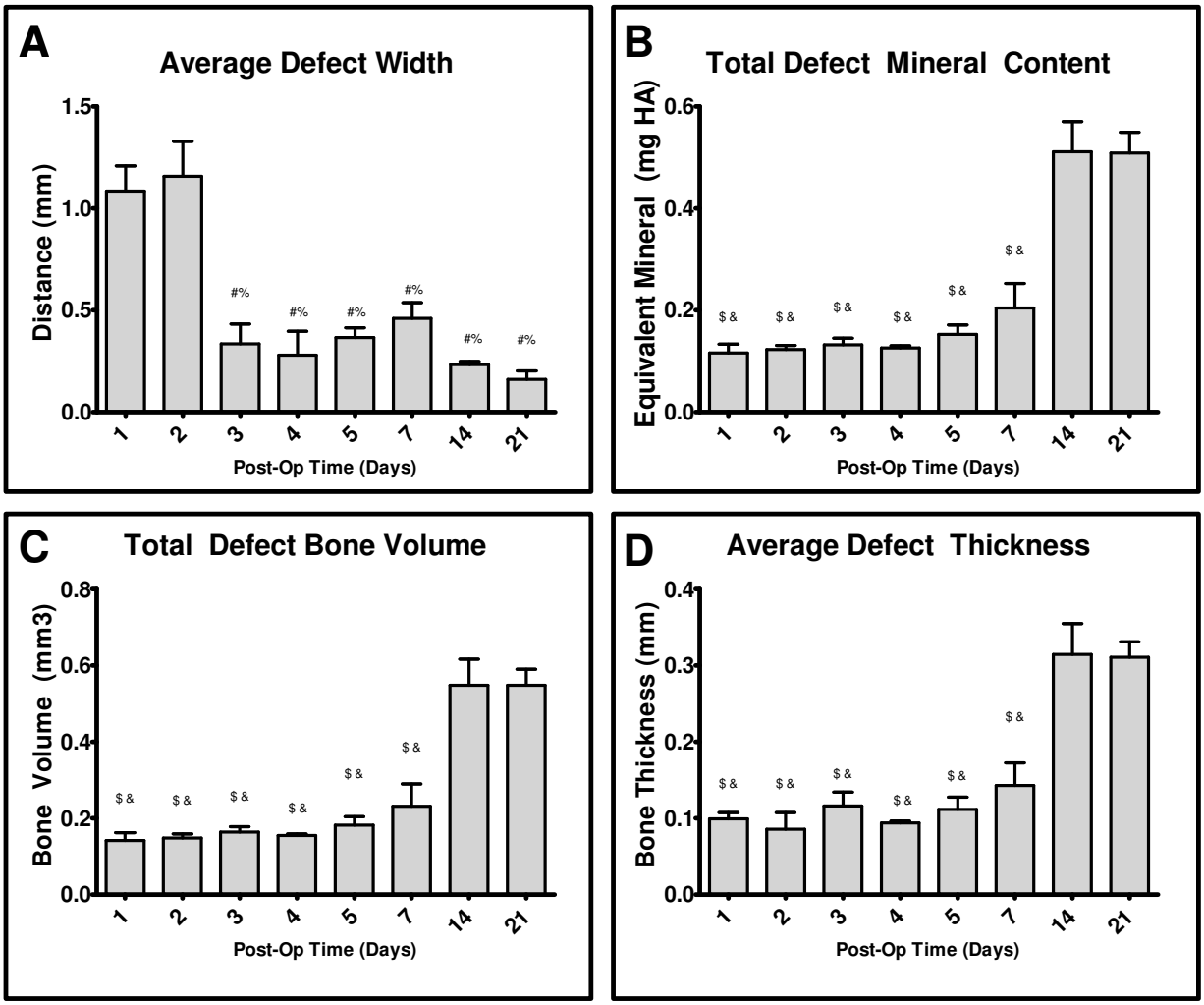

Figure 7-2: Quantification of infant posterior frontal defect healing from µCT images. Results from algorithm analysis of µCT scans of defect. There was a decrease in the distance between the bones of the posterior frontal defect after post-op day 3 (A). The total mineral content and bone volume in the defect remained constant for post-op days 1-7 before increasing on days 14 and 21 (B, C). The average thickness of the bone in the defect showed no changes until an increase on post-op days 14 and 21 (D). $P<0.01$ vs # = 1 day, % = 2 day, $ = 14 day, & = 21 day.

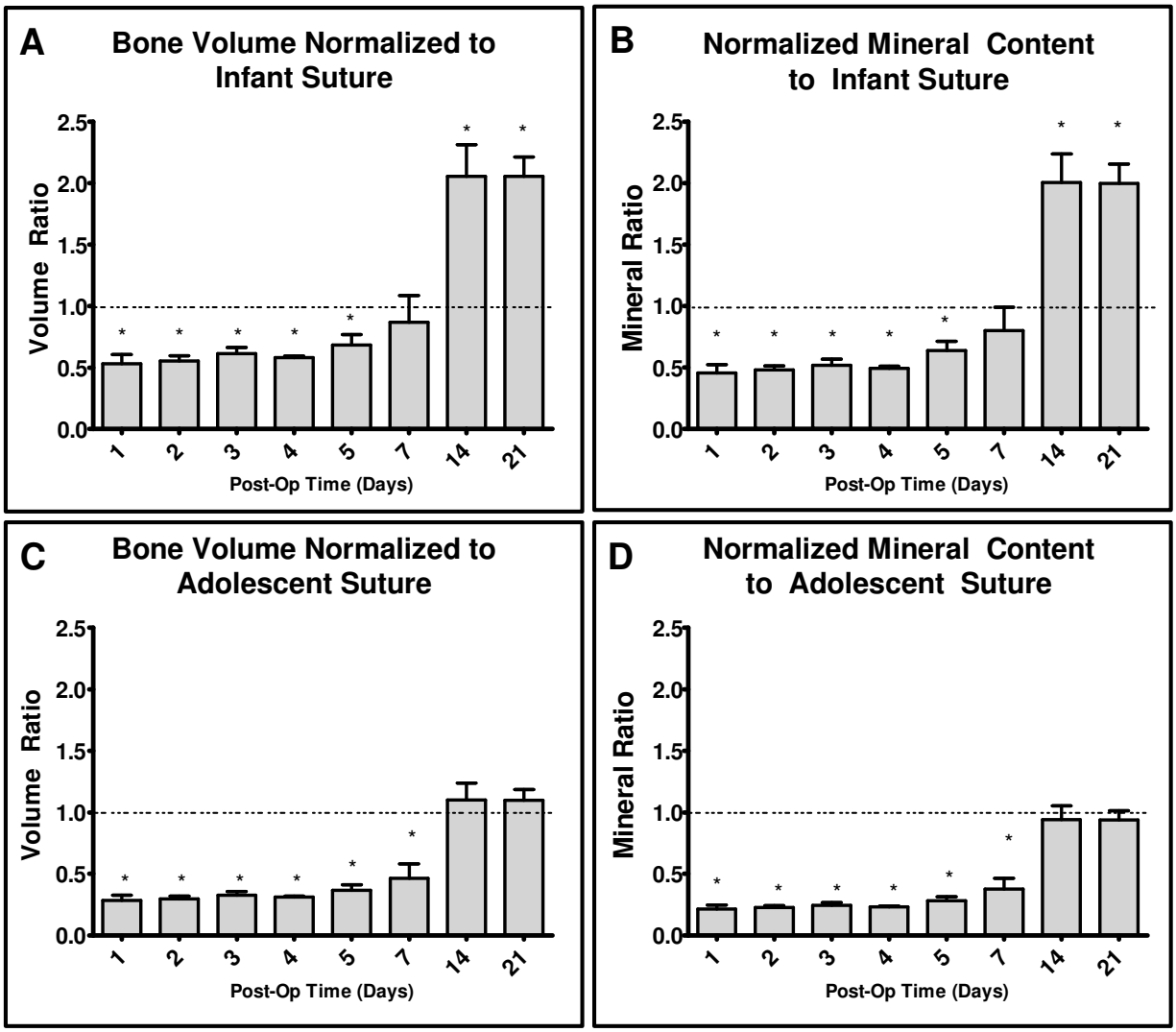

Figure 7-3: Normalized bone volume and mineral content of infant posterior frontal defect to an intact posterior frontal suture. Results are from algorithm analysis of μCT scans of defect and intact suture. The bone volume and mineral content of the defects was less than an intact 21 day old suture for post-op days 1-5 doubled by days 14 and 21 (A-B). Normalizing the bone volume and mass to the fully developed 50 day old posterior frontal suture showed no significant differences in either measure by days 14 or 21 post-op (C-D). * = $P<0.05$ vs intact suture.

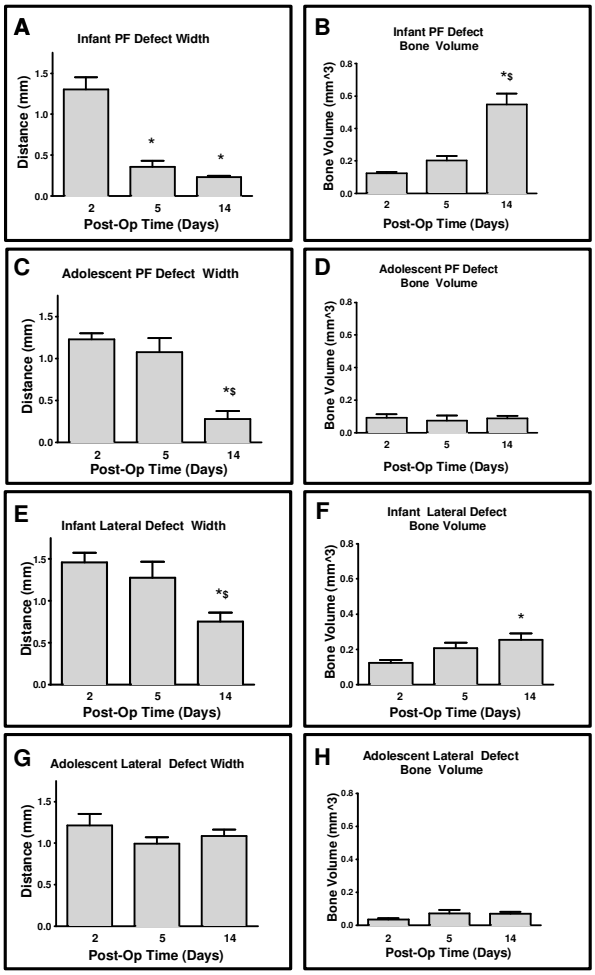

Figure 7-4: The age and location dependence on defect healing. Results are from algorithm analysis of μCT scans. The infant posterior frontal defect was 1.3 mm wide on post-op day 2 then decreased on post-op days 5 and 14 (A). The increase in the volume of bone in the infant posterior frontal defect occurred on 14 days post-op (B). The adolescent posterior frontal defect width showed no changes until decreasing on post-op day 14 (C). There was no change in volume of bone in the adolescent posterior frontal defect (D). There was a decrease in the width of the infant lateral defect from post-op days 2 and 5 to 14 (E). There was a small increase in the volume of bone in the adolescent lateral defect on post-op day 14 (F). There were no changes in the bone volume of the adolescent lateral defect for any of the time points studied (G). There were no changes in the defect distance for the adolescent lateral defect (H). $P<0.05$ vs * = day 2, $ = day 5.5.

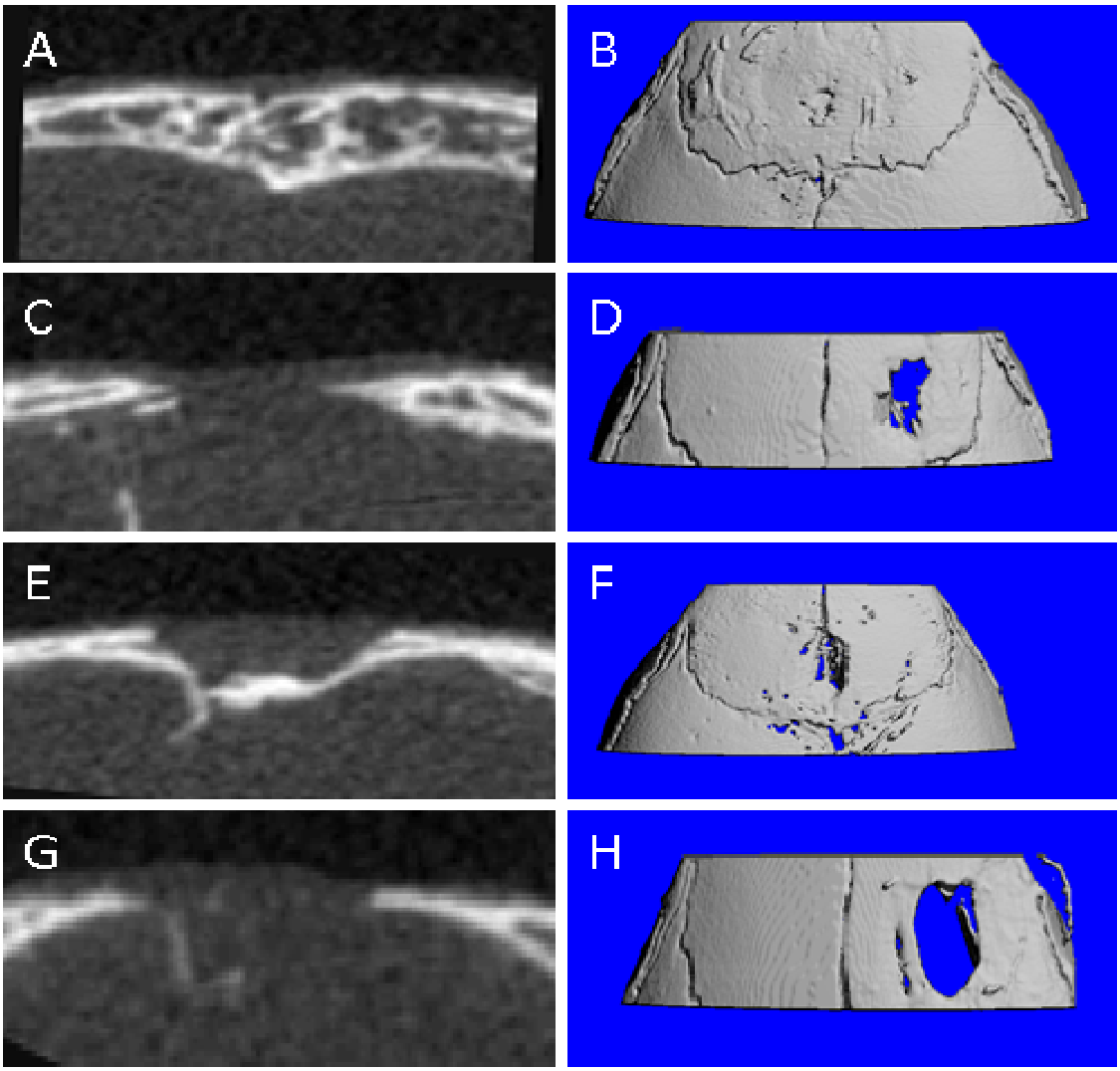

Figure 7-5: Representative 2D and 3D µCT images for the age and location defects on day 14 post-op. The infant posterior frontal defect shows complete bridging and an increase in the thickness of the bones (A-B). The infant lateral defect shows an increase in the thickness of the edges of the bones in the defect but no bridging (C-D). Adolescent posterior frontal defect shows thin discontinuous bridging along the endocranial surface of the defect, but no increase in the thickness of the bone in the defect (E-F). The adolescent lateral defect shows no increase in the thickness or bridging of bone in the defects (G-H).

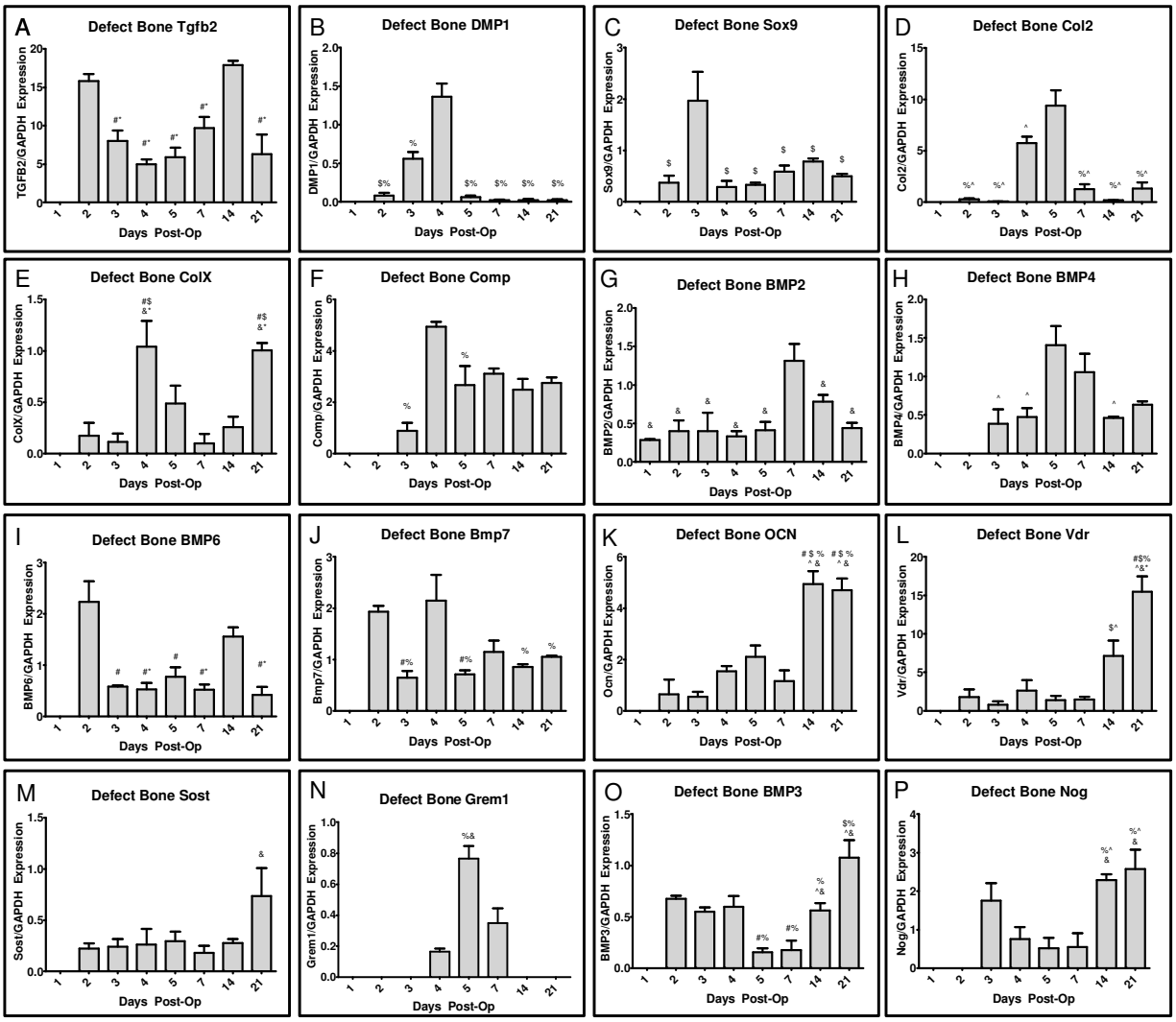

Figure 7-6: Real-time PCR analysis of genes associated with defect healing for Tgfb2 (A), Dmp1 (B), Sox9 (C), Col II (D), Co IX (E), Comp (F), Bmp2 (G), Bmp4 (H), Bmp6 (I), Bmp7 (J), Ocn (K), Vdr (L), Sost (M), Grem1 (N), Bmp3 (O), Nog (P). $p<0.05$ vs # = day 2, $ = day 3, % = day 4, ^ = day 5, & = day 7, * = day 14.

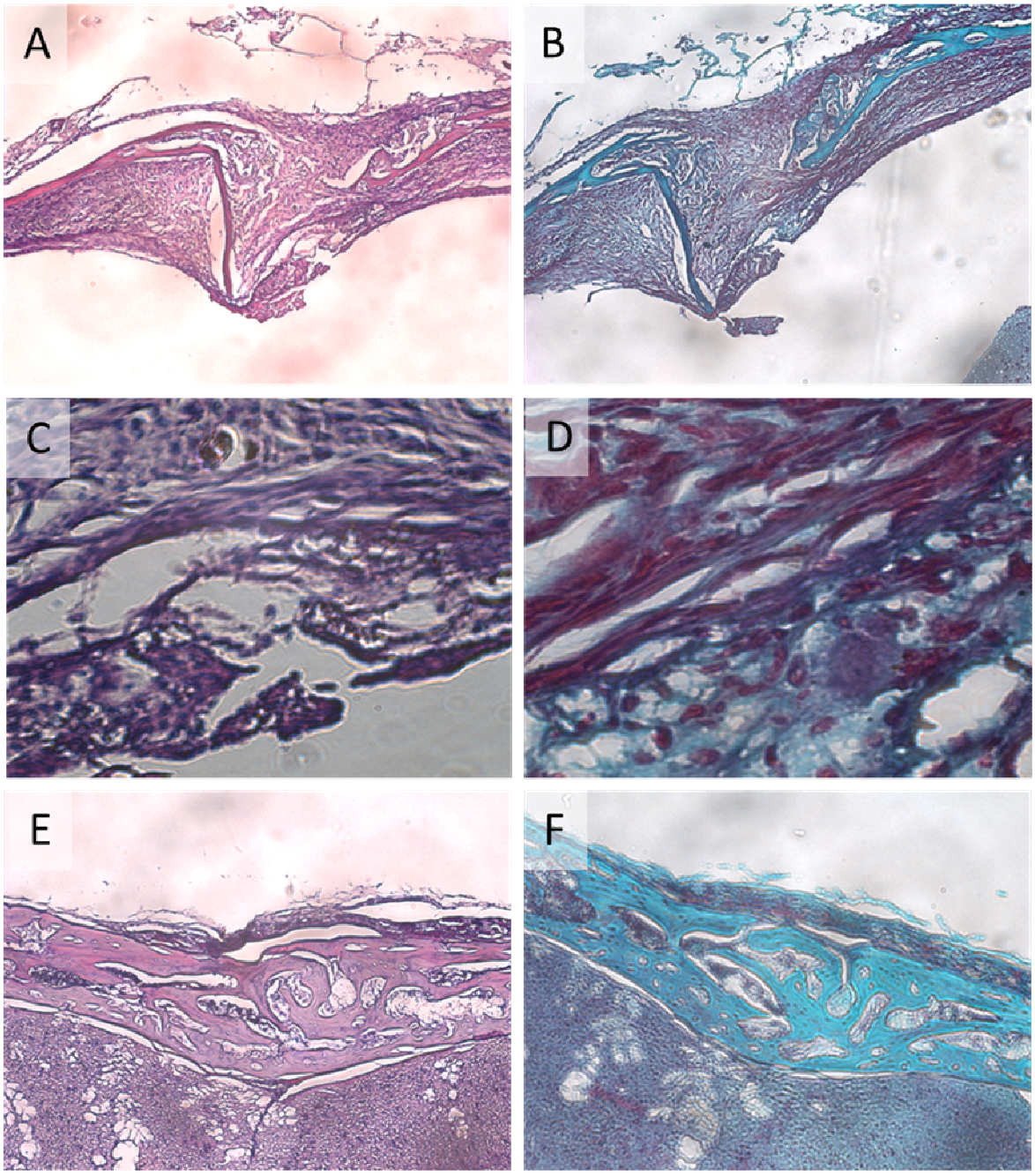

Figure 7-7: Representative histology for infant posterior frontal defect. H&E staining for post-op day 5 (A) and 14 (E) at 10X magnification. Safranin-O staining for post-op day 5 (B) and 14 (F) at 10X magnification. H&E (C) and Safranin-O (D) staining of 5 days post-op showing more organized tissue along the endocranial surface of the defects at 60X magnification.

Table 7-1: Gene name, gene abbreviation, sequence for forward real-time primer, and sequence for reverse real-time primer. Primers for collagen 2 and dentin matrix protein 1 were purchased as pre-designed primers.

Gene Name	Gene Abbreviation	Forward	Reverse
Bone morphogenic protein 2	Bmp2	TGGGTTTGTGGTGGAAGTG	TCGTTTGTGGAGCGGATG
Bone morphogenic protein 3	Bmp3	TATACGCCAACGATGCTG	CTTCTTCCTCCTCTCAACC
Bone morphogenic protein 4	Bmp4	TGGTCTCCGTCCCTGATG	CGCTCCGAATGGCACTAC
Bone morphogenic protein 6	Bmp6	ACGAACAACAGCACAGCGAAG	AAGGCACCAGCGGGAGATG
Bone morphogenic protein 7	Bmp7	CCACAGCAAACGCCTAAG	CGATTACTCCTCAAAGACTCAG
Cartilage oligomeric matrix protein	Comp	GCGACGACGACATAGATG	GTCTTGGTCACTATCACAGG
Collagen X	ColX	TTCTGCTGCTAATGTTCTTGAC	CCTTTACTCTTTATGGCGTATGG
Gremlin1	Grem1	AGAGAGCCACACCCAAAC	TGAAGCAGAGTAACAGGAAG
Noggin	Nog	GCCAGCACTATCTACACATCC	CAGCAGCGTCTCGTTCAG
Osteocalcin	Ocn	GTCTGTTCACTACCTTATTGC	TCTCTCTGCTCACTCTGA
Sclerostin	Sost	GTCGTCGTGCTGTCCTCTG	ATTGTGGGTGGTGCTGTGG
SRY-box containing gene 9	Sox9	CCACCAGTATCAGCGAGGAG	CCAAACAGGCAGGGAGATTC
Transforming growth factor beta 2	Tgfb2	GAGCGGAGCGACGAGGAG	TGTAGAAAGTGGGCGGGATGG
Vitamin D receptor	Vdr	AATAAGCAGAGGAGGTGGTTC	GGGTGGGTGTGAGTAATGG
Dentin matrix protein 1	Dmp1	Pre Designed	
Collagen 2	Col2		

7.4 DISCUSSION

This study demonstrates that rapid regeneration of bone in the mouse cranium is both age and location specific. Complete healing was observed only in infant mice and only when the defect was located over the posterior frontal suture. These defects healed via a biphasic process in which they were first bridged with a discontinuous shell of bone on the endocranial surface of the skull, followed by a robust mineralization of the defect by two weeks following surgery. This is similar to fusion of the normal posterior frontal suture, which also first closes along the endocranial surface of the suture and is followed later by a mineralization phase [177].

On post-op day 14 there was a complex, trabeculated network of mineralized tissue in the defect in the infant mice, evident in µCT and histology images. This very complex trabecular network is not typically seen in the normal mineralization of the murine posterior frontal suture [128]. Normal sutures typically have fewer large bridges of bone spanning the endocranial to ectocranial surfaces of the suture which, increase in thickness as the animal ages.

Real-time PCR and histology also support the biphasic changes in defect healing and indicate that a process involving endochondral ossification is involved. Immediately following the endocranial defect bridging on post-op day 3, there was an increase in the cartilage associated transcription factor, Sox9. This

was then followed by an increase in mRNAs for proteins that are associated with cartilage extracellular matrix. The presence of this extracellular matrix was visible on histologic sections of the defect at 5 days post-op that were stained with Safranin-O. The matrix was not as well organized as what is typically seen with cartilage in the growth plate or articular cartilage, but there were localized regions that stained positive for sulfated glycosaminoglycans. The presence of cartilage in healing of non-suture associated calvarial defects has been previously reported, suggesting that this is one mechanism by which bone repair occurs in the cranium [99, 192].

The production of cartilage associated genes was followed first by an increase in Bmp4 and then by Bmp2 expression, suggesting that up regulation of these factors was required for the transition from chondrogenesis to osteogensis, as has been noted for endochondral ossification. The peak in expression of Bmps on post-op days 4 to 7 was followed by an increase in expression of the late marker of osteoblast differentiation, Ocn, on post-op days 14 and 21. This expression profile of Ocn was nearly identical to the changes in total defect mineral content and bone volume seen with μCT, and correlated with histologic evidence of organized bone by 14 days post-op.

Comparing the healing of the infant posterior frontal defect to the adolescent and lateral defects demonstrates that the rapid regeneration of bone within the defect is both age and location specific. The adolescent posterior frontal suture defect was the only other defect to bridge with a thin discontinuous shell of bone, as seen using 2D μCT images at 14 post-op days. This bridged in

an endocranial to exocranial manner, which is consistent with what is seen in normal suture development and fusion, suggesting an important role for the dura in the regeneration of cranial defects. Unlike the posterior frontal infant defect, the defects in the older adolescent mice displayed no significant increase in bone volume or mineralization by 14 days post-op. Furthermore, by 7 day post-op, the infant posterior frontal defect contained as much bone as an intact suture at the time of surgery. By 14 days post-op, the amount of bone in the defect doubled compared to pre-operative levels. Additionally the defects contained as much bone as a fully developed 50 day old posterior frontal suture, even though the mice were two weeks younger. These data suggest that performing traditional craniotomies in mice actually accelerates the formation of bone in the region of the suture. The increase in bone volume seen was specific to both infant groups and reflects what is seen clinically; children who are less than six months of age are at greater risk of post-operative re-synostosis [11, 12].

The defects lateral to the posterior frontal suture did not display any bone bridging by 14 days post-op. There were no changes in the percentage of the bone in the suture or defect distance until 14 days post-op in the infant lateral defect. Even though there was a small decrease in these measurements, the 2D and 3D µCT images clearly demonstrate that there was no bone bridging in these defects, although there was an increase in both bone volume and mineral content at the edges of the defect. In contrast, no changes in any of the algorithm measurements were observed for the adolescent lateral defects, indicating that no bridging or mineralization occurred.

As with all animal models, the differences in size between an animal and human can pose significant challenges, especially in the case of pediatric mice. While our model accurately replicates what is seen clinically with re-synostosis, the size of the animals at the time of surgery and the location of the defect make this a technically challenging model. While our surgical procedure can reliably and safely create the cranial defects, small variations in defect size necessitate using randomized groups and blinded reviewers. The discontinuity and heterogeneity seen with the both the infant and adolescent defects further complicates analysis of the regenerating bone. While non-serial histology provides extremely detailed morphology of the bone, the discontinuity of the bone in the defect healing limits the validity of making generalizations from a limited number of sections. This same limitation has been reported in literature examining normal cranial suture fusion [28]. While it is possible to achieve complete analysis of the cranial defect using serial histology, this is prohibitively time and resource intensive for use in high throughput applications. The combination of μCT and our imaging algorithms are well suited for examining the discontinuous bone regeneration as they allow for rapid nondestructive quantification of the bone regeneration and concomitant mineralization.

CONCLUSION

The results clearly demonstrate that rapid regeneration of bone occurs when a defect is placed over the posterior frontal suture of an infant, 21 day old animal. To our knowledge this is the first animal model that replicates the rapid re-synostosis seen in very young children who undergo cranial vault

reconstruction. Bridging of defects did not occur in non-suture associated regions, despite their being identical in size, of the embryonic origin, and subject to equivalent mechanical loading. This difference in regeneration that was specific to the posterior frontal suture accurately models the rapid re-synostosis that is seen with cranial vault reconstruction to treat children with craniosynostosis. This model has tremendous potential to improve the understanding of the mechanisms responsible for re-synostosis in children.

CHAPTER 8 INTERRELATIONSHIP OF CRANIAL SUTURE FUSION, BASICRANIAL DEVELOPMENT, AND RE-SYNOSTOSIS

8.1 INTRODUCTION

Craniosynostosis is a pathological condition in which one or more of the cranial sutures close early in development. The incidence of premature fusion is approximately 1 per 1,800 to 2,500 live births [164] and results in both craniofacial abnormalities and delays in cognitive developmental due to compression of the growing brain [49]. This is of particular concern during the early years of life because the brain roughly doubles in size by age 2 [19]. If not corrected, craniosynostosis can result in blindness, deafness, developmental delays, and in severe cases death [172]. Surgical procedures such as suturectomy or frontal-supraorbital advancement have been successful in preventing these abnormalities and symptoms, but rapid resynostosis can increase cranial pressure and further restrict the growing brain and cranial base [95, 193]. Reoperations for correcting resynostosis range from 6 to 27 percent, and have increased morbidity and mortality [63, 95]. Therefore, understanding

the biological mechanisms that cause craniosynostosis and resynostosis would address a significant unmet need.

Craniosynostosis most commonly arises from spontaneous, non-syndromic, causes, but recent advances in genetic sequencing have identified syndromic mutations in genes encoding fibroblast growth factor receptors (FRGR1, FRGR2, FRGR3) and the transcription factors Twist1 and MSX [24, 36, 81, 194]. Mutation in the Twist1 gene, a basic-helix-loop-helix transcription (bHLH) factor expressed early in suture development and in osteoblast differentiation, results in Saethre-Chotzen Syndrome. This syndrome is the most common autosomal dominant form of syndromic craniosynostosis and is typically associated with bicoronal suture synostosis, microtinea, syndactyly, and short stature [53, 195]. Mice engineered with a heterozygous point mutation in the Twist1 gene display coronal suture synostosis before 10 weeks of age [53, 55], with characterized suture fusion timing and morphology based heavily on histological analysis [70, 76, 172]. While these techniques can provide qualitative morphological information of a specific section, this method is not practical for examining the entire suture or for providing precise, quantitative data on suture fusion timing. These data are not only relevant for elucidating the exact mechanisms that cause both syndromic and non-syndromic craniosynostosis, but are also needed to develop more effective procedures and therapeutics to correct craniosynostosis and resynostosis.

Cranial suture fusion is traditionally believed to be controlled by a complex interaction between osteoprogenitor cells and the dura immediately underlying

the suture, but there is a growing body of evidence that deformities in the cranial base can disrupt normal mechanical forces in the suture and result in premature fusion [196, 197]. Surgical intervention to correct non-syndromic craniosynostosis also results in a reduction in the cranial base deformity [198, 199], further supporting this theory. The cranial base has long been considered a guide for maxillary-mandibular complex, midface, and lower face development [200-202]. Unlike the cranial vault, the growth in the skull base is regulated by tissue joints known as synchondroses [200]. Endochondral ossification of the sphenooccipital synchondrosis (SOS), the largest of these bone junctions, has a direct contribution to cranial base growth and subsequent craniofacial development [203, 204]. Therefore, it is important to investigate the potential role this tissue may have in craniosynostosis.

As the SOS begins to be replaced by bone, with total fusion shortly after puberty [200], mineralized struts called tethers form perpendicular to the plane of the SOS and connect the sphenoid and occipital bones at the midline of the cranial base [205]. Although the role of tethers in the SOS is not fully understood, it is regulated by 1α,25-dihydroxy vitamin D_3 via the vitamin D receptor and may play a role in cranial base growth and mechanical stability [205]. Therefore, investigating tether formation in the SOS during craniosynostosis may better elucidate the cranial base's role in premature suture fusion.

To address these unresolved challenges, the overall goals of this study were to determine the interrelationship between suture fusion and cranial base

development during syndromic craniosynostosis and to assess the effect of the syndrome on re-synostosis following suturectomy, using the Twist1+/- mouse model of Saethre-Chotzen Syndrome. A murine model was selected because fusion of the posterior frontal (PF) (analogous to the metopic suture in humans) occurs during the first 3 weeks of age, whereas the remaining sutures stay open throughout the life of the animal [28, 70, 206], providing the opportunity to compare the mechanisms that mediate suture fusion to those that remain open sutures in the same animal. To define the developmental and regenerative changes seen in Twist1$^{+/-}$ mice, we used an advanced active contour algorithm, developed and validated with serial histomorphometric analysis for segmenting micro-computed tomography (μCT) scans of cranial sutures by using the combination of a global threshold and the snake algorithm to segment the cranial sutures [174]. To correct distortions that were artifacts of evaluating in two dimensions the three dimensionally curved coronal suture [196], we previously developed an addition to the algorithm, which allows for reconstruction of images that are perpendicular to the suture about all three axes.

8.2 METHODS

Animal Model

All procedures and animal husbandry were performed under approval of the Georgia Institute of Technology Institutional Animal Care and Use Committee and were consistent with NIH guidelines. Male heterozygous B6.129S7-*Twist1*^{tm1Bhr}/J mice were purchased from Jackson Labs (Bar Harbor, ME) and first or second generation males were used for all breeding. Male mice were bred with first generation female C57Bl/6J (Jackson Labs). All mice were housed in a light and temperature controlled environment and given ad libidum access to food and water. Mice were kept with their natural birth mothers until post-natal day 21 or euthanasia. Mice under 21 days of age were euthanized by intraperitoneal injection of pentobarbital and mice over 21 days of age were euthanized by CO_2 asphyxiation. Mice were genotyped from ear punches or tail clips under general anesthesia with isoflurane. DNA was extracted using NaOH/Tris HCl extraction as previously described and PCR was performed for the neomycin resistance gene (Fwd Primer-CTT GGG TGG AGA GGC TAT TC; Rev Primer- AGG TGA GAT GAC AGG AGA TC) [207].

Micro-CT Analysis of Cranial Sutures

The advanced active contour algorithm was applied to assess temporal changes in fusion of both the posterior frontal and coronal sutures. Six male litter

matched Twist1$^{+/-}$ (Twist) and Twist1$^{+/+}$ (WT) mice were euthanized at each of the following time points: post-natal days 6, 12, 20, 25, and 30. After verifying death by absence of a palpable heart beat and blink reflex, the calvaria and cranial base were removed from soft tissues and fixed in 10% neutral buffered formalin (Sigma, St. Louis, MO). The scan region for the calvaria was identified from the most posterior molars in the maxilla and moved posteriorly 6.6 mm. This region contained both the posterior frontal and coronal sutures. The samples were imaged by μCT with isotropic voxels 10.5 μm in size and an energy of 55 kVp (Viva CT 40, Scanco Medical, Bruttisellen, Switzerland). The exact locations of both sutures were identified on 3D renderings made using a global threshold to create DICOM images for later image processing.

The images were analyzed with an image segmentation algorithm developed and validated with serial histology to quantify both the posterior frontal and coronal sutures [174]. Briefly, the algorithm uses a combination of a global threshold and snake algorithm to segment the bones of the developing sutures, eliminating the distortions seen in the lateral regions of the coronal suture when analyzing straight coronal images. The algorithm thus allows for accurate identification of the varying and irregular mineralization of the developing suture. For the coronal suture, images were reconstructed perpendicular to the suture about all three axes, using a modification of our algorithm described previously [174]. These segmentation boundaries were then used to determine the percentage of suture open; the minimum, mean, and maximum distances

between the bones; the area of the suture; the bone volume, and suture mineralization. Suture mineralization was used as an indicator of bone mineral content and was calculated by converting the pixel intensities to a known hydroxyapatite standard to give the density of each pixel relative to hydroxyapatite. All images were evaluated by a reviewer blinded to the age and genotype of the mice.

MicroCT Analysis of the Cranial Base

To determine the potential role the cranial base may have in craniosynostosis, SOS morphology and tether formation after syndromic premature suture fusion was quantified. The cranial base was scanned with isotropic voxels 8 µm in size at an energy of 45 kVp as previously described in mice that were 25 and 30 days old [205]. These time points were selected because accelerated synchondrosis closure and initial tether formation were previously observed during this stage of postnatal development [205]. Additionally, these time points occur well after previously reported suture fusion in Twist mice [29]. Briefly, the anterior region of the spheno-occipital synchondrosis (SOS) was outlined with user-guided contours and evaluated at a threshold corresponding to 250 mg hydroxyapatite/cm^3, which was previously confirmed to be accurate for evaluating tethers by comparing histomorphometric and µCT results [208]. Scanco software using a direct distance transformation method was used to determine average SOS thickness, SOS volume, tether volume/SOS volume, and tether spacing as described in detail previously [205,

209, 210]. This method resulted in global volumetric measurements that represent averages along all relevant axes.

Re-synostosis Model

The ability to heal cranial defects was assessed in an infant model of re-synostosis. Post-natal day 21 male litter matched Twist and WT mice were used for all cranial defects. A 1.5 by 2.5 mm defect removing the posterior frontal suture was created in all mice, as described previously [211]. When this defect is created in a 21 day old C57Bl/6 mouse, it undergoes rapid re-synostosis. The defect heals in a biphasic process where bridging of the defect is seen as soon as 3 days post-op and the defect becomes fully mineralized by 14 days post-op. On post-op days 4 and 14 five Twist and five WT mice were euthanized and immediately imaged with µCT using the scan settings detailed above. The defect distance, defect bone volume, percentage of defect open, and the defect mineral content were calculated using the algorithm described above.

Following imaging the skulls were fixed in 10% neutral buffered formalin and decalcified in 10% EDTA. The EDTA was changed every two days until the skulls were completely de-calcified as verified with plain x-ray. The samples were dehydrated and embedded in paraffin. After verifying the location of the defect, 7 µm thick sections were made and de-parafinized. Sections were stained with haematoxylin and eosin (H&E) and images were made on a Leica DMLB at 10X and 40 X magnification.

Statistical Analysis

The sample sizes for the sutures (n=6), synchondroses (n=6), and the cranial defects (n=5) were determined on a prospective power analysis using the results of previous scans or surgeries, respectively. The normality of the data was verified using a Komogorov-Smirnov normality test. This was followed with a two-way ANOVA to check for differences between the time points, the genotype, and the interaction between the two terms. In all cases there was significant interaction and the data were analyzed with a one-way ANOVA or Student's t-test. Where appropriate, statistical significance was determined using a Dunnett's Multiple Comparison post-hoc test. A p value less than 0.05 considered significant for all analyses. All analysis was performed using Graphpad Prism 5 software (GraphPad Software, La Jolla, CA).

8.3 RESULTS

Closure of Coronal and Posterior Frontal Sutures

The 3D reconstruction and segmentation algorithm developed to quantify the development of cranial sutures in C57Bl/6 mice was able to successfully analyze the PF and coronal sutures of the Twist and WT mice. The minimum distance between the bones of the coronal suture began at 0.23 mm on post-natal day 6 for the WT mice before reaching a plateau of 0.10 mm by post-natal day 20. The distance between bones remained constant at approximately 0.10 mm in the Twist mice for all ages and was less than the WT mice on post-natal days 6 and 12 (Figure 8-1a). Both the bone volume and total mineral in the coronal suture remained constant for post-natal days 6 to 12, and then increased until reaching a plateau by day 20 in both the Twist and WT mice (Figures 8-1b-c). In the WT mice, total mineral reached a plateau after post-natal day 25, while the mineral content in Twist mice continued to increase for all time points examined. Additionally, there was more bone mineral and volume in the Twist mice on post-natal days 6, 12, and 30 (Figures 8-1b-c).

In contrast to what was seen in the coronal suture, the posterior frontal suture in the Twist mice was more open than in WT mice and mineralized at a faster rate. The WT mice displayed a decrease in the distance between the bones after post-natal day 12 while there was no change in the distance between

the bones of the suture in the Twist mice (Figure 8-1d). Despite this apparent lack of fusion in the Twist mice, the bone volume and mineral content increased earlier and at a faster rate. Both groups of mice started out with no differences in either measure on post-natal day 6, but the Twist mice had an increase in bone immediately while there were no changes in the WT mice until post-natal day 25 (Figures 8-1e-f). By post-natal days 25 and 30 there was no difference in the volume or mineral content of between the two groups (Figures 8-1e-f).

Analysis of representative 3D μCT reconstructions from litter matched WT and Twist mice illustrate the changes seen using our image processing algorithms. At post-natal day 6, the posterior frontal suture was open in the WT mice and the coronal suture was clearly present (Figure 8-2a). As the coronal suture developed from adjacent bones that overlap, it was difficult to visualize the open coronal suture on 3D renderings. In the 6 day old Twist mice, the posterior frontal suture was also open, but the coronal suture appeared nearly completely fused (Figure 8-2b). There were regions in the lateral areas of the suture that had small gaps on the ectocranial surface of the skull but were fused along the endocranial surface of the suture. By 12 days post-natal, the posterior frontal suture began to fuse in the WT mice, but the majority of the suture in the Twist mice remained open (Figures 8-2c-d). Similarly to what was seen with the younger mice, on post-natal day 12 the coronal sutures of the WT mice displayed the characteristic overlap that was not present in the Twist mice (Figures 8-2c-d). On post-natal day 25 the posterior frontal suture appeared mostly fused in the

WT mice, but there were large regions in the Twist mice that remained open (Figures 8-2e-f). The coronal suture in the post-natal day 25 Twist mice was completely fused although remnants of the suture were still present (Figure 8-2f). The post-natal day 25 mice displayed the characteristic overlap seen with the younger mice and the edges of the bones appeared closer together than what was seen in the younger mice (Figure 8-2e). While study was not designed to quantify the sagittal sutures in the Twist mice, they also appeared completely open for all time points (Figures 8-2b,d,f). The 3D images of the 20 and 30 day old mice appeared identical to the 25 day old images (data not shown).

Examination of both the sutures on the 2D µCT scans demonstrates the changes seen with the algorithm over time. The coronal sutures of all the WT mice had the characteristic overlap between the bones of the suture (Figures 8-3a-c), but between post-op days 12 to 25 the bones of the suture increased in volume and the osteogenic fronts came closer together. In contrast, the bones of the coronal suture developed as fused structures, but they never displayed the characteristic overlap that was seen with the WT mice (Figures 8-3d-f). The images from post-natal day 12 and 25 show the coronal suture was fused along the endocranial surface of the suture. It formed an oval structure that was partially open on post-natal day 12 and was completely closed on post-natal day 25 (Figures 8-3e-f). The posterior frontal suture in the WT mice was largely open by post-natal day 6, began to fuse on post-natal day 12, and fused and began to increase in bone volume on post-op day 25 (Figures 8-3g-i). While there was a

substantial increase in the volume of bone present in the posterior frontal suture in the Twist mice, the suture did not appear to fuse after the time points examined (Figures 8-3j-l).

SOS Tethers in WT and Twist Mice

The SOS in WT and Twist mice was similar in size at both post-natal days 25 and 30 as both average thickness and volume were not statistically different among all groups (Figures 8-4a-b). The SOS of Twist mice had a significant increase in tether volume/SOS volume between 25 and 30 days, but this parameter did not change in WT mice during the same time period (Figure 8-4c). Despite the increase in tether volume/SOS volume in Twist mice between 25 and 30 days, a corresponding change in tether number in Twist mice was not significant (Figures 8-4d). Tether width increased in Twist mice between day 25 and day 30 days post-natal, but no change in tether width in WT mice was observed (Figurs 8-4e). Neither WT nor Twist mice exhibited a significant change in tether spacing in the SOS between 25 and 30 days (Figure 8-4f). 3D reconstructions of the SOS in WT mice revealed that tether mineralization was not noticeably different between day 25 and 30 (Figures 8-5a-b) but were different between day 25 and day 30 day in the Twist SOSs (Figures 8-

Resynostosis Model

The cranial defect procedure was well tolerated in both the Twist and WT mice. Survival rates were greater than 90% for the surgeries and mice who

survived the acute post-operative period did not have any complications. Complications from anesthesia and aspiration of the irrigation solution were the most common causes of intraoperative mortality. The distance between the bones of the defect in the Twist mice decreased from 0.60 mm on post-op day 4 to 0.35 mm on post-op day 14 (Figure 8-6a). At both time points, there was no change in this distance for the WT mice, which was less than 0.17 mm (Figure 8-6a). Despite these differences in defect width, there were no differences in the average thickness of the bone in the defect (Figure 8-6b). In both groups the bone increased in thickness from 0.11 mm on post-op day 4 to over 0.32 mm on post-op day 14. For both WT and Twist mice, the mineral content in the defect more than doubled from 4 to 14 days post-op (Figure 8-6c). Additionally, there were no differences between the two groups of mice at either 4 or 14 days post-op (Figure 8-6c). Identical changes and significance were also seen with the volume of bone in the defect (Figure 8-6d).

Representative 2D and 3D images from the posterior frontal defect illustrates the differences in healing between the Twist and WT mice. By 4 days post-op, the defect was bridged by bone in the WT mice, although the 3D renderings show that the mineral was distributed in a heterogeneous manner (Figures 8-7a-c). In contrast, no bridging of the defect was seen in the Twist mice at this same time point (Figures 8-7b-d). By 14 days post-op there was an increase in both the total bone volume and mineral present in both mice (Figures 8-7e-h). As was seen with the algorithm results, there were small regions in the

WT mice and much larger regions in the Twist mice that remained open even out to 14 days post-op (Figures 8-7e-h).

Histological analysis of the regenerating bone in the defect confirmed the μCT results. On post-op day 4 there was a thin endocranial bridge of bone in the defect in the WT mice, but there was little organized bone present in the Twist mice (Figures 8-8a-b). By 14 days post-op there was thick trabeculated bone in the defect in both groups of mice; however, the Twist mice did not have bone that fully bridged the defect (Figures 8-8a-d).

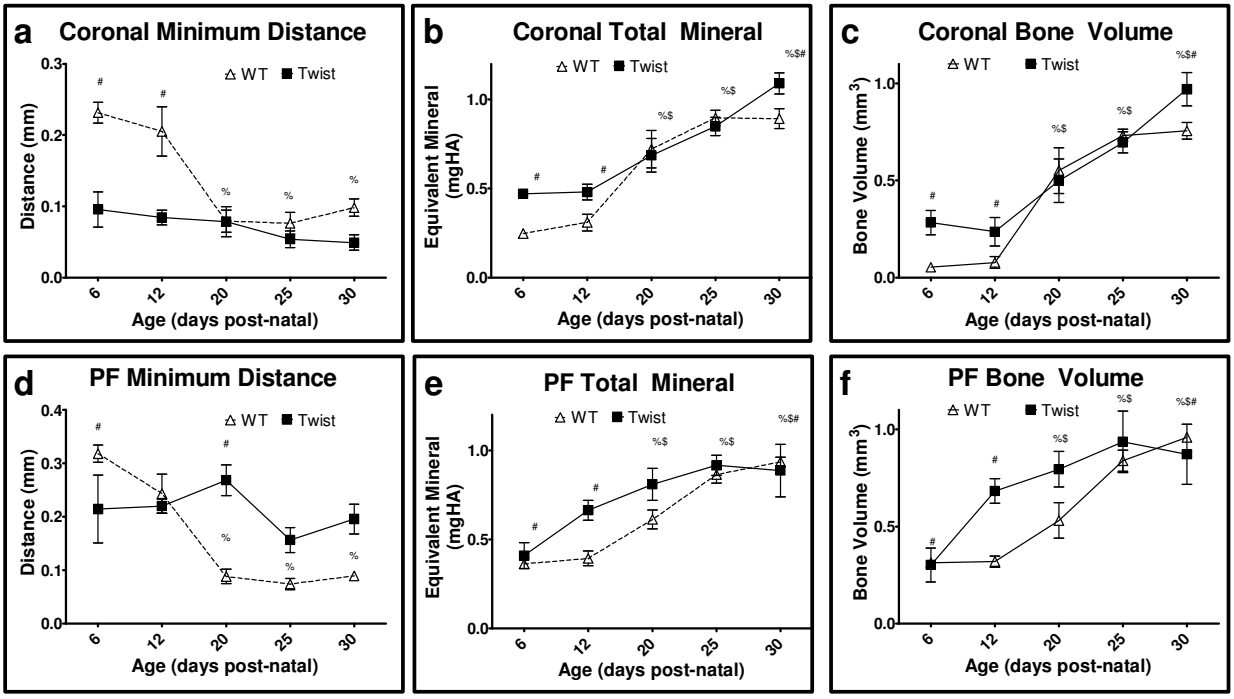

Figure 8-1: Fusion of Coronal and Posterior Frontal Sutures. Comparison of coronal suture development by µCT between the WT and Twist mice for the minimum distance (a), total mineral content (b), and total bone volume (c). Comparison of posterior frontal development by µCT between WT and Twist mice for the minimum distance (d), total mineral content (e), and total bone volume (f). $P<0.05$ # = same age Twist, % = WT 6 days, $ = Twist 6 days.

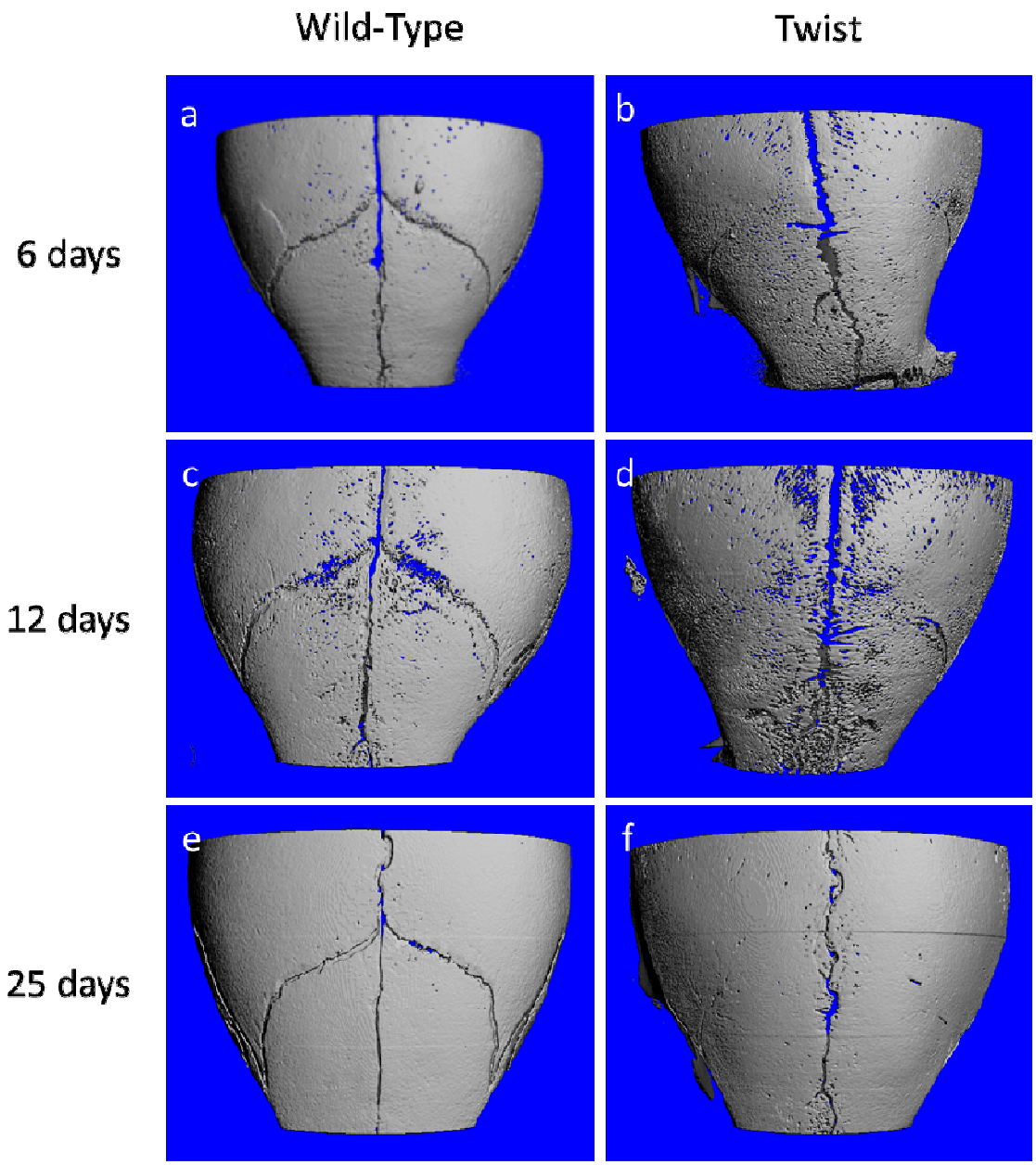

Figure 8-2: 3D µCT renderings showing representative images of WT and Twist mice. Images represent 6 day old WT (a), 6 day old Twist (b), 12 day old WT (c), 12 day old Twist (d), 25 day old WT (e), 25 day old Twist (f).

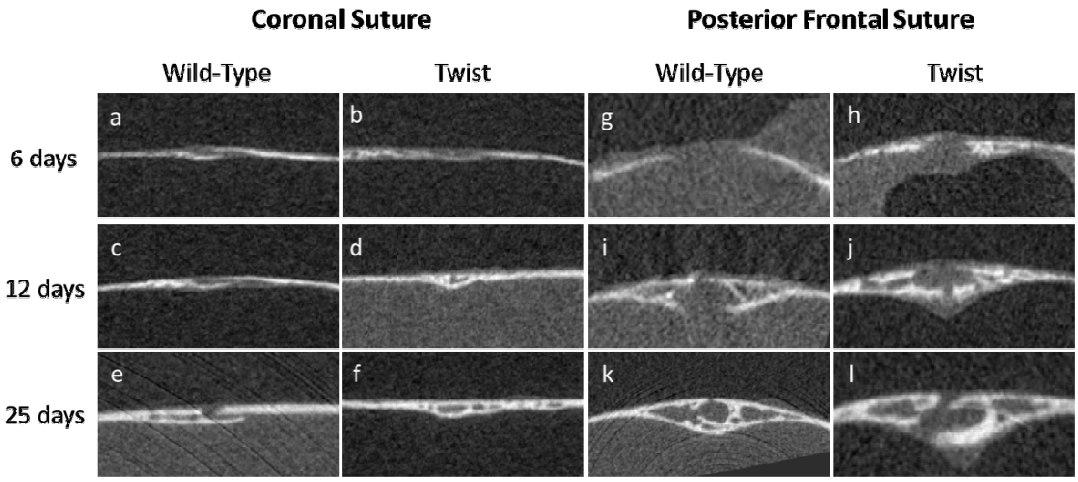

Figure 8-3: Representative 2D µCT images showing changes in morphology of the WT and Twist mice for: 6 day coronal WT (1),6 day coronal Twist (b), 6 day PF WT (c), 6 day PF Twist (d),12 day coronal WT (e),12 day coronal Twist (f), 12 day PF WT (g), 12 day PF Twist (h), 25 day coronal WT (i), 25 day coronal Twist (j), 25 day PF WT (k), 25 day PF Twist (l).

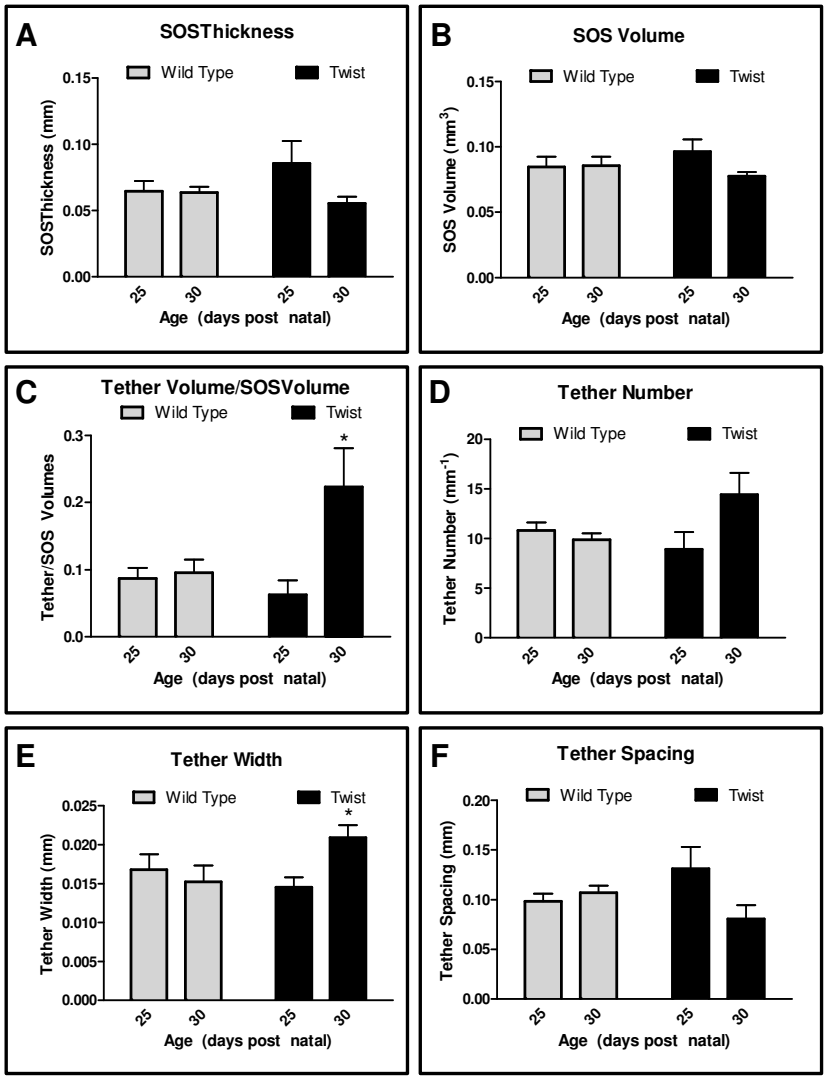

Figure 8-4: Quantification of tissue morphology and tether formation in the sphenooccipital synchondrosis (SOS). Parameters include average SOS thickness (A), SOS volume (B), tether volume/SOS volume (C), tether number (D), tether width (E), and tether spacing (F).

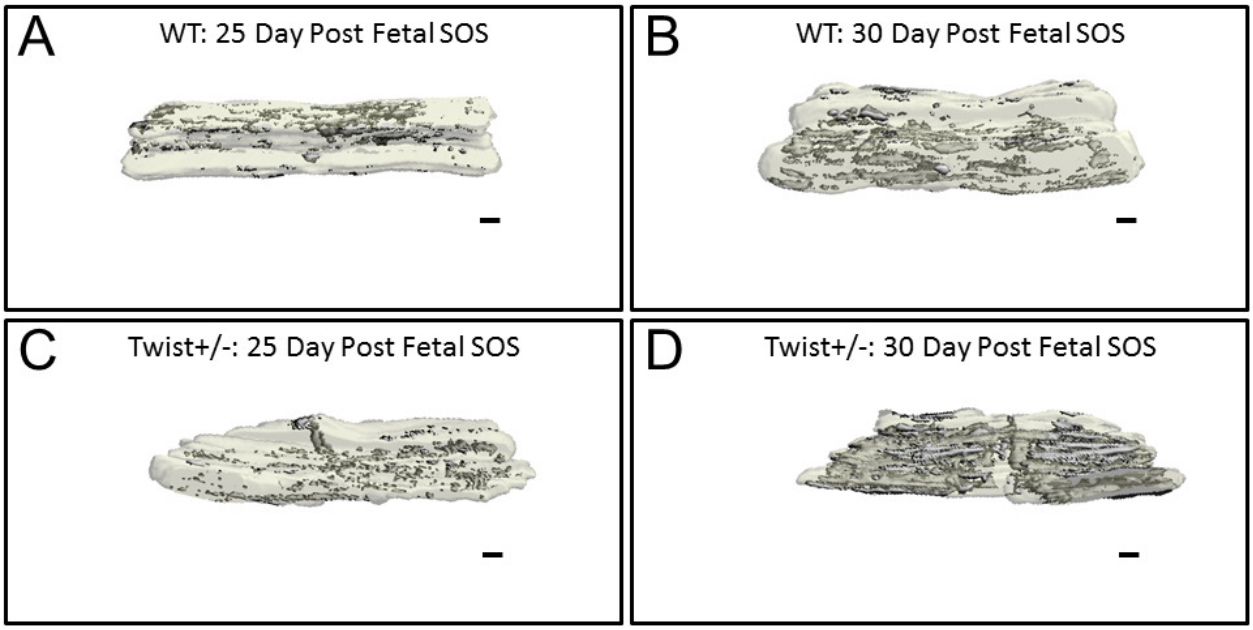

Figure 8-5: Tether accumulation in the sphenooccipital synchondrosis (SOS). Representative 3D images of SOS in 25 day post-natal wild type (WT) mice (A), 30 day post-natal WT mice (B), 25 day post-natal Twist+/- mice (C), and 30 day post-natal Twist+/- mice.

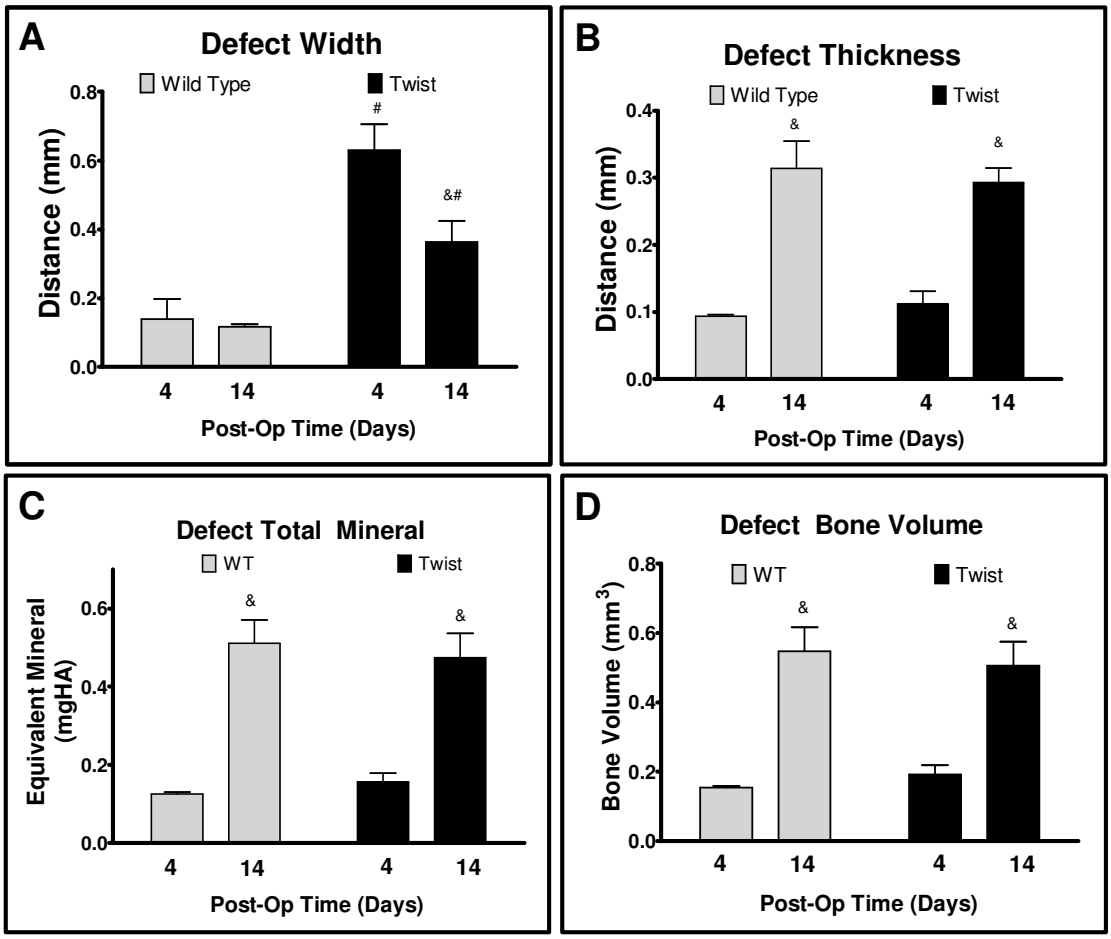

Figure 8-6: Quantification of defect healing in WT and Twist mice at days 4 and 14 post-op for percentage of defect open (A), the average defect distance (B), the total defect mineral (C), and the total bone volume (D).

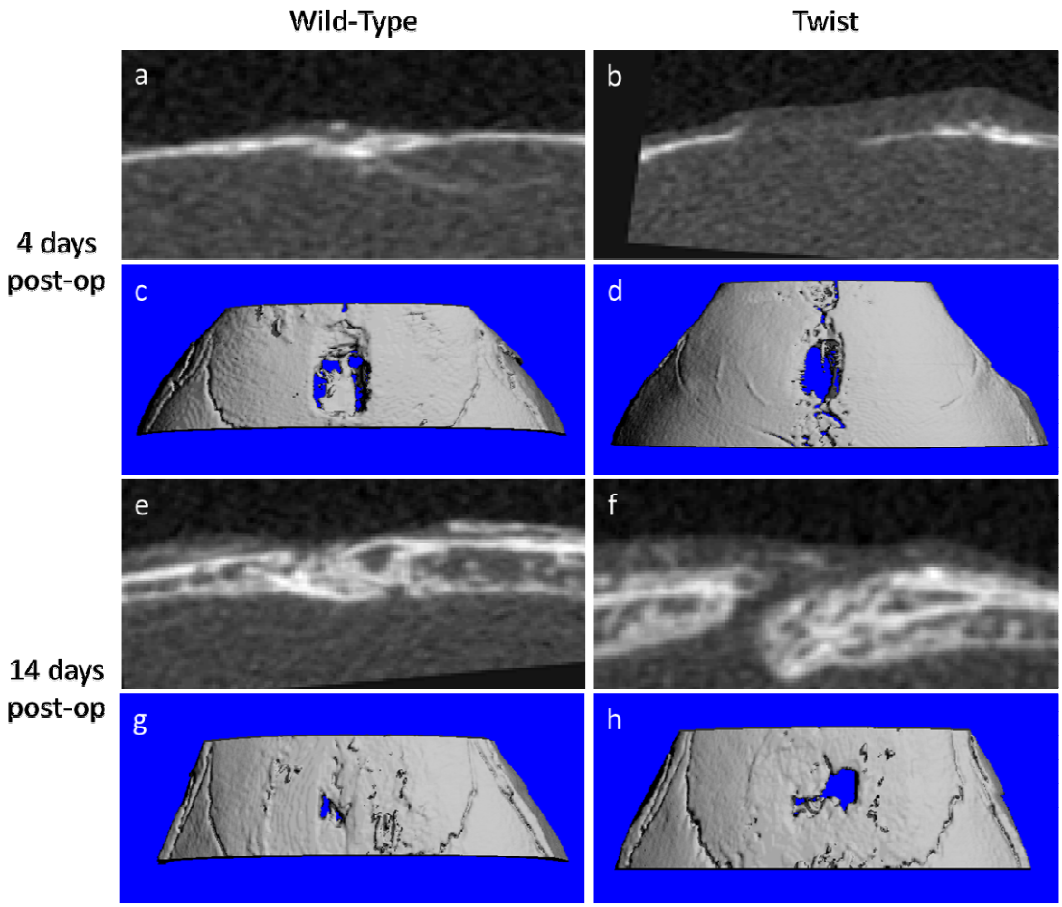

Figure 8-7: Representative 2D and 3D µCT images of WT and Twist mice at 4 and 14 days post-op for: 4 days post-op WT (A,C), 4 days post-op Twist (B,D), 14 days post-op WT (E,G), 14 days post-op Twist (F,H).

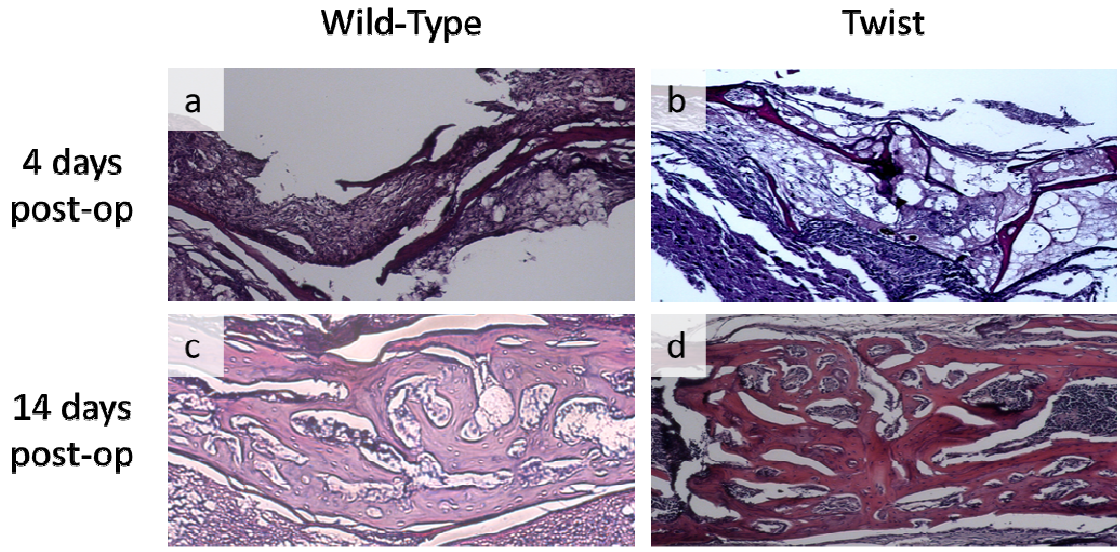

Figure 8-8: Histology stained with H&E from posterior frontal defect in 4 day post-op WT (A), 4 day post-op Twist (B), 14 day post-op WT (C), and 14 day post-op Twist (D) at 10X magnification.

8.4 DISCUSSION

In addressing our objectives, our results show that fusion of the coronal suture in Twist mice occurs by a process different from normal suture fusion, that coronal suture fusion does not appear to be influenced by deformities in the cranial base, and that mutations to the Twist gene impairs healing of a posterior frontal defect. The coronal sutures in WT mice decreased in width and then mineralized after post-natal day 12 while coronal sutures in Twist mice had suture widths that were similar to that of fused sutures at all measured time points. Although this suggests that sutures develop fused in the Twist mice, it is also likely that the coronal sutures fuse prior to post-natal day 6. However, the skull does not contain enough mineral content to identify the bones in either the WT or Twist mice prior to this age.

This timing of coronal suture fusion in Twist mice is slightly different than what has been previously reported [29]. Behr et al. used histology to qualitatively describe the fusion of sutures and suggested that these sutures fused sometime before post-natal day 13. While histology can provide detailed morphologic information, the ability to make generalizations is limited to the irregularities seen with suture fusion [28, 183]. This is further complicated in analyzing pathologic suture fusion in Twist mice due to the variable penetrance and variations in morphology seen along the length of the suture. The 3D reconstructions in the

present study clearly illustrate this variation along the length of the pathologically fused coronal suture with the medial regions of the suture being more fused.

After coronal suture fusion, the SOSs of WT and Twist mice at post-natal day 25 were still open and had limited tether formation compared to fused SOSs in mature mice studied by Lee at al. [205]. In this prior study, Lee et al. showed that post-natal tether development occurred in two stages: an initial stage of tether thickening from 2 to 8 weeks post-natal followed by an accumulation in number starting at post-natal week 6. The WT mice in this study demonstrate a similar pattern in temporal mineralization, but Twist mice exhibit accelerated tether formation – specifically tether thickening – between 25 and 30 days compared to WT mice. This accelerated SOS tether formation in syndromic mice occurred well after normal coronal suture fusion, suggesting that abnormalities in the skull base did not have a role in coronal suture fusion in this model of craniosynostosis.

In comparing the defect healing between the Twist mice to the WT mice, it was apparent that the ability to heal the posterior frontal defect was impaired in the Twist mice. At both post-op time points, the defect distance was greater in the Twist mice. This lack of bridging was also seen in the 2D and 3D μCT images as well as with histology. However, there were no differences in the bone mineral content or volume in the Twist mice. This equivalent mineral content but wider distance was similar to what was seen with the normal development of the posterior frontal suture. It is possible that the fused coronal

suture not only stress shields the posterior frontal suture, but also the regenerating tissue that is contained within the defect.

Surprisingly the posterior frontal suture in the Twist mice did not display the fusion that was seen in the WT mice. Similar to the timing seen previously, the posterior frontal suture fused between post-op days 12 and 20 in the WT mice [177]. This lack of fusion was seen in both the 2D and 3D μCT images. To our knowledge this is the first report demonstrating the lack of fusion in the posterior frontal suture in the Twist mice. This lack of fusion may be caused by stress shielding of the posterior frontal suture by the fused coronal sutures. Others have previously shown that cyclic mechanical stress is required for the fusion of the posterior frontal suture in rodents [74, 212].

In addition to the differences in decreasing widths of coronal and posterior frontal sutures during fusion, there were also differences in how the sutures mineralized. In the coronal suture, Twist mice contained greater mineral and bone volume at both the early and later time points. Additionally, there was no plateau seen in either measurement in the Twist mice, which suggests that the skull may continue to mineralize beyond the developmental period of the WT mice. There were also significant differences in suture morphology seen in both sutures in the Twist mice. The coronal suture in Twist mice never displayed the characteristic overlap that is seen with normal coronal sutures. These sutures appeared to form a small oval structure that was open on the top of the suture and fused first on the endocranial surface. At later time points, this structure fused on the ectocranial surface, but none of the images displayed the

overlapping bones. These differences, when combined with the lack of change in distance measurements, suggest that the pathologic fusion seen with these sutures is a result of abnormal suture development, as opposed to just premature fusion of a relatively normal suture.

Although craniosynostosis has previously been linked to deformities in the cranial base because of alterations in the SOS during suture fusion and restored morphology after surgical intervention [196-199], other theories describing the mechanism of syndromic and non-syndromic suture fusion exist. One hypothesis is that genetic mutations in the dura underlying the suture, lead to altered signaling that results in premature fusion [23, 26, 75]. More recently, several investigators proposed a hybrid theory where there is an abnormality in the skull base, which changes the tension of the dura underlying the suture. This then leads to an alteration in the signaling between the dura and overlying suture, resulting in premature suture fusion [74]. It is also possible that all of these molecular and mechanical alterations, along with others still not characterized, result in the multiple forms of craniosynostosis.

There have been over 50 different mutations in the Twist1 gene associated with Saethre-Chotzen Syndrome [53, 213]. Universally, mutations in Twist1 cause a decrease in the binding capacity to E-protein and an increase in homodimer formation [59], however, it is unclear how these mutations mediate their direct effects on suture fusion. Our results confirm that mutation of the Twist1 gene has effects on developmental processes in sutures involving endochondral ossification [29] and show that these effects occur at multiple

anatomic sites during craniofacial development. Moreover, mutations in the Twist1 gene affect the rate and extent of re-synostosis following suturectomy. When this is due to recruitment and differentiation of chondroprogenitor cells [214], to modulation of chondrocyte hypertrophy [215], or to later effects in endochondral bone formation as is suggested by our study, was not addressed. Our findings indicate that the mutation in the Twist1 gene addressed in this study, impacts mineralization of the extracellular matrix, possibly by modifying regulation of matrix metalloproteinase activity [216] and consequent matrix remodeling and calcification required for osteogenesis.

In conclusion, the results from our μCT analysis demonstrate substantial differences in development and regenerative ability between WT and Twist mice. The Twist mice displayed pathologic development of the fused coronal sutures, which was not dependent on an abnormal cranial base. Additionally, the Twist mice were unable to bridge both the midline posterior frontal sutures and defects, despite having equivalent mineralization.

CHAPTER 9 RAPIDLY POLYMERIZING INJECTABLE CLICK HYDROGEL THERAPY TO DELAY BONE GROWTH IN A MURINE RE-SYNOSTOSIS MODEL

9.1 INTRODUCTION

Given their biocompatibility, ease of delivery, and tunable properties, injectable hydrogels are attractive matrices for drug delivery and tissue engineering. Current hydrogel systems that undergo in situ polymerization are limited due to their toxicity and/or long polymerization times. Here, we present a bio-orthogonal rapidly crosslinking click-based injectable hydrogel for the controlled delivery of co-administered proteins. Our hydrogel is composed of a difunctionalized 4-dibenzocyclooctynol poly(ethylene glycol) conjugate (PEG-DBCO) and a multivalent PEG-based azide (PEG-N3) functionalized polymer, which upon mixing form a crosslinked network in less than 90 seconds. The hydrogel was used to deliver the bone morphogenic protein (BMP) inhibitor rmGremlin1 (Gremlin) to delay rapid post-operative bone growth in a pediatric murine model of re-synostosis. Hydrogels containing Gremlin caused a dose dependent inhibition of re-synostosis. In addition to craniofacial applications, our

injectable click hydrogel has the potential to provide customizable protein, small molecule, and cell delivery to any site assessable via needle or catheter.

Injectable hydrogels are composed of mutually reactive precursors that react in situ to form insoluble networks with a high water content that mimic the material properties of surrounding tissues[217]. Although various polymers have been used to form synthetic injectable hydrogels, by far the most widely studied gels are those formed from macromolecular poly(ethylene glycol) (PEG) precursors. A major advantage of using synthetic materials is that they allow for controllable mesh size, degradation times, mechanical properties, and release rates by varying the concentrations and chemical properties of the soluble precursors[218, 219]. Numerous free radical polymerization mechanisms have been employed to generate hydrogel networks from soluble PEG-based precursors, but the initiators and free radicals produced during polymerization have the potential to damage encapsulated therapeutic molecules and surrounding tissues[153].

The bio-orthogonality and spontaneous reactions seen with “click chemistry” make click reactions ideal gelation mechanisms for in situ network formation. Although, the classical Cu-catalyzed Huiseng cycloaddition has been used to crosslink azide and alkyne functionalized PEG precursors, the toxicity associated with the copper catalyst diminishes the clinical viability of such systems[220]. Anseth introduced a copper-free click hydrogel composed of an azide terminated 4-arm PEG and a polypeptide functionalized with difluorinated cyclooctyne (DIFO) that took approximately one hour to achieve complete

polymerization [162]. While this copper-free click hydrogel represents a major advancement towards true bio-orthogonality, gels that crosslink on a much shorter time scale can improve the effectiveness of hydrogel-based delivery systems by rapidly encapsulating co-administered therapeutics before they diffuse away from the site of injection. In addition, by significantly reducing procedure time, and thus decreasing patient exposure to anesthetic and the potential for infection, hydrogels that crosslink in minutes would dramatically increase patient safety.

Here, we present a bio-orthogonal injectable hydrogel that crosslinks to completion in less than two minutes, and thus has the gelation kinetics required for in situ encapsulation of co-administered biological therapeutics. In order to achieve such rapid network formation, we synthesized multivalent PEG precursors (Figure 9-1a, **1** & **2**), which form an insoluble network upon mixing (Figure 9-1a, **3**) via the ring-strain promoted Cu-free click reaction between DBCO and azides. In addition to being two orders of magnitude faster than previously reported click-based mechanisms, the DBCO-azide reaction proceeds rapidly under physiological conditions and is non-toxic to cells[221].

One important use of these rapidly polymerizing, non-toxic injectable hydrogels is the delivery of therapeutic agents to sites of injury where the retention of the agent at the site is desired over days and weeks. In order to determine if our hydrogel meets this specification we took advantage of a murine model of re-synostosis following suturectomy, which we developed in our lab[211]. In very young children, treatment for craniosynostosis, or premature

fusion of the cranial sutures, involves surgical reconstruction of the cranial vault with the goal of correcting the craniofacial deformities and restoring a more normal intracranial volume. Unfortunately, in a large number of these children, bone rapidly reforms (re-synostosis) resulting in additional neurologic complications and necessitates additional surgical intervention[63][10,11]. Our murine model involves the creation of a standardized defect over the posterior frontal suture in 21-day-old mice. This defect results in rapid bone regeneration comparable to the re-synostosis seen in children. Our previous studies suggested that an inhibitor of bone morphogenic protein (BMP) called Gremlin-1 might be a suitable therapeutic protein to test the effectiveness of the hydrogel as a delivery method capable of localizing, retaining, and releasing the biologically active protein at the treatment site (Figure 9-1c)[211].

To generate a water-soluble non-fouling multivalent azide functionalized polymer, we synthesized PEG-N_3 (Figure 9-1a, **1**) from azide functionalized and non-functionalized PEG methacrylate monomers via reversible addition-fragmentation chain transfer (RAFT) polymerization, which affords tight control of azide functionality. The synthetic strategy presented here generates polymers with molecular weights (M_N) of approximately 25,000 Da and an average azide functionality per polymer of 13 (Figure A-10). The difunctionalized PEG-DBO crosslinker (Figure 9-1a**, 2**) was synthesized by reacting bis-amino-PEG with excess benzyle-2-nitro-carbonate functionalized DBCO. Dynamic time sweep rheological experiments were conducted on gels formed in the presence of serum to monitor network formation kinetics. Upon mixing, hydrogels containing

12.5% PEG-N3 and 4% DBCO-PEG underwent gelation in less than 30 seconds (i.e. G'= G") and were completely crosslinked in under 90 seconds (Figure 9-1b). This rapid polymerization seen with our hydrogel allows for rapid encapsulation and sequestration of co-delivered proteins before they can diffuse away from the site of administration.

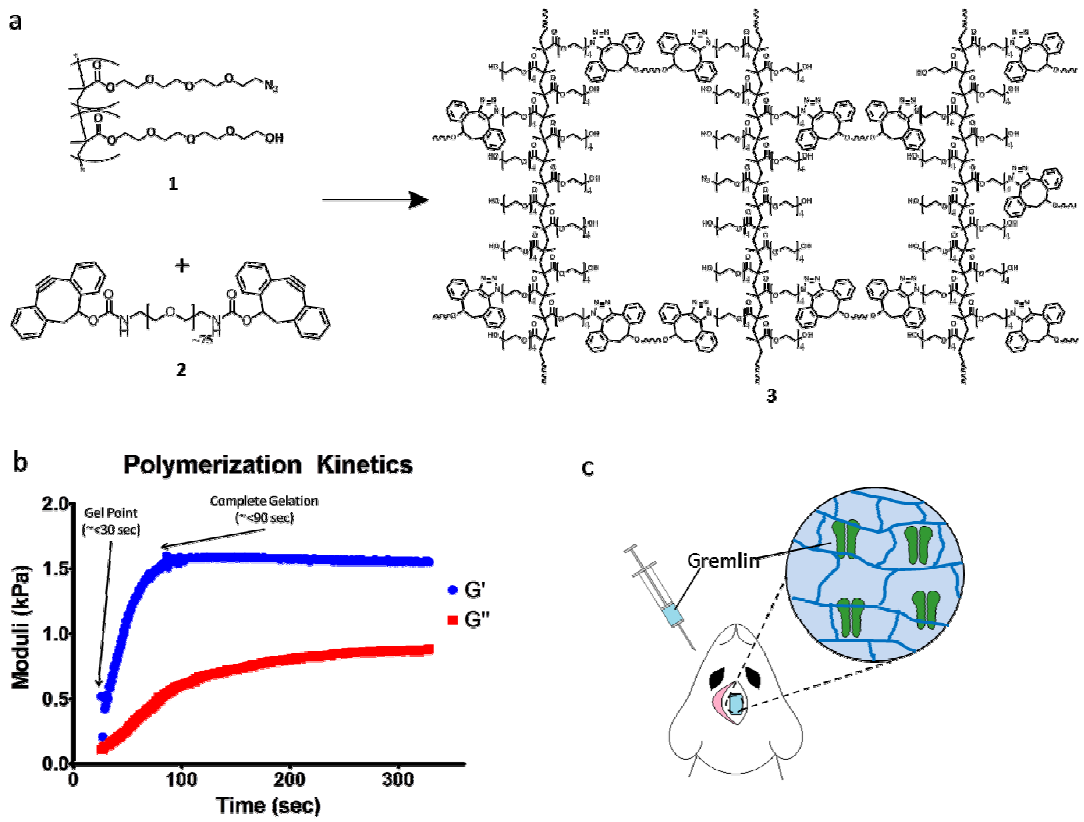

Figure 9-1: Hydrogels formulated from azide functionalized PEG polymers and DBCO functionalized PEG crosslinker gel in less than two minutes: a. Azide-functionalized RAFT-copolymer (PEG N3) **1** rapidly crosslinks with PEG-DBCO crosslinker **2** via the [3 + 2] Huisgen cycloaddition to form a hydrogel. **1** and **2** react fast enough to allow for injection into tissue, hydrogel formation and biomolecule encapsulation. b. Spinning disk rheometry was used to determine the crosslinking dynamics of the hydrogel, and demonstrate that when mixed together, the two components begin to gel in less than 25 s with complete gelation occurring in less than 90 s. c. Cartoon illustrating the co-administration of rmGremlin1, **1**, and **2**, to a non-critical cranial defect and the subsequent entrapment of rmGremlin1 upon in situ crosslinking.

9.2 METHODS

Synthesis of Poly[tetraethylene glycol methacrylate)-co-(azidotetraethylene glycol methacrylate)] (PEG-N3) (1)

Tetraethylene glycol methacrylate (0.9 g, 3.43 mmol) and azido tetraethylene glycol methacrylate (0.28g, 1.0 mmol), benzothioylsulfanyl)acetic acid (6.27 mg, 0.03 mmol), and AIBN (0.5 mg, 0.003 mmol) were combined in dimethylformamide (1.5 ml). The reaction flask was degassed by five freeze-pump-thaw cycles, and then immersed in an oil bath and stirred at 70℃. After 20 h, the reaction was terminated by flash freezing in liquid nitrogen. The reaction product was added to dichloromethane (DCM) (5 ml) and then precipitated via the addition of methanol (25ml). The supernatant was decanted and the precipitated polymer was subjected to three more rounds of resuspension and precipitation before being concentrated under reduced pressure. The purified polymer was analyzed for weight by gel permutation chromatography (tetrahydrofuran) and the structure and purity were verified by ^{1}H NMR (deuterated chloroform) **1H NMR** (Figure A-10). Molecular weight: Mw ~ 24 kDa, Mn ~ 18 kDa.

Synthesis of 4-Dibenzocyclooctynol PEG Conjugate (PEG-DBCO)(2)

To a stirred solution of poly(ethylene glycol) bis(amine)$_{3400}$ (340 mg, 0.1 mmol) and NEt_3 (40 mg, 0.4 mmol) in DCM (15 mL) was added DBCO (90

mg, 0.23 mmol) under an atmosphere of argon. The reaction mixture was kept stirring overnight at ambient temperature, and the solvent was removed under reduced pressure. The residue was dissolved in DCM (30 mL), and washed with water (5 mL) and brine (5 mL). The organic phase was dried over Na_2SO_4, filtered and evaporated to dryness under reduced pressure. The residue was purified by flash column chromatography on silica gel (DCM/CH_3OH, 15/1) to afford (2) (0.31g, 81.3%) and analyzed by H-NMR. 1H NMR (400 MHz, $CDCl_3$) *δ (ppm)* 3.13-3.03 (m, 4H, C*H*$_2$CHO), 3.50-3.75 (m, 300H, 150 PEG C*H*$_2$), 5.42-5.61 (m, 2H, OC*H*CH_2), 7.21-7.46 (m, 16H, aromatic); and 13C NMR (100 MHz, $CDCl_3$) *δ (ppm)* 40.83(*C*H_2CH), 46.08 (*C*H-O), 69.88 (*C*H_2), 70.19 (*C*H_2), 70.46 (*C*H_2), 76.58 (*C*H_2), 77.50 (*C*H_2), 109.91 (alkyne), 112.78 (alkyne), 121.12 (aromatic), 123.68 (aromatic), 123.73 (aromatic), 125.78 (aromatic), 126.07 (aromatic), 126.94 (aromatic), 127.85 (aromatic), 127.96 (aromatic), 129.85 (aromatic), 150.92 (aromatic), 152.12 (C=O), 155.41(C=O).

In Vitro Hydrogel Testing

All in vitro experiments were performed under aseptic conditions. Aqueous stock solutions of DBCO-PEG (12.5%, 6.25%, 4.85%, 3.13%, 1.56%; w:v) and PEG-N3 (50%; w:v) were prepared by sonicating the polymers in PBS at room temperature. Two parts DBCO-PEG and 1 part PEG-N3 were incubated on ice until mixing by pipetting and injected in to a modified syringe mold. The gels were then incubated at 37 ℃ in 1 mL of PBS with 10% FBS until testing. Unconstrained compression testing was performed with the samples immersed in PBS, a 0.1 ± 0.01 N preload, a displacement of 3 mm, and a 2 mm/s

compression velocity (Bose EnduraTEC 3100, Bose Corporation, Eden Prairie, Minnesota). GST was fluorescently labeled with Alexa Fluor 647 carboxylic acid, succinimidyl ester using the manufactures protocol, purified with a PD 10 column, lyophilized overnight, and re-suspended in sterile PBS. Aliquots were diluted 1:5 v/v in sterile PBS and quantified by fluorometry. The biological activity of rmGremlin1 delivered from the 12.5% w:v hydrogel was performed by incubating gels containing 100 ng rmGremlin1 or 4 nM HCl vehicle were incubated at 37 ℃ for 7 days in DMEM. Serum and 100 ng/mL rhBMP2 or vehicle were added to incubated medium and added to MG63 cells at 80% confluence. After 24 hours, cells were harvested and alkaline phosphatase activity was measured in cell layer lysates as previously described[222].

In Vivo Testing

All calvarial defects were created in post-natal day 21 male C57Bl/6J mice. Under 28X magnification a 1.5 mm by 2.5 mm defect was made by removing the posterior frontal suture using a piezoelectric instrument under constant irrigation with sterile PBS as previously described[211]. The defects were left empty or injected with 2 µL of the 12.5% hydrogel with the appropriate concentration of rmGremlin1 or GST-647. The ratios and mixing were performed as described above and the polymerization was verified after 20 seconds with a blunt 25G needle. All mice were randomized to both treatment group and post-operative time point with all analysis conducted by a blinded reviewer. Fluorescence release from mice containing either the hydrogel + GST-647 or PEG-N3 + GST-647 was assessed in anesthetized animals on post-operative

days 0, 2, 5, and 14 (IVIS Lumina II) (2 groups, n=5). Total fluorescent counts over the entire head and in a 1.5 mm by 2.5 mm were determined using the same display scales.

The effect of rmGremlin1 delivered from the hydrogel was assessed by creating the cranial defects described above. Defects were randomized to contain 2 uL of: empty defect, hydrogel only, hydrogel + 300 ng rmGremlin1, hydrogel + 500 ng rmGremlin1, and the un-polymerized PEG-N3 + 500 ng rmGremlin1 (5 groups, n=10). On post-op days 5 and 14, mice were euthanized and imaged with µCT with a voxel size of 31 um (VivaCT 40, Scanco Medical, Basel, Switzerland). The extent of bone regeneration in the defect was assessed using our advanced segmentation algorithm described and validated previously[174, 211]. Histological assessment was performed by haematoxylin and eosin staining of decalcified 7 um axial sections in the middle of the defect and analyzed by light microscopy.

All procedures were approved by the Georgia Tech Institutional Animal Care and Use Committee in accordance with the guide for the Care and Use of Laboratory Animals.

9.3 RESULTS

To generate a water-soluble non-fouling multivalent azide functionalized polymer, we synthesized PEG-N_3 (Figure 9-1a, **1**) from azide functionalized and non-functionalized PEG methacrylate monomers via reversible addition-fragmentation chain transfer (RAFT) polymerization, which affords tight control of azide functionality. The synthetic strategy presented here generates polymers with molecular weights (M_N) of approximately 25,000 Da and an average azide functionality per polymer of 13 (Figure A-10). The difunctionalized PEG-DBO (Figure 9-1a**, 2**) crosslinker was synthesized by reacting bis-amino-PEG with excess benzyle-2-nitro-carbonate functionalized DBCO. Dynamic time sweep rheological experiments were conducted on gels formed in the presence of serum to monitor network formation kinetics. Upon mixing, hydrogels containing 12.5% PEG-N3 and 4% DBCO-PEG underwent gelation in less than 30 seconds (i.e. G'= G") and were completely crosslinked in under 90 seconds (Figure 9-1d). This rapid polymerization seen with our hydrogel allows for rapid encapsulation and sequestration of co-delivered proteins before they can diffuse away from the site of administration.

One of the advantages of synthetic hydrogel is that the mechanical properties can be tailored to match varying tissue types. Varying the relative concentration of DBCO-PEG prior to polymerization allowed for the formation of

gels with highly customizable mechanical properties. To generate gels for in vitro evaluation, 0℃ PBS solutions containing either PEG-DBO (50%; w:v) or PEG-N_3 (12.5%, 6.25%, 4.85%, 3.13%, 1.56%; w:v) were mixed via pipette in a cylindrical form. As with most hydrogels, our gel displayed a highly non-linear behavior in response to compression[223]. A neo-Hookean hyperelastic model, assuming incompressibility and isotropy, was used to fit the non-linear stress-strain response of our gels (Figure A-11). he neo-Hookean coefficient (C_1) was calculated in terms of the stretch ratio (λ) and the engineering stress in the axial direction (σ_{11}^{eng}) : $\sigma_{11}^{eng} = 2C_1(\lambda - \frac{1}{\lambda^2})$. Unconstrained compression testing showed that increasing the concentration of DBCO-PEG resulted in an increase in the mechanical properties of the hydrogel (Figure 9-2a). At the lowest concentration, the neo-Hookean coefficient was less than 0.3. It increased to approximately 2 for the mid concentrations, and then finally peaked at over 5 for the 12.5% DBCO-PEG. For 12.5% gels, this corresponded to a Young's modulus of approximately 32 kPA. Hydrogels with concentrations less than 1.5% or greater than 12.5% did not polymerize (data not shown).

One of the most important aspects of delivery matrices is the ability to tailor the release kinetics of therapeutic factors based on the intended application. Varying the PEG-DBO concentration from 3.13-12.5% in the gel allows for substantial variation of protein release rate. To assess protein release kinetics, Alexa Flour tagged glutathione s-transferase (GST-647) was added to the DBCO-PEG solution, prior to polymerization. This protein has a molecular

weight similar to the Gremlin1 dimer and, for our purposes, did not have biological activity. To mimic the conditions at the treatment site, in vitro release kinetics were assessed by incubating hydrogels containing GST-647 for up to two weeks in sterile PBS containing 10% FBS at 37 ℃. Our results demonstrate that GST-647 release rate from the hydrogel is inversely proportional to the crosslink density of the gel (Figure 9-2b). For example, hydrogels formulated with less crosslinker had a more rapid and non-linear release of incorporated proteins with the 3.1% gel releasing nearly 75% of the protein after only 1 day. In contrast 12.5% gels had a nearly linear release profile out to 14 days. The compressive moduli of the hydrogels were retained for 3 days of incubation, before gradually decreasing for the remaining time points (Figure 9-2c), indicating degradation was occurring.

Gremlin1 is upregulated during cranial defect healing coincident with increased expression of Bmp2 and Bmp4, suggesting it plays a specific role in regulating bone formation at this time[211]. Gremlin is a traditional BMP inhibitor that has a high affinity for BMP2 and BMP4 and blocks their action by preventing these proteins from binding their receptors[124]. Thus we hypothesized that the controlled release of Gremlin1 at the defect site would prevent re-synostosis. To verify that Gremlin1 retains its biological activity following in situ polymerization and subsequent release, we assessed the ability of recombinant murine Gremlin-1 (rmGremlin1) released from the hydrogel to block the action of rhBMP2 in vitro. Delivery of rmGremlin1 in the hydrogel blocked the stimulatory effects of recombinant human BMP2 (rhBMP2) on osteoblastic differentiation of pre-

osteoblast MG63 cells, using alkaline phosphatase specific activity of the cultures as an outcome measure[224, 225]. Preliminary dose response experiments showed that 100 ng/mL rmGremlin1 was able to block the stimulatory effect of a 24h treatment with 100 ng/mL rhBMP2 on alkaline phosphatase activity (Figure A-12). Moreover, rmGremlin1 retained biological activity when delivered over time in the hydrogels. Hydrogels containing 100 ng/mL rmGremlin1 or the rmGremlin1 carrier (4mM HCl) were incubated in medium for 7 days to achieve release of incorporated proteins. MG63 cells treated with rhBMP2 alone or with rhBMP2 plus the hydrogel with carrier caused the expected increase in alkaline phosphatase compared to control cultures and cultures grown with the hydrogel alone. Addition of rmGremlin1 directly to the rhBMP-2 treated cultures or delivered in the polymerized hydrogel blocked the stimulatory effect of rhBMP2.

Given the ability of our hydrogel to encapsulate and release biologically active proteins, we assessed the ability of our hydrogel to localize the continuous release of proteins within cranial defects. Our cranial defect model involves removing the posterior frontal suture in a 21-day-old juvenile C57Bl/6 mouse[211]. Following creation of the defect, mice were randomized into two treatment groups. Mice received either an injection of a solution containing PEG-N3, GST-647, and PEG-DBCO (i.e, polymerized gel) or a solution containing PEG-N3 and GST-647 (i.e, unpolymerized gel). As the gels have a low viscosity prior to polymerization, visual inspection revealed that the solution was able to fill the entire defect before crosslinking into a stable gel. Our results demonstrate that the crosslinked hydrogel was able to retain the fluorescent signal in the

defect site and provide controlled release for up to 14 days (Figure 9-3a-d). In contrast, the fluorescent signal in animals containing the un-polymerized PEG-N3 showed that the protein diffused out of the defect by 2 days post-op and there was essentially no signal seen on days 5 and 14 post-op (Figure 9-3e-h). Quantification of the total fluorescent signal over the head of the animals showed no differences at 0 and 2 days, but there was less signal in the PEG-N3 mice for the later time points on post-op days 5 and 14 (Figure 9-3i). Additionally, the ratio between the signal contained within the defect to the total signal detected was approximately 1 for the mice treated with the hydrogel, indicating that essentially all of the fluorescent proteins were localized to the defect (Figure 9-3j). Defects containing just the un-polymerized PEG-N3 started out having a ratio of approximately 1, but this more than doubled at later time points as the proteins continued to diffuse away from the defect site.

To verify that the in situ polymerization of the hydrogel was not toxic to the surrounding tissues, mice were randomized to have an empty cranial defect or injected with the hydrogel containing PBS only. The extent of bone regeneration was imaged by micro-computed tomography (μCT) on post-operative days 2, 5, and 14 and then quantified using advanced image processing algorithms[174]. We previously developed and validated these algorithms in order to segment bones of varying and heterogeneous mineral content, which are seen in the healing of this pediatric specific model of re-synostosis. There was only a minor and transient reduction of bone within the defect in mice treated with the hydrogel (Figure A-13). By 14 days post-op, there were no differences in either the

average defect width or the volume of bone in the defect compared to empty defects. This indicates that our hydrogel has a space occupying effect early, but in vivo the gel is degraded or replaced by the regenerating bone. These results demonstrate that the hydrogel is able to provide a highly localized, controlled delivery of incorporated proteins to the defect site and that in the absence of any therapeutic protein the gel by itself does not have any long term impact on bone regeneration.

To address the clinical need seen in children who undergo surgical intervention for craniosynostosis, we used our click hydrogel to deliver the BMP inhibitor rmGremlin1 to delay the post-operative bone growth. Cranial defects were created over the posterior frontal suture in 21-day-old male mice and randomized to both the post-operative time point and treatment groups: empty defect, hydrogel + carrier (4 mM HCl), hydrogel + 300 ng rmGremlin1, hydrogel + 500 ng rmGremlin1, and un-polymerized PEG-N3 + 500 ng rmGremlin1. Mice were euthanized and imaged with μCT on post-op days 5 and 14. Empty defects contained a thick trabeculated structure by 14 days post-op, which was visible on both the μCT and histological images. This defect was nearly completely bridged as seen with the 3D rendering, similar to what has been observed previously (Figure 9-4a-c)[211]. The defects containing the hydrogel exhibited the same thick trabeculated structure, but complete bridging was not evident along the midline (Figure 9-4d-f). The 3D rendering showed that this small gap occurred in only a very small region and the majority of the defect was healed (Figure 9-4d). Histology of the site showed disorganized fibrous connective tissue between the

bones of the defect (Figure 9-4f). Inclusion of rmGremlin1 in the hydrogel resulted in a dose dependent decrease in the amount of bone present in the defect (Figure 9-4g-l). None of the animals in these groups displayed bridging of the defect and histology showed more fibrous connective tissue was present (Figure 9-4i,l). Additionally, the 2D μCT images showed a lack of the thick trabecular structure noted above (Figure 9-4h,k). Defects containing the un-polymerized PEG-N3 also had nearly completed bridging of the defect and contained the thick trabecular structure observed in the empty defects (Figure 9-4m-o), indicating that the highest dose of rmGremlin1 did not have an effect on defect healing in the absence of a cross-linked gel.

These observations were supported by quantitative analysis of the □CT images using our advanced segmentation algorithms described above. On post-op day 5, there was a decrease in the width of untreated defects and a slight decrease in the distance between bones for the hydrogel + carrier group. However for both of the groups containing rmGremlin1, there was no decrease from the initial 1.5 mm wide defect (Figure 9-5a). At 14 days post-op, the distance between bones in the hydrogel + carrier and hydrogel + 300 ng rhGremlin1 treatment groups decreased, but there was no change in defect width in sites treated with the hydrogel + 500 ng rmGremlin1, indicating that the effects of rmGremlin1 were dose dependent. As seen previously, the empty defects were bridged early as no changes in distance between bones were observed between 5 and 14 days post-op[211]. Histomorphometric analysis of coronal sections cut through the center of the defect showed significantly wider defects at

14 days post-op in the hydrogel + 500 ng rhGremlin1, but other differences were not present as the variability associated with the non-serial histomorphometry was greater as this only examined one section of the middle of the defect (Figure A-14).

Cross-linking of the gel was necessary to retain rmGremlin1 at the site. PEG-N3 + 500ng rmGremlin1 had no impact on bone formation, as there were no differences at either time point between this group and the empty defect (Figure 9-5a). There were no differences among any of the groups on post-operative day 5 in the defect thickness, defect mineral content, and defect bone volume, as this time point is before the defect undergoes the mineralization that is part of normal defect healing (Figure 9-5b-d). However, defect mineral content and bone volume were decreased in a dose-dependent manner on day 14 when rmGremlin1 was delivered in the crosslinked hydrogel. Both parameters increased on day 14 in the empty defects, in defects treated with hydrogel + carrier, and in defects treated with PEG-N3 + 500 ng rmGremlin1 (Figure 9-5c-d). Additionally, there were no changes in any of the parameters between days 5 and 14 in sites treated with hydrogel + 500 ng rmGremlin1 indicating that no significant bone growth had occurred.

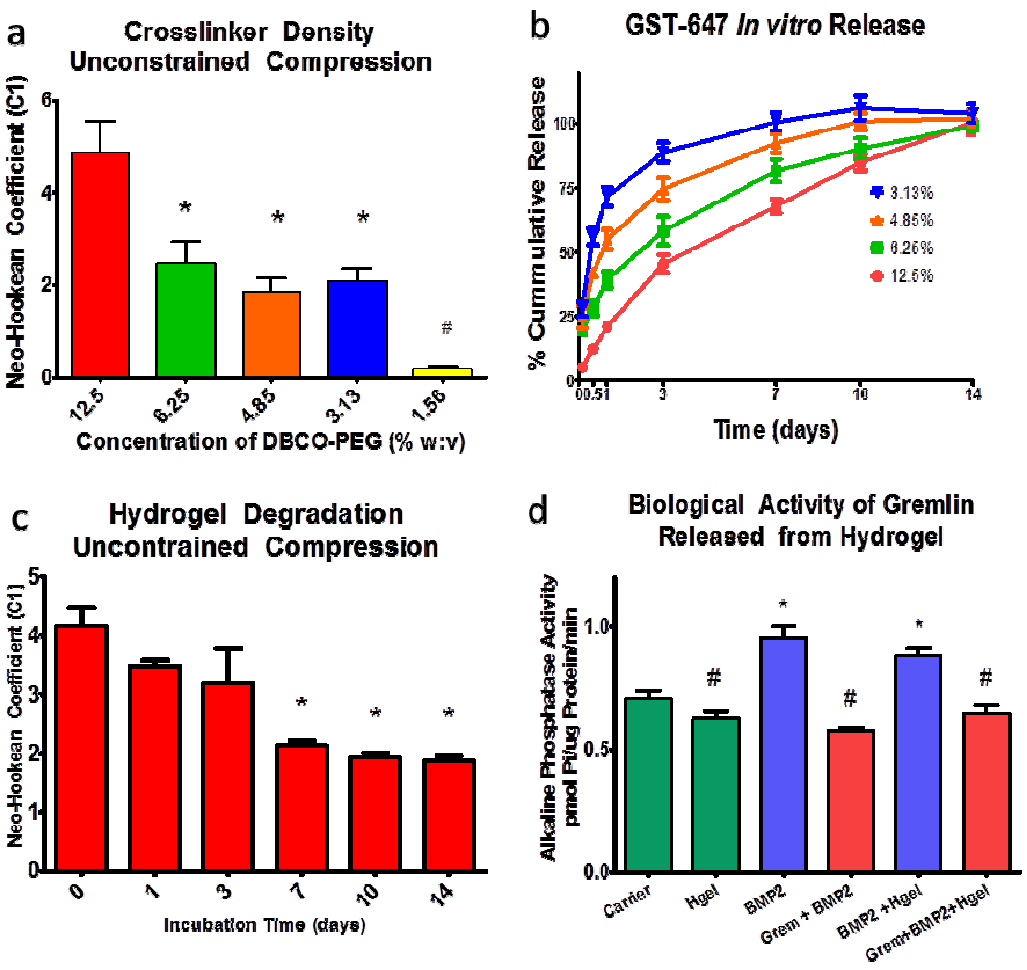

Figure 9-2**:** In vitro testing of hydrogel. Unconstrained compression testing of hydrogel using a Neo-Hookean hyperelastic model showed that increasing the concentration of the DBCO-PEG resulted in an increase in the Neo-Hookean coefficient (C1) (a) *=p<0.05 vs 12.5%. In vitro release of GST-647 from hydrogels with increasing concentrations of DBCO-PEG resulted in a more prolonged and linear release profile with the 12.5% gel having controlled release out to 14 days (b). Degradation of the 12.5% gel assessed by unconstrained compression had a decrease in the Neo-Hookean Coefficient after day 7 (c) *=p<0.05 vs day 0. The biological activity of rmGremlin1 was retained after release following polymerization in the hydrogel as assessed by blocking the BMP-2 mediated increase in alkaline phosphatase specific activity (d) *=p<0.05 vs carrier, #= p<0.05 vs BMP2.

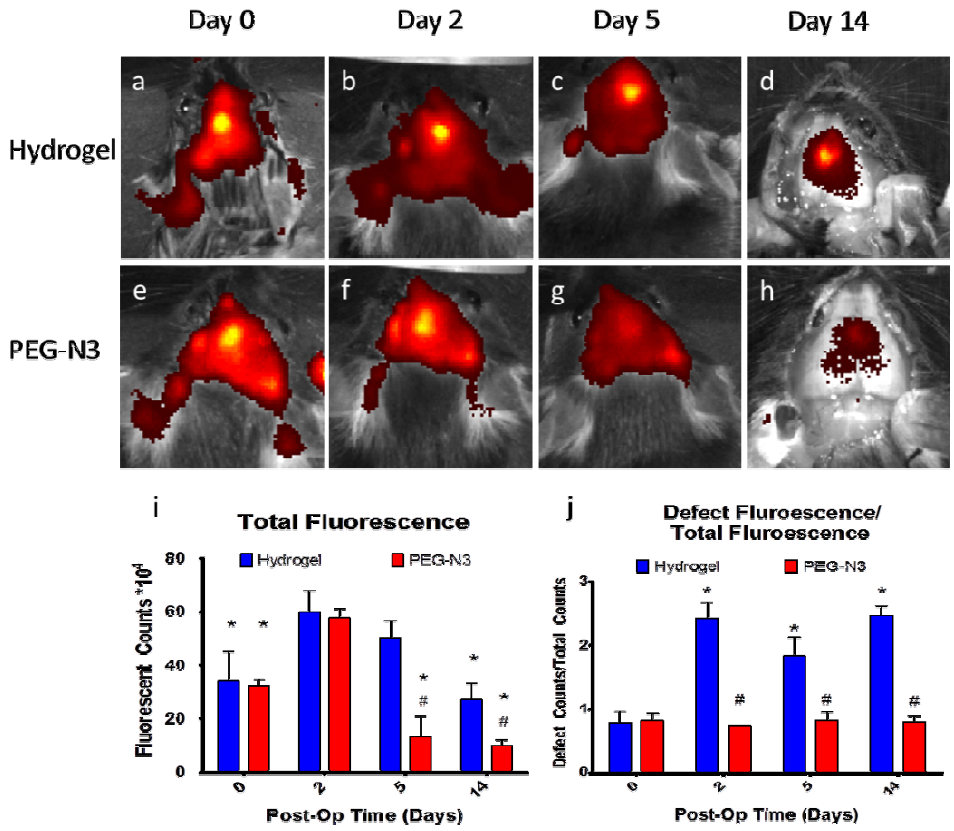

Figure 9-3: In vivo fluorescence release of GST-647 kinetics following in situ polymerization of hydrogel. Fluorescent images of mice with GST-647 in crosslinked hydrogel showed a controlled and localized signal over the defect up to 14 days after administration (a-d). In contrast, the signal of the group containing the un-polymerized PEG-N3 (e-h) showed relatively low levels of fluorescence after 5 and 14 days, demonstrating that, in the absence of crosslinking, the protein rapidly diffused out of the defect. Quantification of the total fluorescent signal over the entire head shows that 2 days after surgery there is more signal in the hydrogel gel group as compared to the PEG-N3 group and there is only a slight decrease in the total fluorescent signal (i) *=$p<0.05$ vs day 2, #=$p<0.01$ vs hydrogel. Comparing the ratio between the fluorescent signal in the defect to the total signal showed that the hydrogel groups had a higher fluorescence intensity 2 to 14 days after surgery, indicating that the hydrogel orchestrated a controlled release of incorporated protein (j) *=$p<0.05$ vs day 0, #=$p<0.05$ vs hydrogel.

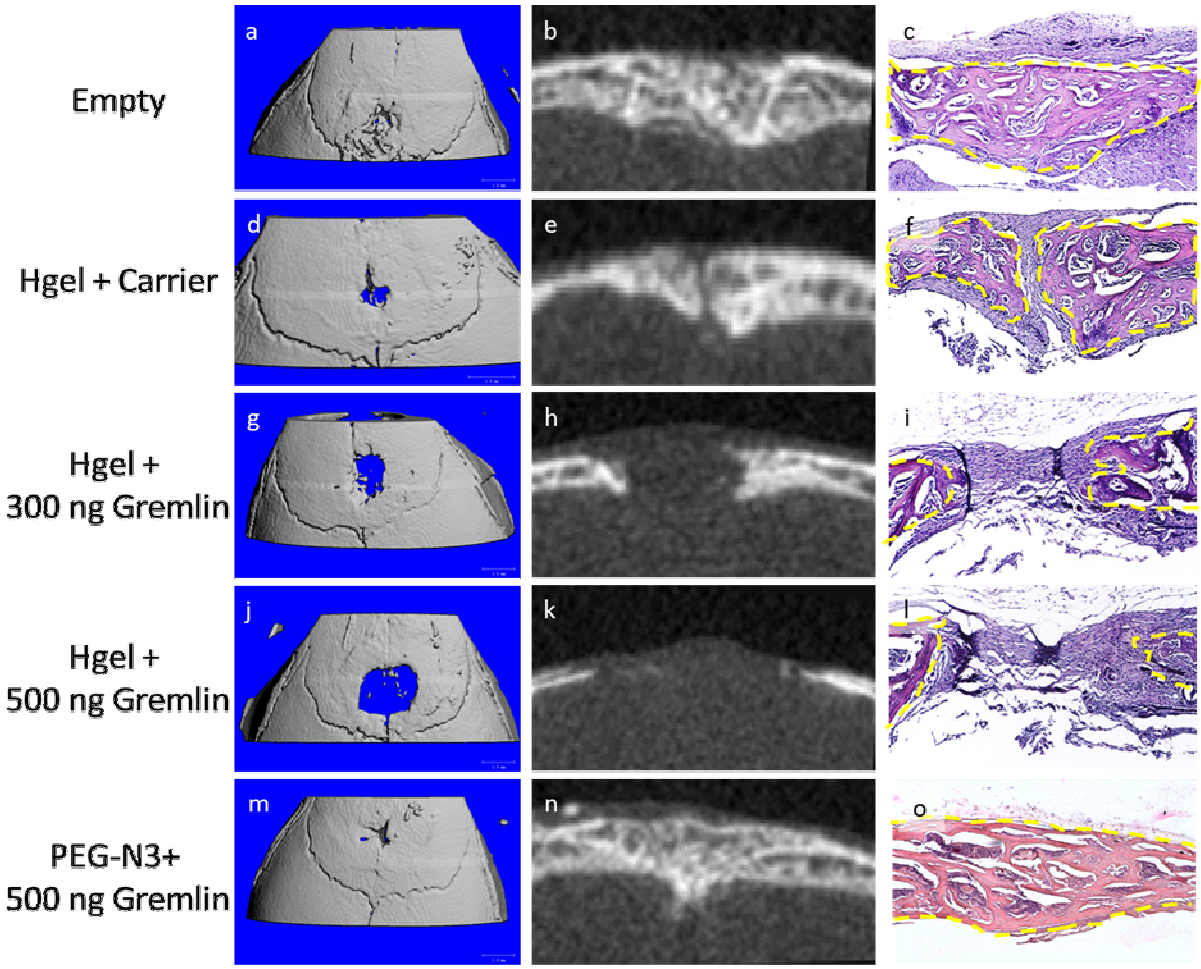

Figure 9-4: Representative µCT and histology from 14 day post-op samples. Empty defects were nearly completely healed and bone bridging the defect (a-c). Defects with the hydrogel had very small regions that remained open, but there was thick trabecular bone present (d-f). Defects containing the hydrogel with rmGremlin1 showed a dose dependent decrease in the amount of bone present (g-l). The defects containing the low 300 ng dose showed no bone bridging of the defect (g-i), but the ends of the bone were thicker than the 500 ng group (j-l). The defects containing 500 ng rmGremlin1 in the un-polymerized PEG-N3 showed complete bridging and the same thick trabecular structure that was seen in the empty defect (m-o).

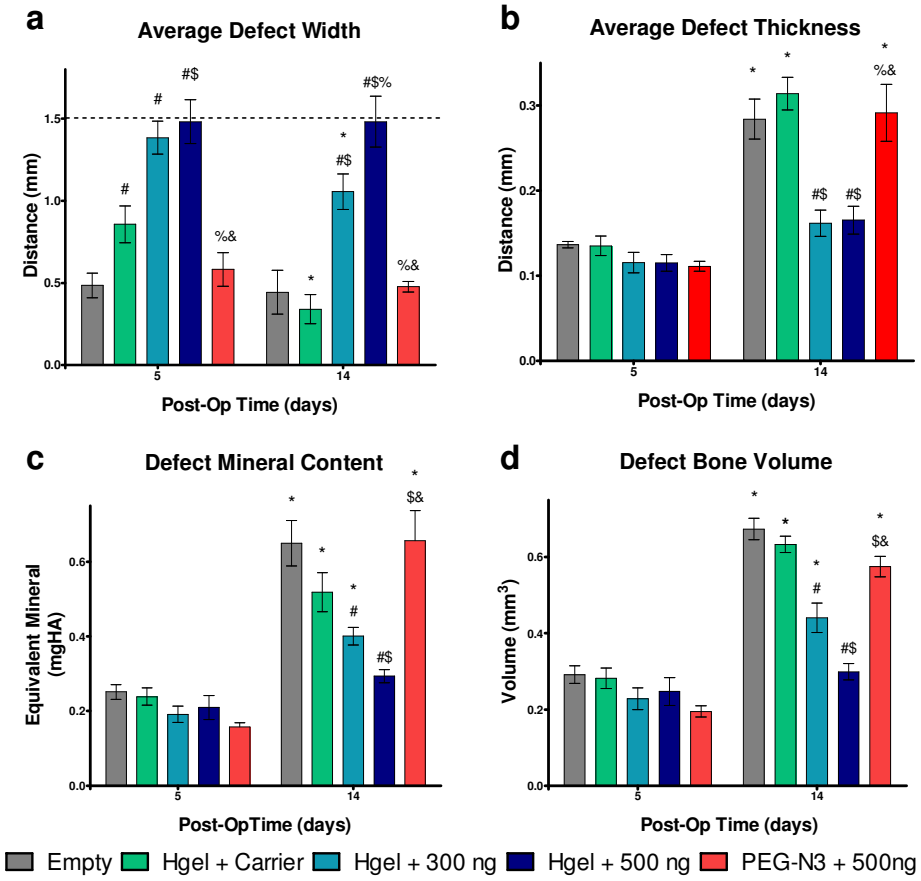

Figure 9-5: Quantification of bone regeneration in defect by µCT imaging algorithm. Defects were left empty (Empty) on injected with hydrogel with 4 nM HCl carrier (Hgel + Carrier), hydrogel with 300 ng rmGremlin1 (Hgel + 300 ng), hydrogel with 500 ng rmGremlin1 (Hgel + 500 ng), or un-polymerized PEG-N3 with 500 ng rmGremlin1 (PEG-N3 + 500 ng). The average defect width had a dose dependent decrease on post-op day 14 and there was no change from the initial 1.5 mm defect (dashed line) for the Hgel + 500 ng group (a). The average defect thickness increased for all groups except the Hgel+300 ng and Hgel + 500 ng groups (b). Both the defect mineral content and bone volume showed a dose dependent decrease for the groups containing rmGremlin1 and there was no change in the Hgel + 500 ng groups (d). There were no differences between the Empty and PEG-N3 + 500 ng groups in any of the measures at either time point. $P<0.05$ vs. # = empty, $ = Hgel + Carrier, % = Hgel + 300 ng, & = Hgel + 500 ng, * = 5 days.

9.4 DISCUSSION

Our results clearly demonstrate that our click-hydrogel permits rapid in situ polymerization for controlled delivery of therapeutic proteins. Polymerization of PEG-N3 and the DBCO-PEG to form hydrogels resulted in very rapid crosslinking that occurred spontaneously without the need for any additional initiators. The polymerization for all applications resulted in a fully cross-linked hydrogel in less than 90 seconds. To our knowledge this is the most rapidly crosslinking hydrogel using Cu-free click chemistry reported, occurring almost two orders of magnitude faster than previously described hydrogels[162]. This rapid spontaneous polymerization has the potential to deliver incorporated factors to any site that can be reachable with a needle. Furthermore, the incorporated proteins retained their biological activity following in situ polymerization both in vitro and in vivo.

To our knowledge this is the first time rmGremlin1 has been delivered to delay the rapid bone growth seen in pediatric patients following suturectomy. Not only does this have tremendous potential to delay the post-operative re-synostosis frequently seen in cases of craniosynostosis, but it also has the potential to dramatically change the surgical management of this disease. This therapy could allow for the endoscopic removal of the fused suture and in effect re-create the function of a normal suture. This minimally invasive procedure has

been largely abandoned clinically as the results from the surgery were temporary. Outside of craniofacial reconstruction, delaying the rate of bone growth has direct applications in treating fractures of the growth plate and heterotopic ossification. In addition to delivering BMP inhibitors, the plug and play architecture of the PEG-N3 RAFT polymerization also allows the hydrogel to be used for other regenerative applications that may necessitate cell adhesion peptides, cleavable linkages, or covalent attachment of therapeutic small molecules.

CHAPTER 10 CONCLUSION AND FUTURE PERSPECTIVES

This work has established a novel therapy to delay the post-operative re-synostosis in a pediatric cranial defect model. We have developed advanced image processing algorithms to segment the bones of the cranial sutures and regenerating bone in the defect. Using this algorithm we have determined the most comprehensive analysis of the temporal changes in murine suture fusion. Based on this time course we developed a murine model of re-synostosis that is both age and location specific. Real-time PCR analysis of genes associated with the healing of this defect showed an increase in expression of chondrocyte differentiation genes, followed by an increase in BMP2 and Bmp4, and then an increase in markers of osteoblast differentiation. The click hydrogel was able to provide a controlled delivery of incorporated proteins out to two weeks following an in situ polymerization. Using this hydrogel to deliver the BMP inhibitor Gremlin, we were able to achieve a dose dependent decrease in the bone healing.

The image processing algorithms developed as a part the work in Aim 1 provide an accurate method to segment the complex and discontinuous cranial

sutures. This algorithm overcomes the substantial limitations with traditional histology and segmentation algorithms. The biggest benefit of our algorithm is that it can analyze the entire suture and does not rely on generalizing based on a limited number of sections. This has the potential to significantly improve the analysis of both the developmental and regenerative studies involving the cranial sutures.

The most direct application of the algorithm is in the diagnosis of craniosynostosis and re-synostosis in humans. Children have a more spherical skull than rodents, which makes the development of the 3D reconstructions even more beneficial. The segmentation and reconstruction algorithms have already been implemented for the analysis of the human cranial sutures and we are currently performing a clinical trial to improve the diagnosis of craniosynostosis. Additionally, we have developed a modification to the algorithm to segment the intracranial volume to better understand the asymmetry of the cranial vault in cases of craniosynostosis.

In addition to craniofacial applications, the algorithm is well suited to analyze other challenging imaging problems. In particular the algorithm was designed to address the segmentation of complex, varying, and discontinuously mineralized structures. We have developed other implementations of the algorithm to asses bone healing in a segmental long bone defect, a metaphyseal long bone defect, long bone growth plates, and the sphenooccipital synchondrosis for basic science applications. In the orthopedic field the most direct applications of the algorithm would involve the analysis of non-union

fractures and heterotopic ossification. Both of these pathologies frequently result in the presence of poorly and heterogeneously mineralized bone. While there would have to be substantial work performed in the initialization phase of the algorithm, the snake algorithm is particularly well suited for this application.

We are also currently developing the 3D reconstruction and snake algorithms for the analysis of pediatric cases of scoliosis. One of the challenges in performing many spine surgeries is the accurate placement of pedicle screws that are used for internal fixation. This is further complicated in patients with scoliosis who frequently have abnormal pedicles. The quantification and identification of these abnormalities is further complicated by the abnormal curvature of the spine that is present in children with scoliosis. Our reconstruction algorithm can be used to first obtain accurate images of the pedicles which can be followed by the snake algorithm to segment the pedicles. This not only has benefit for pre-operative planning, but also could be used with intraoperative navigation to assist with the placement of the pedicle screws.

To our knowledge the time course we developed for the normal fusion of the posterior frontal suture is the most complete study to date. To our knowledge this is the first report of the biphasic process that is responsible for suture fusion. One of the biggest advantages of using μCT for examining the fusion of the cranial sutures is that it allows for the concomitant assessment of the mineral in the skull. All research examining the fusion of the sutures up to this point has relied on de-calcified histology, which as a result of the processing is unable to identify the mineralized tissue. The discontinuity that has recently been

associated with the fusion of the cranial sutures limits the accuracy of traditional analysis methods. As a result, there have been widely differing reports regarding the timing of the suture and the factors involved with driving cranial suture fusion. While histology can provide detailed morphological information, only serial histomorphometic analysis can account for the discontinuities seen with the fusion of the cranial sutures. This methodology is prohibitively expensive and time consuming for high through put studies that are frequently performed with examining the development of the cranial sutures.

We identified the presence of cartilage associated genes and staining of glycosaminoglycans on histology. The presence of this cartilage tissue has been seen previously in the context of normal and pathologic suture fusion. While there is the presence of cartilage like tissue transiently, it is still not clear whether the posterior frontal suture fuses through endochondral or intramembranous ossification. In traditional long bone development, you seen an increase in expression of early chondrocyte transcription factors (Sox9), then the extracellular matrix proteins (Col II, Comp, Aggrecan), and then markers of chondrocyte hypertrophy (Col XII). All of the genes associated with cartilage development showed a large increase on the same day at the onset of suture fusion. The most likely explanation for these differences is that multiple stages of the suture fusion are occurring simultaneously. As a result, the fusion of the bones and differences in associated pathways are dependent on the location of the section that is analyzed.

The focus of this research was to understand the genes associated with the early fusion of the suture, but there is benefit for future work focused on the later mineralization phase of the suture development. Interestingly, the onset of mineralization of the cranial sutures corresponded with the weaning of the mice in post-natal day 21. There are obvious hormonal changes associated with the cessation of maternal feeding that may impact the development of the sutures. Also, this is the first point that the pups are completely reliant on hard food for nutrition. While there is little research examining how mechanics influence the development of the cranial sutures, it is likely that a difference in the cyclical stress associated with eating can play a role in the fusion of the cranial sutures.

The results from examining mice engineered with the mutation seen in Saethre-Chotzen syndrome show significant differences in both the regeneration and developmental of the sutures. It was clear that the coronal suture not only was more fused, but never had the characteristic overlap that is seen with normal coronal suture fusion. This work suggests that the abnormality seen was the result of the suture developing abnormally, as opposed to the current theory that the sutures fuse prematurely.

Interestingly, the Twist mice were unable to bridge both the midline sutures and defects. The ability for one suture to induce an abnormality in other sutures has not been well reported in the craniofacial literature. Further work focused on examining the causes of these abnormalities has the promise to provide additional insights into the mechanisms responsible for the suture fusion. Traditionally it is believed that this premature fusion of the coronal suture results

from an abnormality in the underlying dura. Additionally, the fusion of the coronal suture could stress shield both the normal suture and the defect, which in turn results in the abnormalities seen here. In the murine skull, the masseter muscles originate on the edges of the skull just lateral to the posterior frontal suture. It is believed that as the animal chews there is considerable stress applied to this suture and that this is impart responsible for the differences seen in murine suture fusion. There has been limited work focused on understanding the mechanical regulation of the cranial sutures, but there is evidence that cyclical stress does impact the fusion of the cranial sutures.

The development of a pediatric murine model of re-synostosis has the potential to provide valuable insights into the mechanisms responsible for re-synostosis. To our knowledge the model system described previously in Chapter 6 is the first mouse cranial defect to undergo rapid re-synostosis. Our results demonstrate that this healing is both age and location specific, which explains the why other murine cranial defects do not display rapid defect healing in the absence of any therapeutic intervention. While the craniosynostosis rabbits do display re-synostosis of defects created over the coronal suture, they are not suitable for high throughput studies and are not available to other researchers.

Prior to the development of our animal model there has been little prior work on examining the mechanisms responsible for re-synostosis. Our results indicate that immediately following the onset of the defect bridging there is an increase in the expression of cartilage associated genes. This began with an increase in the early chondrocyte transcription factor Sox9, then an increase in

the cartilage extracellular matrix genes Col II and Comp, and finally an increase in the marker of chondrocyte hypertrophy Col XII. Between this increase in cartilage associated genes and the later mineralization on day 14, there was an increase in the expression of Bmp2 and Bmp4. Even though there has been relatively little research on the members of the BMP family in the craniofacial literature, this provides evidence that BMPs are responsible for the transition from a cartilage like precursor to mineralized tissue. The increase in bone mineral content seen with μCT was also associated with an increase in the late markers of osteoblast differentiation Ocn and Runx2. This was also seen with the normal suture development and further supports the use of μCT to examine both regenerative and developmental changes in the skull vault. Even through there a great deal of evidence suggesting that Noggin is involved with regulating the fusion of the normal cranial suture and has potentially delayed post-operative re-synostosis, there was not an increase in expression until after the defect had fully mineralized. There was however an increase in Gremlin associated with the increase in Bmp2 and Bmp4 prior to defect mineralization. Gremlin was selected as the ideal target molecule based on its expression profile and its target molecules, Bmp2 and Bmp4.

Our click hydrogel was able to provide tunable controlled delivery of incorporated proteins to successfully delay the post-operative bone growth seen in our murine re-synostosis model. By varying the concentration of the cross linker molecule we were able to tune both the mechanical properties and the release kinetics of the hydrogel. At the highest concentration we were able to

achieve a nearly linear release out to two weeks in vitro. This same controlled release was also seen in our cranial defect model after an in situ polymerization of the hydrogel.

Using the hydrogel we were able to provide a controlled delivery of the BMP inhibitor Gremlin to delay the post-operative bone growth in our cranial defect model. Furthermore, there was a dose dependent decrease in the amount of bone in the defect and at the highest concentration there was no bone growth observed. This combination of inhibitor with the hydrogel has the potential to drastically improve the surgical management of children with craniosynostosis. The most direct clinical application for the hydrogel therapy would be to delay or prevent the rapid re-synostosis seen clinically. The fact that gel undergoes rapid self-polymerization makes is possible for surgeons to inject the gel as a liquid and then have it rapidly cross link in the cranial vault. The gel would then provide a controlled release of the incorporated inhibitor with the goal of delaying the post-operative re-synostosis.

While there is essentially no opportunity to delay the initial pathologic suture fusion, in injectable therapy that controls the post-operative re-synostosis could dramatically reduce the morbidity associated with cranial vault reconstruction. Instead of having to remove the entire cranial vault, surgeons could potentially remove just the fused suture through a limited incision and inject the hydrogel to delay the bone growth. This would in effect re-create a functional suture to allow for a more normal cranial vault expansion. The hydrogel could eliminate the internal fixation that is currently used in the reconstruction and allow

for earlier intervention. Operating on the children at a young age could also reduce the risk of permanent neurological problems that currently result from a delay in treatment.

Besides the obvious uses for the treatment of craniosynostosis, the hydrogel with BMP inhibitors also has other applications in treating orthopedic conditions. While the most of the challenges in the orthopedic community are focused on regenerating bone, there are several conditions where there is a need to delay bone growth. The most obvious of these conditions in heterotopic ossification that is seen commonly in individuals who sustain head or blast injuries. In this condition, bone forms in regions that bone is typically not found. The click hydrogel could be injected for in situ polymerization and provide a controlled delivery of therapeutic proteins. This could also be of tremendous benefit for children who sustain fractures that extend through an open physis that frequently result in premature fusion of the growth plates.

In addition to delivering inhibitory factors, the hydrogel could also be used for the regeneration of bone defects. The currently used rhBMP2 has a molecular weight that is similar to both Gremlin1 and the fluorescent protein. With the current formulation the hydrogel could serve as an injectable delivery vehicle to provide controlled release of the hydrogel. Additionally, the chemistry of the hydrogel could be enhanced for regenerative therapies. Currently the hydrogel is not designed to degrade rapidly or to allow for cellular in growth. For our application of re-synostosis our primary concern was to provide controlled delivery of the inhibitors and not promote tissue in growth. The degradation rate

of the hydrogel could be accelerated by using gels with a lower cross linking density or incorporating cleavable sequences. Cellular ingrowth could be enhanced through the introduction of cleavable sequences and also through the covalent attachment of cell adhesion peptides. Additionally, the rapid and non-toxic polymerization that occurs with the hydrogel makes it an ideal candidate for as delivery system for encapsulated cells.

The hydrogel also has the potential to provide delivery for other therapeutic molecules besides whole proteins. There has been a growing interest to use antibodies to alter the rate of bone growth. The crosslinking concentration of the hydrogel could be easily decreased to provide a controlled release of the much larger molecules. One of the limitations to many hydrogel systems is the inability to provide a controlled delivery of small molecules. The highly customizable PEG macromere makes it possible to covalently attach proteins, peptides, and other small molecules to the gel. This would extend the release profile beyond what is possible with simple diffusion and if necessary cleavable linkages could be used to further refine the release kinetics.

The research and new technologies presented in this thesis were able to develop clinically relevant model systems and therapies to prevent postoperative bone growth. The image reconstruction and segmentation algorithms developed provide an accurate tool for both the analysis of cranial structures and also other heterogeneous tissues. Our hydrogel therapy has tremendous potential for the treatment of craniosynostosis and other bone pathologies.

APPENDIX A

Chapter 3 Supplemental Figures

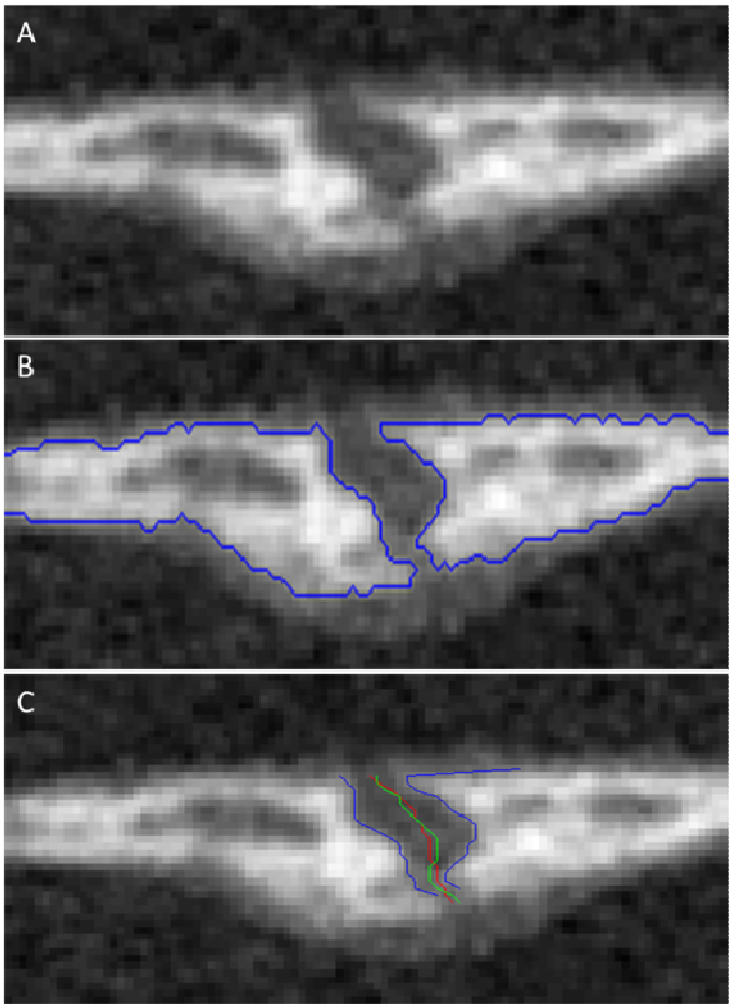

Figure A- 1: Initialization phase for an open suture. (a) A global threshold was applied to the original image to detect the (b) boundary of the bones (blue line). (c) The medial boundary of this boundary was found (blue line) and used to find the midpoint of the suture (red line). To minimize errors resulting from gaps in the medial boundaries, a polynomial was fit through these center points and used to separate the images (green line).

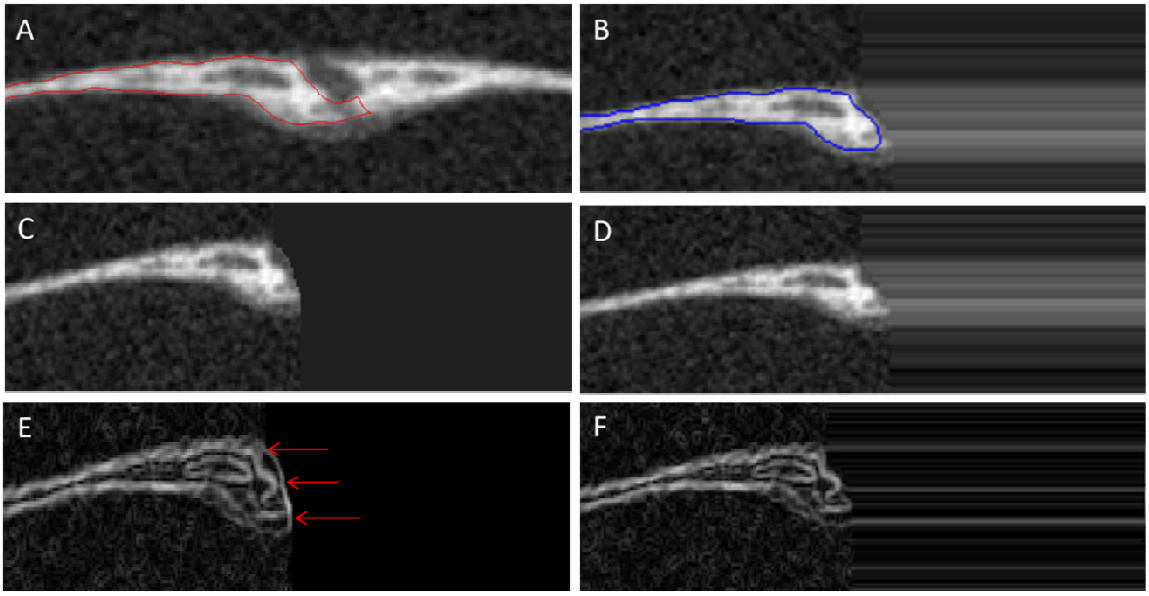

Figure A- 2: Image separation for images where the suture is open. (a) If the images are not separated prior to running the snake can "jump" to the adjacent bone resulting in an error in the final segmentation boundary, but is corrected by (b) separating the images with horizontal replication. (c) If the bones are just separated without any correction this introduces an artifact (red arrows) on the (e) gradient image used for the snake that can cause segmentation errors. (d) To correct for this, the algorithm replicated the midpoint pixel horizontally that eliminates this artifact on the (f) gradient image, resulting in a (b) correct segmentation border. All images shown originated from the identical image.

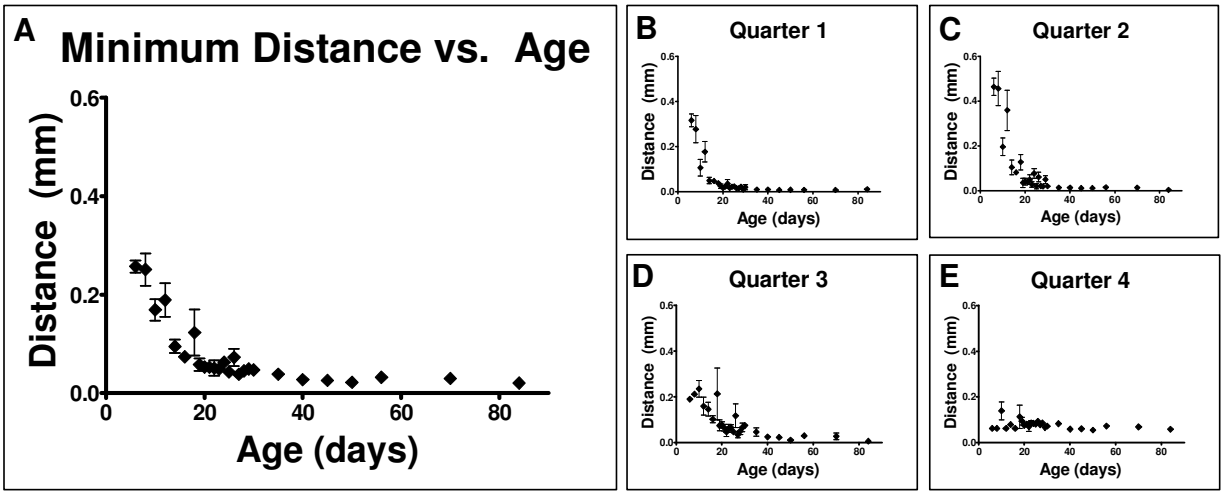

Figure A- 3: Minimum distance between the bones of the posterior frontal suture. The entire suture (A) had a minimum distance of 0.25 mm on day 6, began fusing on day 12, and then reached a plateau of 0.05 mm beginning on day 20. The anterior most quarter (B) of the suture had the first and fastest decrease in distance, followed by the second (C) and third quarter (D). There were no changes seen in the distances for the posterior most fourth quarter (E).

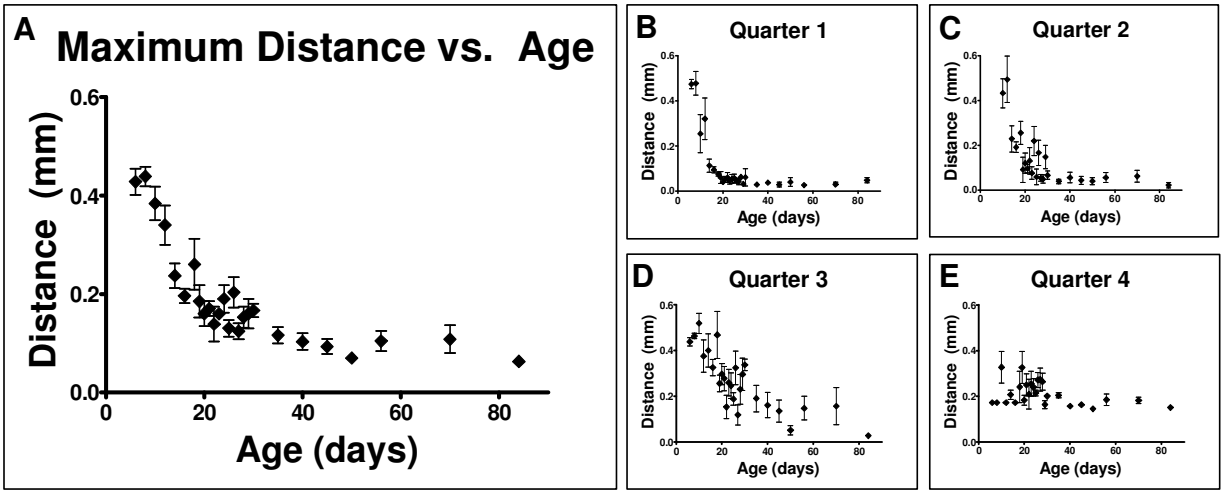

Figure A- 4: Maximum distance between the bones of the posterior frontal suture. The entire suture (A) had a maximum distance of 0.43 mm on day 6, began fusing on day 12, and then reached a plateau of 0.25 mm beginning on day 20. The anterior most quarter (B) of the suture had the first and fastest decrease in distance, followed by the second (C) and third quarter (D). There were no changes seen in the distances for the posterior most fourth quarter (E).

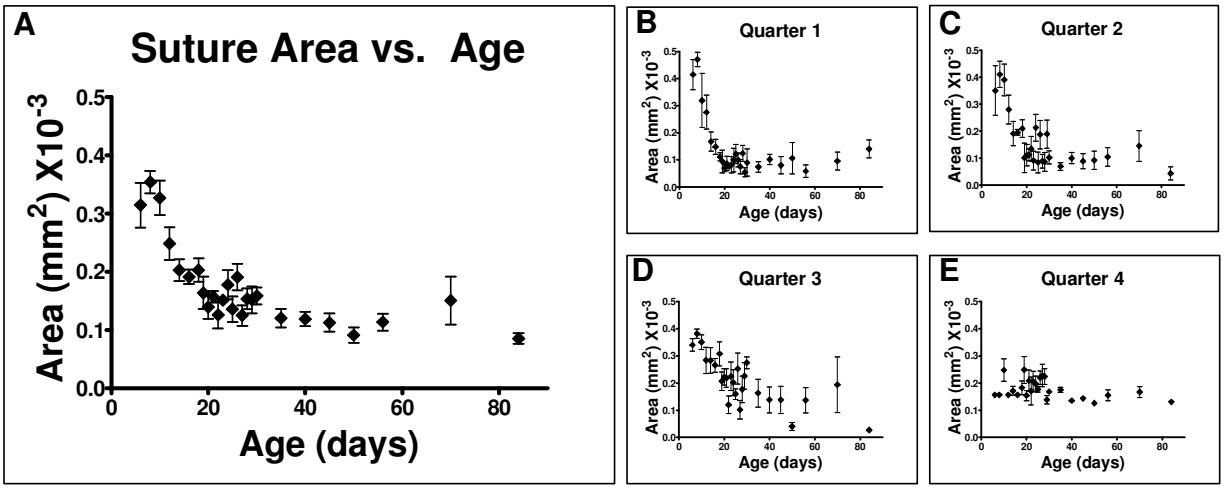

Figure A- 5: Area between the bones of the posterior frontal suture. The entire suture (A) had as area of 0.31*10-3 mm2 on day 6, began decreasing on day 12, and then reached a plateau of 0.13*10-3 mm2 beginning on day 20. The anterior most quarter (B) of the suture had the first and fastest decrease in area, followed by the second (C) and third quarter (D). There were no changes seen in the areas for the posterior most fourth quarter (E).

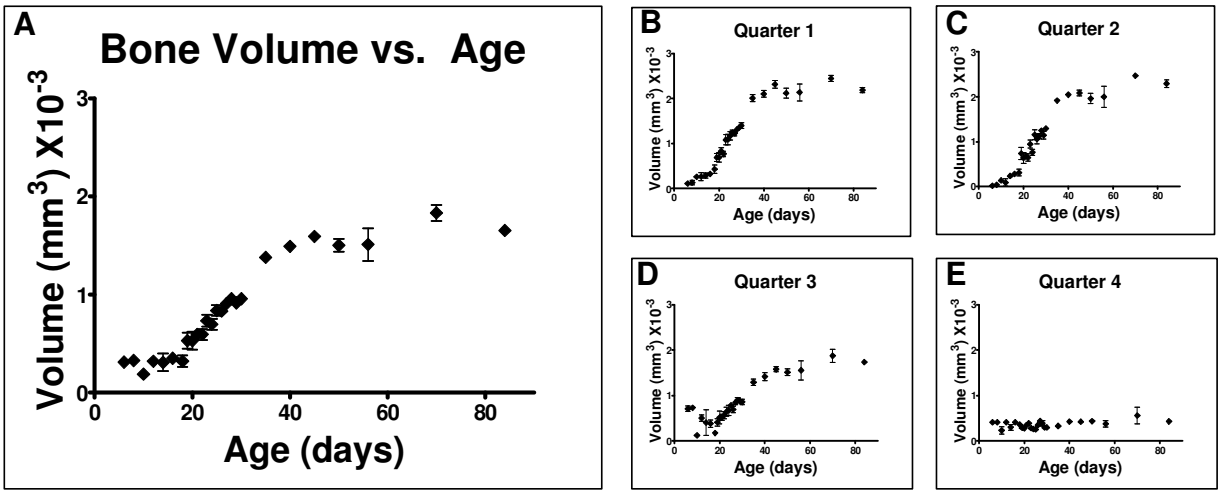

Figure A- 6: Bone Volume in a 1 mm by 1 mm region of the posterior frontal suture. The volume of bone in the entire suture (A) remained relatively constant until day 20 and then reached a plateau beginning on day 40. The anterior most quarter (B) of the suture had the first and fastest increase in volume, followed by the second (C) and third quarter (D). There were no changes seen in the bone volume for the posterior most fourth quarter (E).

Chapter 5 Supplemental Figures

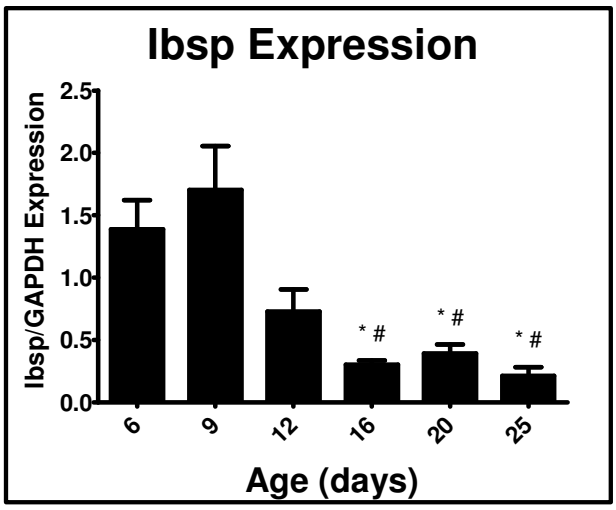

Figure A- 7: Expression of Ibsp in bone from the posterior frontal suture. $p<0.05$ vs *=6d, #=9d.

Table A- 1: Genes symbols for genes analyzed in PCR array

Ahsg	Akp2	Ambn	Anxa5	Bgn	Bmp1	Bmp2	Bmp3	Bmp4	Bmp5	Bmp6	Bmpr1a
Bmpr1b	Cd36	Cdh11	Col10a1	Col11a1	Col12a1	Col14a1	Col1a1	Col1a2	Col2a1	Col3a1	Col4a1
Col4a2	Col5a1	Col6a1	Col6a2	Col7a1	Comp	Csf2	Csf3	Ctsk	Dmp1	Egf	Enam
Fgf1	Fgf2	Fgf3	Fgfr1	Fgfr2	Flt1	Fn1	Gdf10	Icam1	Igf1	Igf1r	Itga2
Itga2b	Itga3	Itgam	Itgav	Itgb1	Mmp10	Mmp2	Mmp8	Mmp9	Msx1	Nfkb1	Pdgfa
Phex	Runx2	Scarb1	Serpinh1	Smad1	Smad2	Smad3	Smad4	Sost	Sox9	Tfip11	Tgfb1
Tgfb3	Tgfb4	Tgfbr1	Tgfbr2	Tgfbr3	Tnf	Tuft1	Twist1	Vcam1	Vdr	Vegfa	Vegfb
Gusb	Hprt1	Gapdh									

Table A- 2: Primer sequences used for real-time PCR confirmation

Gene	Forward	Reverse
Acan	GCTCTGCCTCTGCCTCTG	AATTCCACTGACATCATCTACTCC
ColIa1	GAGGTATGCTTGATCTGTATC	CAGTCCAGTTCTTCATTGC
ColXa1	TTCTGCTGCTAATGTTCTTGAC	CCTTTACTCTTTATGGCGTATGG
ColXII	CTCTGTGAATATCGTGGCTCTC	AGGCTGTTGGTCGTCTCC
Comp	GCGACGACGACATAGATG	GTCTTGGTCACTATCACAGG
Ibsp	TTAGCGGCACTCCAACTG	CTTCCTCTTCTTCTTCTTCTTCC
Sox9	CCACCAGTATCAGCGAGGAG	CCAAACAGGCAGGGAGATTC
Tgfb1	ATTCCTGGCGTTACCTTGG	CCTGTATTCCGTCTCCTTGG
Tgfb2	GAGCGGAGCGACGAGGAG	TGTAGAAAGTGGGCGGGATGG
Tgfb3	AAAGTGTGGGTTGGTTAGG	CTCGCTATCCGTTCTCTAC
Tgfbr1	AGGAGAAGCAGCAACTAATAGC	CAGCAGCAGTGAGAAGACC
Tgfbr2	AATAAGCAGAGGAGGTGGTTC	GGGTGGGTGTGAGTAATGG
Tgfbr3	GTGGTAAGCGAAGGGATTATTAGC	CCGACTCTGGAAGCATAGGAC
Col2a1	Pre Designed	
Dmp1		

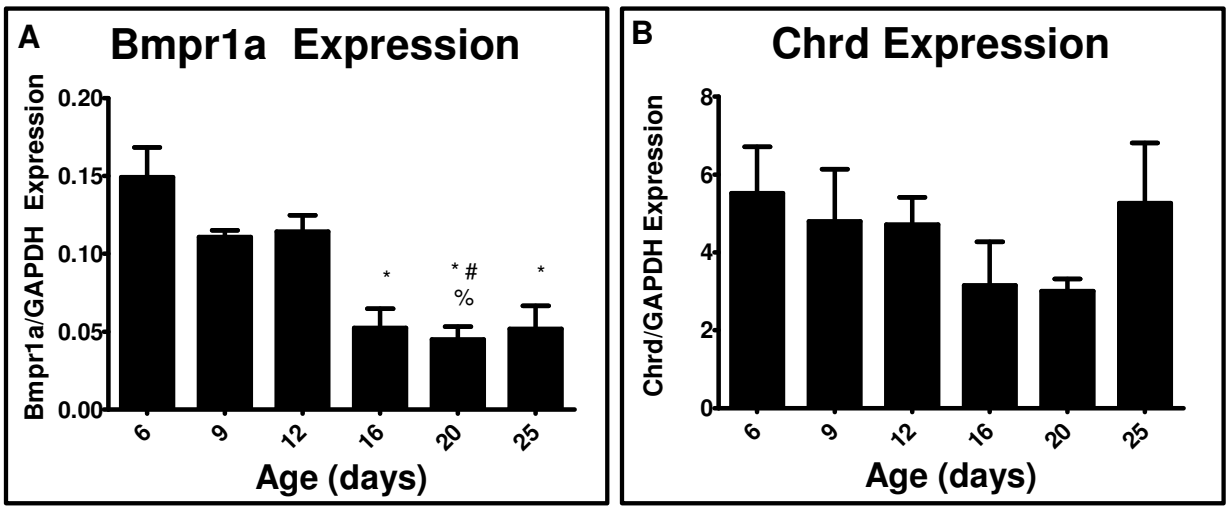

Figure A- 8: Expression of mRNAs for the BMP type Ia receptor and chordin in bone of the posterior frontal suture assessed by real-time PCR. Bmpr1a (A), Chrd (B). $p<0.05$ vs *=6d, #=9d, %=12d, @=16d, ^=20d.

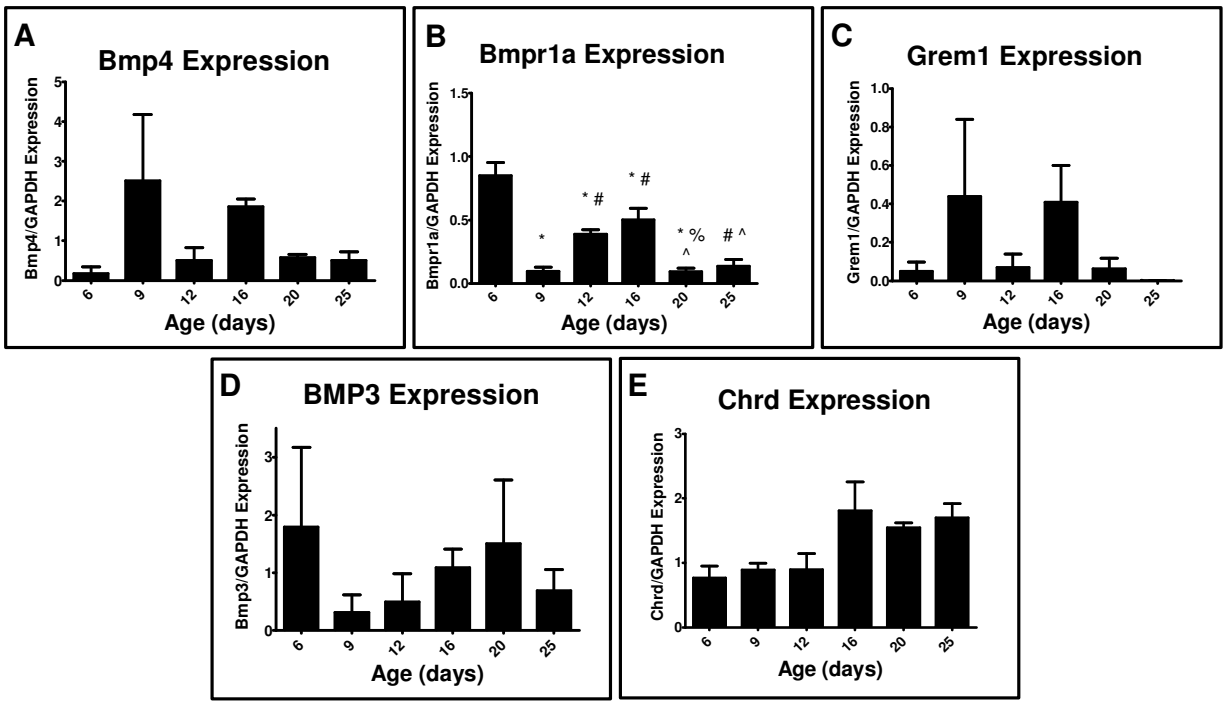

Figure A- 9: : Real-time PCR of posterior frontal dura versus age for Bmp4 (A), Bmpr1a (B), Grem1 (C), Bmp3 (D), and Chrd (E). $p<0.05$ vs *=6d, #=9d, %=12d, @=16d, ^=20d.

Table A- 3: Sequences for all primers used for qPCR confirmation.

Primer	Forward	Reverse
Bmp2	TGGGTTTGTGGTGGAAGTG	TCGTTTGTGGAGCGGATG
Bmp3	TATACGCCAACGATGCTG	CTTCTTCCTCCTCTCAACC
Bmp4	TGGTCTCCGTCCCTGATG	CGCTCCGAATGGCACTAC
Bmp6	ACGAACAACAGCACAGCGAAG	AAGGCACCAGCGGGAGATG
Bmp7	CCACAGCAAACGCCTAAG	CGATTACTCCTCAAAGACTCAG
Bmpr1a	GTGTAGCCCTTGTGGTAATG	CCTTCCTGTCCTCTGTGG
Chrd	CAGAGCATCGCAGTTACAG	TGGTAGGAGACAGAGAAGC
Grem1	AGAGAGCCACACCCAAAC	TGAAGCAGAGTAACAGGAAG
Nog	GCCAGCACTATCTACACATCC	CAGCAGCGTCTCGTTCAG
Ocn	GTCTGTTCACTACCTTATTGC	TCTCTCTGCTCACTCTGA
Runx2	GATAGGATGCTGACGAAGTACC	CCGCCACCACTCACTACC
Sost	GTCGTCGTGCTGTCCTCTG	ATTGTGGGTGGTGCTGTGG

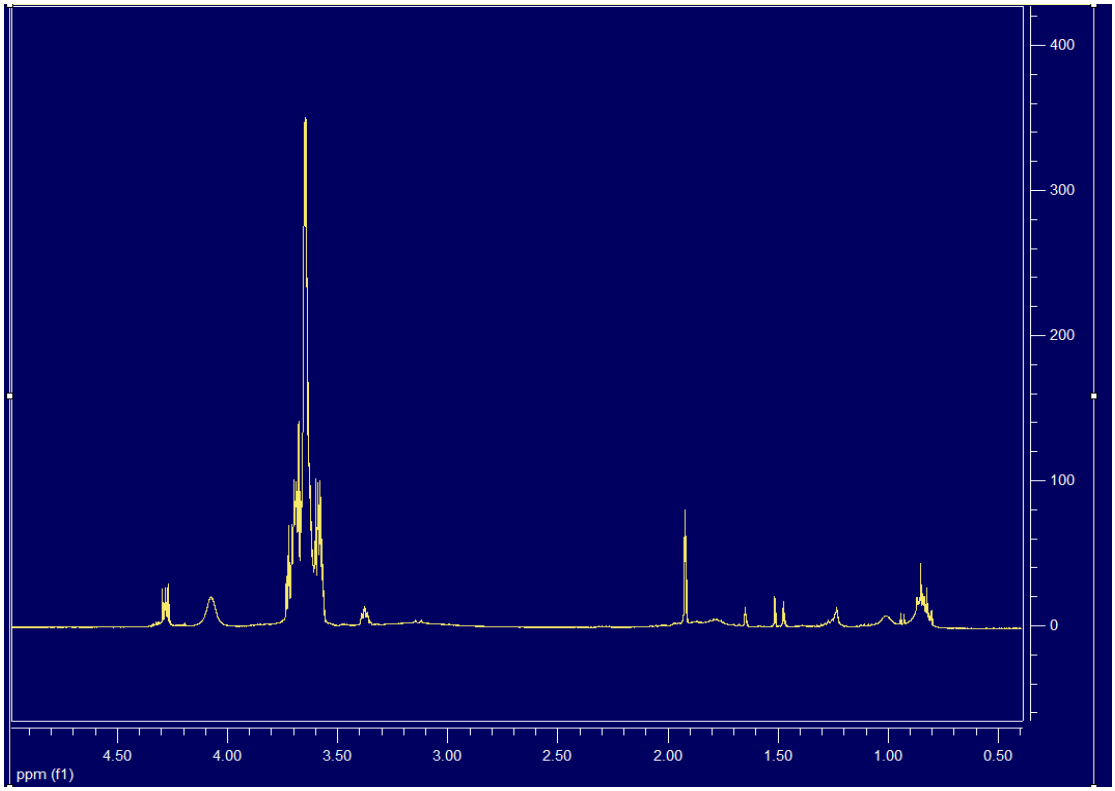

Figure A-10: ^{1}H NMR spectrum of PEG-N3. The azide functionality of the polymer was determined by the ratio of area of the peaks representing the hydrogens from azide and alcohol functionalized monomers.

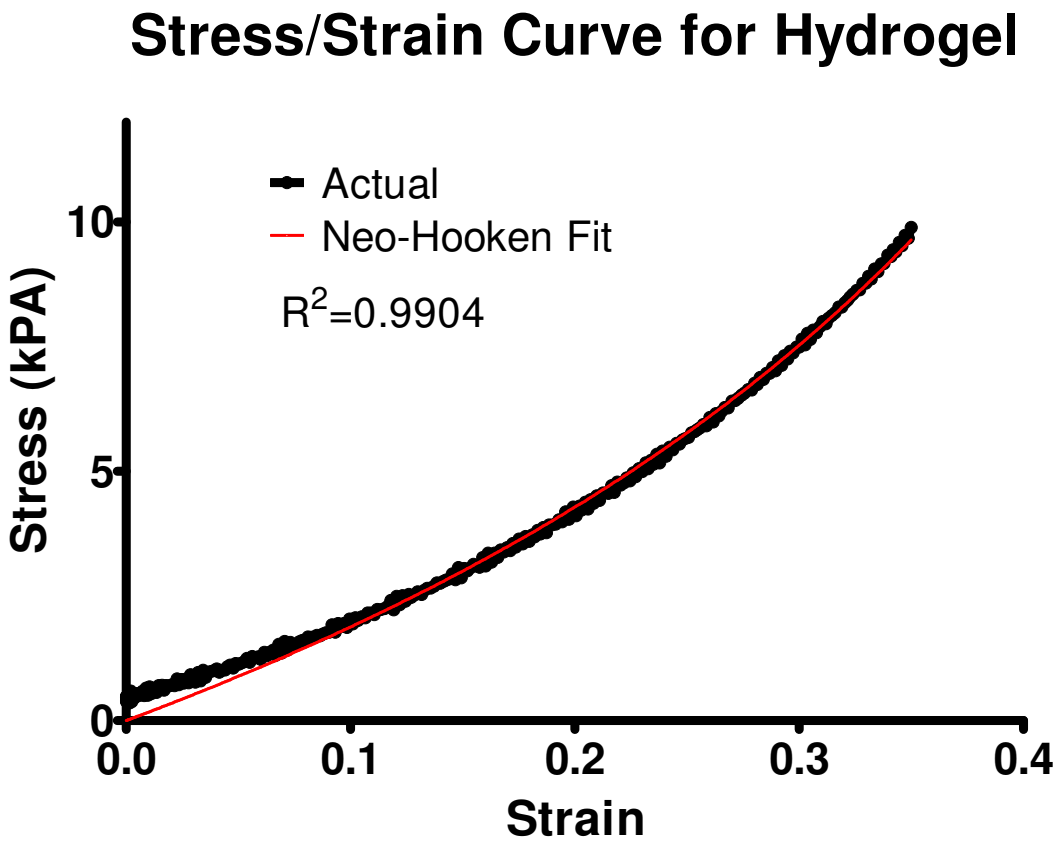

Figure A- 11: Representative stress strain curve for unconstrained compression testing of hydrogel (black line). The Neo-Hooken hyperelastic model (red line) provided an excellent fit with an R^2 value of greater than 0.97 for all samples tested.

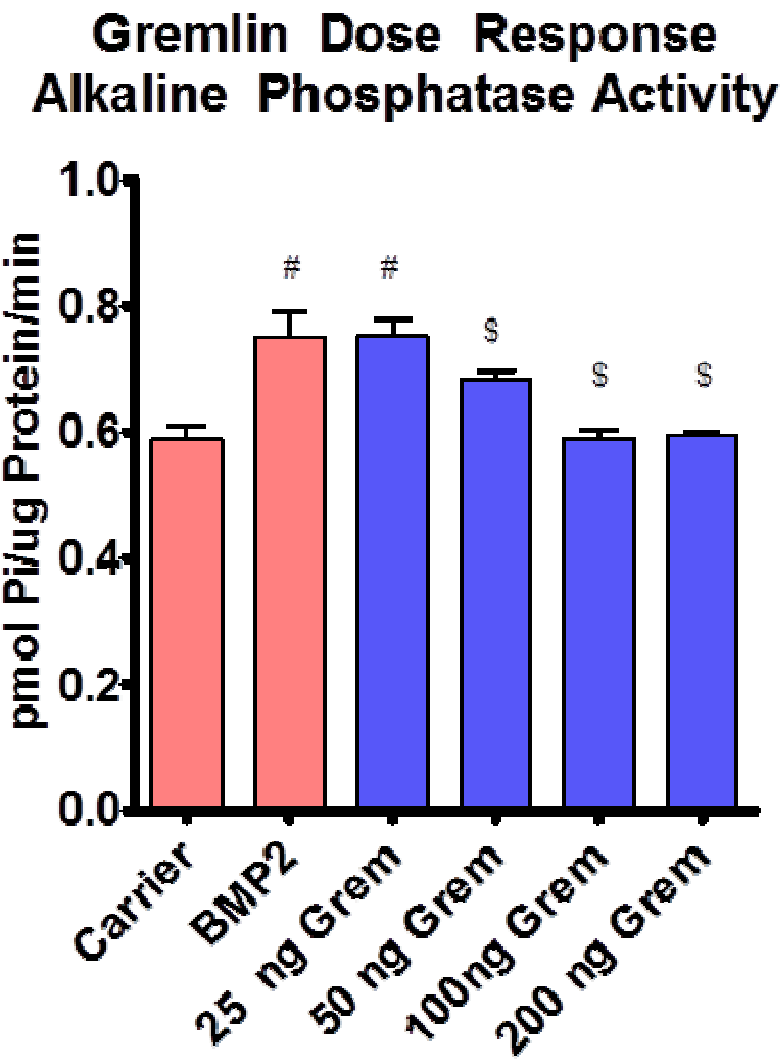

Figure A- 10: Dose response to Gremlin blocking activity of rhBMP2 to induce the differentiation of MG63 cells grown to 80% confluence. There was an increase in alkaline phosphatase specific activity in response to rhBMP2 and this effect was blocked by the addition of Gremlin1 in a dose dependent fashion. #=p<0.05 vs Carrier, $ = p<0.05 vs BMP2.

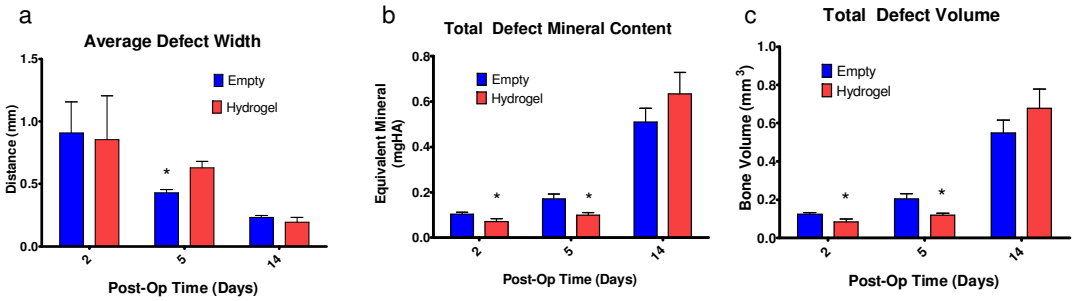

Figure A- 13: Defect healing in response to hydrogel. At 5 days post-op there was a slight decrease in the defect width in the empty defect, but there were no difference on day 14 (a). In groups with the hydrogel there was slightly less total mineral content and bone volume on both post-op days 2 and 5 but no differences by post-op day 14 (b-c). *=$p<0.05$ vs empty.

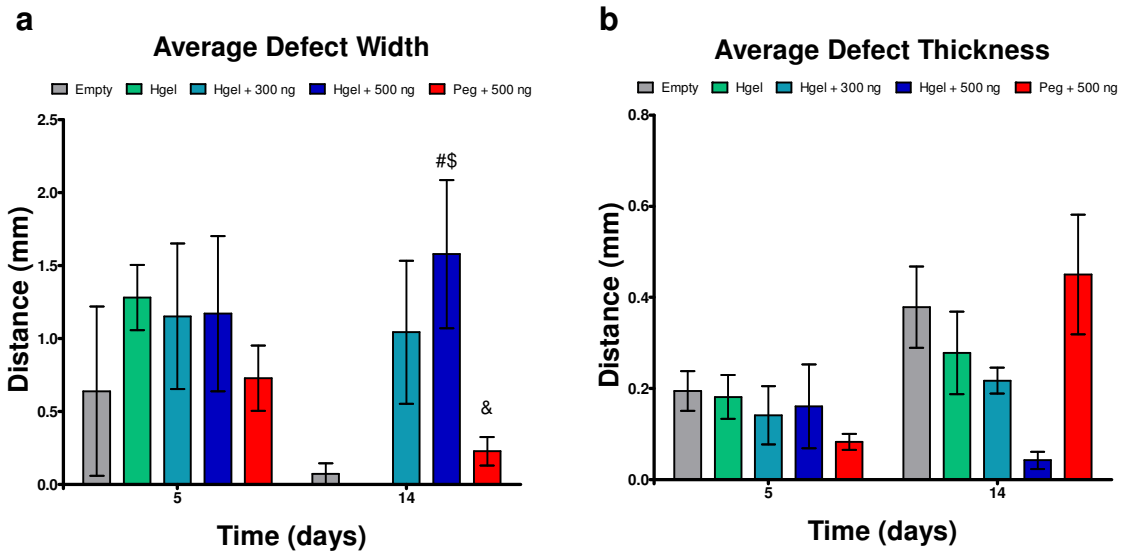

Figure A- 14: Bone regeneration in defect by coronal histology**.** Defects were left empty (Empty) on injected with hydrogel with 4 nM HCl carrier (Hgel + Carrier), hydrogel with 300 ng rmGremlin1 (Hgel + 300 ng), hydrogel with 500 ng rmGremlin1 (Hgel + 500 ng), or un-polymerized PEG-N3 with 500 ng rmGremlin1 (PEG-N3 + 500 ng). A coronal section was made in the middle of the defect and stained with H&E. The average defect width and bone thickness were analyzed by manual segmentation of the histology sections. On 14 days post-op the Hgel + 500 ng group had a greater width than Empty, Hgel, and PEG-N3 groups. $P<0.05$ vs. & = Hgel + 500 ng.

APPENDIX B

Supplemental Methods from Chapter 9:

Materials

Alexa Fluor® 647 carboxylic acid succinimidyl ester were purchased from Invitrogen (Carlsbad, CA). Disposable PD-10 Desalting Columns were from GE Healthcare (Piscataway, NJ).

Synthesis of Tetraethylene Glycol Methacrylate (TEGMA)

Tetraethylene glycol (5.0g, 25.7 mmol), and pyridine (2.0 g, 25.3 mmol) were added to anhydrous dichloromethane (DCM) (100 ml) in a 250 ml flask and stirred for 30 min at 0℃. Methacryloyl chloride (2.6 g, 25 mmol) was added drop-wise to the stirred solution. The reaction was allowed to stir at 0℃ for 2 h, and then at room temperature (rt) for an additional 2 h. The reaction was then concentrated via rotary evaporation, re-suspended in ethyl acetate, and finally evaporated onto silica gel. The mono methacrylate product x was separated from the di-methacrylate byproduct and starting material via flash silica gel chromatography on silica gel using a mixture of ethyl acetate and hexanes (7:3). **1H NMR** (300 MHz, CDCl3) δ 2.01 (t, *J* = 6.0 Hz, 3H,CH3), 2.82(t, *J* = 6.0 Hz, 1H,OH), 3.49-3.65 (m, 16H, 8 × CH2), 6.48 (m, 2H, CH2=C); **13C NMR** (75.5 MHz, CDCl3) δ 167.32 (C=O), δ 136.0 (C=CH2), 125.87 (CH2=C), 61.51 (*C*H2OH), 69.91 (CH2), 70.21 (CH2), 70.46 (CH2), 70.52 (CH2), 70.56 (CH2), 72.43 (CH2), 39.23 (C), 17.83 (CH3).

Synthesis of Tetraethylene Glycol Mono 4-Methylbenzenesulfonate

Tetraethylene glycol (5.0g, 25.7 mmol) and pyridine (2.0 g, 25.3 mmol) were added to anhydrous dichloromethane (100 ml) in a 250 ml flask and stirred for 30 min at 0℃. A solution of 4-toluenesulfonylchloride (4.75, 20 mmol) in 30 ml DCM was added drop-wise via syringe pump to the flask. The reaction mixture was then stirred for 2 h at 0℃, then another 4 hours at rt. The reaction mixture was then poured into ice water and the organic layer was separated then washed 2X with brine and dried over $MgSO_4$ before being concentrated via rotary evaporation. The crude product was then re-suspended in ethyl acetate and evaporated onto silica gel. The mono tosylated product was separated from the di-tosylated byproduct and starting material via flash silica gel chromatography on using a mixture of ethyl acetate and hexanes (6:4). 1H NMR (300 MHz, CDCl3) δ 2.33 (s, 3H, CH3), 2.89 (t, *J* = 6.0 Hz, 1H, OH), 3.42-3.70 (m, 14H, 7×CH2), 4.00-4.12 (m, 2H, C*H*2OTs), 7.24 (d, *J* = 8.0 Hz,2H, 2×Hm), 7.68 (d, *J* = 8.0 Hz, 2H, 2×Ho); 13C NMR (75.5 MHz, CDCl3) δ 21.41 (CH3), 61.40 (*C*H2OH), 68.44 (*C*H2OTs), 69.17 (CH2), 70.10 (CH2), 70.22 (CH2), 70.41 (CH2), 70.46 (CH2),72.34 (CH2), 127.73 (2×CHo), 129.68 (2×CHm), 132.76 (C), 144.68 (C).

Synthesis of Tetraethylene Glycol Mono Azide

Sodium azide (2.0 g, 30.76 mmol) was added to a solution of (2.0 g, 5.74 mmol) in dimethylformamide(100 mL) at room temperature. The reaction mixture was stirred overnight at 90 ℃. The reaction was then filtered and concentrated via rotary evaporation. The crude product was added to cold water and extracted

with ethyl acetate (4×100 mL). The combined organic layers were then dried over $MgSO_4$ and concentrated under vacuum. The viscous liquid was then purified by flash column chromatography on silica gel using a mixture of ethyl acetate and hexanes (6:4) to yield x as a colorless oil (1.63 g, 81%): **1H NMR** (300 MHz, CDCl3) δ 2.91 (t, *J* = 6.0 Hz, 1H,OH), 3.30 (t, *J* = 5.0 Hz, 2H, C*H*2N3), 3.49-3.65 (m, 14H, 7×CH2); **13C NMR** (75.5 MHz, CDCl3) δ 50.54 (*C*H2N3), 61.51 (*C*H2OH), 69.91 (CH2), 70.21 (CH2), 70.46 (CH2), 70.52 (CH2), 70.56 (CH2), 72.43 (CH2).

Synthesis of Azido Tetraethylene Glycol Methacrylate (ATEGMA)

Tetraethylene glycol mono azide (2.0g, 9.13 mmol) and pyridine (2.0 g, 25.3 mmol) were added to anhydrous dichloromethane (DCM) (100 ml) in a 250 ml flask and stirred for 30 min at 0℃. Methacryloyl chloride (2.6 g, 25 mmol) was added drop-wise to the stirred solution. The reaction was allowed to stir at 0℃ for 2 h, and then at room temperature for an additional 2 h. The reaction was then concentrated via rotary evaporation, re-suspended in ethyl acetate, and finally evaporated onto silica gel. The mono methacrylate product x was separated from the di-methacrylate byproduct and starting material via flash silica gel chromatography on silica gel using a mixture of ethyl acetate and hexanes (4:6 v/v). **1H NMR** (300 MHz, CDCl3) δ 2.01 (t, *J* = 6.0 Hz, 3H,CH3), 2.91 (t, *J* = 6.0 Hz, 1H,OH), 3.30 (t, *J* = 5.0 Hz, 2H, C*H*2N3), 3.49-3.65 (m, 14H, 7 × CH2), 6.48 (m, 2H, CH2=C); **13C NMR** (75.5 MHz, CDCl3) δ 167.32 (C=O),136.0 (C=CH2), 125.87 (CH2=C), 50.54 (*C*H2N3), 61.51 (*C*H2OH), 69.91 (CH2), 70.21

(CH2), 70.46 (CH2), 70.52 (CH2), 70.56 (CH2), 72.43 (CH2), 39.23 (C), 17.83 (CH3).

Histomorphometric Analysis

After imaging with μCT the samples were thawed and the brain was removed taking care not to damage the defect. The samples were fixed in 10% neutral buffered formalin, changing the solution after 24 hours. The skulls were decalcified using 10% EDTA changing the solution every 48-72 hours for a period of approximately 3 weeks. Complete de-calcification was verified on a plain x-ray. Under 4x magnification the center of the defect was visualized and a coronal cut was made through the center of the defect. The samples were dehydrated with ethanol and embedded in paraffin. Sections 7 μm in thickness were made and stained with haematoxylin and eosin (H&E) using standard protocols. The samples were imaged at 10x magnification and the bone was manually segmented by a blinded reviewer. The average defect width and average thickness of the bones were calculated (Matlab).

Statistical Analysis

All data are represented as the mean ± standard error of the mean. The sample size for all in vivo and in vitro experiments was determined by a prospective power analysis based on previously reported data. All cell culture experiments were performed with six independent cultures (n=6) and repeated two times. All in vivo experiments were performed in 5 mice per group per time point (n=5). The normality of the data was verified by the D'Agistino-Pearson

omnibus normality test. For all in vitro experiments a one way ANOVA was performed and where appropriate significance among groups was determined by a multiple comparison test with Bonferroni adjustments. For all in vivo experiments a two way ANOVA was performed and as expected there a significant ($P<0.001$) effect of treatment group, time, and interaction for all analysis. Since interactions were found significant, main effect significance was tested by either a conditional one way ANOVA with Bonferroni multiple comparison post-test or an un-paired two-sided t-test not assuming equal variance. Statistical significance for all experiments was declared when the p-value was less than 0.05.

REFERENCES

1. Boskey, A.L., *Mineral-matrix interactions in bone and cartilage.* Clin Orthop Relat Res, 1992(281): p. 244-74.
2. Allori, A.C., A.M. Sailon, and S.M. Warren, *Biological basis of bone formation, remodeling, and repair-part II: extracellular matrix.* Tissue Eng Part B Rev, 2008. **14**(3): p. 275-83.
3. Tencer, A.F. and K.D. Johnson, *Biomechanics in orthopedic trauma : bone fracture and fixation*. 1994, London Philadelphia: M. Dunitz ;Lippincott. viii, 311 p.
4. Boyce, B.F. and L. Xing, *Biology of RANK, RANKL, and osteoprotegerin.* Arthritis Res Ther, 2007. **9 Suppl 1**: p. S1.
5. Panetta, N.J., D.M. Gupta, and M.T. Longaker, *Bone regeneration and repair.* Curr Stem Cell Res Ther, 2010. **5**(2): p. 122-8.
6. Dimitriou, R., E. Tsiridis, and P.V. Giannoudis, *Current concepts of molecular aspects of bone healing.* Injury, 2005. **36**(12): p. 1392-404.
7. Franz-Odendaal, T.A., *Induction and patterning of intramembranous bone.* Front Biosci, 2011. **17**: p. 3734-46.
8. Hojo, H., et al., *Coordination of chondrogenesis and osteogenesis by hypertrophic chondrocytes in endochondral bone development.* J Bone Miner Metab, 2010. **28**(5): p. 489-502.
9. Yamagiwa, H. and N. Endo, *[Bone fracture and the healing mechanisms. Histological aspect of fracture healing. Primary and secondary healing].* Clin Calcium, 2009. **19**(5): p. 627-33.
10. Anderson, H.C., *Mechanism of mineral formation in bone.* Lab Invest, 1989. **60**(3): p. 320-30.
11. Boyan, B.D., et al., *Role of lipids in calcification of cartilage.* Anat Rec, 1989. **224**(2): p. 211-9.
12. Emons, J., et al., *Mechanisms of growth plate maturation and epiphyseal fusion.* Horm Res Paediatr, 2011. **75**(6): p. 383-91.
13. Marino, R., *Growth plate biology: new insights.* Curr Opin Endocrinol Diabetes Obes, 2011. **18**(1): p. 9-13.
14. Moore, K.L., T.V.N. Persaud, and M.G. Torchia, *The developing human : clinically oriented embryology*. 8th ed. 2008, Philadelphia, PA: Saunders/Elsevier. xiv, 522 p.
15. Jiang, X., et al., *Tissue origins and interactions in the mammalian skull vault.* Dev Biol, 2002. **241**(1): p. 106-16.
16. Ranly, D.M., *A synopsis of craniofacial growth*. 2nd ed. 1988, Norwalk, Ct: Appleton & Lange. 225 p.

17. Opperman, L.A., *Cranial sutures as intramembranous bone growth sites.* Dev Dyn, 2000. **219**(4): p. 472-85.
18. Sgouros, S., *Skull vault growth in craniosynostosis.* Childs Nerv Syst, 2005. **21**(10): p. 861-70.
19. Kabbani, H. and T.S. Raghuveer, *Craniosynostosis.* Am Fam Physician, 2004. **69**(12): p. 2863-70.
20. James, A.W., et al., *Differential effects of TGF-beta1 and TGF-beta3 on chondrogenesis in posterofrontal cranial suture-derived mesenchymal cells in vitro.* Plast Reconstr Surg, 2009. **123**(1): p. 31-43.
21. Opperman, L.A., A.A. Nolen, and R.C. Ogle, *TGF-beta 1, TGF-beta 2, and TGF-beta 3 exhibit distinct patterns of expression during cranial suture formation and obliteration in vivo and in vitro.* J Bone Miner Res, 1997. **12**(3): p. 301-10.
22. Vu, H.L., et al., *The timing of physiologic closure of the metopic suture: a review of 159 patients using reconstructed 3D CT scans of the craniofacial region.* J Craniofac Surg, 2001. **12**(6): p. 527-32.
23. Bradley, J.P., et al., *Studies in cranial suture biology: regional dura mater determines in vitro cranial suture fusion.* Plast Reconstr Surg, 1997. **100**(5): p. 1091-9; discussion; 1100-2.
24. Rice, D.P., *Craniofacial sutures. Development, disease and treatment. Preface.* Front Oral Biol, 2008. **12**: p. xi.
25. Kwan, M.D., et al., *Microarray analysis of the role of regional dura mater in cranial suture fate.* Plast Reconstr Surg, 2008. **122**(2): p. 389-99.
26. Levine, J.P., et al., *Studies in cranial suture biology: regional dura mater determines overlying suture biology.* Plast Reconstr Surg, 1998. **101**(6): p. 1441-7.
27. Warren, S.M., et al., *Regional dura mater differentially regulates osteoblast gene expression.* J Craniofac Surg, 2003. **14**(3): p. 363-70.
28. Sahar, D.E., M.T. Longaker, and N. Quarto, *Sox9 neural crest determinant gene controls patterning and closure of the posterior frontal cranial suture.* Dev Biol, 2005. **280**(2): p. 344-61.
29. Behr, B., M.T. Longaker, and N. Quarto, *Craniosynostosis of coronal suture in twist1 mice occurs through endochondral ossification recapitulating the physiological closure of posterior frontal suture.* Front Physiol, 2011. **2**: p. 37.
30. Boulet, S.L., S.A. Rasmussen, and M.A. Honein, *A population-based study of craniosynostosis in metropolitan Atlanta, 1989-2003.* Am J Med Genet A, 2008. **146A**(8): p. 984-91.
31. Hunter, A.G. and N.L. Rudd, *Craniosynostosis. I. Sagittal synostosis: its genetics and associated clinical findings in 214 patients who lacked involvement of the coronal suture(s).* Teratology, 1976. **14**(2): p. 185-93.
32. Hunter, A.G. and N.L. Rudd, *Craniosynostosis. II. Coronal synostosis: its familial characteristics and associated clinical findings in 109 patients lacking bilateral polysyndactyly or syndactyly.* Teratology, 1977. **15**(3): p. 301-9.
33. Lajeunie, E., et al., *Genetic study of nonsyndromic coronal craniosynostosis.* Am J Med Genet, 1995. **55**(4): p. 500-4.

34. Aviv, R.I., E. Rodger, and C.M. Hall, *Craniosynostosis.* Clin Radiol, 2002. **57**(2): p. 93-102.
35. Panchal, J. and V. Uttchin, *Management of craniosynostosis.* Plast Reconstr Surg, 2003. **111**(6): p. 2032-48; quiz 2049.
36. Wilkie, A.O., *Craniosynostosis: genes and mechanisms.* Hum Mol Genet, 1997. **6**(10): p. 1647-56.
37. Kirman, C.N., et al., *Difficulties of delayed treatment of craniosynostosis in a patient with Crouzon, increased intracranial pressure, and papilledema.* J Craniofac Surg, 2011. **22**(4): p. 1409-12.
38. Fujimoto, T., et al., *Tracheobronchial anomalies in syndromic craniosynostosis with 3-dimensional CT image and bronchoscopy.* J Craniofac Surg, 2011. **22**(5): p. 1579-83.
39. Gosain, A.K., J.G. McCarthy, and J.H. Wisoff, *Morbidity associated with increased intracranial pressure in Apert and Pfeiffer syndromes: the need for long-term evaluation.* Plast Reconstr Surg, 1996. **97**(2): p. 292-301.
40. Gault, D.T., et al., *Intracranial pressure and intracranial volume in children with craniosynostosis.* Plast Reconstr Surg, 1992. **90**(3): p. 377-81.
41. Baird, L.C., et al., *Craniofacial reconstruction as a treatment for elevated intracranial pressure.* Childs Nerv Syst, 2011.
42. Jabs, E.W., et al., *A mutation in the homeodomain of the human MSX2 gene in a family affected with autosomal dominant craniosynostosis.* Cell, 1993. **75**(3): p. 443-50.
43. Muenke, M., et al., *A unique point mutation in the fibroblast growth factor receptor 3 gene (FGFR3) defines a new craniosynostosis syndrome.* Am J Hum Genet, 1997. **60**(3): p. 555-64.
44. Oldridge, M., et al., *Mutations in the third immunoglobulin domain of the fibroblast growth factor receptor-2 gene in Crouzon syndrome.* Hum Mol Genet, 1995. **4**(6): p. 1077-82.
45. Wilkie, A.O., et al., *Apert syndrome results from localized mutations of FGFR2 and is allelic with Crouzon syndrome.* Nat Genet, 1995. **9**(2): p. 165-72.
46. Spivak-Kroizman, T., et al., *Heparin-induced oligomerization of FGF molecules is responsible for FGF receptor dimerization, activation, and cell proliferation.* Cell, 1994. **79**(6): p. 1015-24.
47. Neilson, K.M. and R.E. Friesel, *Constitutive activation of fibroblast growth factor receptor-2 by a point mutation associated with Crouzon syndrome.* J Biol Chem, 1995. **270**(44): p. 26037-40.
48. Galvin, B.D., et al., *Constitutive receptor activation by Crouzon syndrome mutations in fibroblast growth factor receptor (FGFR)2 and FGFR2/Neu chimeras.* Proc Natl Acad Sci U S A, 1996. **93**(15): p. 7894-9.
49. Morriss-Kay, G.M. and A.O. Wilkie, *Growth of the normal skull vault and its alteration in craniosynostosis: insights from human genetics and experimental studies.* J Anat, 2005. **207**(5): p. 637-53.
50. Esparza, J. and J. Hinojosa, *Complications in the surgical treatment of craniosynostosis and craniofacial syndromes: apropos of 306 transcranial procedures.* Childs Nerv Syst, 2008. **24**(12): p. 1421-30.

51. Esparza, J., et al., *Surgical treatment of isolated and syndromic craniosynostosis. Results and complications in 283 consecutive cases.* Neurocirugia (Astur), 2008. **19**(6): p. 509-29.
52. El Ghouzzi, V., et al., *Mutations within or upstream of the basic helix-loop-helix domain of the TWIST gene are specific to Saethre-Chotzen syndrome.* Eur J Hum Genet, 1999. **7**(1): p. 27-33.
53. el Ghouzzi, V., et al., *Mutations of the TWIST gene in the Saethre-Chotzen syndrome.* Nat Genet, 1997. **15**(1): p. 42-6.
54. Kress, W., et al., *Saethre-Chotzen syndrome caused by TWIST 1 gene mutations: functional differentiation from Muenke coronal synostosis syndrome.* Eur J Hum Genet, 2006. **14**(1): p. 39-48.
55. Carver, E.A., K.F. Oram, and T. Gridley, *Craniosynostosis in Twist heterozygous mice: a model for Saethre-Chotzen syndrome.* Anat Rec, 2002. **268**(2): p. 90-2.
56. Gripp, K.W., E.H. Zackai, and C.A. Stolle, *Mutations in the human TWIST gene.* Hum Mutat, 2000. **15**(2): p. 150-5.
57. Johnson, D., et al., *Expression patterns of Twist and Fgfr1, -2 and -3 in the developing mouse coronal suture suggest a key role for twist in suture initiation and biogenesis.* Mech Dev, 2000. **91**(1-2): p. 341-5.
58. Lee, M.S., et al., *TWIST, a basic helix-loop-helix transcription factor, can regulate the human osteogenic lineage.* J Cell Biochem, 1999. **75**(4): p. 566-77.
59. Connerney, J., et al., *Twist1 dimer selection regulates cranial suture patterning and fusion.* Dev Dyn, 2006. **235**(5): p. 1345-57.
60. Berry-Candelario, J., et al., *Endoscope-assisted strip craniectomy and postoperative helmet therapy for treatment of craniosynostosis.* Neurosurg Focus, 2011. **31**(2): p. E5.
61. Schaaf, H., et al., *Three-dimensional photographic analysis of outcome after helmet treatment of a nonsynostotic cranial deformity.* J Craniofac Surg, 2010. **21**(6): p. 1677-82.
62. Czerwinski, M., et al., *Major morbidity and mortality rates in craniofacial surgery: an analysis of 8101 major procedures.* Plast Reconstr Surg, 2010. **126**(1): p. 181-6.
63. Foster, K.A., D.M. Frim, and M. McKinnon, *Recurrence of synostosis following surgical repair of craniosynostosis.* Plast Reconstr Surg, 2008. **121**(3): p. 70e-76e.
64. Williams, J.K., et al., *A longitudinal, statistical study of reoperation rates in craniosynostosis.* Plast Reconstr Surg, 1997. **100**(2): p. 305-10.
65. Seruya, M., et al., *Long-term outcomes of primary craniofacial reconstruction for craniosynostosis: a 12-year experience.* Plast Reconstr Surg, 2011. **127**(6): p. 2397-406.
66. Rice, D.P., et al., *Gli3Xt-J/Xt-J mice exhibit lambdoid suture craniosynostosis which results from altered osteoprogenitor proliferation and differentiation.* Hum Mol Genet, 2010. **19**(17): p. 3457-67.
67. Nagata, M., et al., *The primary site of the acrocephalic feature in Apert Syndrome is a dwarf cranial base with accelerated chondrocytic differentiation due to aberrant activation of the FGFR2 signaling.* Bone, 2011. **48**(4): p. 847-56.

68. Hatch, N.E., *FGF signaling in craniofacial biological control and pathological craniofacial development.* Crit Rev Eukaryot Gene Expr, 2010. **20**(4): p. 295-311.
69. Bradley, J.P., et al., *Studies in cranial suture biology: in vitro cranial suture fusion.* Cleft Palate Craniofac J, 1996. **33**(2): p. 150-6.
70. Bradley, J.P., et al., *Studies in cranial suture biology: IV. Temporal sequence of posterior frontal cranial suture fusion in the mouse.* Plast Reconstr Surg, 1996. **98**(6): p. 1039-45.
71. Recinos, R.F., et al., *Microfocal CT: a method for evaluating murine cranial sutures in situ.* J Surg Res, 2004. **116**(2): p. 322-9.
72. Opperman, L.A., K. Adab, and P.T. Gakunga, *Transforming growth factor-beta 2 and TGF-beta 3 regulate fetal rat cranial suture morphogenesis by regulating rates of cell proliferation and apoptosis.* Dev Dyn, 2000. **219**(2): p. 237-47.
73. Opperman, L.A., et al., *Cranial sutures require tissue interactions with dura mater to resist osseous obliteration in vitro.* J Bone Miner Res, 1995. **10**(12): p. 1978-87.
74. Fong, K.D., et al., *Mechanical strain affects dura mater biological processes: implications for immature calvarial healing.* Plast Reconstr Surg, 2003. **112**(5): p. 1312-27.
75. Greenwald, J.A., et al., *Immature versus mature dura mater: II. Differential expression of genes important to calvarial reossification.* Plast Reconstr Surg, 2000. **106**(3): p. 630-8; discussion 639.
76. Slater, B.J., et al., *The role of regional posterior frontal dura mater in the overlying suture morphology.* Plast Reconstr Surg, 2009. **123**(2): p. 463-9.
77. Aalami, O.O., et al., *Differential transcriptional expression profiles of juvenile and adult calvarial bone.* Plast Reconstr Surg, 2005. **115**(7): p. 1986-94.
78. Gosain, A.K., et al., *Osteogenesis in calvarial defects: contribution of the dura, the pericranium, and the surrounding bone in adult versus infant animals.* Plast Reconstr Surg, 2003. **112**(2): p. 515-27.
79. Greenwald, J.A., et al., *Biomolecular mechanisms of calvarial bone induction: immature versus mature dura mater.* Plast Reconstr Surg, 2000. **105**(4): p. 1382-92.
80. Eswarakumar, V.P., et al., *Attenuation of signaling pathways stimulated by pathologically activated FGF-receptor 2 mutants prevents craniosynostosis.* Proc Natl Acad Sci U S A, 2006. **103**(49): p. 18603-8.
81. Marie, P.J., K. Kaabeche, and H. Guenou, *Roles of FGFR2 and twist in human craniosynostosis: insights from genetic mutations in cranial osteoblasts.* Front Oral Biol, 2008. **12**: p. 144-59.
82. Centrella, M., T.L. McCarthy, and E. Canalis, *Transforming growth factor beta is a bifunctional regulator of replication and collagen synthesis in osteoblast-enriched cell cultures from fetal rat bone.* J Biol Chem, 1987. **262**(6): p. 2869-74.
83. Robey, P.G., et al., *Osteoblasts synthesize and respond to transforming growth factor-type beta (TGF-beta) in vitro.* J Cell Biol, 1987. **105**(1): p. 457-63.
84. Most, D., et al., *Studies in cranial suture biology: up-regulation of transforming growth factor-beta1 and basic fibroblast growth factor mRNA correlates with*

posterior frontal cranial suture fusion in the rat. Plast Reconstr Surg, 1998. **101**(6): p. 1431-40.
85. Roth, D.A., et al., *Immunolocalization of transforming growth factor beta 1, beta 2, and beta 3 and insulin-like growth factor I in premature cranial suture fusion.* Plast Reconstr Surg, 1997. **99**(2): p. 300-9; discussion 310-6.
86. Mayahara, H., et al., *In vivo stimulation of endosteal bone formation by basic fibroblast growth factor in rats.* Growth Factors, 1993. **9**(1): p. 73-80.
87. Rice, D.P., R. Rice, and I. Thesleff, *Molecular mechanisms in calvarial bone and suture development, and their relation to craniosynostosis.* Eur J Orthod, 2003. **25**(2): p. 139-48.
88. Wilkie, A.O., et al., *Functions of fibroblast growth factors and their receptors.* Curr Biol, 1995. **5**(5): p. 500-7.
89. Connerney, J., et al., *Twist1 homodimers enhance FGF responsiveness of the cranial sutures and promote suture closure.* Dev Biol, 2008. **318**(2): p. 323-34.
90. Noda, M. and R. Vogel, *Fibroblast growth factor enhances type beta 1 transforming growth factor gene expression in osteoblast-like cells.* J Cell Biol, 1989. **109**(5): p. 2529-35.
91. Li, X. and X. Cao, *BMP signaling and skeletogenesis.* Ann N Y Acad Sci, 2006. **1068**: p. 26-40.
92. Cooper, G.M., et al., *Noggin inhibits postoperative resynostosis in craniosynostotic rabbits.* J Bone Miner Res, 2007. **22**(7): p. 1046-54.
93. Cooper, G.M., et al., *Ex vivo Noggin gene therapy inhibits bone formation in a mouse model of postoperative resynostosis.* Plast Reconstr Surg, 2009. **123**(2 Suppl): p. 94S-103S.
94. Mooney, M.P., et al., *Correction of coronal suture synostosis using suture and dura mater allografts in rabbits with familial craniosynostosis.* Cleft Palate Craniofac J, 2001. **38**(3): p. 206-25.
95. Mooney, M.P., et al., *Anti-TGF-beta2 antibody therapy inhibits postoperative resynostosis in craniosynostotic rabbits.* Plast Reconstr Surg, 2007. **119**(4): p. 1200-12; discussion 1213-5.
96. Mooney, M.P., et al., *A rabbit model of human familial, nonsyndromic unicoronal suture synostosis. I. Synostotic onset, pathology, and sutural growth patterns.* Childs Nerv Syst, 1998. **14**(6): p. 236-46.
97. Mooney, M.P., et al., *Craniosynostosis with autosomal dominant transmission in New Zealand white rabbits.* J Craniofac Genet Dev Biol, 1996. **16**(1): p. 52-63.
98. Cray, J., Jr., et al., *Blocking bone morphogenetic protein function using in vivo noggin therapy does not rescue premature suture fusion in rabbits with delayed-onset craniosynostosis.* Plast Reconstr Surg, 2011. **127**(3): p. 1163-72.
99. Schmitz, J.P., et al., *Characterization of rat calvarial nonunion defects.* Acta Anat (Basel), 1990. **138**(3): p. 185-92.
100. Neovius, E. and T. Engstrand, *Craniofacial reconstruction with bone and biomaterials: review over the last 11 years.* J Plast Reconstr Aesthet Surg, 2010. **63**(10): p. 1615-23.
101. Kwan, M.D., et al., *Differential expression of sclerostin in adult and juvenile mouse calvariae.* Plast Reconstr Surg, 2011. **127**(2): p. 595-602.

102. Einhorn, T.A., *The cell and molecular biology of fracture healing.* Clin Orthop Relat Res, 1998(355 Suppl): p. S7-21.
103. Marsell, R. and T.A. Einhorn, *The biology of fracture healing.* Injury, 2011. **42**(6): p. 551-5.
104. Lehmann, W., et al., *Tumor necrosis factor alpha (TNF-alpha) coordinately regulates the expression of specific matrix metalloproteinases (MMPS) and angiogenic factors during fracture healing.* Bone, 2005. **36**(2): p. 300-10.
105. Einhorn, T.A., et al., *The expression of cytokine activity by fracture callus.* J Bone Miner Res, 1995. **10**(8): p. 1272-81.
106. Cho, T.J., L.C. Gerstenfeld, and T.A. Einhorn, *Differential temporal expression of members of the transforming growth factor beta superfamily during murine fracture healing.* J Bone Miner Res, 2002. **17**(3): p. 513-20.
107. Lieberman, J.R., A. Daluiski, and T.A. Einhorn, *The role of growth factors in the repair of bone. Biology and clinical applications.* J Bone Joint Surg Am, 2002. **84-A**(6): p. 1032-44.
108. Hunziker, E.B., *Mechanism of longitudinal bone growth and its regulation by growth plate chondrocytes.* Microsc Res Tech, 1994. **28**(6): p. 505-19.
109. Glowacki, J., *Angiogenesis in fracture repair.* Clin Orthop Relat Res, 1998(355 Suppl): p. S82-9.
110. Cheng, H., et al., *Osteogenic activity of the fourteen types of human bone morphogenetic proteins (BMPs).* J Bone Joint Surg Am, 2003. **85-A**(8): p. 1544-52.
111. Gerstenfeld, L.C., et al., *Fracture healing as a post-natal developmental process: molecular, spatial, and temporal aspects of its regulation.* J Cell Biochem, 2003. **88**(5): p. 873-84.
112. Barnes, G.L., et al., *Growth factor regulation of fracture repair.* J Bone Miner Res, 1999. **14**(11): p. 1805-15.
113. Zelzer, E., et al., *VEGFA is necessary for chondrocyte survival during bone development.* Development, 2004. **131**(9): p. 2161-71.
114. Ferrara, N., H.P. Gerber, and J. LeCouter, *The biology of VEGF and its receptors.* Nat Med, 2003. **9**(6): p. 669-76.
115. Urist, M.R., *Bone: formation by autoinduction.* Science, 1965. **150**(698): p. 893-9.
116. Bragdon, B., et al., *Bone morphogenetic proteins: a critical review.* Cell Signal, 2011. **23**(4): p. 609-20.
117. von Bubnoff, A. and K.W. Cho, *Intracellular BMP signaling regulation in vertebrates: pathway or network?* Dev Biol, 2001. **239**(1): p. 1-14.
118. Walsh, D.W., et al., *Extracellular BMP-antagonist regulation in development and disease: tied up in knots.* Trends Cell Biol, 2010. **20**(5): p. 244-56.
119. Ross, J.J., et al., *Twisted gastrulation is a conserved extracellular BMP antagonist.* Nature, 2001. **410**(6827): p. 479-83.
120. Warren, S.M., et al., *The BMP antagonist noggin regulates cranial suture fusion.* Nature, 2003. **422**(6932): p. 625-9.
121. Groppe, J., et al., *Structural basis of BMP signalling inhibition by the cystine knot protein Noggin.* Nature, 2002. **420**(6916): p. 636-42.

122. Zimmerman, L.B., J.M. De Jesus-Escobar, and R.M. Harland, *The Spemann organizer signal noggin binds and inactivates bone morphogenetic protein 4.* Cell, 1996. **86**(4): p. 599-606.
123. Topol, L.Z., et al., *Biosynthesis, post-translation modification, and functional characterization of Drm/Gremlin.* J Biol Chem, 2000. **275**(12): p. 8785-93.
124. Gazzerro, E., et al., *Skeletal overexpression of gremlin impairs bone formation and causes osteopenia.* Endocrinology, 2005. **146**(2): p. 655-65.
125. Khokha, M.K., et al., *Gremlin is the BMP antagonist required for maintenance of Shh and Fgf signals during limb patterning.* Nat Genet, 2003. **34**(3): p. 303-7.
126. Canalis, E., K. Parker, and S. Zanotti, *Gremlin1 is required for skeletal development and postnatal skeletal homeostasis.* J Cell Physiol, 2012. **227**(1): p. 269-77.
127. King, M.A., et al., *Radiation exposure from pediatric head CT: a bi-institutional study.* Pediatr Radiol, 2009. **39**(10): p. 1059-65.
128. Stadler, J.A., 3rd, et al., *A reinvestigation of murine cranial suture biology: microcomputed tomography versus histologic technique.* Plast Reconstr Surg, 2006. **118**(3): p. 626-34.
129. Sankur, B. and M. Sezgen, *Survey over image thresholding techniques and quantitative performance evaluation.* Journal of Electronic Imagin, 2004. **13**(1): p. 146-165.
130. Sezgin, M. and B. Sankur, *Survey over image thresholding techniques and quantitative performance evaluation.* Journal of Electronic Imaging, 2004. **13**(1): p. 146-168.
131. Petitjean, C. and J.N. Dacher, *A review of segmentation methods in short axis cardiac MR images.* Med Image Anal, 2011. **15**(2): p. 169-84.
132. Bertalmio, M., G. Sapiro, and G. Randall, *Region tracking on level-sets methods.* IEEE Trans Med Imaging, 1999. **18**(5): p. 448-51.
133. Chan, T.F. and L.A. Vese, *Active contours without edges.* IEEE Trans Image Process, 2001. **10**(2): p. 266-77.
134. Kass, M., A. Witkin, and D. Terzopoulos, *Snakes: Active contour models.* International Journal of Computer Vision, 1988. **1**(4): p. 321-331.
135. Farmaki, C., et al., *Spatially adaptive active contours: a semi-automatic tumor segmentation framework.* Int J Comput Assist Radiol Surg, 2010.
136. Marsousi, M., A. Eftekhari, and J. Alirezaie, *Object contour extraction in medical images by fast adaptive B-Snake.* Conf Proc IEEE Eng Med Biol Soc, 2008. **2008**: p. 3068-71.
137. El-Husseiny, M., et al., *Biodegradable antibiotic delivery systems.* J Bone Joint Surg Br, 2011. **93**(2): p. 151-7.
138. Glassman, S.D., et al., *Posterolateral lumbar spine fusion with INFUSE bone graft.* Spine J, 2007. **7**(1): p. 44-9.
139. Bessa, P.C., M. Casal, and R.L. Reis, *Bone morphogenetic proteins in tissue engineering: the road from laboratory to clinic, part II (BMP delivery).* J Tissue Eng Regen Med, 2008. **2**(2-3): p. 81-96.
140. Seeherman, H., J. Wozney, and R. Li, *Bone morphogenetic protein delivery systems.* Spine (Phila Pa 1976), 2002. **27**(16 Suppl 1): p. S16-23.

141. Woo, E.J., *Adverse Events Reported After the Use of Recombinant Human Bone Morphogenetic Protein 2.* J Oral Maxillofac Surg, 2011.
142. Lindley, T.E., et al., *Complications associated with recombinant human bone morphogenetic protein use in pediatric craniocervical arthrodesis.* J Neurosurg Pediatr, 2011. **7**(5): p. 468-74.
143. Epstein, N.E., *Pros, cons, and costs of INFUSE in spinal surgery.* Surg Neurol Int, 2011. **2**: p. 10.
144. Zustiak, S.P. and J.B. Leach, *Hydrolytically degradable poly(ethylene glycol) hydrogel scaffolds with tunable degradation and mechanical properties.* Biomacromolecules, 2010. **11**(5): p. 1348-57.
145. Yu, L. and J. Ding, *Injectable hydrogels as unique biomedical materials.* Chem Soc Rev, 2008. **37**(8): p. 1473-81.
146. Burdick, J.A., et al., *Delivery of osteoinductive growth factors from degradable PEG hydrogels influences osteoblast differentiation and mineralization.* J Control Release, 2002. **83**(1): p. 53-63.
147. Humber, C.C., et al., *Bone healing with an in situ-formed bioresorbable polyethylene glycol hydrogel membrane in rabbit calvarial defects.* Oral Surg Oral Med Oral Pathol Oral Radiol Endod, 2010. **109**(3): p. 372-84.
148. Saito, N., et al., *A biodegradable polymer as a cytokine delivery system for inducing bone formation.* Nat Biotechnol, 2001. **19**(4): p. 332-5.
149. Mauch-Mani, B. and A.J. Slusarenko, *Arabidopsis as a model host for studying plant-pathogen interactions.* Trends Microbiol, 1993. **1**(7): p. 265-70.
150. Zisch, A.H., et al., *Cell-demanded release of VEGF from synthetic, biointeractive cell ingrowth matrices for vascularized tissue growth.* FASEB J, 2003. **17**(15): p. 2260-2.
151. Koch, S., et al., *Enhancing angiogenesis in collagen matrices by covalent incorporation of VEGF.* J Mater Sci Mater Med, 2006. **17**(8): p. 735-41.
152. Lutolf, M.P. and J.A. Hubbell, *Synthetic biomaterials as instructive extracellular microenvironments for morphogenesis in tissue engineering.* Nat Biotechnol, 2005. **23**(1): p. 47-55.
153. Fournier, E., et al., *Biocompatibility of implantable synthetic polymeric drug carriers: focus on brain biocompatibility.* Biomaterials, 2003. **24**(19): p. 3311-31.
154. Akdemir, Z.S., et al., *Preparation of biocompatible, UV-cured fumarated poly(ether-ester)-based tissue-engineering hydrogels.* J Biomater Sci Polym Ed, 2011. **22**(7): p. 857-72.
155. McCollum, A.T., P. Nasr, and S. Estus, *Calpain activates caspase-3 during UV-induced neuronal death but only calpain is necessary for death.* J Neurochem, 2002. **82**(5): p. 1208-20.
156. Mendelev, N., S. Witherspoon, and P.A. Li, *Overexpression of human selenoprotein H in neuronal cells ameliorates ultraviolet irradiation-induced damage by modulating cell signaling pathways.* Exp Neurol, 2009. **220**(2): p. 328-34.
157. Cheng, I.H., et al., *Collagen VI protects against neuronal apoptosis elicited by ultraviolet irradiation via an Akt/phosphatidylinositol 3-kinase signaling pathway.* Neuroscience, 2011. **183**: p. 178-88.

158. Kolb, H.C., M.G. Finn, and K.B. Sharpless, *Click Chemistry: Diverse Chemical Function from a Few Good Reactions.* Angew Chem Int Ed Engl, 2001. **40**(11): p. 2004-2021.
159. Bock, V.D., et al., *Click chemistry as a route to cyclic tetrapeptide analogues: synthesis of cyclo-[Pro-Val-psi(triazole)-Pro-Tyr].* Org Lett, 2006. **8**(5): p. 919-22.
160. Chang, P.V., et al., *Copper-free click chemistry in living animals.* Proc Natl Acad Sci U S A, 2010. **107**(5): p. 1821-6.
161. Jewett, J.C. and C.R. Bertozzi, *Cu-free click cycloaddition reactions in chemical biology.* Chem Soc Rev, 2010. **39**(4): p. 1272-9.
162. DeForest, C.A., B.D. Polizzotti, and K.S. Anseth, *Sequential click reactions for synthesizing and patterning three-dimensional cell microenvironments.* Nat Mater, 2009. **8**(8): p. 659-64.
163. Sgouros, S., et al., *Intracranial volume change in craniosynostosis.* J Neurosurg, 1999. **91**(4): p. 617-25.
164. Robin, N.H., *Molecular genetic advances in understanding craniosynostosis.* Plast Reconstr Surg, 1999. **103**(3): p. 1060-70.
165. Medina, L.S., *Three-dimensional CT maximum intensity projections of the calvaria: a new approach for diagnosis of craniosynostosis and fractures.* AJNR Am J Neuroradiol, 2000. **21**(10): p. 1951-4.
166. Yang, F., et al., *The study of abnormal bone development in the Apert syndrome Fgfr2+/S252W mouse using a 3D hydrogel culture model.* Bone, 2008. **43**(1): p. 55-63.
167. Holmes, G., et al., *Early onset of craniosynostosis in an Apert mouse model reveals critical features of this pathology.* Dev Biol, 2009. **328**(2): p. 273-84.
168. Wang, Y., et al., *Activation of p38 MAPK pathway in the skull abnormalities of Apert syndrome Fgfr2(+P253R) mice.* BMC Dev Biol, 2010. **10**: p. 22.
169. Perlyn, C.A., et al., *The craniofacial phenotype of the Crouzon mouse: analysis of a model for syndromic craniosynostosis using three-dimensional MicroCT.* Cleft Palate Craniofac J, 2006. **43**(6): p. 740-8.
170. Parkinson, I.H., A. Badiei, and N.L. Fazzalari, *Variation in segmentation of bone from micro-CT imaging: implications for quantitative morphometric analysis.* Australas Phys Eng Sci Med, 2008. **31**(2): p. 160-4.
171. Farmaki, C., et al., *Spatially adaptive active contours: a semi-automatic tumor segmentation framework.* International Journal of Computer Assisted Radiology and Surgery, 2010. **5**(4): p. 369-384.
172. Warren, S.M. and M.T. Longaker, *The pathogenesis of craniosynostosis in the fetus.* Yonsei Med J, 2001. **42**(6): p. 646-59.
173. Gosain, A.K., et al., *Application of micro-computed tomographic scanning to characterize patterns of murine cranial suture fusion.* Plast Reconstr Surg, 2011. **127**(5): p. 1847-54.
174. Hermann, C.D., et al., *Algorithm to Assess Cranial Suture Fusion with Varying and Discontinuous Mineral Density* Annals of Biomedical Engineering, 2012. **In Press**.

175. Li, R., et al., *Relationships of dietary fat, body composition, and bone mineral density in inbred mouse strain panels.* Physiol Genomics, 2008. **33**(1): p. 26-32.
176. Greenwald, J.A., et al., *Regional differentiation of cranial suture-associated dura mater in vivo and in vitro: implications for suture fusion and patency.* J Bone Miner Res, 2000. **15**(12): p. 2413-30.
177. Hermann, C.D., et al., *Biphasic Fusion of the Murine Posterior Frontal Suture Part 1: Complete Time Course.* Plast Reconstr Surg, 2012. **Submitted**.
178. Ganss, B., R.H. Kim, and J. Sodek, *Bone sialoprotein.* Crit Rev Oral Biol Med, 1999. **10**(1): p. 79-98.
179. Qin, C., R. D'Souza, and J.Q. Feng, *Dentin matrix protein 1 (DMP1): new and important roles for biomineralization and phosphate homeostasis.* J Dent Res, 2007. **86**(12): p. 1134-41.
180. Opperman, L.A., et al., *Cranial suture obliteration is induced by removal of transforming growth factor (TGF)-beta 3 activity and prevented by removal of TGF-beta 2 activity from fetal rat calvaria in vitro.* J Craniofac Genet Dev Biol, 1999. **19**(3): p. 164-73.
181. Pan, Q., et al., *Sox9, a key transcription factor of bone morphogenetic protein-2-induced chondrogenesis, is activated through BMP pathway and a CCAAT box in the proximal promoter.* J Cell Physiol, 2008. **217**(1): p. 228-41.
182. Schmid, T.M., et al., *Late events in chondrocyte differentiation: hypertrophy, type X collagen synthesis and matrix calcification.* In Vivo, 1991. **5**(5): p. 533-40.
183. Hermann, C.D., et al., *Biphasic Fusion of the Murine Posterior Frontal Suture Part 2: Genes Associated with Early Cartilage Induction in Suture Fusion.* Plast Reconstr Surg, 2012. **Submitted**.
184. Hoffman, L.M., et al., *BMP action in skeletogenesis involves attenuation of retinoid signaling.* J Cell Biol, 2006. **174**(1): p. 101-13.
185. Perry, M.J., et al., *Impaired growth plate function in bmp-6 null mice.* Bone, 2008. **42**(1): p. 216-25.
186. Kusu, N., et al., *Sclerostin is a novel secreted osteoclast-derived bone morphogenetic protein antagonist with unique ligand specificity.* J Biol Chem, 2003. **278**(26): p. 24113-7.
187. Dieudonne, S.C., et al., *Opposite effects of osteogenic protein and transforming growth factor beta on chondrogenesis in cultured long bone rudiments.* J Bone Miner Res, 1994. **9**(6): p. 771-80.
188. Fearon, J.A., R.A. Ruotolo, and J.C. Kolar, *Single sutural craniosynostoses: surgical outcomes and long-term growth.* Plast Reconstr Surg, 2009. **123**(2): p. 635-42.
189. Drake, D.B., et al., *Calvarial deformity regeneration following subtotal craniectomy for craniosynostosis: a case report and theoretical implications.* J Craniofac Surg, 1993. **4**(2): p. 85-9; discussion 90.
190. Turner, P.T. and A.F. Reynolds, *Generous craniectomy for Kleeblattschadel anomaly.* Neurosurgery, 1980. **6**(5): p. 555-8.
191. Gonzalez-Lagunas, J. and J. Mareque, *Calvarial bone harvesting with piezoelectric device.* J Craniofac Surg, 2007. **18**(6): p. 1395-6.

192. Gurevitch, O., et al., *Reconstruction of cartilage, bone, and hematopoietic microenvironment with demineralized bone matrix and bone marrow cells.* Stem Cells, 2003. **21**(5): p. 588-97.
193. Mooney, M.P., et al., *Increased intracranial pressure after coronal suturectomy in craniosynostotic rabbits.* J Craniofac Surg, 1999. **10**(2): p. 104-10.
194. Rice, D.P., et al., *Integration of FGF and TWIST in calvarial bone and suture development.* Development, 2000. **127**(9): p. 1845-55.
195. Paznekas, W.A., et al., *Genetic heterogeneity of Saethre-Chotzen syndrome, due to TWIST and FGFR mutations.* Am J Hum Genet, 1998. **62**(6): p. 1370-80.
196. Richtsmeier, J.T. and V.B. Deleon, *Morphological integration of the skull in craniofacial anomalies.* Orthod Craniofac Res, 2009. **12**(3): p. 149-58.
197. Smartt, J.M., Jr., et al., *Intrauterine fetal constraint induces chondrocyte apoptosis and premature ossification of the cranial base.* Plast Reconstr Surg, 2005. **116**(5): p. 1363-9.
198. Perlyn, C.A., et al., *Plasticity of the endocranial base in nonsyndromic craniosynostosis.* Plast Reconstr Surg, 2001. **108**(2): p. 294-301.
199. Marsh, J.L. and M.W. Vannier, *Cranial base changes following surgical treatment of craniosynostosis.* Cleft Palate J, 1986. **23 Suppl 1**: p. 9-18.
200. Ranly, D.M., *A Synopsis of Craniofacial Growth*. 2nd ed. 1988, Norwalk, Conneticut: Appleton and Lange.
201. Proff, P., et al., *Cranial base features in skeletal Class III patients.* Angle Orthod, 2008. **78**(3): p. 433-9.
202. Lei, W.Y., R.W. Wong, and A.B. Rabie, *Factors regulating endochondral ossification in the spheno-occipital synchondrosis.* Angle Orthod, 2008. **78**(2): p. 215-20.
203. Shum, L., et al., *BMP4 promotes chondrocyte proliferation and hypertrophy in the endochondral cranial base.* Int J Dev Biol, 2003. **47**(6): p. 423-31.
204. Rosenberg, P., et al., *The role of the cranial base in facial growth: experimental craniofacial synostosis in the rabbit.* Plast Reconstr Surg, 1997. **99**(5): p. 1396-407.
205. Lee, C.S., et al., *Coordinated tether formation in anatomically distinct mice growth centers is dependent on a functional vitamin D receptor and is tightly linked to three-dimensional tissue morphology.* Bone, 2011. **49**(3): p. 419-27.
206. Warren, S.M., et al., *New developments in cranial suture research.* Plast Reconstr Surg, 2001. **107**(2): p. 523-40.
207. Truett, G.E., et al., *Preparation of PCR-quality mouse genomic DNA with hot sodium hydroxide and tris (HotSHOT).* Biotechniques, 2000. **29**(1): p. 52, 54.
208. Chen, J., et al., *Formation of tethers linking the epiphysis and metaphysis is regulated by vitamin d receptor-mediated signaling.* Calcif Tissue Int, 2009. **85**(2): p. 134-45.
209. Rubin, J., et al., *Caveolin-1 knockout mice have increased bone size and stiffness.* J Bone Miner Res, 2007. **22**(9): p. 1408-18.
210. Hildebrand, T., et al., *Direct three-dimensional morphometric analysis of human cancellous bone: microstructural data from spine, femur, iliac crest, and calcaneus.* J Bone Miner Res, 1999. **14**(7): p. 1167-74.

211. Hermann, C., et al., *Rapid Re-synostosis Following Suturectomy in Pediatric Mice is Age and Location Dependent.* Bone, 2012. **Submitted**.
212. Shibazaki, R., et al., *Biomechanical strain and morphologic changes with age in rat calvarial bone and sutures.* Plast Reconstr Surg, 2007. **119**(7): p. 2167-78; 2179-81.
213. Gripp, K.W., E.H. Zackai, and C.A. Stolle, *Mutations in the human TWIST gene.* Hum Mutat, 2000. **15**(5): p. 479.
214. Cakouros, D., et al., *Twist-ing cell fate: mechanistic insights into the role of twist in lineage specification/differentiation and tumorigenesis.* J Cell Biochem, 2010. **110**(6): p. 1288-98.
215. Guzzo, R.M., et al., *Persistent expression of Twist1 in chondrocytes causes growth plate abnormalities and dwarfism in mice.* Int J Dev Biol, 2011. **55**(6): p. 641-7.
216. Okamura, H., K. Yoshida, and T. Haneji, *Negative regulation of TIMP1 is mediated by transcription factor TWIST1.* Int J Oncol, 2009. **35**(1): p. 181-6.
217. Wang, F., et al., *Injectable, rapid gelling and highly flexible hydrogel composites as growth factor and cell carriers.* Acta Biomater, 2010. **6**(6): p. 1978-91.
218. Browning, M.B., et al., *Compositional control of poly(ethylene glycol) hydrogel modulus independent of mesh size.* J Biomed Mater Res A, 2011. **98**(2): p. 268-73.
219. Hsu, C.W., et al., *Cathepsin K-sensitive poly(ethylene glycol) hydrogels for degradation in response to bone resorption.* J Biomed Mater Res A, 2011. **98**(1): p. 53-62.
220. Hein, J.E. and V.V. Fokin, *Copper-catalyzed azide-alkyne cycloaddition (CuAAC) and beyond: new reactivity of copper(I) acetylides.* Chem Soc Rev, 2010. **39**(4): p. 1302-15.
221. Ning, X., et al., *Visualizing metabolically labeled glycoconjugates of living cells by copper-free and fast huisgen cycloadditions.* Angew Chem Int Ed Engl, 2008. **47**(12): p. 2253-5.
222. Hurst-Kennedy, J., B.D. Boyan, and Z. Schwartz, *Lysophosphatidic acid signaling promotes proliferation, differentiation, and cell survival in rat growth plate chondrocytes.* Biochim Biophys Acta, 2009. **1793**(5): p. 836-46.
223. Lee, S.Y., et al., *Unconfined compression properties of a porous poly(vinyl alcohol)-chitosan-based hydrogel after hydration.* Acta Biomater, 2009. **5**(6): p. 1919-25.
224. Hsu, D.R., et al., *The Xenopus dorsalizing factor Gremlin identifies a novel family of secreted proteins that antagonize BMP activities.* Mol Cell, 1998. **1**(5): p. 673-83.
225. Bergmeyer, H.U., J. Bergmeyer, and M. Grassl, *Methods of enzymatic analysis*. 3rd ed. 1983, Weinheim ; Deerfield Beach, Fla.: Verlag Chemie. v. <1-9, 14 >.